Max-Planck-Institut
für Meteorologie

MAX-PLANCK-GESELLSCHAFT

The Arctic hydrologic cycle and its variability in a regional coupled climate model

Anne Laura Niederdrenk

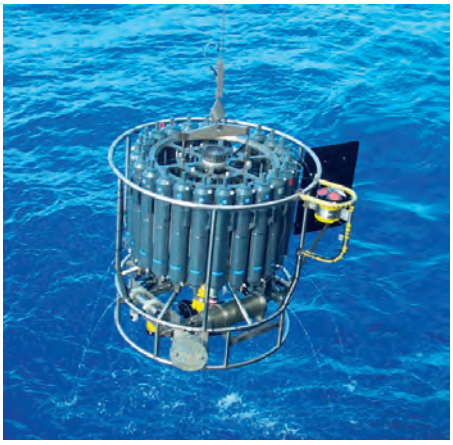

Berichte zur Erdsystemforschung 138
2013

Reports on Earth System Science

Hinweis

Die Berichte zur Erdsystemforschung werden vom Max-Planck-Institut für Meteorologie in Hamburg in unregelmäßiger Abfolge herausgegeben.

Sie enthalten wissenschaftliche und technische Beiträge, inklusive Dissertationen.

Die Beiträge geben nicht notwendigerweise die Auffassung des Instituts wieder.

Die "Berichte zur Erdsystemforschung" führen die vorherigen Reihen "Reports" und "Examensarbeiten" weiter.

Notice

The Reports on Earth System Science are published by the Max Planck Institute for Meteorology in Hamburg. They appear in irregular intervals.

They contain scientific and technical contributions, including Ph. D. theses.

The Reports do not necessarily reflect the opinion of the Institute.

The "Reports on Earth System Science" continue the former "Reports" and "Examensarbeiten" of the Max Planck Institute.

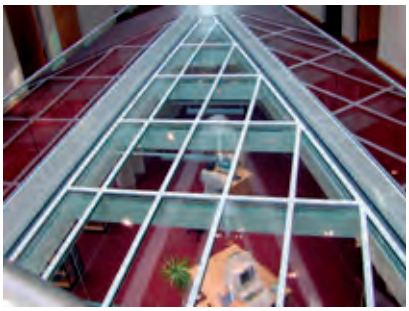

Anschrift / Address

Max-Planck-Institut für Meteorologie
Bundesstrasse 53
20146 Hamburg
Deutschland

Tel.: +49-(0)40-4 11 73-0
Fax: +49-(0)40-4 11 73-298
Web: www.mpimet.mpg.de

Layout:

Bettina Diallo, PR & Grafik

Titelfotos:
vorne:
Christian Klepp - Jochem Marotzke - Christian Klepp
hinten:
Clotilde Dubois - Christian Klepp - Katsumasa Tanaka

Berichte zur Erdsystemforschung 138/2013

The Arctic hydrologic cycle and its variability in a regional coupled climate model

Anne Laura Niederdrenk

aus Aachen

Hamburg 2013

Reports on Earth System Science 138/2013

ISSN 1614-1199

Anne Laura Niederdrenk
Max-Planck-Institut für Meteorologie
Bundesstrasse 53
20146 Hamburg

Als Dissertation angenommen
vom Department Geowissenschaften der Universität Hamburg

auf Grund der Gutachten von
Prof. Dr. Lars Kaleschke
und
Dr. Uwe Mikolajewicz

Hamburg, den 12. Juli 2013
Prof. Dr. Jürgen Oßenbrügge
Leiter des Departments für Geowissenschaften

ISSN 1614-1199

The Arctic hydrologic cycle and its variability in a regional coupled climate model

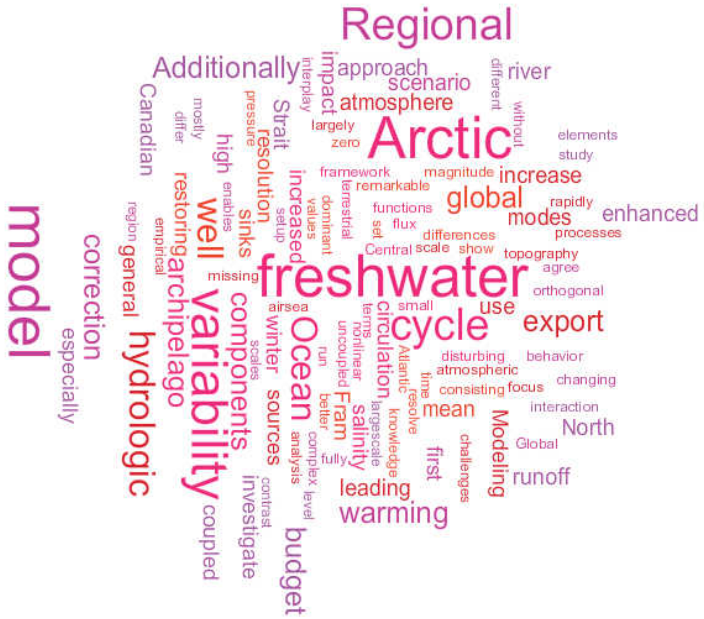

Anne Laura Niederdrenk

Hamburg 2013

Abstract

Modeling the Arctic hydrologic cycle implies big challenges because of the non-linear behavior and interplay of its elements on different scales. Additionally, the Arctic environment is rapidly changing due to global warming and so are the freshwater components. Global general circulation models show remarkable differences in modeling the Arctic freshwater cycle. While they agree on the general sinks and sources of the freshwater budget, they differ largely in the magnitude of the mean values as well as in the variability of the freshwater terms. Regional models can better resolve the complex topography and small scale processes, but they are often uncoupled, thus missing the air-sea interaction. Additionally, regional models mostly use some kind of salinity restoring or flux correction, thus disturbing the freshwater budget.

Our approach to investigate the Arctic hydrologic cycle and its variability is a regional atmosphere - ocean model setup, consisting of a global ocean model with high resolution in the Arctic coupled to a regional atmosphere model. To account for all sinks and sources of freshwater, we include a discharge model providing lateral terrestrial waterflows. In contrast to most regional setups, we run the model without salinity restoring but with freshwater correction. Additionally, this freshwater correction is set to zero in the Central Arctic. To our knowledge, this enables for the first time the analysis of a closed freshwater budget in the Arctic region with a fully coupled high resolution model.

In the framework of this study, we investigate how the dominant modes of large-scale atmospheric variability impact the variability in the freshwater components. We focus on the two leading empirical orthogonal functions of winter mean sea level pressure, as well as on the North Atlantic Oscillation and the Siberian High. These modes have a large impact on the Arctic Ocean circulation as well as on the solid and liquid export through Fram Strait and through the Canadian archipelago. However, they cannot explain the variability in river runoff. We find that not only winter conditions are responsible for increased river runoff, but also an enhanced summer cyclone activity, especially over Eurasia.

To analyze how the freshwater components change in a global warming scenario, we perform experiments for the first half of the 21st century and use data from an A1B scenario simulation from the fourth IPCC Assessment Report as forcing. Consistent with other model studies, we see an amplification of the Arctic hydrologic cycle. Our model simulates strongly enhanced precipitation, especially over land, leading to an increase in net freshwater input into the Arctic. The additional freshwater is partly stored within the Arctic Ocean and accumulates north of the Canadian archipelago, but so far the export of freshwater through the archipelago does not increase. The increased export through Fram Strait and the warming of the surface temperature lead to a decrease in deep-water formation in the Nordic Seas as well as in Labrador Sea.

Our approach to simulate the freshwater fluxes in the Arctic gives realistic results compared with observations. This model is a useful tool for understanding the underlying mechanisms causing the variability in the hydrologic cycle.

Contents

Chapter 1

Introduction

Observations and model results indicate that the Arctic climate changes rapidly (Anisimov et al. 2007; Meehl et al. 2007). Substantial changes can be seen in all climate components.

In the atmosphere, the air temperatures over large land areas increased by several degrees (Thompson and Wallace 1998; Anisimov et al. 2007) and the records of the warm surface air temperature anomalies for the recent decades have the greatest extent in the instrumental record (Overland et al. 2004). This warming, which is accompanied by a decrease in sea level pressure (Thompson and Wallace 1998), led to several minima of sea ice extent in the last decades. The smallest extent in satellite records was observed only recently in September 2012 (Maslanik 1999) and supports a long-term negative trend in Arctic summer sea ice extent (Parkinson et al. 1999; Comiso et al. 2008). The decrease in sea ice extent comes along with a decrease in sea ice thickness (Rothrock et al. 1999; Giles et al. 2008).

On land, the runoff from Eurasian rivers into the Arctic Ocean is increasing (Peterson et al. 2002) caused by an enhanced poleward moisture transport (Zhang et al. 2012).

As a result, the amount of freshwater (FW), defined as the amount of water with zero-salinity contained in a volume of water with salinity s relative to a reference salinity $s_{ref} = 34.8$ (Aagaard and Carmack 1989), stored within the Arctic Ocean is increasing (Giles et al. 2012). An accumulation of this FW within the Beaufort Gyre as well as a southeast shift of the gyre has been observed since the 1990s (Proshutinsky et al. 2009). Additionally, the Atlantic water that is entering the Arctic Ocean mostly via Barents Sea shows a warming and salinification over recent decades (Polyakov et al. 2004).

The Arctic hydrologic cycle, which is in delicate balance, is strongly affected by this rapidly changing Arctic environment. Changes in the FW cycle, such as increased FW export from the Arctic into the North Atlantic, can change the thermohaline circulation and consequently have the potential to influence the global climate (Anisimov et al. 2007). Understanding today's interplay between the different FW components and its variability is crucial to understand the already ongoing and the projected future changes.

1.1 The Arctic hydrologic cycle

Although only containing approximately 1 % of the total oceanic water, the Arctic Ocean receives about 11 % of the world's annual river runoff (Shiklomanov and Shiklomanov 2003). The drainage area of four of the world's major river systems - Ob, Yenisey, Lena

and Mackenzie - covers a huge area in the northern part of Eurasia and North America. Thus, the FW balance of the Arctic Mediterranean is dominated by terrestrial discharge.

Net precipitation (= precipitation minus evaporation) is positive over the Arctic Ocean and hence also a FW source. Additionally, the inflow of relatively fresh water from the Pacific into the Arctic Ocean through the narrow Bering Strait feeds the Arctic Ocean with FW.

On the other hand, the poleward flow of saline Atlantic-derived water through eastern Fram Strait and into Barents Sea is a FW sink for the Arctic Ocean. Ice and liquid water exported through Fram Strait and the Canadian Arctic archipelago (CAA) are the major sinks of FW in the Arctic Ocean. An overview of the sinks and sources contributing to the Arctic hydrologic cycle is given in the next section and in Figure 1.1.

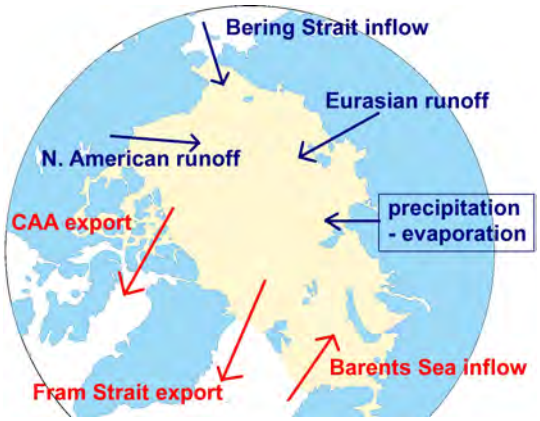

Figure 1.1: Schematic of the sinks (in red) and sources (in blue) of FW in the Arctic.

1.2 Observations and model studies

1.2.1 Observations

Even though the Arctic is a rapidly changing environment with large regional and global impacts on climate and society, "it is a region with a limited record of observations – low density, and with limited duration and coordination" (Committee on Designing an Arctic Observing Network 2006). Fortunately, and with large support from the research initiatives within the International Polar Year (2007-2008) activities, a lot of work has been done to collect and provide long-term Arctic-wide observational data including many different observational types, such as from satellites, ocean buoys and moorings, weather stations and hydrologic monitoring stations (Lichota and Wilson 2010; Committee on Designing an Arctic Observing Network 2006).

In the following, we explain in more detail the different sinks and sources of FW in the Arctic and the availability of observational information.

American and Eurasian river runoff Arctic river runoff is the major source of FW and a result of many different processes such as precipitation, evaporation, permafrost dynamics and soil infiltration. It provides the largest amount of the FW input into the Arctic Ocean (Serreze et al. 2006). Most of the Arctic runoff is given by four of the world's largest river systems: Ob, Yenisey and Lena in Eurasia and Mackenzie in North America. They contribute about 68 % of the annual volume discharging into the Arctic Ocean. Only the three Eurasian rivers contribute on average 57 % of the total discharge (Serreze and Barry 2005). The river discharge, excluding Hudson Bay, is about 4300 km^3/year (≈ 0.14 Sv), which is several times the net input of FW from net precipitation over the Arctic Ocean (Shiklomanov and Shiklomanov 2003). Other studies suggest a much smaller discharge (for example ~ 3300 km^3/year (≈ 0.1 Sv) by Aagaard and Carmack (1989), ~ 3200 km^3/year by Serreze et al. (2006)) underestimating the unmonitored discharge from adjacent continents and Arctic islands. The drainage basin of the Arctic Ocean includes an area thousands of kilometers beyond the Arctic circle, reaching 47 °N. Because of the very low winter temperature, more than 60 % of the runoff occurs from April to July, with high flow rates resulting from snow-melt in spring and floods in summer and autumn. The amplitude of the seasonal cycle in runoff depends strongly on climate conditions. For example in Siberia, a region with continental climate and continuous permafrost, the snow-melt contributes up to 80 % of the total annual runoff. The contribution of snow-melt in Europe and northeastern Canada is only about 50 % of the annual runoff. Rivers in continuous permafrost zones have practically no runoff during winter because of the very low supply of groundwater (International Arctic Science Committee 2010).

R-ArcticNET is probably the most comprehensive river discharge database for the Arctic (Vörösmarty et al. 1998) and was compiled from original national sources by investigators at the University of New Hampshire. It is a regional, hydrometeorological data network for the pan-Arctic region, with more than 3700 gauges covering the entire land draining into the Arctic Ocean including Hudson Bay, James Bay and Northern Bering Strait. The R-ArcticNET data base is composed of monthly data from 1877 to 1996 but the number of gauges as well as the number of measured time steps for the gauges is highly variable. Since 1985, there has been a decrease in the number of gauges, especially in Eurasia (Lammers et al. 2001; Shiklomanov and Shiklomanov 2003). But still, the area covered with observations exceeds 50 %, with the lowest numbers in North America. Greenland's glacier is not covered within R-ArcticNET.

A global discharge dataset is given by the NCAR Climate and Global Dynamics Division's Climate Analysis Section: The Dai and Trenberth Global River Flow and Continental Discharge Dataset (Dai and Trenberth 2002). It is a time series of monthly river flow rates for the world's 925 largest rivers, long-term river flow rates and continental discharge into the individual oceans, measured at the farthest downstream stations, respectively. The basic data for estimating continental discharge are gauge records of streamflow rates, but observational and reanalysis datasets are also used to compile these time series, for example from the United Nations Educational Scientific and Cultural Organisation (UNESCO), the United States Geological Survey (USGS), Russia's State Hydrological Institute and from the Global Runoff Data Centre (GRDC). Since the gauge data collection

from R-ARcticNET is also the basis for the data from Dai and Trenberth, the time series for the large Arctic rivers look similar.

Based on the data from GRDC, time series for monthly mean data for large catchments are also available in a technical report from Dümenil Gates et al. (2000). Some of the discharges used in this report are also taken from the Global River Discharge Database constructed by Vörösmarty, who is also a responsible for the R-ArcticNET data. Thus all these datasets use basically the same gauge data even though different analysis methods are used to construct the time series.

Inflow through Bering Strait Bering Strait, located between Alaska and Eastern Siberia, is the only ocean gateway between the Pacific and the Arctic. It is approximately 85 km wide and only about 55 m deep. The Diomede Islands divide the strait into two channels.

Spatial salinity variations in the upper ocean correspond to variations in density, thus causing variations in sea level. The salinity difference between the Pacific and the North Atlantic leads to a flow of low-salinity water from the North Pacific through Bering Strait, through the Arctic Ocean into the North Atlantic. Even though the annual mean flow at the Bering Strait is northward, there can be a flow southward for a week or more. The total annual mean flow is about 0.8 Sv. The variability of this mean flow is large (from 0.4 Sv to 1.2 Sv), mainly driven by the local winds, which oppose the oceanic pressure gradient (Woodgate et al. 2005). In winter, the throughflow provides cold waters stabilizing the upper Arctic Ocean and thereby influencing the upper ocean mixing and ice thickness.

While linking the global oceans, Bering Strait plays an important role in the global FW cycle. It provides approximately 2500 km^3/year ($\approx$ 0.08 Sv) of FW to the Arctic Ocean making it to the second largest source of Arctic FW (Serreze et al. 2006; Woodgate and Aagaard 2005). This number used to be highly underestimated for a long time (for example with 1670 km^3/year $\approx$ 0.05 Sv from Aagaard and Carmack (1989)), but thanks to long-term mooring programs, measuring temperature, salinity and velocity at different depths, and ship-based observations this number was increased by Woodgate and Aagaard (2005).

Precipitation minus evaporation In the region north of 50 °N net precipitation is mainly positive and thus provides FW for the Arctic rivers. As mentioned before, Arctic river runoff is much larger than any other source of FW in the Arctic region. In addition to that, a source of FW is given by precipitation over the Arctic Ocean directly. According to Serreze et al. (2006) the total amount of precipitation over the Arctic Ocean is approximately 2000 km^3/year ($\approx$ 0.06 Sv), calculated from the ECMWF reanalysis data ERA-40 for the years 1979 to 2001 (ECMWF 2002). However, there are big uncertainties in direct measurements of precipitation as well as evaporation not only over the Arctic Ocean but also over land. Windy conditions and wind-blown snow dispersal makes it impossible to give realistic stationary or ship measurements. In reanalysis data as well as in observations a seasonal cycle of precipitation minus evaporation can clearly be seen, with a maximum in July or August and a minimum in winter (for example in Cullather et al. (2000)).
The Hamburg Ocean Atmosphere Parameters and Fluxes from Satellite Data (HOAPS)

is a dataset providing a spatial distribution of precipitation and evaporation for the time period July 1987 to December 2005 (Andersson et al. 2010). The data is derived from the Special Sensor Microwave Imager (SSM/I) passive microwave satellite data over the global (ice-free) ocean. Additionally, the Global Precipitation Climatology Center (GPCC) provides global precipitation and evaporation data over land only for a time period from 1901 to 2007, varying over time in the number of stations (Rudolf and Schneider 2005; Rudolf et al. 2010). It is thus a complementary dataset to HOAPS and we use these two datasets combined for model validation in Chapter 3.

Fram Strait ice and liquid export The export through Fram Strait is the biggest sink of FW for the Arctic, bringing about $4700\,\mathrm{km}^3/\mathrm{year} \approx 0.15\,\mathrm{Sv}$ (Serreze et al. 2006) southward and thereby driving the large-scale thermohaline circulation. Besides ice melting, the ice export through Fram Strait is the main loss mechanism of Arctic sea ice. In addition to a large interannual variability there is a strong seasonal cycle of ice export with a maximum in February or March and a minimum in August or September. Spreen et al. (2009) calculate Fram Strait sea ice volume export using satellite data for the winter months October to May for the years 2003 to 2008 and compute a mean value of about $200\,\mathrm{km}^3/\mathrm{month}$ ($\approx 0.07\,\mathrm{Sv}$). They show that, in contrast to earlier studies of sea ice volume export (Vinje 2001; Kwok et al. 2004), a decreasing trend of ice export cannot be seen until 2008. According to Spreen et al. (2009) and also Kwok et al. (2004), the ice volume flux estimated from mooring and satellite data reaches about $2200\,\mathrm{km}^3/\mathrm{year}$ ($\approx 0.07\,\mathrm{Sv}$). These numbers have not been converted yet to the amount of FW within the sea ice. The salinity of sea ice is dependent on its age and thickness, with values up to 12 g/kg for newly formed ice and 4 - 6 g/kg for multi-year ice (Weeks 2010). Applying the average value of 5 g/kg, which is used in our model, the value given by Spreen et al. (2009) and Kwok et al. (2004) reduces to $1884\,\mathrm{km}^3/\mathrm{year}$ ($\approx 0.06\,\mathrm{Sv}$), which defines the FW fraction of the total amount of sea ice transport through the strait.

The variability in ice export through Fram Strait accounts for most of the variability in the total amount of FW exported through that strait. Nevertheless, the amount of FW exported in liquid form is nearly as large as the amount exported in ice form, but with much less variability. The estimates of the export of FW in liquid form vary, from rather low values of about $820\,\mathrm{km}^3/\mathrm{year}$ ($\approx 0.03\,\mathrm{Sv}$, Aagaard and Carmack (1989)) to $1900\,\mathrm{km}^3/\mathrm{year}$ ($\approx 0.06\,\mathrm{Sv}$, Serreze et al. (2006)).

Canadian Arctic archipelago ice and liquid export Due to a very complex topography and sparse measurements in the Canadian archipelago, there is still a big lack of understanding on how and how much of the FW is transported from the Arctic Ocean into Baffin Bay and Labrador Sea through the Canadian channels. In contrast to the export through Fram Strait, most of the FW is exported in liquid form. The seasonal cycle in the amount of exported FW is not as strong as in Fram Strait export. According to Serreze et al. (2006), approximately one third of the total FW is exported through the Canadian archipelago, which is about $3360\,\mathrm{km}^3/\mathrm{year}$ ($\approx 0.1\,\mathrm{Sv}$). Prinsenberg and Hamilton (2005) extrapolate from measurements with Acoustic Doppler Current Profilers moored in one

of the straits, in Lancaster Sound, the amount of FW through all channels and come up with a similar number of about 0.1 - 0.13 Sv. They admit that this might underestimate the total FW export because the Conductivity-Temperature-Depth sensors are located in a depth of 25 - 30 m and thus miss the fresher water above. The solid contribution to this amount is only about 5 % (Prinsenberg and Hamilton 2005), because for most of the year the ice is landfast.

Inflow through Barents Sea The relatively saline water coming from the North Atlantic and entering the Arctic through Barents Sea is a FW sink because the mean salinity is larger than the commonly used reference salinity of 34.8 g/kg. The water entering Barents Sea can be separated into different fluxes: the relatively fresh Norwegian coastal current, the relatively saline North Cape current and recirculated Atlantic water in the Bear Island Through. Rawlins et al. (2010) combine current-meter mooring data with other measurements and come up with a *freshwater export* of about 84 km^3/year ($\approx$ 0.027 Sv) as a sum of the three separated currents. The largest of them is the North Cape current, which is the only one counting as a FW sink, because of the saline Atlantic water. This number is consistent with calculations from Dickson et al. (2007) using observations from the EU VEINS and ASOF programs. Converting the number to the same reference salinity, they state 0.022 Sv as Barents Sea FW export (as it is Atlantic, thus saline, water import).

Freshwater storage within the Arctic Ocean Besides within sea ice, FW is also stored in liquid form in the Arctic Ocean. Because of a dominating anticyclonic atmospheric climate regime, which promotes Ekman pumping over Beaufort Sea, most of this liquid FW is stored in this Beaufort Gyre. The University of Washington Polar Science Center provides a Hydrographic Climatology (PHC, see Steele et al. (2001)), a monthly climatology for temperature and salinity merging a version of the World Ocean Atlas with a new regional Arctic Ocean Atlas. Estimated errors in FW content are about 10 %, reflecting the sparse hydrographic data and small spatial scales of salinity variations. Using a reference salinity of 34.8 g/kg and ignoring waters saltier than this reference value (to avoid negative FW volume) Serreze et al. (2006) come up with a number of approximately 84000 km^3 of total FW stored in the Arctic Ocean. About 74000 km^3 of this FW is in liquid form. It is discussed in the literature (Proshutinsky et al. 2002) that only a few percent of this amount exported into the North Atlantic could lead to a North Atlantic salinity anomaly comparable to the *Great Salinity Anomaly* of the 1970s. The amount of FW stored within sea ice is also very uncertain, because data of seasonal distribution of sea ice thickness are rare. Therefore the FW stored in sea ice is commonly calculated by a monthly distribution of sea ice extent exceeding 15 %, multiplied by an assumed mean sea ice thickness of 2 m, a salinity of 4 g/kg and a density of 900 kg/m^3. This yields 10000 km^3. It has to be mentioned that there is progress in measuring sea ice thickness via satellite data, for example from the European Space Agency (ESA) within the Soil Moisture and Ocean Salinity (SMOS) mission. The SMOSIce project is aiming to develop an algorithm for sea ice thickness retrieval from a 1.4 GHz (L-band) radiometry of the above mentioned mission from ESA. However, the uncertainties are still large and the first operational prototype of

a retrieval algorithm is limited to measuring sea-ice thicknesses of up to 0.5 m (Kaleschke et al. 2010).

1.2.2 Model studies

There are remarkable differences in the results of various coupled atmosphere ocean general circulation models simulating the hydrologic cycle of the Arctic. This is mainly caused by the too coarse spatial resolution of these global models, which prohibits resolving complex topographic features, such as the Canadian archipelago. The global models often lack an adequate representation of the small scale processes within the Arctic Ocean such as slope convection or overflows.

With an increase in northward moisture transport, some models project an increasing FW export through Fram Strait (Holland et al. 2006), while others simulate an increase in the storage of FW within the Arctic Ocean for the first half of the 21st century and an increasing export starting in the second half (Koenigk et al. 2007). The differences in these results highlight the lack of understanding of the main processes in the hydrologic cycle in such a highly coupled environment. It still remains unclear how the FW cycle responds to an increase of moisture transport northward to high latitudes as we expect in an environment warming due to anthropogenic changes. The mechanisms behind the variability of the FW export are also not fully understood, especially for the liquid FW export.

To overcome the limitation of resolution in global models, there are attempts to investigate the variability of the Arctic FW cycle with regional models. A recently published model intercomparison analysis is performed by Jahn et al. (2012). They compare several, mostly regional, ocean - sea ice model hindcast runs, conducted by several groups participating in the Arctic Ocean model intercomparison project (AOMIP). Since the experiments were performed with uncoordinated model forcing and model physics and with different lengths of integration, the comparable time window is only ten years. The models agree on the overall sinks and sources of the climatological FW budget of the Arctic but differ widely in the total amount and variability of the fluxes.

There also are regional coupled models used for Arctic climate investigations, for example by Koenigk et al. (2010); Döscher and Koenigk (2013); Mikolajewicz et al. (2005). Koenigk et al. (2010) use the Rossby Centre Atmosphere Ocean model RCAO, with regional focus on the Arctic and analyze, inter alia, the influence of surface salinity restoring on the variability in (surface) salinity and perform several experiments differing in the treatment of the surface salinity restoring or rather salinity flux correction. However, any kind of correction is an intervention in the modeled FW cycle. In a recent publication, Dorn et al. (2012) identify the limitations of the regional coupled model HIRHAM - NAOSIM, developed at the Alfred Wegener Institute for Polar and Marine Research, in the reproduction of the observed Arctic sea ice retreat. This model is not comparable to our setup, because the model domain is smaller, Arctic runoff is not included, and the Bering Strait is seen as a closed boundary, preventing the inflow of Pacific water into the Arctic.

We are to our knowledge the only group with a regional model setup including all sinks and sources of the FW cycle within the Arctic. Furthermore, we run experiments without any kind of flux correction in the Central Arctic, which allows, for the first time, for an analysis of a closed hydrologic budget.

1.3 Thesis Objective: A high resolution model setup to simulate a closed freshwater budget in the Arctic

To overcome the problem of coarse resolution, which is typical for global climate models, we use a global ocean model with shifted model grid poles. This leads to high horizontal resolution in the region of interest, the Arctic. Because the model is still global, no lateral boundary forcing is needed. The sea ice - ocean model is coupled to a regional atmosphere model covering the catchment areas of all rivers draining into the Arctic Ocean. To close the hydrologic cycle, we include into the atmosphere model a hydrological discharge model calculating terrestrial lateral runoff. Although the model is partly regional, we perform model experiments without any flux correction in the Arctic Ocean. This allows for an analysis of the FW budget without any artificial term arising from restoring. Such a model, including all components of the Arctic hydrologic cycle, in high resolution did not exist so far, especially not without any restoring in the Central Arctic. For more details to the model setup and the restoring procedure used in this study see Chapter 2.

We use this model setup for simulations with forcing from reanalysis data as well as with forcing from a global model run. In our analysis, we focus on the impact of dominant modes of large-scale atmospheric variability on the variability of the Arctic FW components. While analyzing the variability in the second half of the 20^{th} century, we want to answer the following question:

- How do atmospheric leading modes influence the variability of the Arctic hydrologic cycle?

As atmospheric leading modes we consider beside the first and second leading orthogonal function of winter mean sea level pressure also the North Atlantic Oscillation as well as the strength of the Siberian high. Since these modes do not explain runoff's variability, we add the following research question:

- What drives the variability in Arctic river runoff?

We also perform experiments using a global warming scenario and project future changes in the hydrologic cycle. Thereby, we want to answer:

- How do the components of the Arctic freshwater cycle change in the 21^{st} century?
- How do changes in the freshwater cycle affect the global ocean circulation?

1.4 Thesis Outline

In Chapter 2 we give an overview of our coupled regional model setup, consisting of the global sea ice - ocean model MPIOM and the regional atmosphere model REMO, as well as of the performed experiments.

In Chapter 3 we validate our model results against observations and reanalysis data. We compare experiments performed with different boundary forcing, either with NCEP reanalysis data or with data from a global model run. We show that the model reasonably simulates the Arctic climate and its FW components.

In Chapter 4 we analyze the variability of the Arctic FW components for the second half of the 20^{th} century. Thereby we focus on the variability induced by atmospheric leading modes as well as on the variability in Arctic river runoff.

In Chapter 5 we examine how the components of the Arctic FW cycle change in the first half of the 21^{st} century, using forcing data from a global warming experiment.

We conclude the thesis with a summary of our main results and give a perspective of possible future research.

Chapter 2

Model setup and experimental design

In this study we use a special setup of the global sea ice - ocean model of the Max Planck Institute for Meteorology coupled to the regional atmosphere model REMO. Since our focus is on the Arctic region, we use the ocean model with shifted grid poles leading to high resolution in the Arctic Ocean. The atmosphere model covers the Arctic region with all the catchment areas of the rivers draining into the Arctic Ocean, see Figure 2.1. A detailed description of the performed experiments is given in 2.4.

The model coupling and setup was developed by Dmitry Sein (Aldrian et al. 2005). The first application for the Arctic region is described in Mikolajewicz et al. (2005). It has also been applied for other regions, for instance for investigations on the water vapor transport and precipitation over the Mediterranean Sea (Elizalde et al. 2011; Elizalde and Jacob 2012). The model components are shortly described in the following sections.

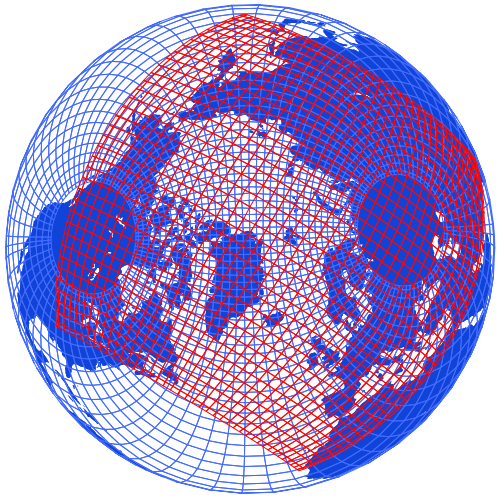

Figure 2.1: The computational grids of the model components. The ocean model grid is plotted in blue and the atmosphere model grid is plotted in red. Not every line is shown.

2.1 The regional atmosphere model REMO

The regional climate model REMO is a three-dimensional, hydrostatic atmospheric circulation model solving the primitive equations for atmospheric motion for a certain domain (Jacob 2001). It is based on the Europa - Modell (Majewski 1991), the former numerical

model for weather prediction of the German Weather Service DWD. The physical parameterization package is taken from the general circulation model ECHAM 4 (Roeckner et al. 1996). The prognostic variables in REMO are the horizontal wind velocity components, surface pressure, temperature, specific humidity and cloud liquid water. They are calculated horizontally on an Arakawa C-grid. The vertical variations of these prognostic variables are calculated on a hybrid vertical coordinate system, following the topography near the surface and pressure levels in the upper atmosphere. Our setup has 27 vertical levels and a horizontal resolution of approximately 55 km. Since it is a regional model, lateral boundaries are needed, either from a global model simulation or from reanalysis data. In any case, the prognostic variables of REMO are adjusted in a lateral sponge zone of several grid boxes to the large-scale forcing to avoid abrupt changes in their behavior. At the lower boundary REMO is coupled to the ocean model and receives the boundary values either from the ocean model, such as the sea surface temperature and the sea ice distribution, or from land surface characteristics that are included in the model.

2.1.1 The hydrological discharge model

We include, into the atmosphere model, the hydrological discharge (HD) model (Hagemann and Dümenil 1998) providing lateral terrestrial waterflow into the ocean. The HD model is part of the (global) Max Planck Institute Earth System Model (MPI-ESM), but it is usually not implemented in regional setups. The model uses the land surface characteristics to calculate the translation and retention of lateral discharge, thereby separating the waterflow into overland flow, baseflow and riverflow. The grid resolution is 0.5° and the input fields, precipitation and drainage (from REMO), are interpolated to this grid. Runoff is transferred to the ocean together with the difference of precipitation and evaporation.

2.2 The global sea ice - ocean model MPIOM

The Max Planck Institute Ocean Model (MPIOM) is a global general circulation model based on the primitive equations for a hydrostatic Boussinesq fluid on a rotating sphere with a free surface (Marsland et al. 2003). Parameterizations of sub-grid scale mixing processes, such as isopycnal diffusion of thermohaline fields, and a bottom boundary layer slope convection scheme for the flow across steep topography are included. A Hibler-type zero-layer dynamic thermodynamic sea ice model with viscous-plastic rheology is included (Hibler 1979). MPIOM allows for an arbitrary placement of the model's poles on an orthogonal curvilinear grid, based on an Arakawa C-grid. In our setup the grid poles are shifted over Russia and North America (as can be seen in Figure 2.1). Firstly, the placement over land removes the numerical singularity caused by the convergence of the meridians at the pole. Secondly, the non-diametric placement gives the possibility to reach high resolution in a region of interest.

As forcing data at the ocean's surface, the model needs heat, freshwater and momentum fluxes. Where coupled to the regional atmosphere model, the data is given by the atmosphere model itself and interpolated onto the ocean grid. Outside the coupled domain,

the data has to be provided externally. For more information on the forcing we refer to Section 2.4.

Restoring procedure within MPIOM

To avoid an undesirable model drift regional and / or uncoupled ocean models run usually with a sea surface salinity and / or sea surface temperature restoring, or more rarely with three dimensional salinity and / or temperature restoring. Moreover, the salinity restoring helps to correct for an unbalanced integrated surface freshwater (FW) flux. On the other hand it does not only damp the model variability but also affects the total amount of FW fluxes by adding or substracting an artificial term. A correction of the FW flux is calculated in the ocean model by adaptation of the surface salinity:

$$eminpo = \Delta z_1 * \left(\frac{\max\left(oldso, 10^{-3}\right)}{\max\left(sao, 10^{-3}\right)} - 1 \right), \tag{2.1}$$

where $eminpo = eminpo(t, x, y)$ is the water flux correction, Δz_1 the first model layer thickness, $oldso = oldso(t, x, y, z = 1)$ is the surface salinity calculated by the model and $sao = sao(t, x, y, z = 1)$ is the modified surface salinity, calculated by

$$sao = oldso + zzrestore \tag{2.2}$$

with the restoring term

$$zzrestore = dt * relsal * (relsao - oldso)\,. \tag{2.3}$$

The restoring salinity field $relsao = relsao(t, x, y, z = 1)$ can be time independent or, as in our case, time dependent. The constant value $1/relsal$ determines the relaxation time on salinity.
The salinity restoring to the observational dataset (Boyer et al. 1998), that is commonly used as a climatology for restoring, is in our setup too strong, especially at those coastal areas, where large input of FW enters the ocean, at the mouth of rivers. The climatology does not include the FW entering from rivers and shows higher than expected salinity values at the river mouth locations. In order to avoid artificial FW fluxes due to this deficiency in the salinity climatology, the restoring term in the coastal areas was modified as follows (Dmitry Sein, personal communication):

$$zzrestore = dt * zzrelsal * \max\left(\min\left(relsao - sao, \frac{1}{2} \right), -\frac{1}{2} \right), \tag{2.4}$$

with

$$zzrelsal = \frac{1}{2}\left(1 + \tanh\left(\frac{sao - 27}{1.1} \right) \right) * relsal. \tag{2.5}$$

The inequality $|relsao - sao| \leq \frac{1}{2}$ leads to a limitation in the restoring and thus avoids large amounts in the FW correction term. The hyperbolic tangent damps the restoring at areas with low salinity values, thus especially at the coastal areas, because for values smaller than around 30 g/kg the term *zzrestore* is reduced, strongest for values lower than 25 g/kg.

Anyway, as explained before, it is still undesirable to run the model with any form of salinity restoring because it affects the FW budget in a not completely determinable way. Therefore, in a first step we run the model without salinity restoring within the Arctic Ocean (see Figure 2.2 a)) for a few decades. Outside this domain, we use the restoring procedure as explained above. In a second step, we run the model in the whole coupled domain with FW flux correction instead of salinity restoring, using a climatology of the FW flux correction term from the previous run. This leads to a completely known (= constant) term in the coupled domain, which additionally equals zero in the Arctic and thus provides an *undisturbed* FW cycle in our region of interest. Outside the coupled domain we use salinity restoring to a surface salinity climatology with a relaxation time of about 77 days. Depending on the simulation, we relax the salinity fields either to the Levitus climatology or to a corrected version of the surface salinity fields from a global model run performed with ECHAM 5 / MPIOM. This corrected salinity fields are obtained by subtracting from the global salinity fields a climatology of the same salinity field for the years 1940 - 2000 and adding the Levitus climatology.

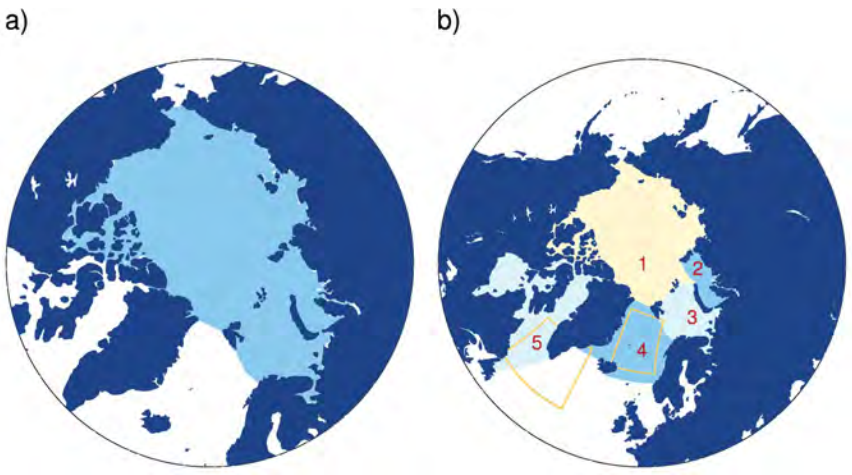

Figure 2.2: a) The light blue domain, covering the Arctic Ocean, shows the area where the restoring is set to zero. Outside this domain we run the model either with restoring or with a climatological freshwater correction. b) The different basins as used in this study: 1 Central Arctic Ocean, 2 Kara Sea, 3 Barents Sea, 4 GIN Sea, 5 Labrador Sea. The orange marked domains refer to the regions of deep-water production as used for calculation for the volume of ventilated water.

2.3 OASIS coupling scheme

The atmosphere model REMO and the sea ice - ocean model MPIOM are connected by the coupler OASIS 3 (Valcke 2006). This coupling is performed every six hours. OASIS transfers heat, momentum and FW fluxes from the atmosphere to the ocean. It performs the interpolation onto the grid of the ocean model. In exchange, sea surface temperature and sea ice characteristics are transferred from the ocean to the atmosphere. Glacier calving is included in the model such that precipitation over Greenland is instantaneously transferred into the ocean. A schematic representation of the coupling procedure and the transferred fluxes is given in Figure 2.3.

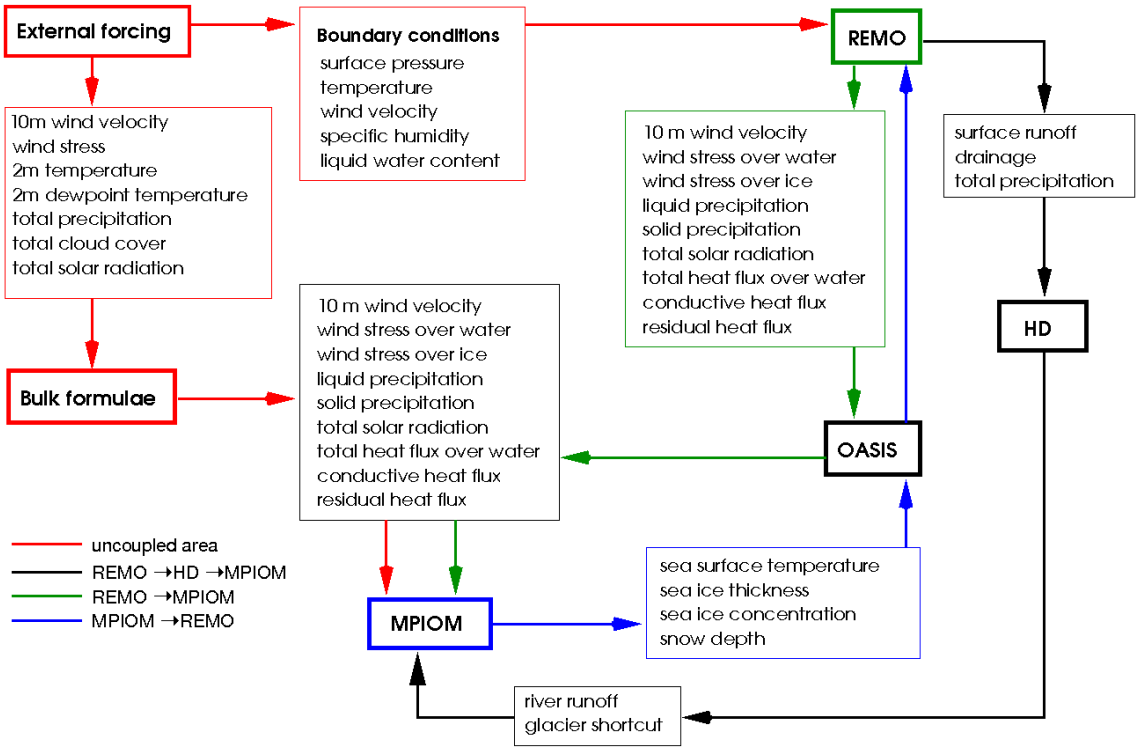

Figure 2.3: Schematic of the coupling between REMO, the HD model, MPIOM and the external forcing. The figure is based on a previous plot of Dmitry Sein (personal communication).

2.4 Experimental design

We have two different types of experiments. Firstly, we run the model with forcing taken from NCEP / NCAR reanalysis data (Kalnay et al. 1996). Secondly, we force the model with output from a global model run performed with ECHAM 5 / MPIOM. The forcing fields were provided by Dmitry Sein.

NCEP-forced experiments With NCEP forcing, we perform two similar experiments with only minor changes. After several decades for spin-up we perform an experiment

starting in the year 1949. This experiment is run with surface salinity restoring with a relaxation time on salinity of about 77 days. Secondly, we perform an experiment without restoring in the Arctic (as defined in Figure 2.2 a)). Outside this domain we run the experiment with the same relaxation time as the previous experiment. The second experiment is run for the years 1960 - 2007.

We use these two experiments, later referred to as NCEP-forced experiments, primarily for model validation and comparison with the other experiments, but not for the analysis of FW variability in the 20th century in Chapter 4.

ECHAM-forced experiments To analyze the FW variability in the 20th century as well as the projected changes within the 21st century we force the same model setup with output from an experiment performed with the Earth System Model ECHAM 5 / MPIOM in the framework of the Fourth Assessment Report of the Intergovernmental Panel of Climate Change (IPCC, Meehl et al. (2007)). For the 20th century, we use data from a global run, that was performed under historical forcing (C20 experiments). For projection experiments, we use data from a run, where the A1B scenario was used. The A1B scenario implies a monotonously increasing CO_2 concentration until the end of the 21st century, as highlighted in Figure 2.4, and was discussed in the Fourth Assessment Report as a rather realistic scenario. Radiative effects of the A1B scenario are prescribed within the atmosphere model.

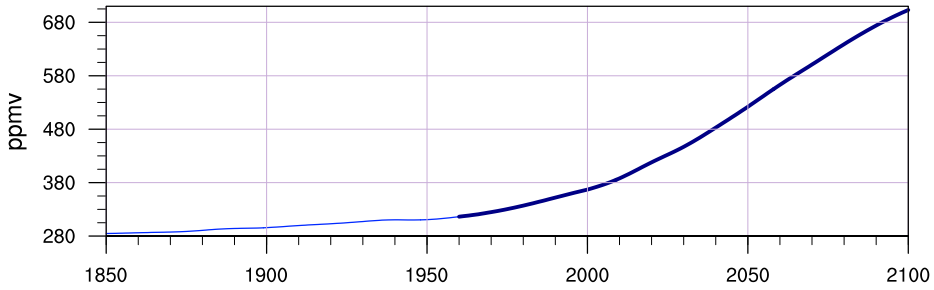

Figure 2.4: CO_2 concentration underlying the A1B scenario of the IPCC AR4 experiments.

We use different experiments, later referred to as ECHAM-forced experiments, that are forced with this global model output. The experiments mainly differ in the restoring procedure and the restart file. All experiments are run without salinity restoring in the coupled domain, but with FW correction. As explained before, there is no correction in the Arctic. In two experiments we use a ten years mean of a FW climatology term, and in two experiments we use a twenty years mean climatology from a different run. This means that the previous runs that were performed as spin-up with salinity restoring might have had a slightly different climate. This is within the model variability and might even be smaller than the variability within these four experiments that are used in this thesis. As mentioned before, the salinity restoring damps the variability of FW. Even though we use different restart and FW correction climatology files we can count the experiments as members of an ensemble run, although it is not an ensemble in the classical sense.

Table 2.1 gives an overview of the performed runs used for the analysis in this thesis.

The experiments 3 to 6 are used for the analysis of the 20th century in Chapter 3 and Chapter 4. The experiments 8 and 9 are the continuations from the experiments 6 and 4, respectively. They are used for the analysis of the changing Arctic climate in Chapter 5. The experiments 5 - 7 are parts of the corresponding control run used for comparison in the same chapter. We repeat the forcing data every 32 years.

Validation period For model validation we use the NCEP-forced experiments (1 and 2) and the four ECHAM-forced experiments 3 - 6. Since observations improved a lot with the start of satellite measurements after 1979, we mostly use the twenty year climatology of the years 1980 - 1999. Since the experiments 5 and 6 end after the year 1991 we only use the ten years period 1980 - 1989 in these two experiments.

	Forcing	Restoring	Years	Validation period
1.	NCEP	with salinity restoring, relaxation time of 77 days	1949 - 2007	1980 - 1999
2.	NCEP	with salinity restoring, set to zero in Central Arctic, relaxation time of 77 days	1960 - 2007	1980 - 1999
3.	ECHAM	without salinity restoring 10 year FW climatology as correction term	1960 - 1999	1980 - 1999
4.	ECHAM	without salinity restoring 20 year FW climatology as correction term	1960 - 1999	1980 - 1999
5.	ECHAM	without salinity restoring 20 year FW climatology (control run)	1960 - 1991	1980 - 1989
6.	ECHAM	without salinity restoring 20 year FW climatology (control run; continuation of 5.)	1960 - 1991	1980 - 1989
7.	ECHAM	without salinity restoring 20 year FW climatology (control run; continuation of 6.)	1960 - 1985	
8.	ECHAM	without salinity restoring (continuation of 6.)	1992 - 2043	
9.	ECHAM	without salinity restoring (split from 4. in after 1991)	1992 - 2069	

Table 2.1: Overview of performed experiments that are forced with NCEP and ECHAM forcing. The experiments 5., 6. and 7. add up to the control integration and cover the time period 1960 - 2049. The scenario experiments imply the experiments 4. and 9. (1960 - 2069), and 6. and 8. (1960 - 2043).

Chapter 3

Model validation

Modeling the Arctic freshwater (FW) cycle is challenging and model results differ widely in the mean state as well as in the variability of the FW components (Jahn et al. 2012). In this chapter we describe the mean state of the Arctic climate in the second half of the 20^{th} century as modeled with our regional setup, focusing thereby on surface and oceanic quantities that are most important for the hydrologic cycle.

Always when referring to FW, we use the following definition: An amount of FW is defined as the amount of water with zero-salinity contained in a volume V of water with a given salinity s relative to a reference salinity s_{ref}:

$$V_{FW} = \left(1 - \frac{s}{s_{ref}}\right) V = \frac{s_{ref} - s}{s_{ref}} V.$$

The commonly used reference salinity for the Arctic Ocean is given by $s_{ref} = 34.8\,\text{g/kg}$ (Aagaard and Carmack 1989), which is about the mean salinity of the Arctic Ocean. For convenience this reference salinity is also used in this study.

In Section 3.1 we compare model results from the experiments that are forced with NCEP reanalysis data as well as results from the experiments that are forced with ECHAM output from a global coupled experiment from ECHAM 5 / MPIOM to observational data. A detailed experiment description is given in Section 2.4. We describe the simulated mean state of important parameters of northern high latitudes. We focus on the components of the Arctic freshwater cycle and show beside the mean state also the time evolution of some of these variables.

In Section 3.2 we shortly compare results from the ECHAM-forced experiments with results from the global model run that is the base for the forcing data. We emphasize the added value of high resolution compared to lower resolution as used in global coupled experiments.

3.1 Comparison of model results with reanalysis and observational data

Since observations improved a lot after 1978 with the start of satellite measurements, we use for comparison of climatological mean values for the NCEP-forced experiments

a twenty years mean from 1980 - 1999 and for the ECHAM-forced runs either a twenty years or a ten years mean from 1980 - 1999 or 1980 - 1989, respectively. The reason for taking only 10 years from some experiments is due to a repetition of a 32 years period of the forcing for the control run. This leads to simulations from 1960 - 1991. Two of them are used for comparison in this chapter and from these runs we take the ten years period (1980 - 1989) only. The results do not differ strongly when taking the shorter interval for all experiments and observations; we prefer to include as much data as possible using the 20 years and 10 years intervals.

For some variables the seasonal mean values are shown in Appendix B.

3.1.1 Mean Arctic climate in the model

Mean sea level pressure Figure 3.1 shows the twenty years mean sea level pressure in the NCEP / NCAR reanalysis data (Figure 3.1 a)) and in the model experiments (Figure 3.1 b) and c)). The large scale atmospheric pressure system in the reanalysis is defined by high pressure systems over the North Atlantic and the North Pacific and over Siberia. Low pressure cells can be identified over Iceland, extending far into Barents Sea, and over the Aleutian Islands. Altogether, these patterns are leading to a mainly anticyclonic wind regime in the Central Arctic as well as to the so-called transpolar drift; winds from the western Siberian coast across the Arctic to Fram Strait and to northern Greenland. The pressure systems in the Arctic, especially the Siberian high, are more pronounced in the winter season, thus bringing stronger winds in winter than in summer (see Figure B.1 for seasonal mean values).

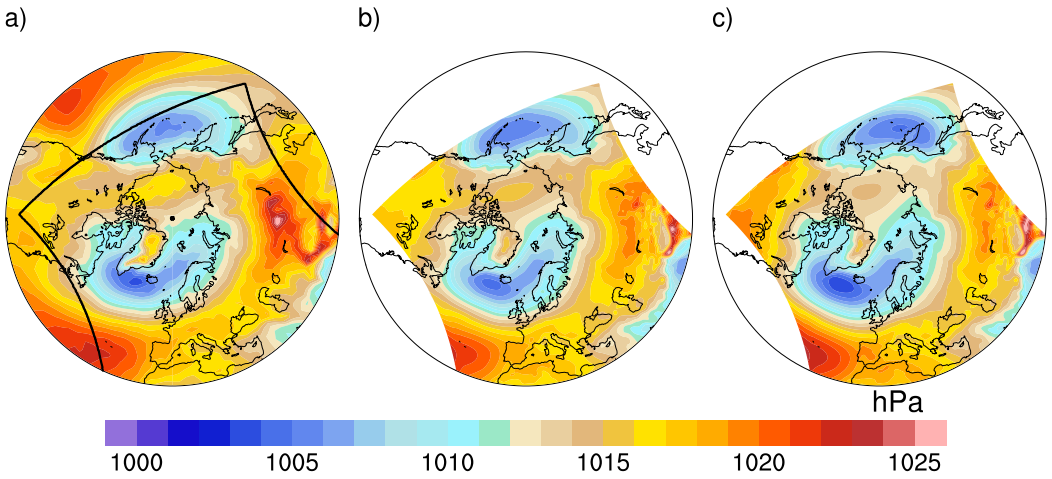

Figure 3.1: Annual mean sea level pressure in hPa from a) NCEP data for the time period 1980 - 1999, b) model data from the NCEP-forced experiments for the time period 1980 - 1999 and c) model data from the ECHAM-forced experiments for the periods 1980 - 1989 and 1980 - 1999. The black contour line in a) indicates the regional domain from the atmospheric model.

The simulated mean sea level pressure reproduces in both experiment setups the main features of the reanalysis pressure distribution. Since the model is regional and thus strongly influenced by the boundary data, it is not surprising, that the features, closed

to the model boundaries such as the Azores high in the North Atlantic, match very well for the NCEP-forced experiments in size and strength. This is true especially at these boundaries where there is a strong inflow of winds into the model domain. The ECHAM-forced experiments show the same features even though they do not receive the NCEP reanalysis data at the boundaries. In the NCEP-forced experiments (Figure 3.1 b)) the extension from the Icelandic low into Labrador Sea is slightly weaker than in the reanalysis, which can be seen also in Figure 3.2 a). The Siberian high is also somewhat weaker than in the reanalysis but the extension westward into Europe fits nicely. The mean sea level pressure over the eastern Central Arctic Ocean is slightly underestimated, thus decreasing the pressure gradient and thereby reducing the geostrophic winds over the Arctic Ocean from the Siberian coast to the Canadian Arctic Archipelago and to northern Greenland. The same is true for the ECHAM-forced experiments (Figure 3.1 c) and Figure 3.2 b)). The mean sea level pressure in the Central Arctic and in Siberia is underestimated by approximately 2 to 4 hPa. Nevertheless, the model data forced with NCEP as well as with ECHAM data is in good agreement with the reanalysis.

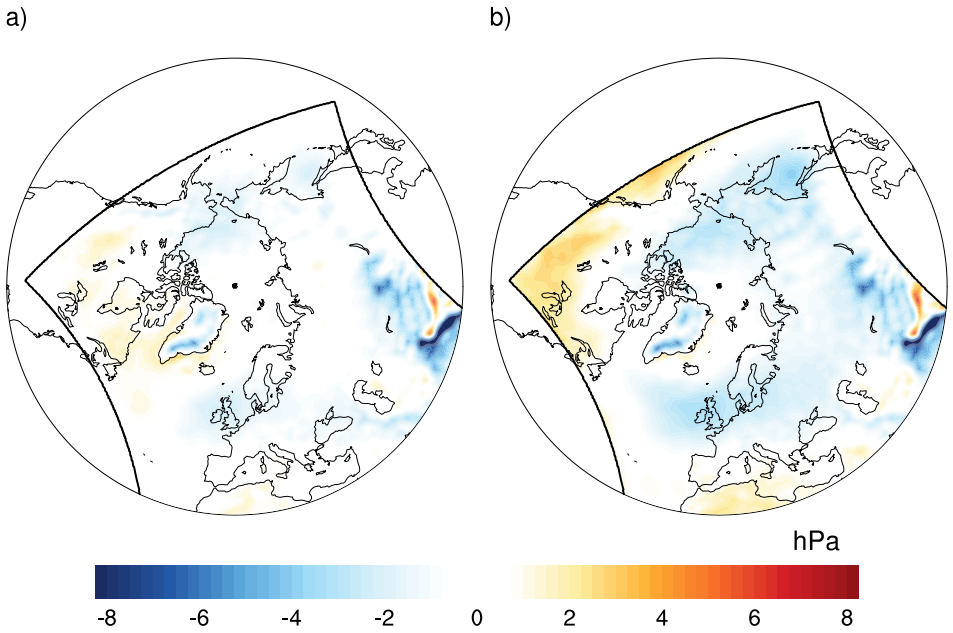

Figure 3.2: Annual mean sea level pressure difference from a) model data from the NCEP-forced experiments and NCEP data for the time period 1980 - 1999 in hPa and b) model data from the ECHAM-forced experiments and NCEP data.

Air temperature The multi-year two meter air temperature, averaged over the time period 1980 - 1999 from NCEP reanalysis data, shows the expected north - south gradient (Figure 3.3 a)). The temperature is lowest in the Central Arctic Ocean and Greenland reaching temperatures of less than -20 °Celsius and temperatures exceedind 20 °Celsius in the Subtropics. The main deviations from this zonal temperature gradient appear in three main regions. In the North Atlantic, where warm air masses are reaching high latitudes

due to heat transport of the North Atlantic Current and due to southwesterly winds, it is warmer than in other regions of this latitude. The landmass of Asia leads to cooling in winter, which leads to colder annual mean temperatures than in the zonal mean. The same effect can be seen over the landmasses of North America but not as pronounced as in Asia.

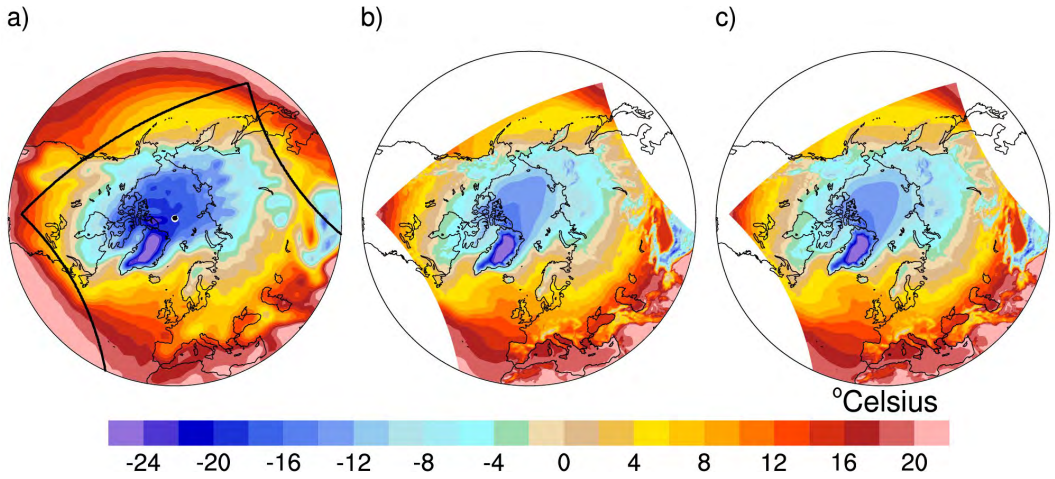

Figure 3.3: Annual mean 2 m air temperature in °Celsius from a) NCEP data for the time period 1980 - 1999, b) model data from NCEP-forced experiments for the time period 1980 - 1999 and c) model data from ECHAM-forced experiments for the time period 1980 - 1989 and 1980 - 1999. The black contour line in a) indicates the regional domain from the atmospheric model.

Again, the simulated air temperatures, for both model setups, reproduce the main features of the spatial distribution in the reanalysis but they are slightly too warm over the Arctic Ocean (Figure 3.3 b) and Figure 3.3 c)). In Figure 3.4 it can be seen that this is most pronounced, in both experiment setups, over Kara Sea. The difference between modeled data and reanalysis reaches about 5 °Celsius in this region. The bias is somewhat smaller in the ECHAM-forced experiments (Figure 3.3 b)). As can be seen in Figure B.2 in Appendix B, the model is too warm in both experiment setups, in nearly all seasons, but especially in winter (December - February) and spring (March - May). The strongest bias appears in the NCEP-forced experiments in spring, where the model is too warm, not only over the Arctic Ocean, but also over Eurasia as well as over North America.

Sea water temperature Whereas the global ocean is dominantly characterized by a stable upper-ocean stratification with less dense and warmer water at the sea surface, the Arctic Ocean stratification is not determined by temperature but by salinity. The effect of salinity on density is in high latitudes larger than the effect of temperature. This leads to a surface layer of relatively fresh and cold water, which is fed by river runoff and the inflow of relatively fresh Pacific water. Below this cold layer, there is a warmer (and saltier) water layer, which is mainly fed by Atlantic derived water. In the deep Arctic Ocean it is becoming colder again with depth.

Consequently, the vertical temperature structure of the Arctic Ocean is characterized

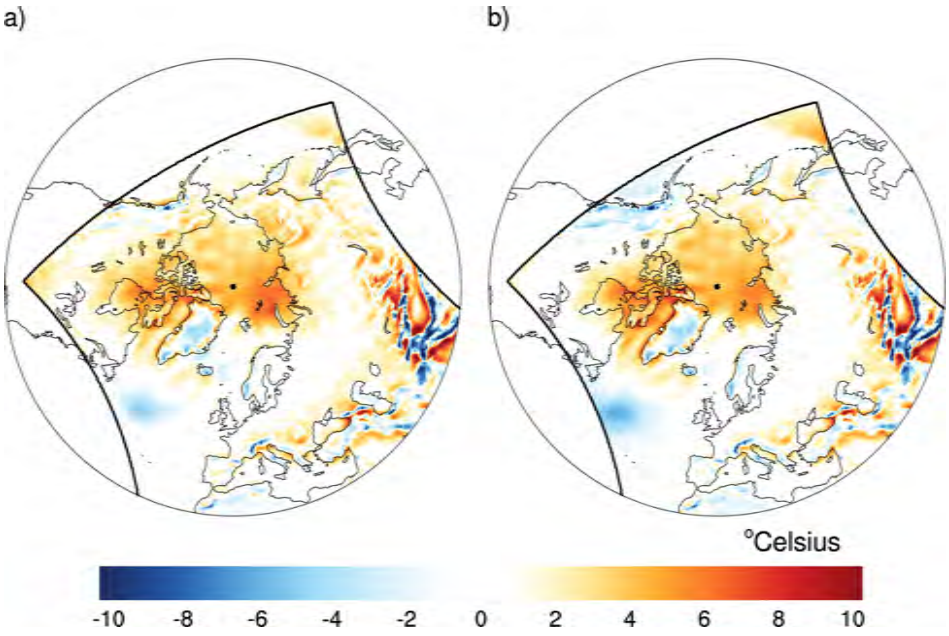

Figure 3.4: Annual mean 2 m air temperature difference from a) model data from NCEP-forced experiments and NCEP data for the time period 1980 - 1999 and b) model data from ECHAM-forced experiments for the time period 1980 - 1989 and 1980 - 1999 and NCEP data.

by a stable stratification with a strong thermocline between 200 and 300 m (upper row in Figure 3.5). Below this, the warm layer of Atlantic waters has temperatures of more than 0.5 °Celsius. The sea surface temperature and salinity observations in Figure 3.5 to Figure 3.7 are taken from the Polar science center Hydrographic Climatology (PHC), a gridded ocean climatology for temperature and salinity based on the World Ocean Atlas (Antonov et al. 1998; Boyer et al. 1998) and the regional Arctic Ocean Atlas (Arctic Climatology Project 1997, 1998). The model is not able to reproduce the strength of the Arctic thermocline (Figure 3.5 a)). In the NCEP-forced experiments (middle column in Figure 3.6) the water temperature below 300 m is underestimated by more than 1 °Celsius. This bias is somewhat smaller in the ECHAM-forced experiments, but nevertheless the thermocline is not as steep as in the observational data. Below 300 m the ECHAM-forced experiments do show warmer temperatures than the NCEP-forced experiments in all basins. The difference from the ECHAM-forced experiments to observations is largest below 900 m and reaches nearly 2 °Celsius in Labrador Sea. In Kara Sea, however, the temperatures do fit nicely to observations, whereas the NCEP-forced experiments are about 0.5 °Celsius too cold.

The seasonal cycle in sea water temperature only affects the surface layer and is in the Central Arctic as well as in Kara Sea very small compared to the other areas around the Central Arctic Ocean (left column in Figure 3.6). The model overestimates in both setups the strength of the seasonal cycle in Kara Sea. A difference between the two different model setups can be seen only in the strength of the seasonal cycle in the vertical profile of GIN Sea (Figure 3.6 c)). The NCEP-forced experiments underestimate not only the

winter temperature at the surface but also the water temperatures in 100 m - 400 m depth.

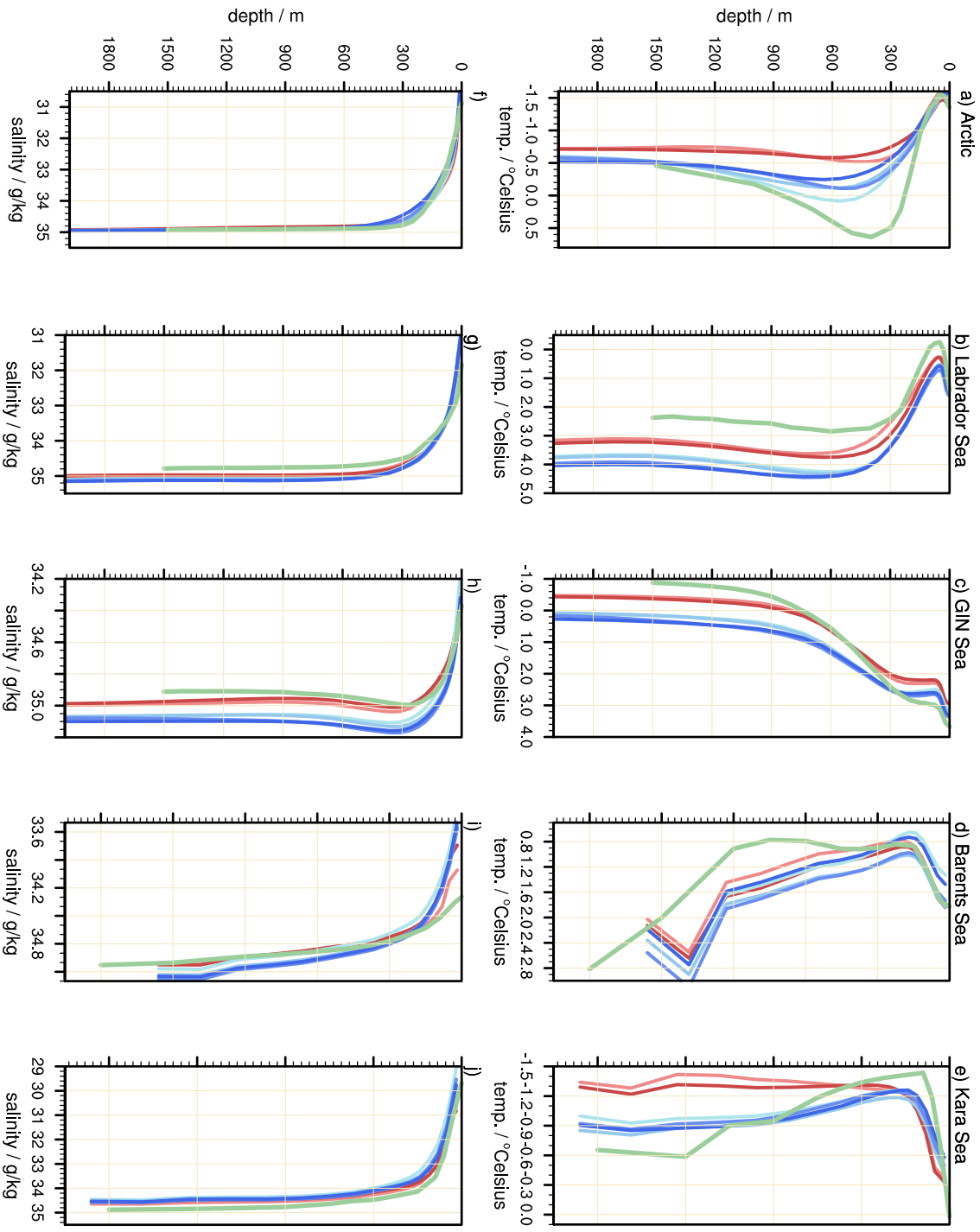

Figure 3.5: Temperature (a)-e)) and salinity (f)-j)) profiles from observations (PHC, in green), the NCEP-forced experiments (in red) and for the ECHAM-forced experiments (in blue). The time period used for these vertical profiles is the same as used in Figure 3.6 and Figure 3.7.

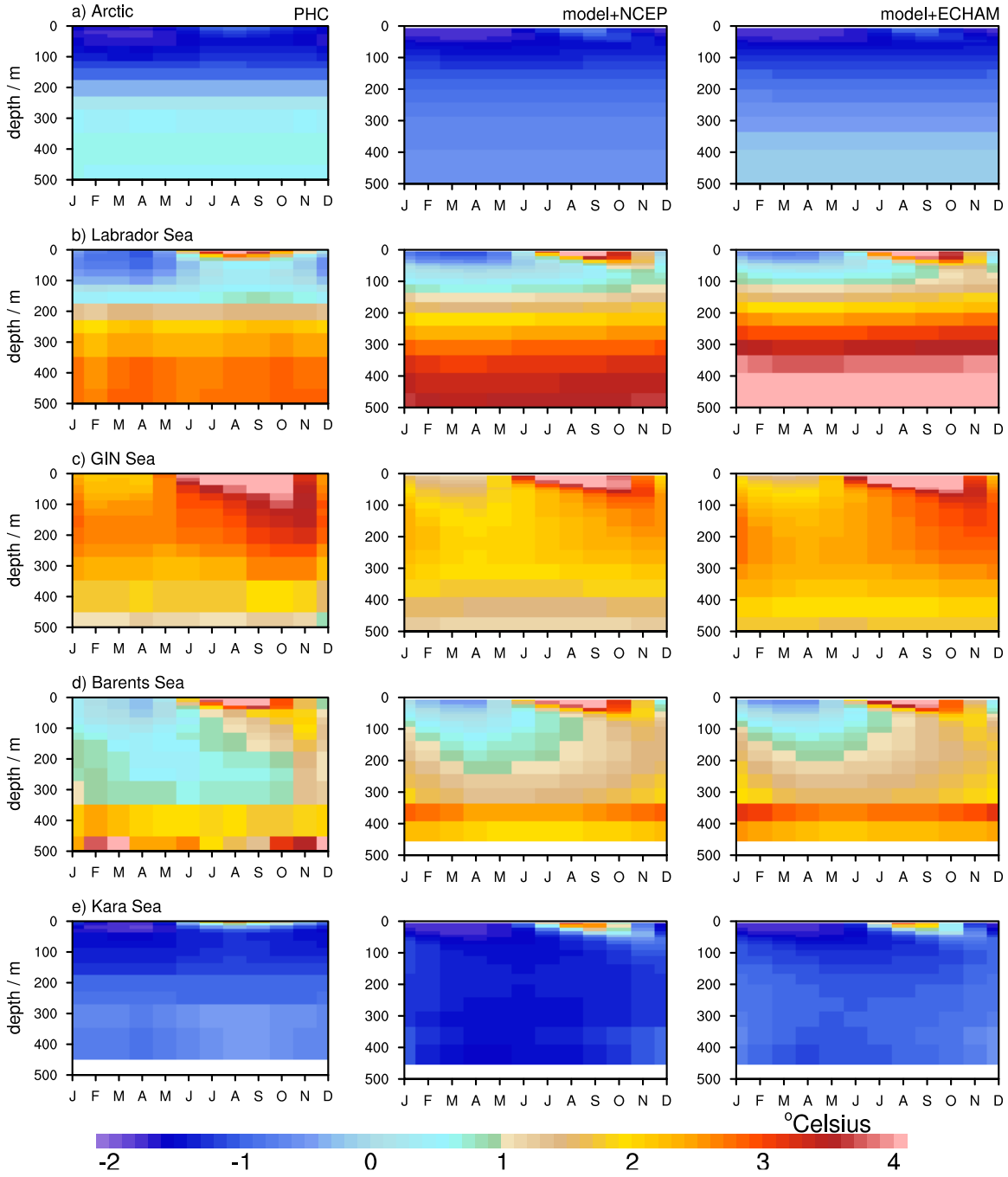

Figure 3.6: Annual cycle of sea water temperature (in °Celsius) in different basins of the Arctic Ocean, on the left side from PHC data, in the middle column from the NCEP-forced experiments (for the years 1980 - 1999) and on the right side from the experiments forced with ECHAM data (either for the years 1980 - 1989 or 1980 - 1999). Only the upper 500 m of each basin are shown.

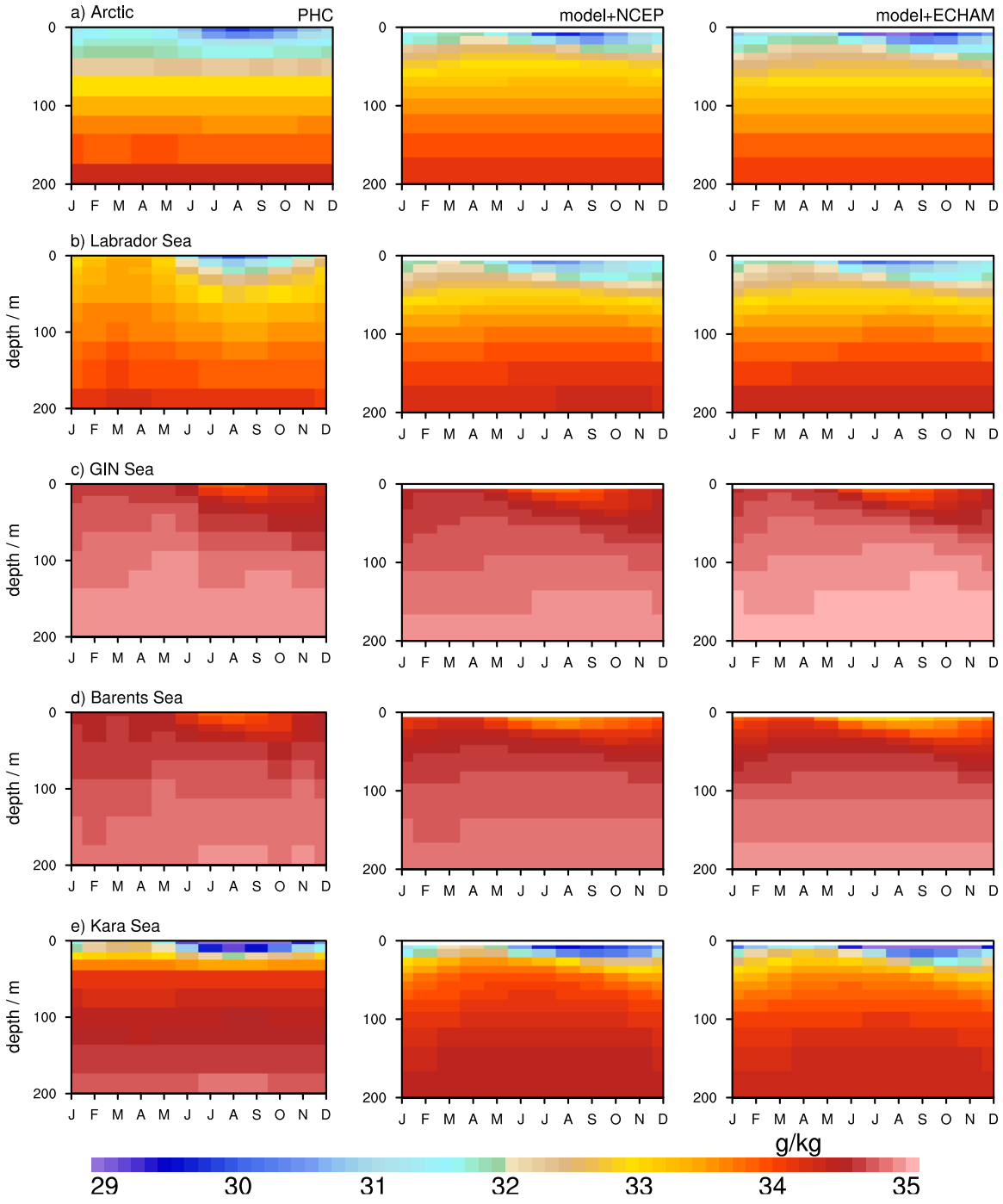

Figure 3.7: Annual cycle of salinity (in g/kg) in different basins of the Arctic Ocean, on the left side from PHC data, in the middle column from the NCEP-forced experiments (for the years 1980 - 1999) and on the right side from the experiments forced with ECHAM data (either for the years 1980 - 1989 or 1980 - 1999). Only the upper 200 m of each basin are shown.

Salinity As mentioned before, the vertical density structure of the Arctic Ocean is mostly determined by the vertical salinity structure, with relatively fresh water at the top and a strong increase of salinity below the surface layer. Lower salinity means lower density, consequently the strong increase in salinity, called halocline, goes along with a strong increase in density with depth, called pycnocline. This leads to a stable stratification within the Arctic Ocean and inhibits vertical mixing. The surface layer with comparably low salinity is fed mainly by the large freshwater input of the rivers draining into the Arctic Ocean. Additionally, the inflow of low saline Pacific water through the Bering Strait contributes to the fresh surface layer as well as net precipitation over the ocean (Serreze and Barry 2005).

Unlike temperature, salinity stays nearly uniform below 200 m at values ranging from 34.8 g/kg to about 35 g/kg, depending on the Ocean basin (Figure 3.5). The strength of the halocline fits in both model setups nicely to the observations. In Barents Sea the model means and the observations show some discrepancies in the upper 50 m, which might be due to a small overestimation of precipitation in that area (Figure 3.14). The seasonal cycle in salinity is as well as in temperature restricted to the upper few hundred meters. In summer, with the melt of sea ice and snow and the maximum in runoff, salinity decreases at the surface to values lower than 30 g/kg in the Central Arctic as well as in Kara Sea (Figure 3.7 a) and e)). GIN Sea and Barents Sea are saltier in the upper 200 m than the Arctic basin because of the inflow of relatively salty water from the North Atlantic. The salinity of the surface layer strongly depends on the growth and melt of sea ice. In winter, when sea ice forms, rejection of brine leads to an increase of density of the surface layer and thereby to an increase of the depth of vertical mixing. In summer, when sea ice melts, the surface layer becomes fresher and thereby inhibits the vertical mixing. The model results are in all basins in good agreement to the observations.

Sea ice The sea ice model data is compared with data products from the Special Sensor Microwave/Imager (SSM/I). The data are produced by remote sensing systems and are part of the NASA's Pathfinder Program. For better comparison the data was interpolated onto the model grid. The number of months per year with a sea ice concentration exceeding 0.15 (which is the probability of the sea ice concentration exceeding 0.15 times 12) is displayed in Figure 3.8, for both observational and model data.

The ice edge in the NCEP-forced simulations (Figure 3.8 b)) extends a bit too far south and reaches the northern coast of Iceland whereas it does not in the observational data. The fit is better in the ECHAM-forced experiments (Figure 3.8 c)). However, the ice edge corresponds well in both setups to the observations, especially in Barents Sea and along the coastlines, where one sees most improvement compared to a global setup (see Figure 2 in Koenigk et al. (2007) for global model performance). The tongue-like form in GIN Sea in the observations is not present in the modeled mean values, but in certain years the model also forms this ice tongue, independently from the forcing (not shown). In Kara Sea the model has less months with a sea ice concentration exceeding 0.15 than the observations, particularly the values in the NCEP-forced experiments are too low.

The mean annual number of months in the model in the Central Arctic is also somewhat

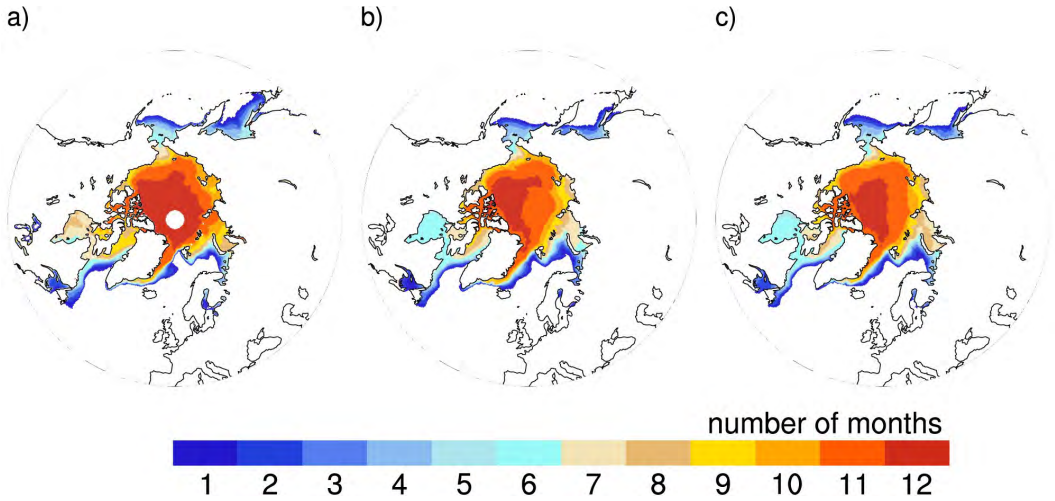

Figure 3.8: Number of months per year with sea ice concentration exceeding 0.15 for a) observations from SSM/I (1980 - 1999), b) model data from NCEP-forced experiments (1980 - 1999) and c) from experiments forced with ECHAM (two times 1980 - 1989 and two times 1980 - 1999).

smaller than in observations. This can also be seen in the time series of September and March sea ice area, that are shown in Figure 3.9. In both model setups the September sea ice area is underestimated with up to 2 million km^2. The bias is smaller in the time series of ice extent (Figure 3.10) but still in March it reaches about 1 million km^2. This is consistent to the 2 m temperature mean values of the model, with large positive biases over the Arctic Ocean (Figure 3.4).

Comparing sea ice related variables in different models has already proven difficult. Especially for sea ice thickness and thus for sea ice volume, the spread between different models is large, not only for the CMIP3 experiments (Kwok 2011) but still for the new generation of these models, CMIP5 (Massonnet et al. 2012; Stroeve et al. 2012). Kwok (2011) shows that sea ice thickness data from 10 of 17 models show correlations of less than 0.2 with observations. Fewer than five models show a correct distribution of sea ice thickness with the thickest ice off the north margins of Greenland and the Canadian Arctic Archipelago and thinner ice along the Alaskan and Siberian coast. In contrast to the global version of MPIOM (Koldunov et al. 2010), our model setup is able to reproduce this large-scale climatic feature of sea ice thickness distribution (Figure 3.11 and Figure 3.12). We compare our model results for the NCEP-forced experiments (Figure 3.11 b), Figure 3.12 b)) as well as the ECHAM-forced experiments (Figure 3.11 c), Figure 3.12 c)) with data from the Pan-Arctic Ice Ocean Modeling and Assimilation System (PIOMAS). PIOMAS is a sea ice reanalysis for the Arctic that is obtained by assimilating sea ice concentration and sea surface temperature into an ocean-sea ice model (Schweiger et al. 2011). As can be seen in Figure 3.11, the model is able to reproduce the sea ice thickness distribution as simulated with PIOMAS, but in both model setups, with NCEP and with ECHAM forcing, the sea ice thickness is overestimated in the Central Arctic and at the Siberian coast. In September (Figure 3.12), however, the model underestimates the sea ice

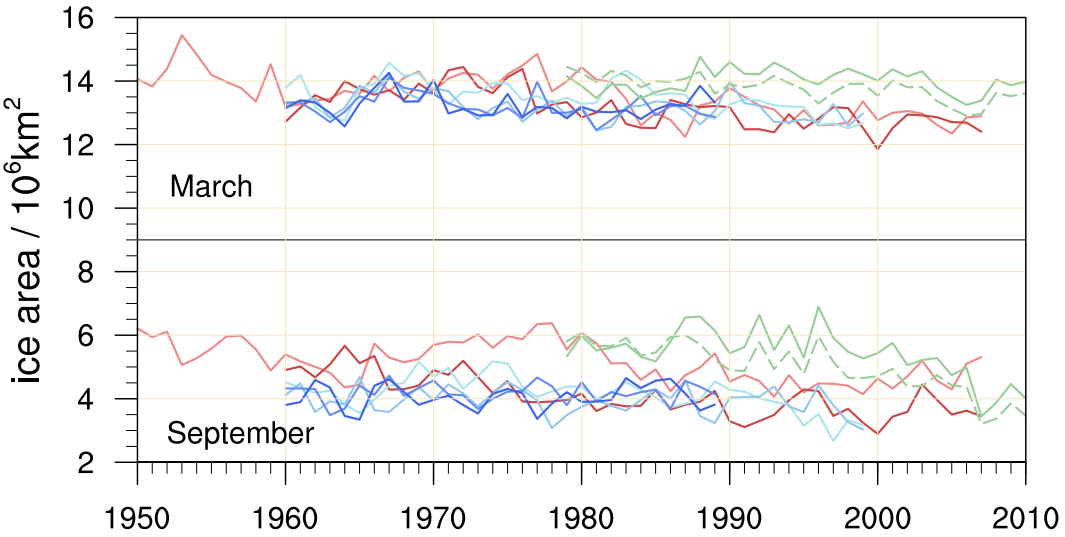

Figure 3.9: March and September sea ice area (exceeding 0.15 % concentration) from the NCEP-forced experiments (in red), the ECHAM-forced experiments (in blue) and from observations from NSIDC (in green). The green dashed line represents data calculated by using the NASA Team algorithm (Cavalieri et al. 1996), the green solid line represents data calculated by using the Bootstrap algorithm (Comiso 1999).

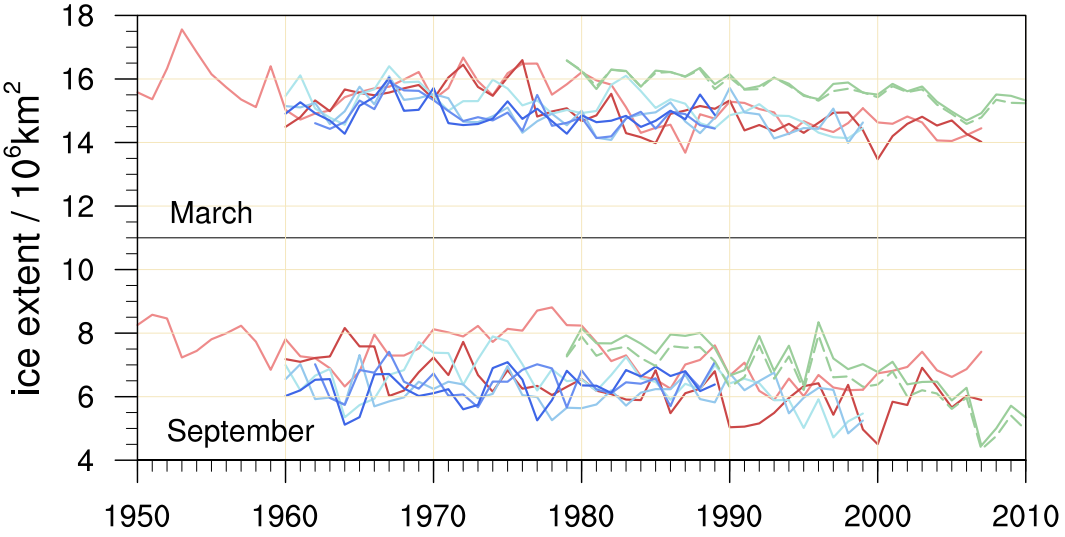

Figure 3.10: March and September sea ice extent from NCEP-forced experiments (in red), the ECHAM-forced experiments (in blue) and from NSIDC (in green). The green dashed line represents data calculated by using the NASA Team algorithm (Cavalieri et al. 1996), the green solid line represents data calculated by using the Bootstrap algorithm (Comiso 1999).

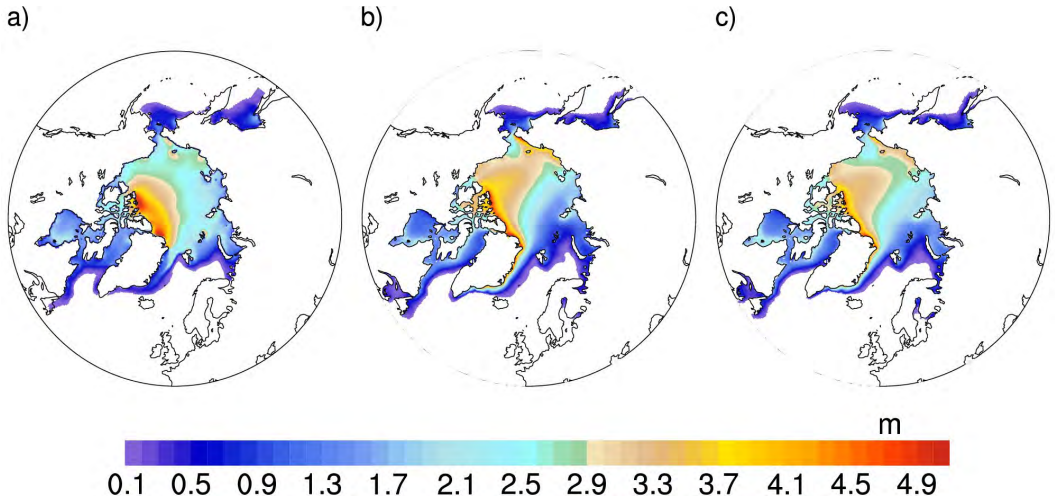

Figure 3.11: March sea ice thickness in m from a) PIOMAS data for the years 1980 - 1999, b) model data from NCEP-forced experiments (1980 - 1999) and c) from experiments forced with ECHAM (two times 1980 - 1989 and two times 1980 - 1999).

thickness, especially in Lincoln Sea and north of the Canadian Arctic Archipelago. The model, particularly with ECHAM forcing, also underestimates sea ice thickness, compared to the PIOMAS data, in Laptev Sea and in Kara Sea, where no summer sea ice remains in the model. This is also reflected in the time series of September sea ice volume in Figure 3.13. The sea ice volume time series for March agrees well with the PIOMAS data. The ECHAM-forced experiments have a mean March sea ice volume of 29200 km^3 (mean over the years 1960 - 1999 and 1960 - 1989), the NCEP-forced value is slightly higher with about 315000 km^3 (mean over 1960 - 1999) and PIOMAS has a March sea ice volume of about 29900 km^3 (mean over 1960 - 1999). The modeled interannual variability is in the range but not in face of the observed variability, because our model is coupled and runs freely, not forced directly by observed climatic conditions.

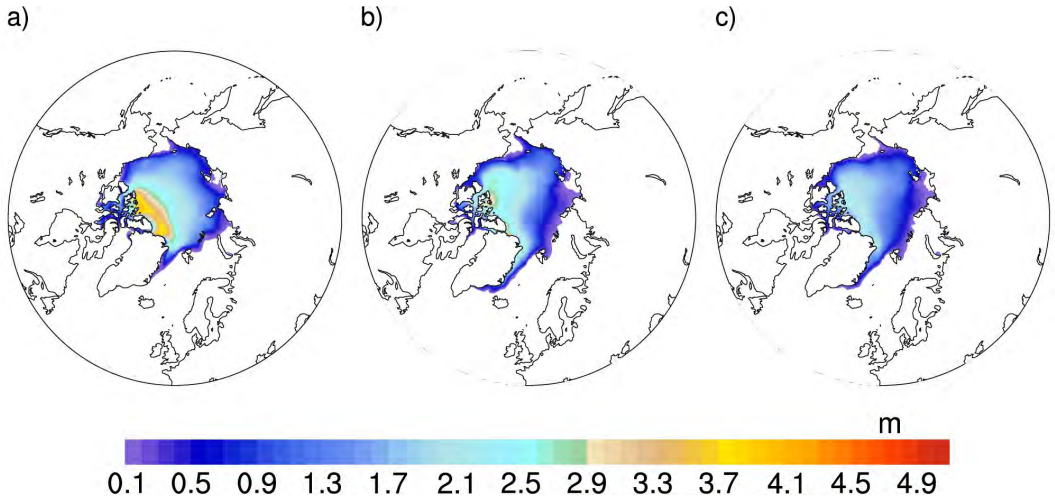

Figure 3.12: September sea ice thickness in m from a) PIOMAS data for the years 1980 - 1999, b) model data from NCEP-forced experiments (1980 - 1999) and c) from experiments forced with ECHAM (two times 1980 - 1989 and two times 1980 - 1999).

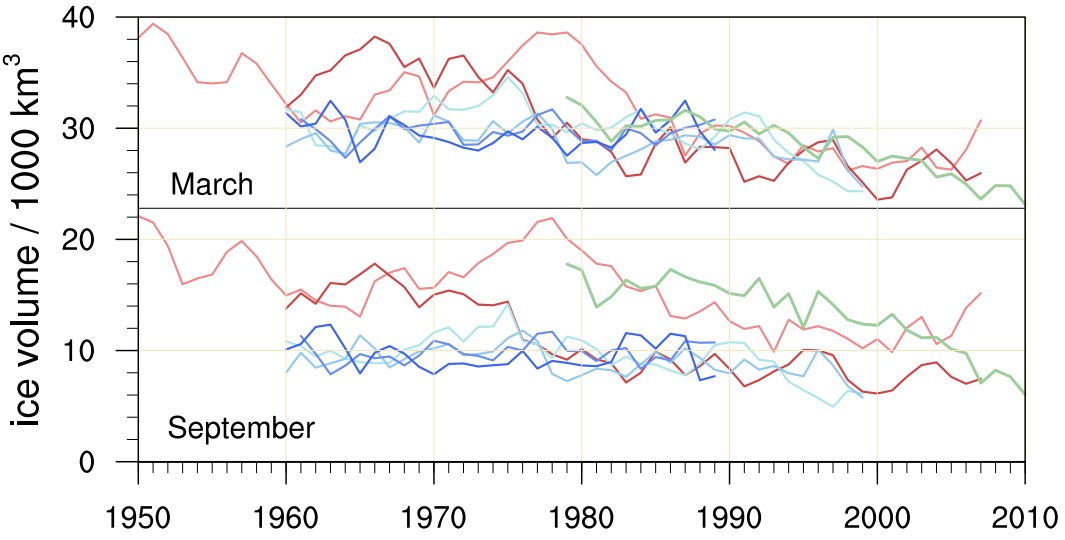

Figure 3.13: March and September sea ice volume from NCEP-forced experiments (in red), the ECHAM-forced experiments (in blue) and from PIOMAS data (in green).

Precipitation In Figure 3.14, modeled precipitation (Figure 3.14 b) and c)) is compared with observational data (Figure 3.14 a)). As mentioned in Chapter 1, we merge the two datasets from HOAPS (Andersson et al. 2010), providing gridded data over the (ice-free) ocean, with the GPCC data product (Rudolf and Schneider 2005; Rudolf et al. 2010), providing gridded precipitation data for the land-surface. Since the HOAPS dataset is available from 1987 only, we use for the observations the climatological mean from 1990 - 1999, whereas for the model data we use the mean from 1980 - 1999. (The results do not differ strongly when taking 1990 - 1999.)

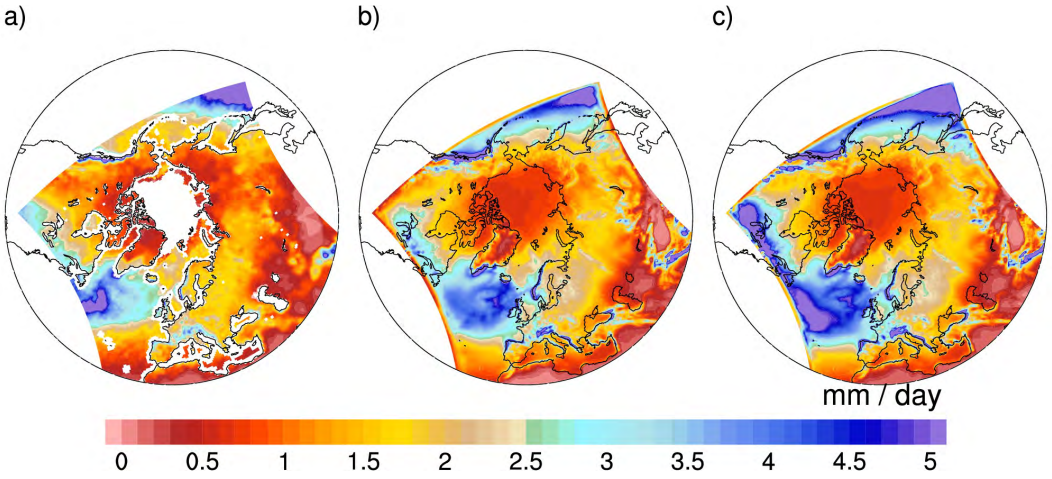

Figure 3.14: Mean precipitation in mm / day from a) observations for the years 1990 - 1999, b) model data from NCEP-forced experiments for the years 1980 - 1999 and c) model data from ECHAM-forced experiments for the years 1980 - 1989 and 1980 - 1999. The observations are merged over land from GPCC and over ocean from HOAPS. The different datasets are separated with a white line. There are no observations over sea ice.

Precipitation over the Central Arctic is very low with values of less than 10 mm to 30 mm per month. In North America and Central Asia the values are also comparably small and do not exceed 30 mm per month. In the North Atlantic region, especially in the Gulf Stream area, and in the mountainious western coast of Alaska the annual mean values exceed 150 mm per month.

Arctic precipitation does not only show a large amplitude in its spatial distribution but it does also show a strong seasonality (Figure B.3 in Appendix B); in the North Atlantic there is a cold season maximum and a summer minimun, according to the seasonality of the North Atlantic cyclone track. Over land and over the Central Arctic Ocean there is a summer maximum and a cold season minimum. The summer maximum is mainly given by surface evaporation, and the maximum over the Arctic Ocean is given by a maximum in vapor flux convergence (Serreze and Barry 2005).

The large scale spatial pattern of the model agrees well with the observations. However, the model slightly overestimates the precipitation nearly everywhere, particularly in spring and summer (Figure B.3 in Appendix B). Especially in the North Atlantic, the amount is about 30 % too large (Figure 3.14). Nevertheless, the high resolution of the model allows

for resolving mountain ranges properly, which can be seen over parts of Russia. The largest difference between the NCEP-forced experiments and the ECHAM-forced experiments can be seen in the region of the North Atlantic, where the ECHAM-forced experiments show extremely large values.

Arctic river runoff As mentioned in Section 1.2.1, we use the R-ArcticNET river discharge database to validate simulated runoff (Shiklomanov et al. 2000). In Figure 3.15 the domain used for total runoff calculation is marked with red dots, indicating grid cells from the HD model.

Figure 3.15: Locations of grid points in the HD model that are used for calculation of the Arctic river runoff (in red) as presented in Figure 3.16 a).

The spatial sum over these grid cells, used as total Arctic river runoff, is presented in Figure 3.16 a). To show the variability of river runoff in the model, we show the time evolution of all NCEP-forced and ECHAM-forced experiments separately, in red and blue, respectively. The thick lines in Figure 3.16 show the 5 year running mean values. The total model runoff is in the same range as the observations and varies around 0.17 Sv. In the model output a slight increase can be seen after 1980 which seems to be larger than in observations. The amplitude of interannual variability (thin lines represent yearly values) is comparable to observations, the standard deviation varies between 5.6 mSv and 7.9 mSv for all model experiments and is about 7.7 mSv in the observations. Both setups show the same amplitude of interannual variability, the NCEP-forced experiments (with standard deviations of 5.6 mSv and 7.9 mSv) and the ECHAM-forced experiments (the standard deviation of the four experiments varies between 5.9 mSv and 7.4 mSv). However, the peaks do not overlap and the yearly modeled runoff of the NCEP-forced experiments and the observed do not correlate significantly.

In Figure 3.16 b) the total runoff is split into the Eurasian and into the North American part. In the model, the data exactly sums up to the total runoff as presented in Figure 3.16 a), but this is for some reason not the case in the observational data taken from (Shiklomanov et al. 2000). The total amount of runoff is larger in Eurasia than in North America, and the same is true for the year to year variability. The variability for

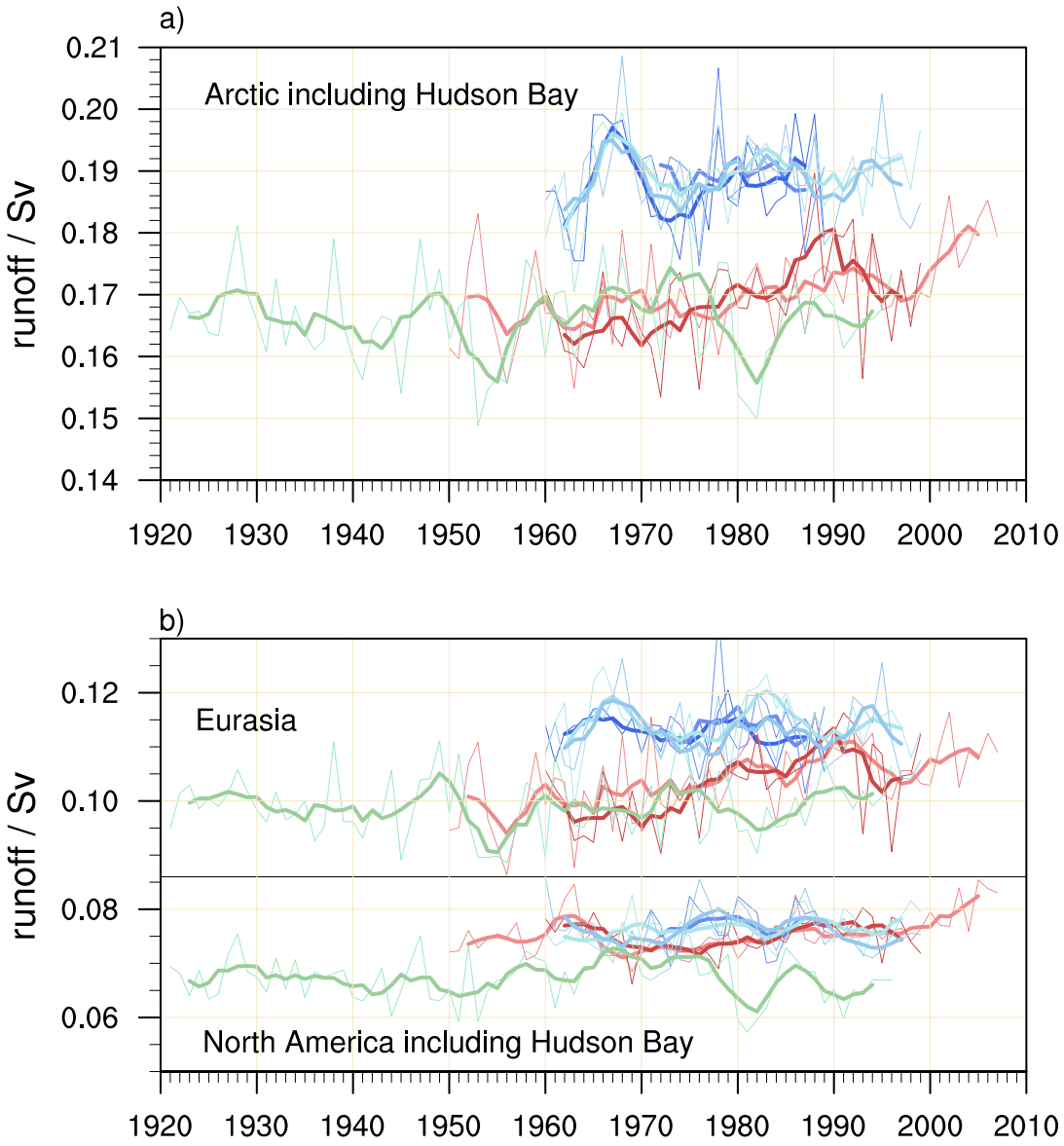

Figure 3.16: River runoff from the experiments forced with NCEP (in red), the modeled data from the experiments forced with ECHAM (in blue) and from observations (in green) for a) the total Arctic region including Hudson Bay, and b) split into Eurasia and North America including Hudson Bay. The thin lines indicate yearly data, the thick lines 5 years running mean values.

the Eurasian runoff is slightly overestimated in the model whereas the variability in the North American runoff is slightly underestimated. The total amount draining into the Arctic Ocean from the North American coast as well as from Eurasia is overestimated, in both model setups. This is also reflected in Figure 3.17, a comparison of annual cycles of the largest Arctic rivers draining into the Arctic Ocean. The observations in Figure 3.17 are provided by Dümenil Gates et al. (2000) and are mean values over several decades. Even though the modeled annual cycle of the largest Arctic rivers is well represented and thus the start of the melting season, the amplitude of the cycle is too small for the Rus-

sian rivers Lena, Yenisey and Ob. As seen already in Figure 3.16 b) the ECHAM-forced experiments show a larger runoff in the Eurasian part, thus in the amount of runoff of the rivers Ob, Yenissey and Lena. However, the total amount of these three rivers is quite similar in the modeled and observational data and sums up to more than a quarter of the total amount of freshwater delivered to the Arctic Ocean.

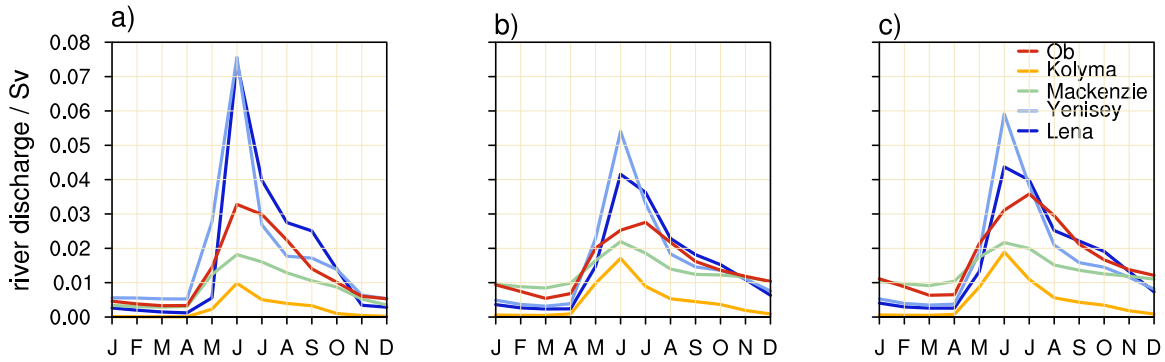

Figure 3.17: Annual cycle of river discharge of the largest Arctic rivers from a) observations and b) modeled data from the NCEP-forced experiments and c) modeled data from the ECHAM-forced experiments. The annual cycle from the NCEP-forced experiments is calculated from the time period 1980 - 1999 and from the ECHAM-forced experiments for the years 1980 - 1989 and 1980 - 1999.

Freshwater storage within the Arctic Ocean Most of the freshwater is stored in the Beaufort Gyre. The Arctic high winds drive the ice and ocean in an anticyclonic direction in the Beaufort Sea. Ekman convergence and associated downwelling of fresh surface water leads to an accumulation of liquid freshwater in that region. In summer, the wind is much weaker, the direction might even reverse and freshwater can be released. In addition to the atmospheric influence, sea ice melt (and freeze) plays an important role. More than 70000 km^3 are stored in liquid form in the upper Arctic Ocean (Serreze et al. 2006). Using satellite measurements Giles et al. (2012) estimate an increase of about 8000 km^3 in the western Arctic Ocean in the years 1995 - 2010. They also speculate, that a reversal in the wind field could lead to a release of large amounts of the freshwater accumulated in that area.

As in Serreze et al. (2006), we calculate the freshwater stored within the Arctic Ocean ignoring water that is saltier than the reference salinity of 34.8 g/kg. This corresponds roughly to an integration of the upper 200 - 300 m, where the 34.8 salinity level is located. Most of the freshwater is found above this level, separated by the strong halocline from the warm and saline water beneath.

In Figure 3.18 we compare the freshwater content from PHC data with modeled ensemble mean freshwater content from the NCEP-forced and the ECHAM-forced experiments. Both model setups agree well with the observational data and show the accumulation of freshwater in the Canada basin.

In both model setups the amount of freshwater stored within the Arctic Ocean shows

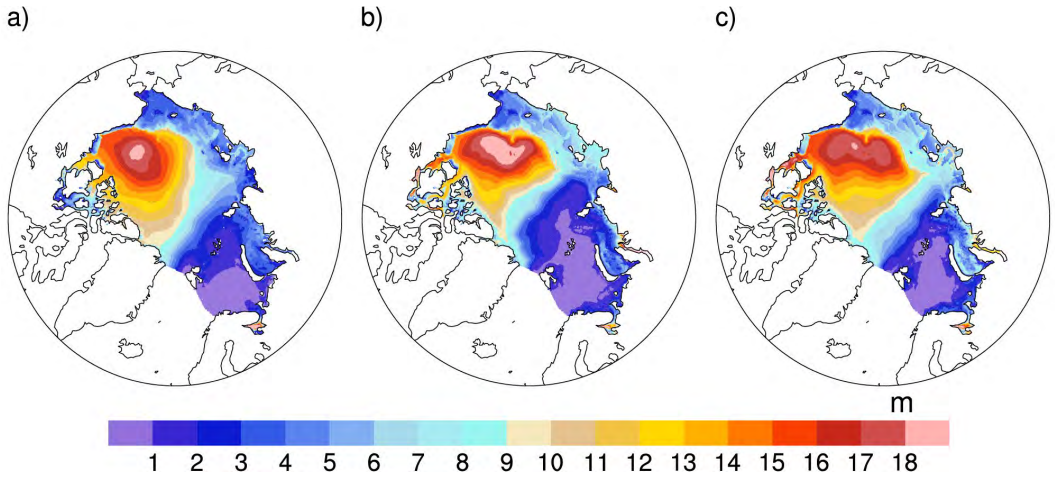

Figure 3.18: Mean freshwater content excluding sea ice of the Arctic Ocean in m for a) PHC data and b) model data from the NCEP-forced experiments for the years 1990 - 1999, and c) model data from the ECHAM-forced experiments for the years 1980 - 1999 and 1980 - 1989.

a large variability among the experiments. The ECHAM-forced experiments store more freshwater in the Arctic than the NCEP-forced experiments which might be a result of a difference in the atmospheric state in the model. Nevetheless, the amount of stored liquid freshwater in the model is lower than in observations, numbers are given in Table 3.1 at the end of this section. Nearly all experiments show a positive trend in the freshwater content.

Ice export through Fram Strait Most of the sea ice from the Arctic is exported through Fram Strait. The export is mainly determined by local winds, thus by the cross-strait air pressure difference. Ice volume export is rarely measured; however, some time series exist, derived either using a parameterization that is only dependent on the pressure difference over the strait (Vinje 2001) or using satellite-based estimates (Spreen et al. 2009). Even though a recent decline in Arctic summer sea ice is reported, no positive trend in Fram Strait ice export can be observed (Spreen et al. 2009). The mean sea ice export amounts to about 220 km^3/month ($\approx$ 80 mSv) with a maximum in March and a minimum in summer. Our model reproduces the seasonal cycle well (Figure 3.19) and lies within the range of variability of the observations. How large the variability is within the model can be seen in Figure 3.20. The NCEP-forced experiments as well as the ECHAM-forced experiments agree well with the reconstructed ice volume flux time series from Vinje (2001) (Figure 2 in his paper) not only in the amount but also in the year to year variability. However, the modeled variability seems to be somewhat larger than the observed. In the time series from our model experiments no clear trend can be seen. In Figure 3.21 the 12 months running mean sea ice volume transport of the NCEP-forced experiments is shown again. Because our model is coupled, it produces large internal variability (the two experiments do only correlate with 0.38), which is not in face with the observed variability. The peaks do not overlap and the model results do not show the large export events leading to the salinity

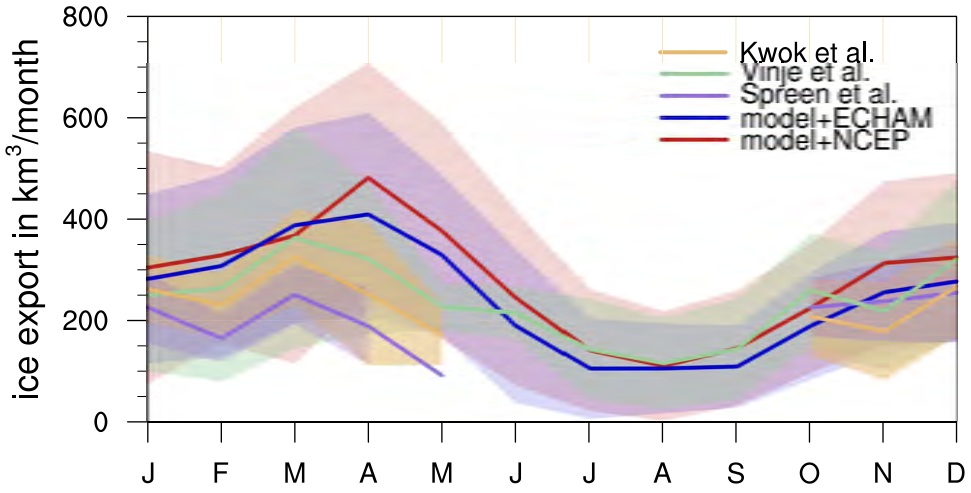

Figure 3.19: Annual cycle of sea ice volume export through Fram Strait from observational data from Kwok et al. (2004) (years 1991 - 1999, in yellow), Vinje (2001) (years 1990 - 1996, in green), Spreen et al. (2009) (years 2003 - 2008, in blue), and from the model data in red. The shadowed areas indicate ± one standard deviation. The modeled data is the ensemble mean of the NCEP-forced experiments for the years 1980 - 1999 (in red) and for the ECHAM-forced experiments for the years 1980 - 1989 and 1980 - 1999 (in blue).

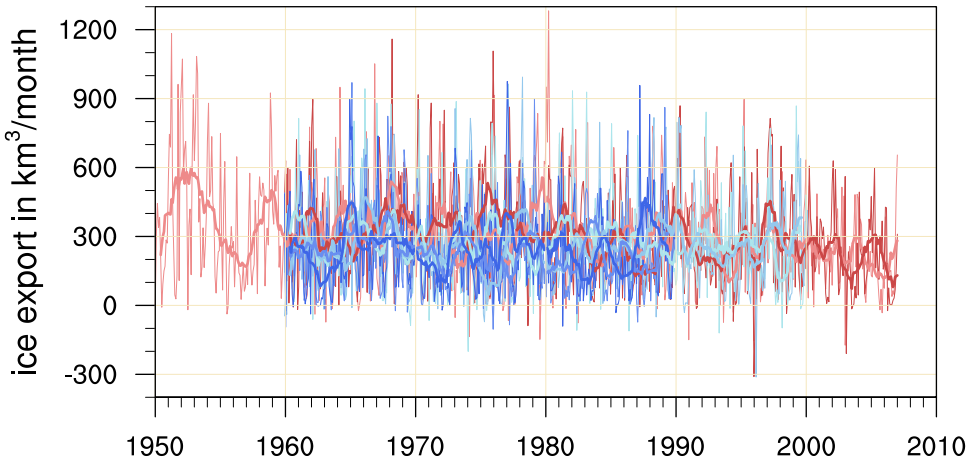

Figure 3.20: Sea ice volume export through Fram Strait from the NCEP-forced experiments (in red) and from the ECHAM-forced experiments (in blue). Thin lines represent monthly mean values and thick lines 12 months running means.

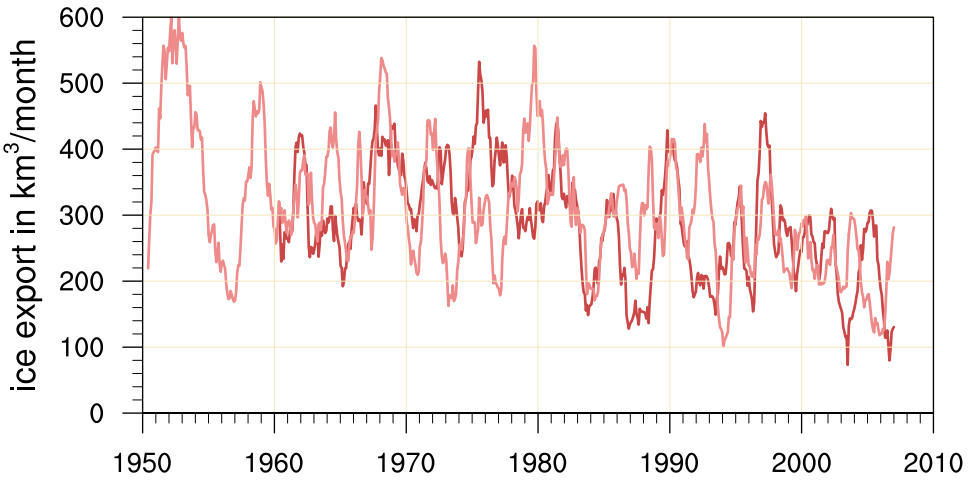

Figure 3.21: 12 months running mean of sea ice volume export through Fram Strait from the NCEP-forced experiments. The data is the same as in Figure 3.20 but the scale is different.

anomalies in the 1970s, 1980s and 1990s. This is in contrast to the uncoupled ocean-sea ice model forced with NCEP data (Haak et al. 2003). However, both model experiments show a large variability in the ice volume export through Fram Strait suggesting that the coupled model setup has enough freedom to evolve such salinity anomalies as for example the large salinity anomaly in the 1970s (Dickson et al. 1988).

Deep water formation and meridional overturning Convection in the Nordic Seas and in Labrador Sea is the main source of deep water formation within the global ocean and thereby an important driver of the thermohaline circulation. The convection is very sensitive not only to surface temperature but also to surface salinity. In Figure 3.22 the mixed layer depth for February of the NCEP- and the ECHAM-forced experiments is shown. The mixed layer depth, defined as the depth where the density has increased by 0.125 kg/m^3 compared to the value at the surface, is a good indicator for the strength of convection. In both regions, Greenland Iceland Norwegian (GIN) Sea and Labrador Sea, the winter mixed layer depth exceeds 2000 m. In the NCEP-forced experiments (Figure 3.22 a)) convection also occurs in the Central Arctic Ocean. This might be explained by a too strong inflow of Atlantic derived waters via Barents Sea into the Arctic Ocean. Below ice there is no convection expected.

In Irminger Sea, the modeled winter mixed layer depth reaches about 1000 m, which fits to the observations from Bacon et al. (2003) that show a convection of the same order for the winter 1996 - 1997. However, compared to observations the modeled depths in Labrador Sea are somewhat too large. Lavender et al. (2002) used floats showing mixed layer depths of more than 1300 m in 1997, but less than 1000 m in 1998. In Greenland Sea, the observed and estimated mixed layer depth varies between 1000 m and 2000 m (Rudels et al. 1989; Morawitz et al. 1996). Nevertheless, there are also deep convective chimneys with depths exceeding 2400 m observed (Wadhams et al. 2002).

The stream function of the Atlantic ocean meridional overturning (MOC) for two ex-

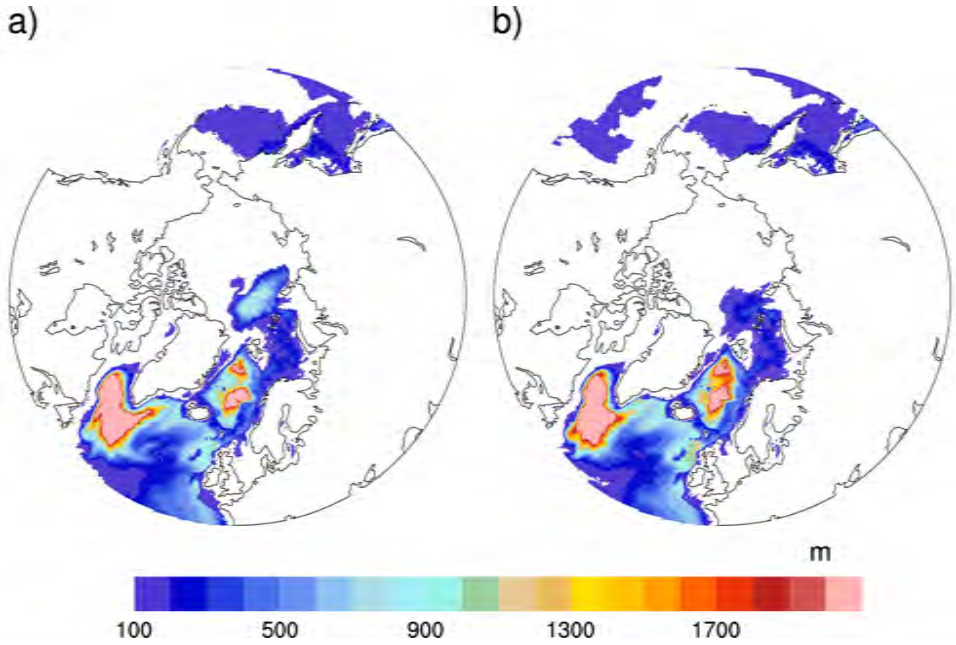

Figure 3.22: February mixed layer depth in m from a) model data from NCEP-forced experiments for the years 1980 - 1999 and b) model data from ECHAM-forced experiments for the years 1980 - 1989 and 1980 - 1999.

periments is shown in Figure B.4 in Appendix B. The black cross marks the location, 26 °N at a depth of 1020 m, of the time series presented in Figure 3.23. The MOC as well as its standard deviation of the ECHAM-forced experiments is larger than of the NCEP-forced experiments. The mean value of the years 1960 - 1999 for the NCEP-forced experiments is 16.35 Sv with a standard deviation of about 0.74 Sv and from the ECHAM-forced experiments 18.57 Sv with a standard deviation of about 1 Sv. This fits nicely to observations from the joint U.K.-U.S. Rapid Climate Change-MOC program measuring the strength and vertical structure of the MOC in the Atlantic with a moored instrument array along 26.5 °N. For the years 2004 to 2010, McCarthy et al. (2012a) state a mean observed MOC ranging between 17.6 Sv and 19.4 Sv with a yearly standard deviation of 0.7 Sv. Similar numbers from observations can be found in McCarthy et al. (2012b) and in Kanzow et al. (2010).

While the correlations between the experiments with the same forcing are high, the correlation for the years 1960 - 1989 between the NCEP-forced experiments is 0.64 and the correlations between the ECHAM-forced experiments range between 0.57 and 0.75, there is no significant correlation between the experiments with different forcings. This can probably be explained by differing variability in the Ekman transport due to different wind forcings, the location for the time series is in the uncoupled domain.

Our model reproduces a reasonable ocean circulation in the North Atlantic; the values for the Atlantic MOC are in range with observations. The deep-water formation in Labrador Sea and GIN Sea are very deep, but convective chimneys of these depths are observed as well.

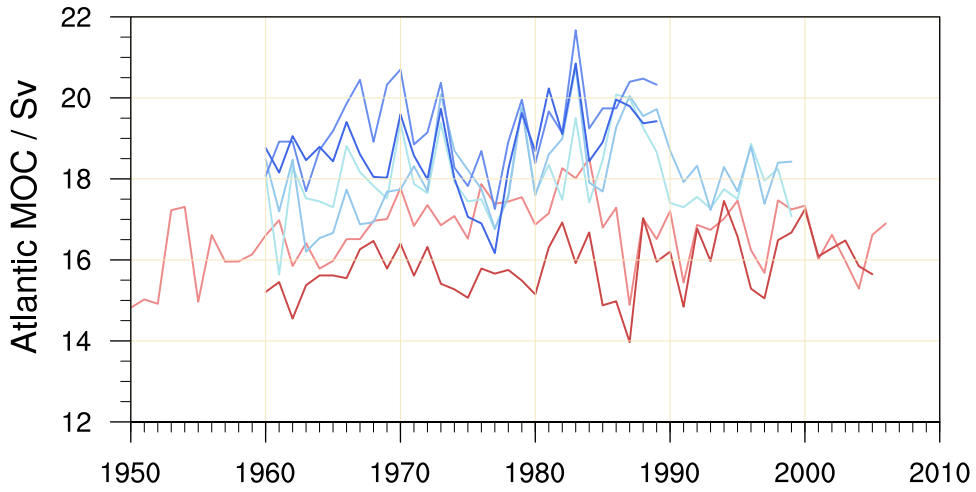

Figure 3.23: Time series of yearly mean values of the meridional overturning circulation in Sv at 26 °N at a depth of 1020 m. Again, the NCEP-forced experiments are shown in red and the ECHAM-forced experiments are shown in blue.

3.1.2 The Arctic freshwater components

We compared in the previous section the main components of the Arctic hydrologic cycle simulated by our model setup with NCEP forcing as well as with ECHAM forcing to observations. The oceanic components, such as the sea ice distribution, sea ice export and the freshwater stored within the Beaufort Gyre, are in good agreement with observations, irrespective of the underlying forcing. A difference caused by the different forcings can be seen in the amount of precipitation. While the spatial distribution is similar, the ECHAM-forced experiments overestimate the total amount of precipitation even more than the NCEP-forced experiments (Figure 3.24).

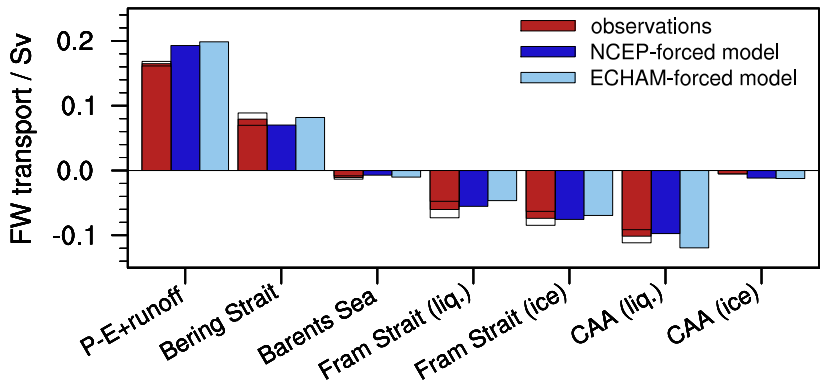

Figure 3.24: Freshwater budget of observations and reanalysis data from Serreze et al. (2006) (in red), from the ensemble mean from the NCEP-forced experiments (in dark blue) and for the ECHAM-forced experiments (in light blue), both for the years 1960 - 1999. Error bars from observational data are added where available.

	observations	NCEP-forced model	ECHAM-forced model
P - E + runoff	165 (±3.5)	182 (±7.8)	198.5 (±12.3)
Bering Strait	92 (±9.5)	69.3 (±9.6)	82.1 (±16.6)
Barents Sea	−11 (±2.5)	−5.8 (±3.1)	−9.7 (±9.3)
Fram Strait liquid	−60 (±12.7)	−48.4 (±10.3)	−47.2 (±16.8)
Fram Strait ice	−74 (±10.8)	−85 (±18.9)	−70.0 (±21.8)
CAA liquid	−101 (±10.1)	−82.9 (±15.9)	−118.7 (±19.7)
CAA ice	−5.	−12.3 (±3.1)	−12.4 (±3.6)
Oceanic storage liquid	74000 (±7400)	32315 (±4143.4)	34360 (±7117.3)
Oceanic storage ice	10000	15013 (±1893.9)	13118 (±1128.1)
$\sum$ transports	6	16.9	22.6

Table 3.1: Tabular of the mean values in mSv for the fluxes and km^3 for the storage terms of the FW budget of the Arctic from observations and reanalysis data (Serreze et al. 2006) and from modeled data for the years 1960 - 1999 and 1960 - 1989. Displayed in brackets are error estimates from observations where available and for modeled data one interannual standard deviation.

The observations from Serreze et al. (2006) are from several different sources and the error estimates are arguable, especially for precipitation minus evaporation, where observational data are sparse. The systematic overestimation of precipitation results in an overestimation of runoff, especially when using ECHAM forcing (Figure 3.16).

The interannual evolution of the FW components in the NCEP-forced and in the ECHAM-forced experiments can be seen in Figure 3.25 and Figure 3.26, respectively. The difference between the differently forced experiments is largest in the amount and the variability of FW transport through Fram Strait and through the Canadian archipelago. While in the NCEP -forced experiments, the FW export through Fram Strait is in general larger than the FW export through the Canadian Arctic archipelago, this is not the case in the ECHAM-forced experiments. As can be seen in Table 3.1, the ice transport through Fram Strait is smaller, while the FW transport in liquid form through the Canadian archipelago is about 40 % larger in the ECHAM-forced experiments compared to the NCEP-forced simulations.

We have seen that the atmosphere model used in our coupled setup develops internal variability that is not in phase with the observed variability, not even when the NCEP forcing is used. Nevertheless, as can be seen for example in Figure 3.16 for runoff and in Figure3.13 for ice volume, the modeled interannual variability in the freshwater terms is, in general, in range with the observed variability.

A summary of the freshwater components is given in Figure 3.24 as well as in Table 3.1. We conclude that the Arctic freshwater components and their variability (Figure 3.25 and Figure 3.26) are well represented in our model.

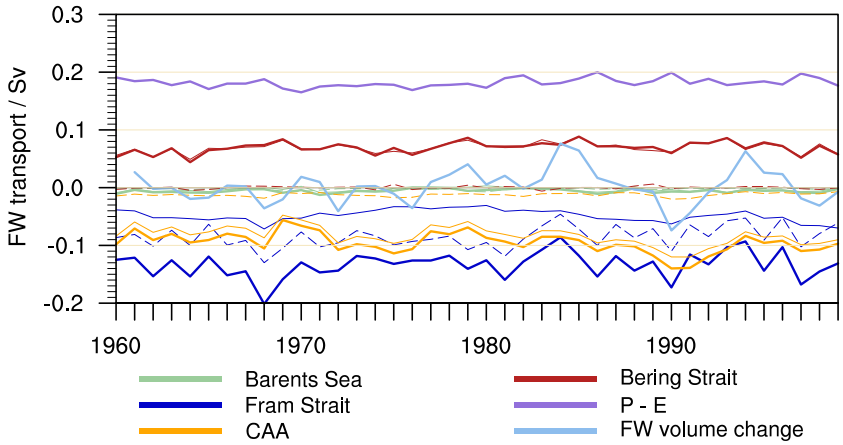

Figure 3.25: Ensemble mean of the yearly mean freshwater components of the experiments forced with NCEP data. Thick lines indicate the total transport, thin and thin dashed lines indicate the liquid and ice component, respectively.

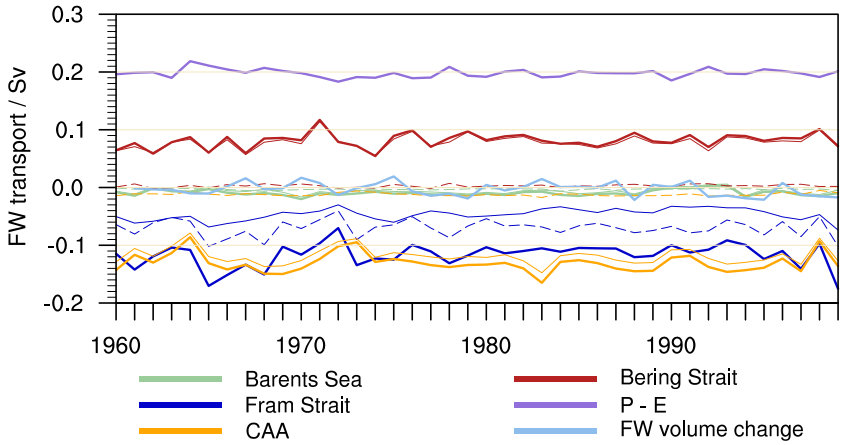

Figure 3.26: Ensemble mean of the yearly mean freshwater components of the ECHAM-forced experiments. Until 1989 the ensemble contains four members and for 1990 - 1999 the ensemble only contains two members. Thick lines indicate the total transport, thin and thin dashed lines indicate the liquid and ice component, respectively.

3.2 High resolution versus global model results

One main advantage of a regional model over a global climate model is the resolution, which allows for a better representation of the topography as well as of small scale processes in the ocean and in the atmosphere. Slope convection along shallow coastal areas for example is much better resolved by increased grid resolution. In the atmosphere model, for instance, the track and intensity of cyclones can be calculated more precisely. Having lower resolution, global models tend to *wash out* extreme events and to smooth the results.

In the Arctic, a better representation of the topography, for example of the Canadian archipelago or of the Greenland ice sheet, leads to large improvements in the model results. The shallow and narrow channels around the archipelago are in most global models represented by only one broad channel influencing the result and the relative role of the transport of FW from the Canada Basin through this channel into Labrador Sea. Reaching a mean resolution in the ocean model component of our setup of about 15 km in the coupled domain, the archipelago can be represented more realistically. As can be seen in Figure 3.27, the transport of FW in liquid form through the Canadian archipelago is strongly underestimated in the results of the global model, compared to observations and compared to our regional coupled setup. This has a direct impact on the amount of the FW stored within the Arctic Ocean as well as on the role of the FW export through Fram Strait and on convection in Labrador Sea. Our model setup improves compared to the global model in the im- and export through all straits (Figure 3.27). This is true for FW transports in liquid as well as in solid form.

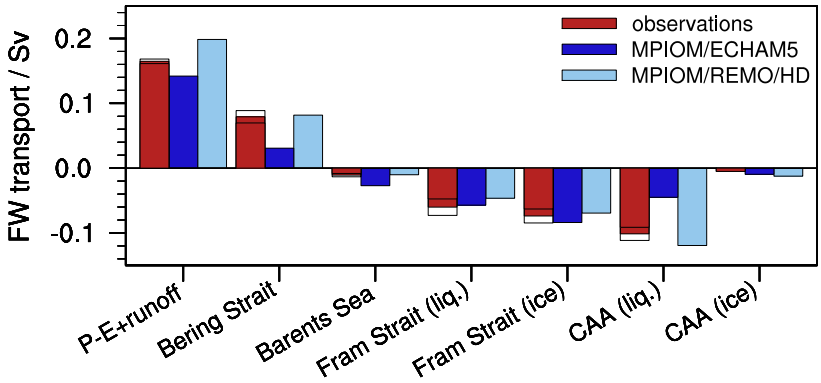

Figure 3.27: Freshwater budget of observations and reanalysis data from Serreze et al. (2006), from the ensemble mean from the NCEP-forced experiments for the years 1990-1999 (MPIOM / REMO / HD) and from the global model experiment performed with MPIOM / ECHAM 5.

Chapter 4

Variability of the Arctic freshwater cycle in the 20th century

The components of the Arctic hydrologic cycle show large interannual variability, that is not fully understood so far. While in Chapter 3 we mainly focused on the mean state of the Arctic freshwater (FW) components, in this chapter we investigate the mechanisms causing the FW variability in the second half of the 20th century of the ECHAM-forced experiments. To understand the highly coupled processes leading to the variability, we examine linkages between atmospheric leading modes and the variability of the Arctic FW components. Since the Arctic runoff variability seems not to be explained by the chosen leading modes, we analyze the interannual variability of Arctic rivers draining into the Arctic Ocean separately.

In Section 4.1, we analyze how different modes in winter mean sea level pressure act on the variability of the FW transports in ocean, sea ice and atmosphere, using composites of these atmospheric leading modes. The analysis of the transports includes not only the ice export, but also the transport in liquid form. Even though the geostrophic winds do not have a direct influence on the oceans' deeper layers, there are remarkable differences in the liquid FW export through the Canadian Arctic archipelago as well as through Fram Strait. We use the method of splitting the phase space of mean sea level pressure in empirical orthogonal functions. We calculate the time series of the principal components of these empirical orthogonal functions to perform a composite analysis. By using only years exceeding one standard deviation of the mean value, we calculate for atmospheric and oceanic variables so-called composite fields to analyze the influence from extreme mean sea level pressure situations on FW transports. Beside the first and second leading mode of winter mean sea level pressure, we analyze the impact from the North Atlantic Oscillation and from the Siberian high.

In Section 4.2, we discuss the variability of the largest source of FW in the Arctic, the Arctic river runoff. We focus on changes in atmospheric mean sea level pressure and corresponding changes in heat and moisture transport over the catchment areas of the rivers, using a regression analysis.

We close the chapter with a summary and concluding remarks about the Arctic FW cycle variability in the 20th century.

4.1 Atmospheric circulation and its impact on freshwater transports

The winter mean atmospheric circulation in the Arctic is dominated by three centers of action, the Siberian high, the Icelandic low and the Aleutian low. The intensity of the Siberian high varies substantially, being strongest in January and February, and thereby causes cold outbreaks over East Asia. The Icelandic low as well as the Aleutian low are parts of the cyclone tracks in the North Atlantic and the North Pacific, respectively. The cyclone activity is largest in winter, depending on the strength of the Icelandic low as well as on the pressure gradient over the North Atlantic region (Serreze and Barry 2005). Numerous studies investigate the influence of the variability of these pressure patterns on Arctic FW transport, especially on sea ice export. The variability in ice export through Fram Strait on interannual to decadal timescales is investigated by Koenigk et al. (2006). They use a global coupled model and find variations in sea level pressure over Fram Strait to be the key driver of the ice export variability. Tsukernik et al. (2009) come to a similar result using observational data.

Using our regional coupled general circulation model that includes all sinks and sources of FW within the Arctic, we analyze the impact of the leading mode of winter mean sea level pressure in Section 4.1.1. The variability driven by the second leading mode of winter mean sea level pressure, characterized by a tripole pattern, is discussed in Section 4.1.2. Measuring the strength of the mean sea level pressure gradient over the North Atlantic, the so-called North Atlantic Oscillation describes the variability in cyclone tracks arriving from the Atlantic region. Its impact on the FW components' variability is studied in Section 4.1.3. We study the variability in the strength of the Siberian high, as it leads to cold and dry winter conditions in large parts of Eurasia, and its influence on Arctic FW components in Section 4.1.4.

4.1.1 Leading empirical orthogonal function of DJF mean sea level pressure

We calculate the first empirical orthogonal function (EOF) of the winter (DJF) mean sea level pressure for all four ECHAM-forced experiments together. A short description of the general method of EOFs is given in Appendix A. For further explanations on this method we refer to von Storch and Zwiers (1999). Our leading mode of winter mean sea level pressure explains about 38 % of the total variance of the winter mean sea level pressure. This EOF also explains about 36 % of the yearly mean variability and consequently represents a leading mode for most of the variability in mean sea level pressure throughout the year.

The leading EOF of the winter mean sea level pressure over the region north of 20 °N is often referred to as the Arctic Oscillation (AO) and its corresponding principal component as the AO index (Thompson and Wallace 1998; Fyfe et al. 1999). The Arctic Oscillation pattern is characterized by sea level pressure anomalies of one sign in the Arctic and anomalies of the opposite sign in mid-latitudes. In the negative phase, higher than normal

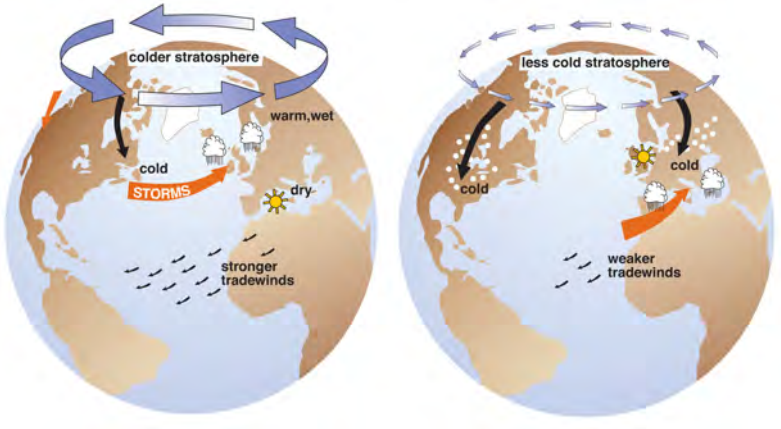

Figure 4.1: Sketch of the Arctic Oscillation in the positive phase (left) and the negative phase (right). Image courtesy of J. Wallace, University of Washington, and the National Snow and Ice Data Center, University of Colorado, Boulder.

pressure in the Arctic and lower than normal pressure at about 45 °N weaken the westerly winds over the Atlantic which results in colder temperatures in northern Europe and Asia and storms over the Mediterranean region. Weaker than normal westerlies over North America lead to lower than usual winter temperatures in the United States in lower latitudes (Figure 4.1, right panel). In the positive phase, lower than normal pressure in the Arctic and higher than normal pressure in mid-latitudes lead to a strengthening of the Atlantic westerlies bringing higher temperatures and more precipitation toward northern Europe and dryer conditions to the Mediterranean region. Enhanced westerlies over North America keep the cold temperatures in high latitudes and allow for warmer temperatures in the United States (Figure 4.1, left panel).

4.1.1.1 Comparison of the first empirical orthogonal function with the Arctic Oscillation

Figure 4.2 a) illustrates the leading EOF from NCEP/NCAR reanalysis DJF sea level pressure for 1960 - 1999 in the region north of 20 °N. This pattern is known as the AO; the center of the Arctic low anomaly is close to the eastern coast of Greenland in the Greenland Iceland Norwegian (GIN) Sea reaching the Central Arctic Ocean and Barents Sea (indicated by the white contour line). However, the spatial pattern differs in the model simulations. The leading EOF of the NCEP/NCAR reanalysis DJF sea level pressure for 1960 - 1999 calculated in our model domain explains about 26 % of the total variance in our model data. The spatial distribution is similar to the EOF as shown in Figure 4.2 a). This indicates, even though the leading EOF of our model (Figure 4.2 c) looks different, the main structure of the EOF calculated from the reanalysis (in our model domain) resembles the EOF calculated from our model.

The differences in the EOFs can be explained as follows: Firstly, the model experiments are not forced with NCEP data outside the coupled domain but with the output of the global model run with ECHAM/MPIOM. The corresponding leading EOF of the global

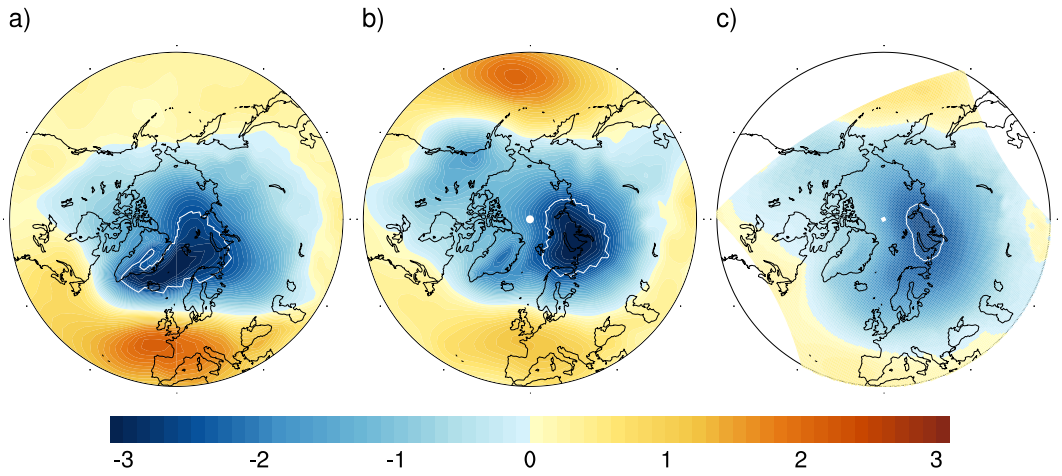

Figure 4.2: Leading EOF of winter (DJF) mean sea level pressure from a) NCEP/NCAR reanalysis data for the years 1960 - 1999, b) the global model run with ECHAM / MPIOM for the 20th century for the years 1960 - 1999, and c) the four ECHAM-forced experiments for the years 1960 - 1999 and 1960 - 1989, depending on the simulation. The white contour line indicates the -2.5 hPa isoline.

output data for 20 °N is shown in Figure 4.2 b). It can clearly be seen that the center of action is shifted to Kara Sea and the adjacent Russian coastal area , which is the case in our model simulations as well (Figure 4.2 c)).

Secondly, the domain of our regional atmosphere model does not cover the whole domain northward of 20 °N and thus our leading EOF of the winter mean sea level pressure does not equal the definition given above. In our model region, we lack especially the Pacific influence in the EOFs. Additionally, the domain of our model is large enough to allow for a certain freedom of the model to develop the leading EOF. The regression coefficients from the DJF mean sea level pressure of the ECHAM-forced experiments and the AO from the global ECHAM data do not resemble the Arctic Oscillation pattern from the ECHAM data, but show beside a maximum in the region where the center of action is located, the Kara and Laptev sea, a second maximum in North America reaching in some experiment into Beaufort Sea. The regression coefficients for all four experiments are shown in Figure C.1 in Appendix C.1, the AO of the global run in Figure 4.2 b).

This comparison of the EOFs of the NCEP / NCAR reanalysis, the global model run, and the regional model run shows that in the analysis of the influence of the leading orthogonal function one has to be aware that the leading EOF in our regional model is not equivalent to the AO.

4.1.1.2 Principal component of the leading empirical orthogonal function

We use the normalized principal component (PC) time series of the leading EOF (EOF 1) as an index, referred to as PC 1 from now on. The PC 1 for each simulation is illustrated in Figure 4.3. The values exceeding one standard deviation are marked in red (called positive EOF 1 years), the values underrunning minus one standard deviation are marked in blue

(called negative EOF 1 years). In the following, we use mean values of these marked positive and negative years as composites and compare them with the mean state of the model.

The correlation between the indexes of the different simulations is very high and varies between 0.41 and 0.71, depending on the experiments. Thus, the events for the composites are not fully independent but determined to a certain part by the forcing.

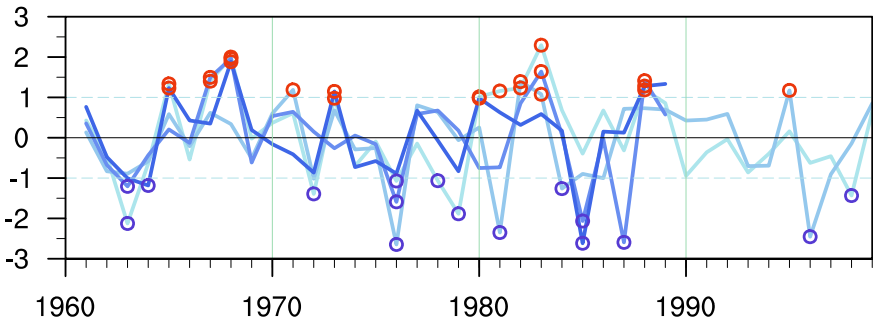

Figure 4.3: Principal component time series of the leading EOF for the winter (DJF) mean sea level pressure of the ECHAM-forced experiments; each blue-colored line stands for one of the experiments. The dashed lines indicate ± one standard deviation. The red circles mark all years exceeding one standard deviation and the blue circles mark all years underrunning minus one standard deviation.

4.1.1.3 Response in the atmosphere

Mean sea level pressure As can be seen in Figure 4.4 a), in the positive EOF 1 years, the Siberian high is weaker than usual and does not exceed so far northward. The Icelandic low is stronger than usual and extends from GIN Sea into Barents Sea. In contrast to this, in the negative EOF 1 years, the Icelandic low is not that pronounced as usual and the Siberian high is much stronger than in the ensemble mean (Figure 4.4 b)).
Large areas differ significantly from the mean value of winter mean sea level pressure, as indicated by the grey contour line. (For absolute values of the DJF mean sea level pressure see Figure C.2.)
For the positive EOF 1 years, the low pressure systems arriving from the Atlantic are much stronger than usual. They proceed far into Barents Sea and extend beyond the coastal regions of Scandinavia to Russia. In contrast to this, in the negative EOF 1 years, the Siberian high pressure system is that strong that it blocks the anyway weaker low cells arriving from the Atlantic.
This difference in the mean sea level pressure fields is persistent only in winter, more precisely until February to April and looses strength rapidly. Figure 4.5 shows the regression coefficients between the PC 1 and the three months running mean of mean sea level pressure for the winter months (see Appendix A for a short description of a regression and correlation analysis in general). The correlation between PC 1 and winter mean sea level pressure exceeds 0.8 in large parts of the Arctic.

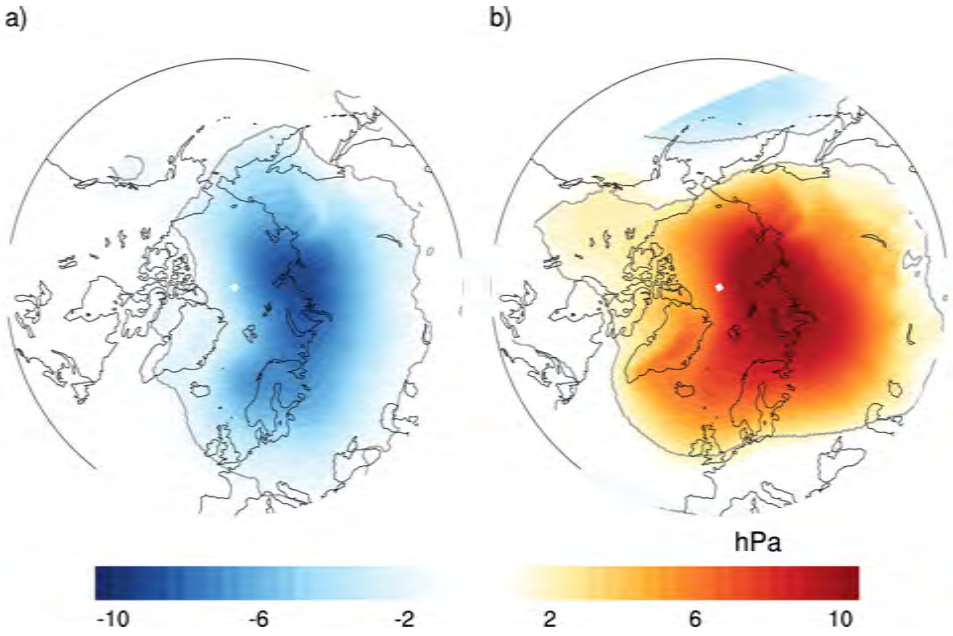

Figure 4.4: Difference between DJF mean sea level pressure in a) the positive EOF 1 years and b) the negative EOF 1 years and the overall mean of DJF mean sea level pressure. The grey contour line indicates the region where the composite years differ significantly from the mean value (as defined in equation A.6 in Appendix A.3).

The grey contour line in Figure 4.5 highlights the data that correlate highly significantly ($\alpha = 0.01$) assuming that we have 140 independent model years, which is the total number of years used in this analysis. In contrast, the pink contour line indicates all values exceeding a highly significant correlation assuming only 40 independent years, the minimum of independent years and spread of the time period 1960 - 1999 used in this analysis. This means that approximately all values exceeding this pink contour line explain more than 16 % of its variance. The difficulty in the determination of significance levels is that we have a total number of 140 years, adding all modeled years used for this analysis, but, as the correlations of the principal components are high between the ensemble members, the years are not fully independent of each other. This is obvious as the different ensemble members see the same forcing outside the coupled domain. The minimum number of independent years is 40, which is the length of the time period of our experiments. Thus, the grey and pink contour lines give of minimum and maximum value for $\alpha = 0.01$.

For the mean sea level pressure in December to February, the explained variance exceeds 60 %. The influence of EOF 1 on the mean sea level pressure pattern is decreasing with time and can be neglected after February to April.

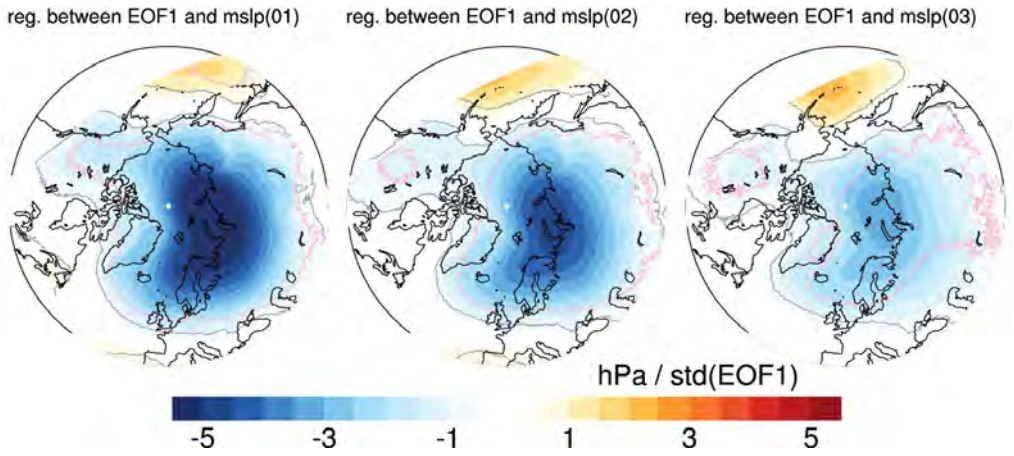

Figure 4.5: Regression coefficient between PC 1 and 3 months running mean sea level pressure in hPa per standard deviation of PC 1. The term mslp(01) refers to the mean value of mean sea level pressure for the period December - February, mslp(02) to the mean value for January - March, and so forth. The grey contour line indicates the level of highly significant ($\alpha = 0.01$) values for all model years and the pink line indicates the level of highly significant ($\alpha = 0.01$) values for 40 years.

2 m temperature How much does the large change in winter mean sea level pressure influence the temperature in the Arctic region? The stronger than usual low pressure system over Iceland and GIN Sea in the positive EOF 1 years leads to anomalously strong winds from the North Atlantic over Europe into Siberia. Thus, the strong low pressure cells transport warm and moist air masses from low to high latitudes and the Eurasian continent, where a large scale warming of up to 4 °Celsius can be seen (Figure 4.6 a)). The same is true for the North American region, but not that extensively as in Eurasia. In the negative EOF 1 years, the weaker pressure gradient between the (lower than usual) Icelandic low and the midlatitudinal high slows down the winds bringing heat and moisture in high latitudes. As mentioned already above, the stronger than usual Siberian high additionally blocks the northward transported heat leading to colder than usual temperatures over Eurasia (Figure 4.6 b)). Furthermore, a strong positive bias in winter 2 m temperature over Greenland and in Lincoln Sea as well as over Alaska can be seen. The warm temperatures do not reach the Eurasian continent but are aligned more northward. Again, the explained variance from PC 1 on the 2 m temperature pattern exceed more than 60 % for the winter months, December to February. Since the response of the 2 m temperature on PC 1 is widely linear, the regression pattern does largely resemble Figure 4.6 a) (not shown). The influence remains highly significant until February to April. As temperature changes are largely wind driven and the strength of the geostrophic winds depends on the pressure gradient, the influence on summer temperatures in the Arctic can not be explained by the winter index PC 1.

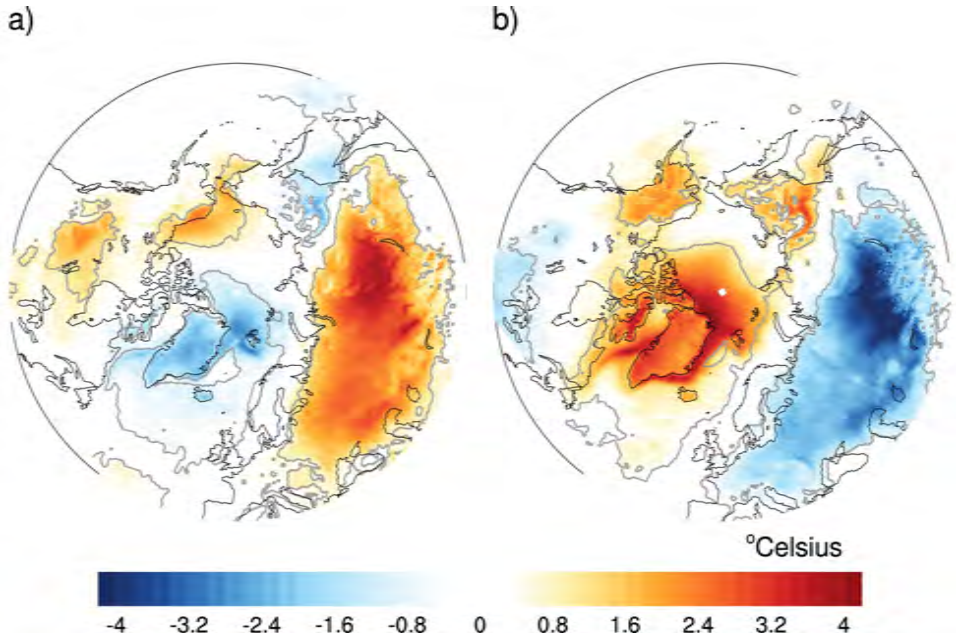

Figure 4.6: Difference between DJF 2 m temperature in a) the positive EOF 1 years and b) the negative EOF 1 years and the overall mean of DJF 2 m temperature. The grey contour line indicates the region where the composite years differ significantly from the mean value (as defined in equation A.6 in Appendix A.3).

Geopotential height Thompson and Wallace (1998) propose to interpret the Arctic Oscillation "as the surface signature of modulations in the strength of the polar vortex aloft". Baldwin and Dunkerton (1999) suggest that large stratospheric anomalies can be seen as precursors to tropospheric changes and detect high correlations of the 10 hPa anomaly and the 1000 hPa anomaly lagged by about three weeks. Kodera and Kuroda (2000) divide strong AO events in two groups, depending on whether they are driven by downward propagation of zonal-mean wind anomalies in the stratosphere or events occurring only in the troposphere. They conclude that the AO is formed in early winter by tropospheric processes only, but its strength and extrapolation in the stratosphere, especially in late winter, depends on the strength of the overlying polar vortex. They argue, that the strength of the polar vortex depends on the stratospheric mode of variability of the Polar-night Jet Oscillation which is independent of underlying tropospheric events. In our model simulations, the signature of the positive and negative EOF 1 years can clearly be seen in the 500 hPa as well as in the 200 hPa geopotential heights (Figure 4.7). An explanation could be that in the positive EOF 1 years, when the westerlies in mid-latitudes are stronger polewards than usual, the planetary waves are refracted equatorward, leading to less planetary wave propagation upward at high latitudes and consequently to a stronger polar vortex (Figure 4.7 a) and c)). On the other hand, in the negative EOF 1 years, the weaker than usual westerly winds or a displacement of the subtropical jet equatorward lead to increased stationary wave propagation into higher latitudes and a weaker stratospheric vortex (Figure 4.7 b) and d)) (Limpasuvan and Hartmann 2000).

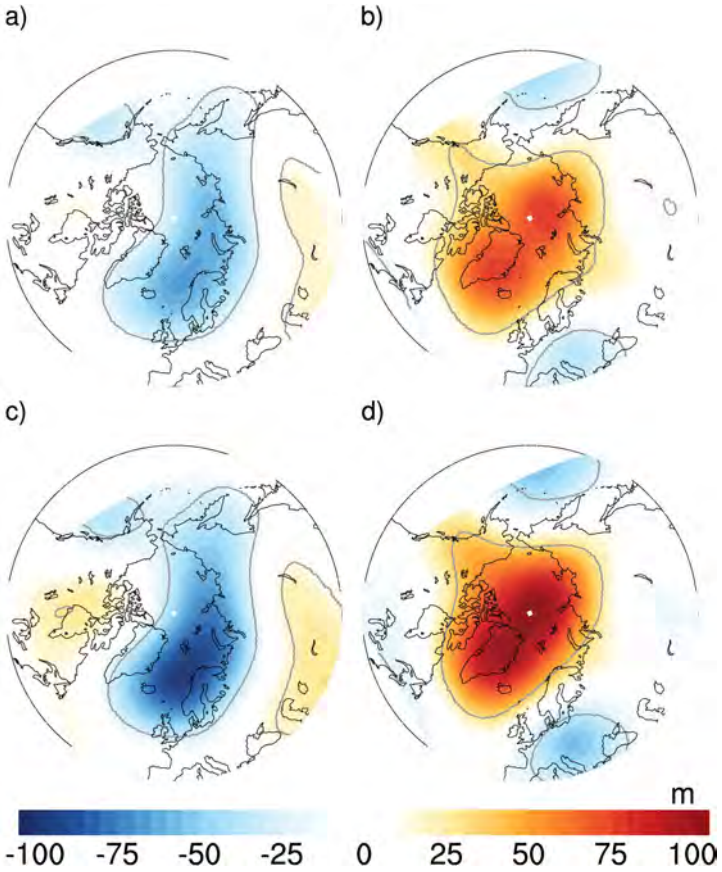

Figure 4.7: Difference between DJF geopotential height in a), c) the positive EOF 1 years for the 500 hPa and 200 hPa pressure level and b), d) the negative EOF 1 years for the 500 hPa and 200 hPa pressure level, respectively, and the overall mean of DJF geopotential height. The grey contour line indicates the region where the composite years differ significantly from the mean value (as defined in equation A.6 in Appendix A.3).

Precipitation and river runoff Is the precipitation field also influenced and if so, how much does this change the amount of river runoff? The anomalous atmospheric circulation regime does not only affect the heat but also the moisture transports to high latitudes. In the positive EOF 1 years, the stronger westerly winds bring more moisture into Eurasia while in the negative EOF 1 years precipitation over Eurasia is reduced. A large difference in the positive as well as in the negative years compared to the winter mean precipitation is in Norwegian Sea, where the Norwegian mountains block a large amount of the arriving moisture, see Figure 4.8. However, the ocean is warm compared to the atmosphere in winter, thus evaporation over the ocean reduces this effect, especially in the negative EOF 1 years (see Figure C.4 in Appendix C.1 for the analogue plot for precipitation minus evaporation). The influence of evaporation is largest south and east of Greenland, especially in the positive EOF 1 years. Over land, the effect of evaporation is negligible in winter, the corresponding pattern for precipitation minus evaporation does not change significantly over land. As can be seen in Figure 4.9 showing the regression coefficient between PC 1

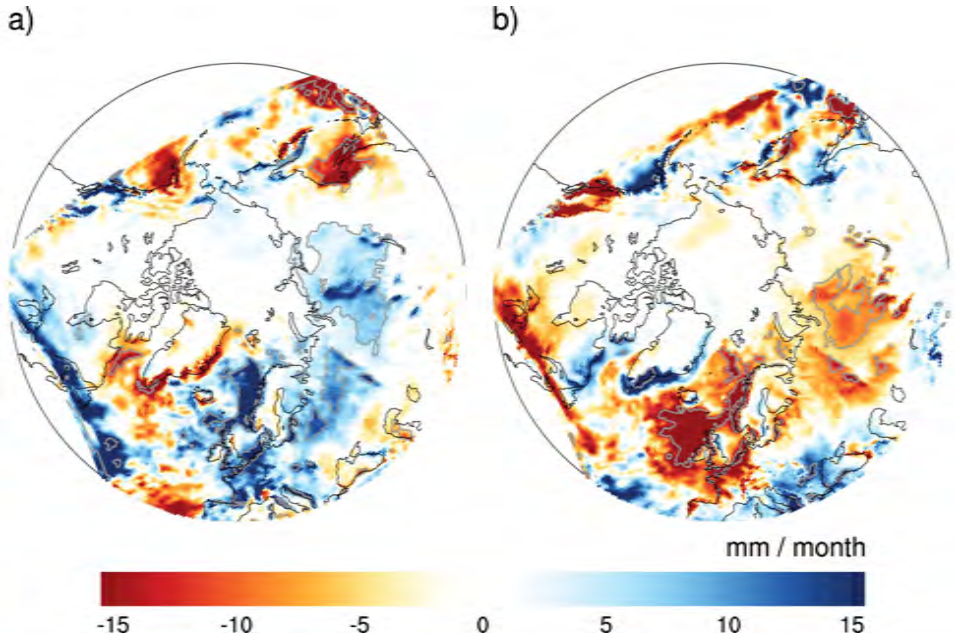

Figure 4.8: Difference between DJF precipitation in a) the positive EOF 1 years and b) the negative EOF 1 years with the overall mean of DJF precipitation. The grey contour line indicates the region where the composite years differ significantly from the mean value (as defined in equation A.6 in Appendix A.3).

and net precipitation (= precipitation minus evaporation), the influence, especially over land, from PC 1 on net precipitation is rather small and again decreasing with time.

As there are only small signals in the precipitation patterns, the differences in the amount of runoff in the EOF 1 years are rather small, too. In Figure 4.10 the total runoff into the Arctic Ocean (Figure 4.10 a)) is split in the Eurasian part (Figure 4.10 b)) and the amount originating from North America (Figure 4.10 c)). Neither the maxima in June differ significantly nor the annual cycle. The largest difference can be seen in the negative EOF 1 years in the runoff of river Ob (annual cycles of some Arctic rivers are presented in Figure C.5 in Appendix C.1), where the mean value differs by about two standard deviations from the mean of the negative years (Figure C.5 c)). The catchment area of the river Ob is exactly that area where the signal in precipitation changes over land is strongest (Figure 4.9). The reduction in the Eurasian runoff in the negative EOF 1 years leads to a decrease of more than 5 % of the total runoff in the Arctic Ocean (Table 4.1).

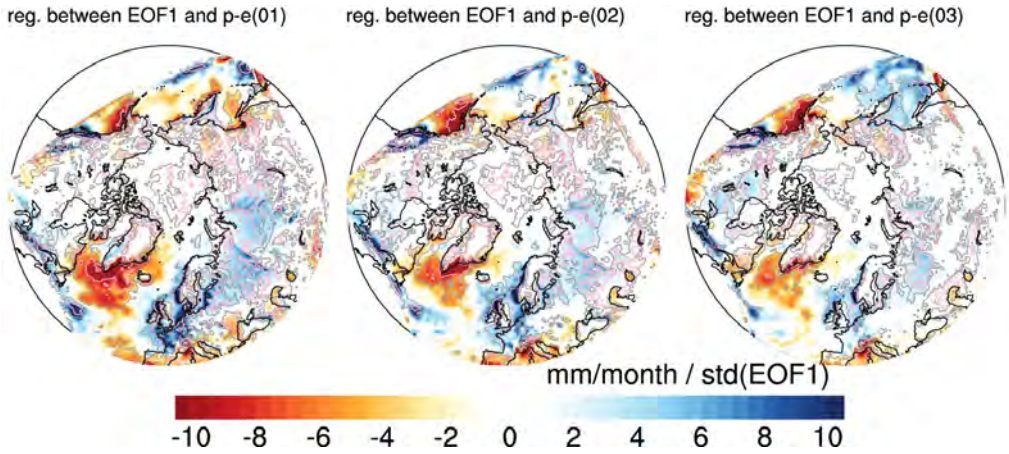

Figure 4.9: Regression coefficient between PC 1 and 3 months running mean net precipitation in mm/month per standard deviation of PC 1. The term p-e(01) refers to the mean value of net precipitation for the period December - February, p-e(02) to the mean value for January - March, and so forth. The grey contour line indicates the level of highly significant ($\alpha = 0.01$) values for all model years and the pink line indicates the level of highly significant values ($\alpha = 0.01$) for 40 years.

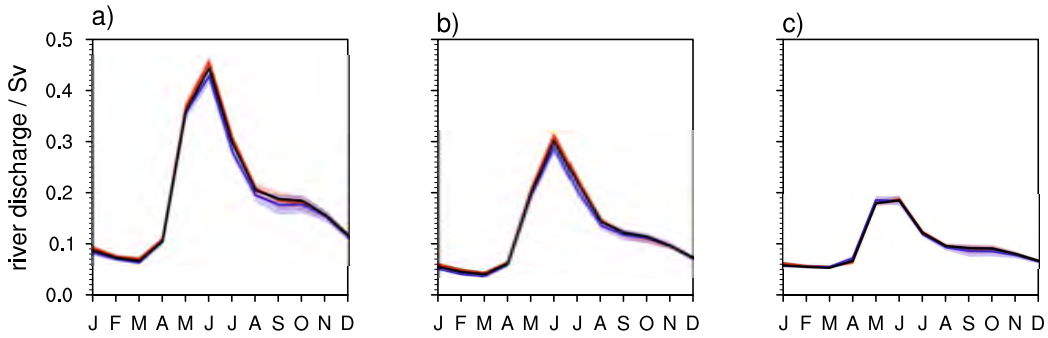

Figure 4.10: Annual cycle of river runoff from a) the total Arctic, b) Eurasia and c) North America. The black line shows the ensemble mean over the whole time period, the red and blue lines represent the positive and negative EOF 1 years, respectively. The shaded areas indicate ± two standard deviations of the given subsets for positive and negative EOF 1 years (see Appendix A.3).

4.1.1.4 Response in the ocean

In the following, we investigate the changes in the ocean caused by the changes occurring in the atmosphere.

Sea ice The sea ice distribution is not only controlled by temperature, but also substantially by the wind forcing. As we have seen already in Section 4.1.1.3, the differences in the mean sea level pressure are significant and thus we see corresponding changes in the near-surface wind field. The regression coefficient between PC 1 and the 3 months running mean sea ice thickness is presented in Figure 4.11. In the positive EOF 1 years, there is a remarkable increase in Lincoln Sea as well as at the north-eastern coast of Greenland, whereas there is a negative bias in East Siberian and Laptev Sea. This structure is persistent for most of the year, the rightmost panel of Figure 4.11 shows the regression coefficient between PC 1 and August to October mean sea ice thickness.

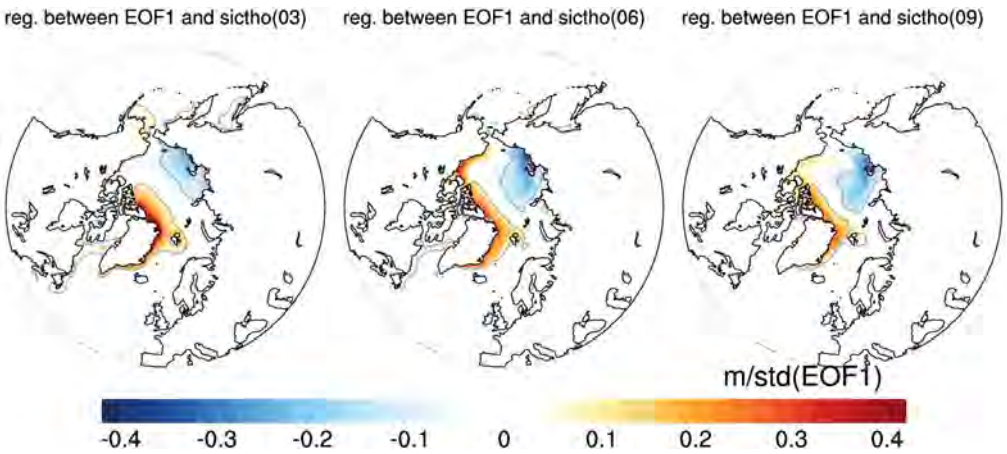

Figure 4.11: Regression coefficient between PC 1 and 3 months running mean sea ice thickness in m per standard deviation of PC 1. The term sictho(03) refers to the mean value of sea ice thickness for the period February - April, sictho(06) to the mean value for May - July, and sictho(09) to the mean value for August - October. The grey contour line indicates the level of highly significant ($\alpha = 0.01$) values for all model years and the pink line indicates the level of highly significant ($\alpha = 0.01$) values for 40 years.

As can be seen in Figure 4.12, displaying the winter sea ice transport for positive and negative EOF 1 years, the sea ice distribution anomalies are caused by variations in the wind-driven sea ice transport. In the negative EOF 1 years, a strong anticyclonic Beaufort Gyre transports the ice from the North American coast to the East Siberian Sea. In the positive EOF 1 years, the strong winds, caused by the large and strong low pressure cells arriving far into the Arctic, lead to a strong transpolar sea ice drift from the Siberian coast to Lincoln Sea and thus to an accumulation north of Greenland and the Canadian archipelago. In the negative EOF 1 years, the stronger than usual Siberian high, extending far northward, leads to the opposite situation. The wind direction does not lead to a sea

ice transport towards Greenland and through Fram Strait, but to a closed recirculation in the Arctic Ocean.

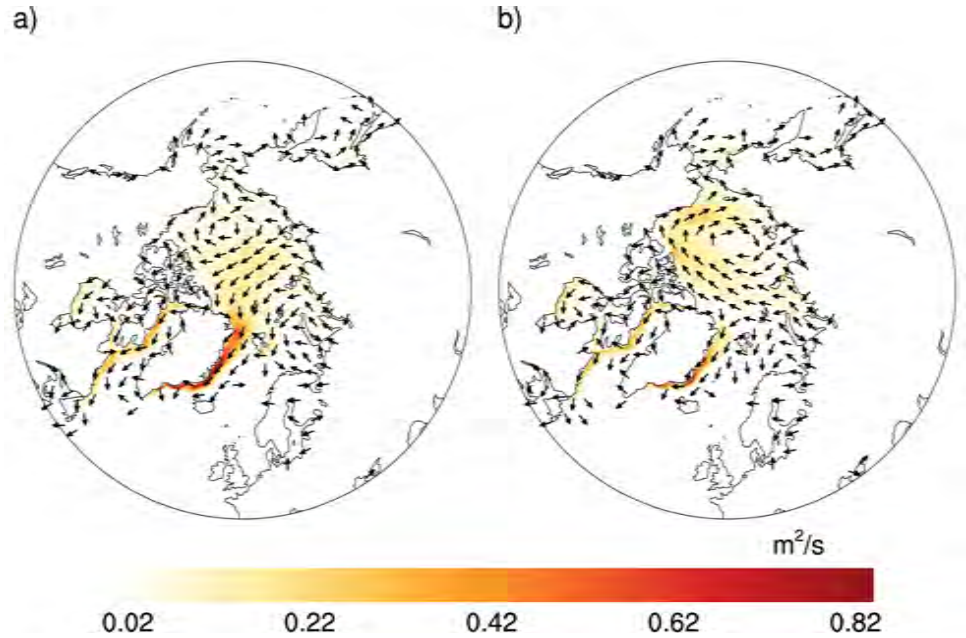

Figure 4.12: DJF sea ice transport in m^2/s in a) the positive EOF 1 years and b) the negative EOF 1 years. The strength of the velocity vector is given by the color coding.

Sea surface height In our model setup, the mean ocean circulation in the Arctic Ocean is dominated by a large anticyclonic Beaufort Gyre. The response of the ocean circulation on the wind fields of the specific EOF 1 years is non-linear; while in the positive EOF 1 years (Figure 4.13 a)) the difference to the mean state in the Arctic Ocean is rather small, in the negative EOF 1 years the strength of the Beaufort Gyre is enhanced by more than 1 Sv (Figure 4.13 b)). Although the anomalous wind forcing is only strong in winter, the response is persistent for most of the year. Enhanced convergence within the gyre leads to an increase of sea surface height of about 3 to 4 cm in a large part of the Arctic Ocean (Figure 4.14). In constrast to that, in the positive EOF 1 years, the stronger than usual transpolar drift, from Siberia to Greenland and the Canadian archipelago, leads to a negative anomaly in the sea surface height along the Siberian coast.

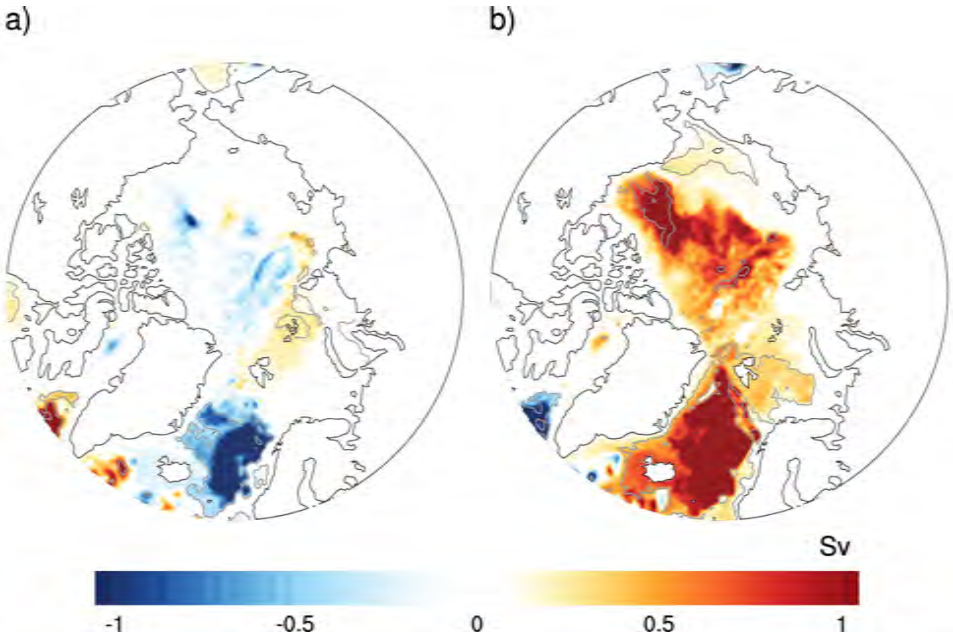

Figure 4.13: Difference between the DJF mean barotropic stream function in Sv in a) the positive EOF 1 years and b) the negative EOF 1 years and the overall DJF mean of the barotropic stream function. The grey contour line indicates the region where the composite years differ significantly from the mean value (as defined in equation A.6 in Appendix A.3).

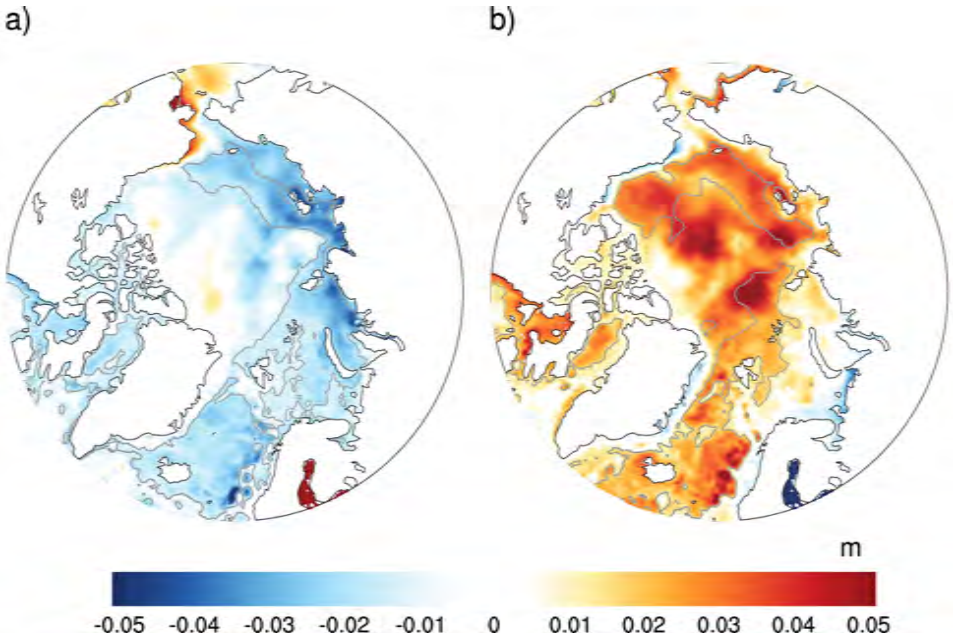

Figure 4.14: Difference between DJF mean sea surface height in m in a) the positive EOF 1 years and b) the negative EOF 1 years and the overall mean of the DJF mean sea surface height. The grey contour line indicates the region where the composite years differ significantly from the mean value (as defined in equation A.6 in Appendix A.3).

FW storage within the Arctic Ocean The increased convergence within the Beaufort Gyre in the negative EOF 1 years leads to enhanced downwelling of the transport of near-surface water, which is fresher than the layers below. This increase of fresh water in the upper layer can be seen in Figure 4.15; the depth of the 33 g/kg isohaline is deeper in the negative EOF 1 years in the Central Arctic Ocean, while in the positive EOF 1 years, the changes occur in Lincoln Sea and close to the Canadian archipelago. This response cannot be seen anymore in larger isohalines, because of the stable stratification within the Arctic Ocean. The signal is anyway rather small, already in these smaller depths, and so is the change in FW content in the specific EOF 1 years.

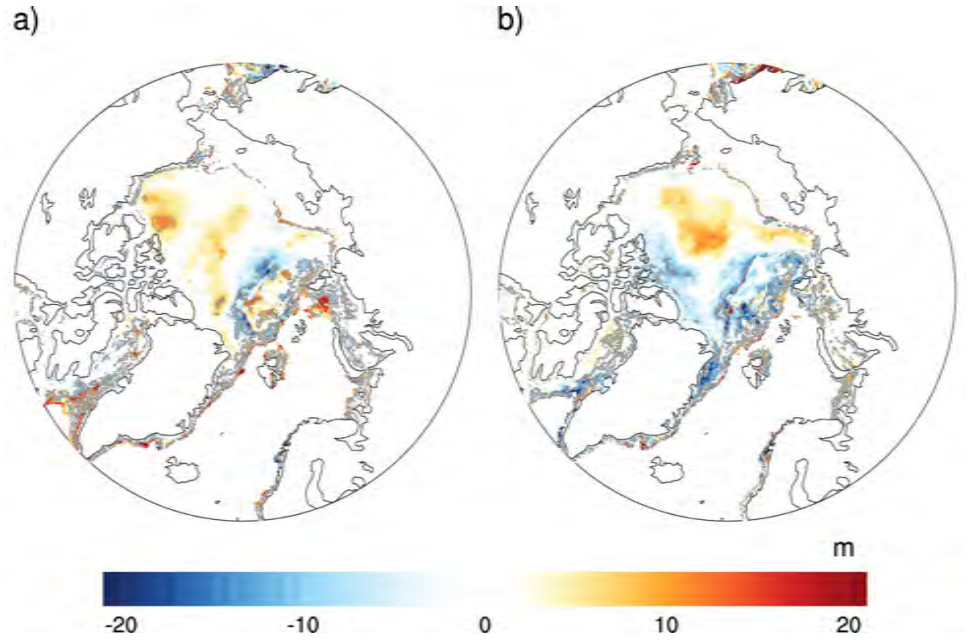

Figure 4.15: Difference between DJF mean depth of the 33 g/kg isohaline in m in a) the positive EOF 1 years and b) the negative EOF 1 years and the overall mean of the depth of the 33 g/kg isohaline. The grey contour line indicates the region where the composite years differ significantly from the mean value (as defined in equation A.6 in Appendix A.3).

For FW content, we do not show the anomalies as for the other variables, but the change within the EOF 1 years, because the decadal variability in FW storage is quite large. We calculate the difference between September values after DJF that are chosen for the EOF 1 years and September values in the corresponding previous years. The pattern of the FW content change (Figure 4.16) resembles the largescale pattern of the anomalies of the depth of the 33 g/kg isohaline. Again, in the positive EOF 1 years, there is an accumulation of FW in Lincoln Sea and north of the Canadian archipelago, whereas in the negative years, it is accumulated in the center of the Arctic Ocean. As mentioned already in Chapter 3.1.1, the variability of FW storage is large, which means these rather small signals might be within the variability.

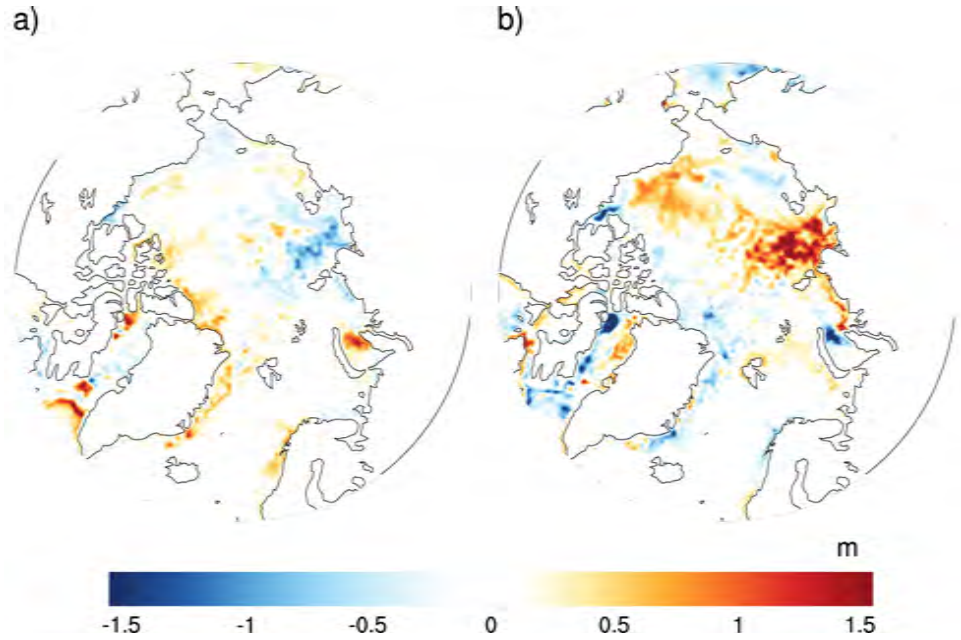

Figure 4.16: Difference of September FW content in m in a) the positive EOF 1 years and b) the negative EOF 1 years. The difference is calculated between September values from the year after and the year before the corresponding EOF 1 values that are defined for DJF.

Fram Strait ice and liquid FW export In Figure 4.17 the annual cycle of FW transport in liquid (Figure 4.17 a)) and in solid form (Figure 4.17 b)) through Fram Strait is presented. We show the year before and after the DJF season used for EOF 1 composite definition. The amplitude of the annual cycle of the liquid FW transport through Fram Strait is small, with a maximum in autumn. The standard deviation of the composite years is quite large (the shaded areas indicate ± two standard deviations from the given subset) and the mean of the annual cycle does not differ significantly for most of the year from the annual cycle of the positive or the negative EOF 1 years. A difference in the positive and negative EOF 1 years can only be seen in the winter months, particularly in January and February.

The increase / decrease of this winter FW liquid transport through Fram Strait can be explained by a change in the total liquid export through the strait. Even though the correlation between the total liquid volume transport and the liquid FW transport through Fram Strait is small, this is not true for the surface export. The correlation of the yearly mean exports (only the southward transports are used for calculation) through Fram Strait in the upper 100 m exceeds 0.76, thus the amount of FW liquid export does increase / decrease with an increasing / decreasing total export of Arctic surface waters. The values of the positive and negative EOF 1 January and February data of FW export as a function of total export is shown in Figure 4.18.

Nearly all of the FW transport through Fram Strait occurs in the upper layer via the East Greenland current. The FW liquid transport of the upper 100 m and the total FW liquid transport integrated over all depths correlate with 0.94. Therefore, in the following

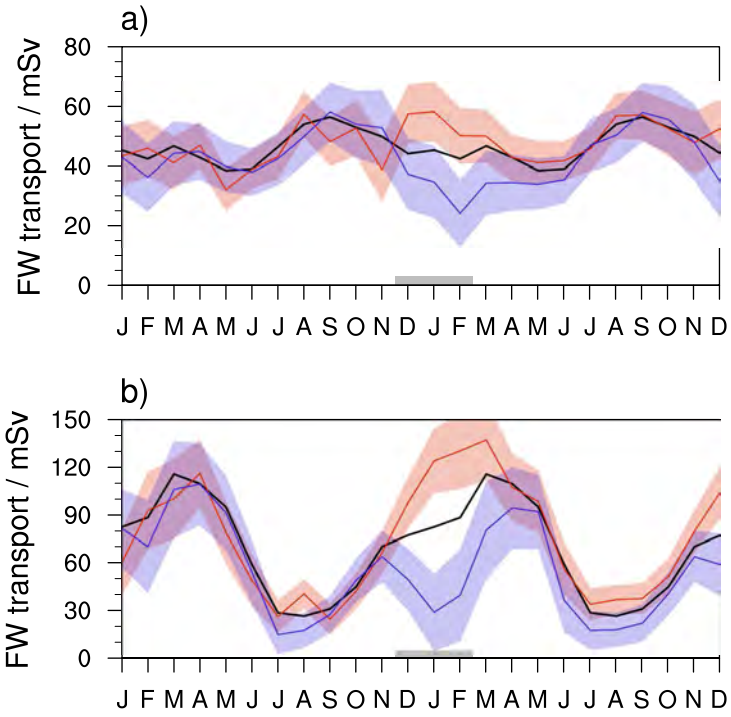

Figure 4.17: Annual cycle of FW transport through Fram Strait in mSv in a) liquid form, and b) in solid form. The black line shows the ensemble mean over the whole time period, the red and blue lines represent the positive and negative EOF 1 years, respectively. The shaded areas indicate ± two standard deviations of the given subsets for positive and negative EOF 1 years (see Appendix A.3). The months used for the index composites are marked by the grey line at the x-axis of the plots.

we only consider the upper 100 m of the strait. To be able to distinguish between the influence of salinity changes and volume changes on the FW transport on interannual time scales, we follow an approach used, among others, by Jahn et al. (2010) and decompose the FW liquid flux F_{FW} perpendicular to any strait A, or more precisely the upper 100 m of the strait, in time mean and time varying parts:

$$F_{FW} = \int_A \underbrace{\frac{s_{ref} - s}{s_{ref}}}_{=:\mathbf{s}} \mathbf{v}_\perp \tag{4.1}$$

$$= \int_A \bar{\mathbf{s}}\,\overline{\mathbf{v}_\perp} + \int_A \mathbf{v}'_\perp \bar{\mathbf{s}} + \int_A \mathbf{s}'\overline{\mathbf{v}_\perp} + \int_A \mathbf{s}'\mathbf{v}'_\perp, \tag{4.2}$$

with the reference salinity again defined as $s_{ref} = 34.8\,\mathrm{g/kg}$, s being the salinity at strait A, and $\mathbf{v}_\perp$ the water velocity perpendicular to strait A. The time mean values are defined by $(\bar{\cdot})$ and the time varying terms by $(\cdot')$. The annual cycle of this transport through the upper 100 m of Fram Strait is presented in Figure 4.19. The anomalous mean FW transport (in green) is dominated by the FW transport associated with the advection of salinity anomalies by the mean flow (in yellow). This is not the case in the composite years for EOF 1 for the winter months. In January and February, in the positive as well

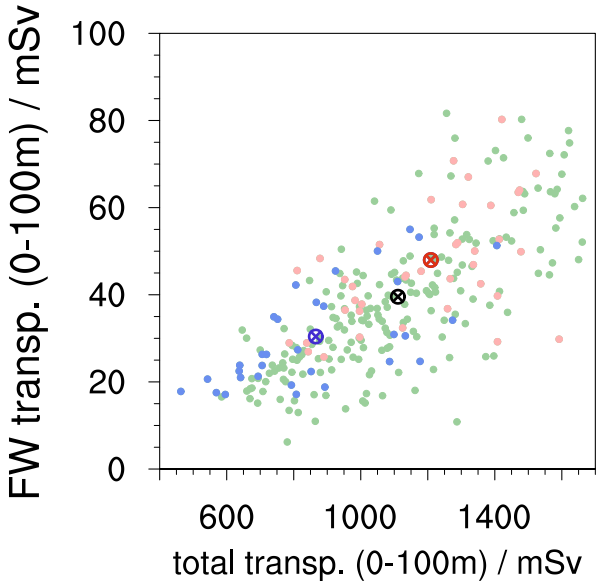

Figure 4.18: Scatter plot of FW liquid export (only southward velocities are counted) in mSv and total volume export in mSv for the upper 100 m. Displayed are all January and February values in green, January and February for the positive EOF 1 years in light red and in light blue for the negative EOF 1 years. The mean values (of JF values) are represented in black, red and blue, respectively.

as in the negative EOF 1 years, the influence of the FW flux due to advection of the mean salinity by the volume flux anomaly (in blue) has the largest influence on the anomalous mean FW transport. While in the positive EOF 1 composite this term has a positive sign, it is negative in the negative EOF 1 years. This confirms the argument of a change in the total export driving the change in the FW export. Yet, this argument is restricted to the upper 100 m and not true for the whole depth of the strait. The liquid export through all depths of Fram Strait shows variability on decadal time scales, which could counteract the short-term effect of the upper layer.

As can clearly be seen in Figure 4.17 b) the winter sea ice export through Fram Strait is strongly enhanced in the positive EOF 1 years while it is significantly reduced in the negative EOF 1 years. This can be explained by changes in the wind field over the strait. Tsukernik et al. (2009) use NCEP reanalysis data to show that the variability of Fram Strait sea ice transport is mainly driven by an east-west dipole pattern of sea level pressure anomalies. In their study, the centers of these anomalies are located over Greenland and over Barents Sea. Using JFM mean sea level pressure data from our model output, the correlation map with JFM mean Fram Strait ice export (Figure 4.20) roughly resembles the corresponding map from Tsukernik et al. (2009). In our experiments, the pressure anomaly over Greenland seems to be less important and is shifted in the direction of Hudson Bay, but the main conclusion remains the same. This dipole pattern is associated with anomalous meridional winds across the strait. Stronger pressure gradients lead to larger wind speeds and thus to more ice transport through the strait. We calculate the mean sea level pressure difference for JFM from two areas next to the strait. The domains

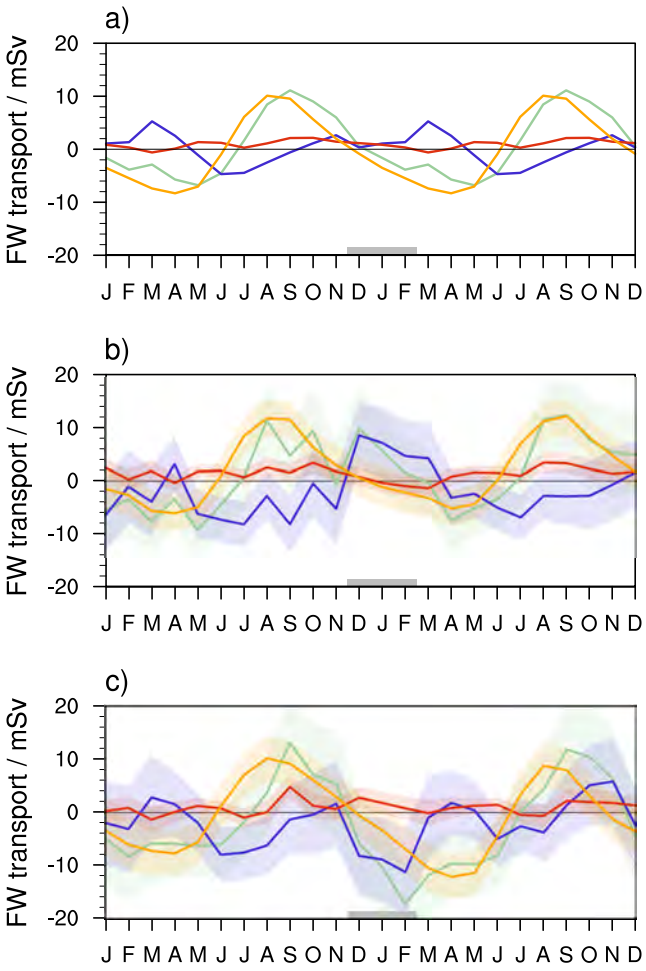

Figure 4.19: Annual cycle of liquid FW transport in mSv through Fram Strait for a) all years, b) the positive EOF 1 years and c) the negative EOF 1 years. The color coding is referred to equation 4.2 as follows: $F_{FW} - \int_A \overline{\mathbf{s}}\,\overline{\mathbf{v}_\perp}$, the difference between the total and the mean FW flux, in green, $\int_A \mathbf{v}'_\perp \overline{\mathbf{s}}$, the advection of the mean salinity by the volume flux anomaly, in blue, $\int_A \mathbf{s}'\overline{\mathbf{v}_\perp}$, the advection of the salinity anomaly by the mean flow, in orange, and $\int_A \mathbf{s}'\mathbf{v}'_\perp$, the adection of the salinity anomaly by the anomalous volume flow, in red. The shaded areas indicate ± two standard deviations from the respective terms. The months used for the composites definition are marked by the grey line at the bottom of the plots.

are indicated in Figure 4.20, its area mean difference is a measure for the pressure gradient over the strait. The normalized difference over all model years correlates with the JFM Fram Strait ice export with 0.69. The absolute JFM mean sea level pressure difference for all years equals 7.03 hPa, for the positive EOF 1 years 12.1 hPa, and for the negative EOF 1 years 0.18 hPa. Thus, the stronger than usual gradient in the positive EOF 1 years leads to this increase of ice export through Fram Strait, while in the negative EOF 1 years the weaker than usual gradient leads to the decrease. Koenigk et al. (2006) analyze the variability of sea ice export through Fram Strait in a 500-year control simulation of the global coupled model ECHAM 5 / MPIOM and come to the similar conclusion that the

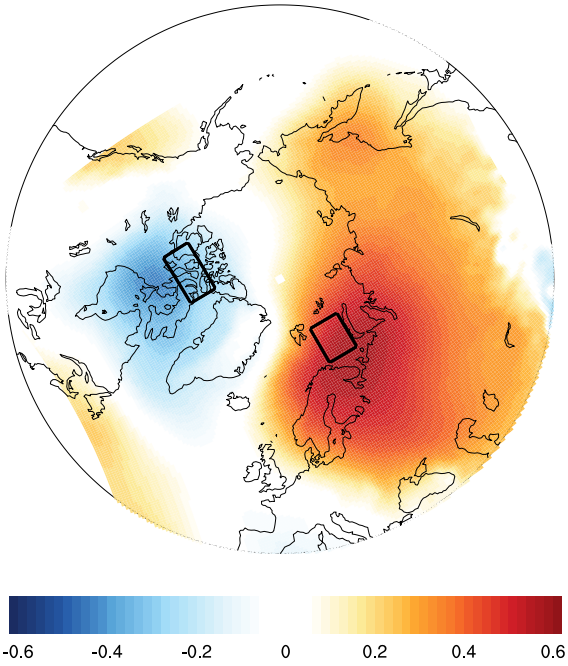

Figure 4.20: Correlation map between JFM mean sea level pressure and JFM sea ice transport through Fram Strait. The black boxes indicate the domain used for calculation of the sea level pressure difference over the strait.

sea level gradient across the strait is the driver for the variability in ice export.

Canadian Arctic archipelago ice and liquid FW export As already mentioned in the introductory chapter, the sea ice export through the Canadian Arctic archipelago is very small, because most of the ice in the small straits is landfast. Thus, the influence of the changes in mean sea level pressure is relatively small (Figure 4.21 b)), the annual cycle of sea ice transport in the positive EOF 1 years does not differ significantly from the mean. In the negative EOF 1 years, a difference can be seen in May and June, but the maximum of the summer ice export is the same as in the overall mean.

The FW liquid transport through the Canadian archipelago is mainly controlled by the total liquid transport through the strait. The correlation between the yearly mean FW liquid and the total liquid transport is larger than 0.8. Consequently, the difference in spring within the positive and negative EOF 1 years in FW liquid transport is driven by changes in the FW flux due to advection of the mean salinity by the volume flux anomaly (Figure 4.22). The positive FW anomaly north of the archipelago (Figure 4.16 a)) as well as the negative sea surface height anomaly in between the islands (Figure 4.14 a)) lead to the increased FW liquid transport throughout the positive EOF 1 years. Further investigations would be needed to explain why the largest difference occurs in late autumn, nearly one year after the winter months used for the definition of the composites.

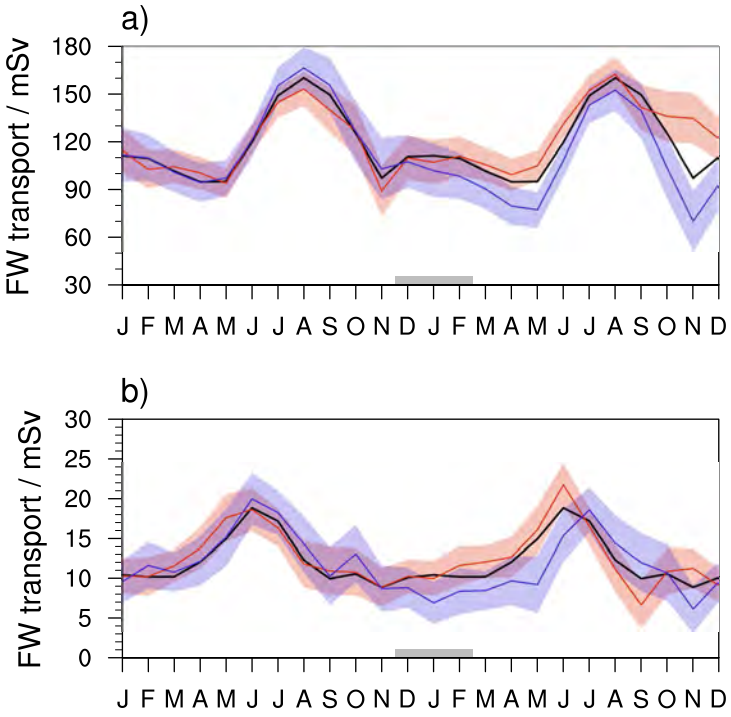

Figure 4.21: Annual cycle of the FW transport through the Canadian Arctic archipelago in mSv in a) liquid form, and b) in solid form. The black line shows the ensemble mean over the whole time period, the red and blue lines represent the positive and negative EOF 1 years, respectively. The shaded areas indicate ± two standard deviations of the given subsets for positive and negative EOF 1 years (see Appendix A.3).

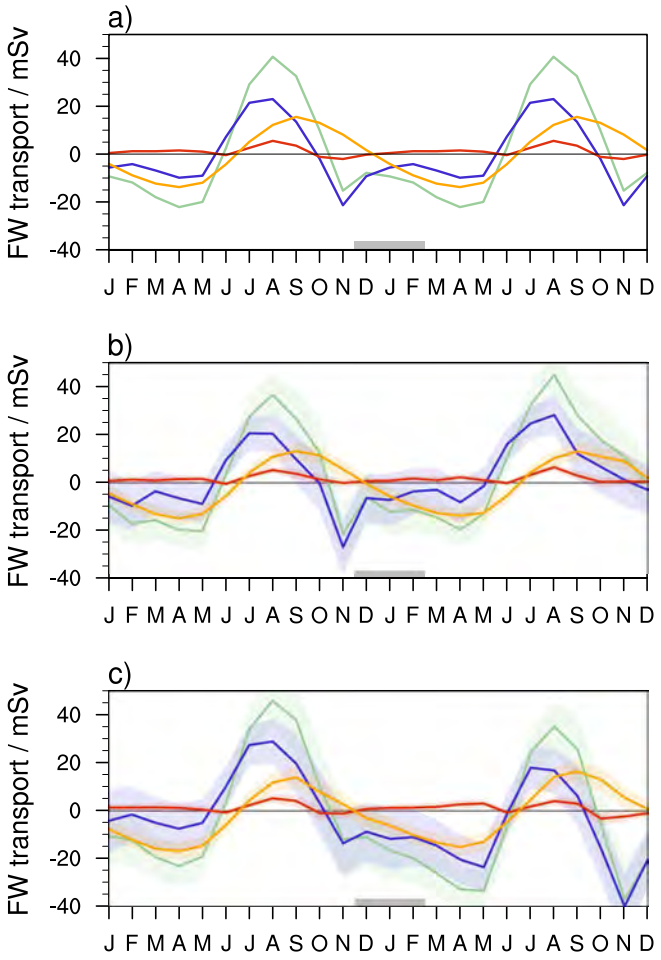

Figure 4.22: Annual cycle of liquid FW transport in mSv through the Canadian Arctic archipelago for a) all years, b) the positive EOF 1 years and c) the negative EOF 1 years. The color coding is referred to equation 4.2 as follows: $F_{FW} - \int_A \overline{\mathbf{s}}\,\overline{\mathbf{v}_\perp}$, the difference between the total and the mean FW flux, in green, $\int_A \mathbf{v}'_\perp \overline{\mathbf{s}}$, the advection of the mean salinity by the volume flux anomaly, in blue, $\int_A \mathbf{s}'\overline{\mathbf{v}_\perp}$, the advection of the salinity anomaly by the mean flow, in orange, and $\int_A \mathbf{s}'\mathbf{v}'_\perp$, the advection of the salinity anomaly by the anomalous volume flow, in red. The shaded areas indicate $\pm$ two standard deviations from the respective terms.

Comparison of FW fluxes To summarize the influence on the Arctic FW fluxes we calculate the yearly mean budgets of the positive and negative EOF 1 years and compare them to the mean value. In Table 4.1, the numbers for all years differ slightly for the yearly mean values over all years as they were presented already in Chapter 3, Table 3.1, because they are calculated from October to September. In the columns for the positive and negative EOF 1 years, we calculate the yearly mean over all positive and negative years, respectively. We use the formula presented in Appendix A.3 to calculate the standard deviation of the given subsets. In contrast to the paragraphs in this chapter, but consistent to Table 3.1, sources of FW within the Arctic Ocean have positive and sinks negative sign. The FW transports are given in mSv. All numbers that differ more than two standard deviations from the mean over all years are highlighted in red.

The most striking changes can be seen in Fram Strait transport, especially in solid form. While in the positive EOF 1 years the total FW transport through the strait increases by about 13 %, the total FW export through the strait decreases in the negative EOF 1 years by more than 20 %. The FW transport through the Canadian archipelago differs by more than one standard deviation compared to the mean. However, the influence on the FW transport through the archipelago is restricted to the negative phase of EOF 1. The increased transport of FW in solid form leads to a decrease in ice storage in the positive EOF 1 years, whereas in the negative EOF 1 years FW is accumulated within the Arctic Ocean, especially in liquid form.

	all years	positive EOF 1 years	negative EOF 1 years
(P-E)+runoff	65.7 + 132.8 = 198.5	65.4 + 132.9 = 198.3 (±2.48)	65.2 + 125.8 = *191.0* (±2.98)
Bering Strait	81.2	83.2 (±3.36)	*87.1* (±4.03)
Barents Sea	−10.1	*-13.6* (±1.62)	−8.2 (±1.94)
Fram Strait liquid	−46.2	*-49.3* (±2.98)	*-41.4* (±3.58)
Fram Strait ice	−69.4	*-81.1* (±4.02)	*-49.8* (±4.82)
CAA liquid	−118.8	−120.4 (±3.7)	*-111.0* (±4.44)
CAA ice	−12.2	−12.4 (±0.7)	*-11.2* (±0.84)
Change in storage liquid		−2.8	38.4
Change in storage ice		−12.7	4.3
$\sum$ transports	23.0	4.7	56.5

Table 4.1: Mean values in mSv of the FW budget of the Arctic for all modeled years, for the positive EOF 1 years, and for the negative EOF 1 years. Mean values are calculated from the end of September one year before the EOF 1 event until the end of September of the next year. Displayed in brackets are ± one standard deviation of the subsets. Italic numbers in black differ more than one standard deviation from the mean value, italic numbers in red differ more than two standard deviations. The change in storage is calculated as the difference from the end of September until the end of September of the next year.

4.1.2 Second empirical orthogonal function of DJF mean sea level pressure

We calculate the second leading mode of the EOFs of winter sea mean level pressure, which accounts for about 12.8 % of the total variance. This EOF explains more than 11 % of the yearly mean variability and differs largely from the second EOF from the corresponding global model run with ECHAM / MPIOM. If we interpolate the global model output to our regional grid and calculate the correlations in grid space between our EOFs and the second EOF from the global model, we achieve highest correlations, of about 0.85, with our third EOF. This indicates that our model permutes the order of the EOFs compared to the global model. However, the explained variance of our third EOF is with about 9.3 % considerably smaller than that of our second EOF.

The second EOF of winter mean sea level pressure in a region north of 20 °N, for example from NCEP reanalyis or in the global model, often represents the so-called Arctic Dipole anomaly, with a negative center of action along the coastal area of Kara Sea and a positive pole in GIN Sea. This leads to a largest pressure gradient over the Arctic Ocean. In our case, the second EOF is characterized by a tripole pattern, with strong negative values in the region of the Aleutian low and over the Baltic, extending over southeastern Europe. The positive pole over Greenland reaching into the Arctic Ocean is slightly smaller in amplitude (Figure 4.23, centers of actions are marked by the white contour line).

Since our second EOF explains considerably more variability than the *common* second EOF, mostly resembled by our third EOF, we analyze in this chapter the influence of our second EOF on the FW variability.

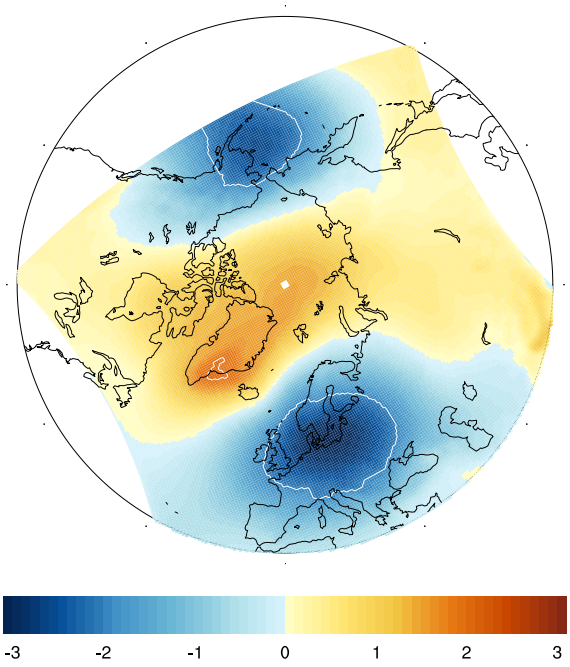

Figure 4.23: Second orthogonal function of winter (DJF) mean sea level pressure from the four ECHAM-forced experiments for the years 1960 - 1999 and 1960 - 1989, depending on the simulation. The white contour line indicates the ± 2 hPa isolines.

4.1.2.1 Principal component of the second empirical orthogonal function

As a second index, we use the principal component time series of the second EOF (Figure 4.24), referred to hereafter as PC 2, and use again the positive and negative years exceeding more than one standard deviation for a composite analysis. The correlation of these principal components between the different experiments is again very high. It varies between 0.56 to 0.88 depending on the experiments. This again indicates that the occurred positive and negative events are not independent of each other.

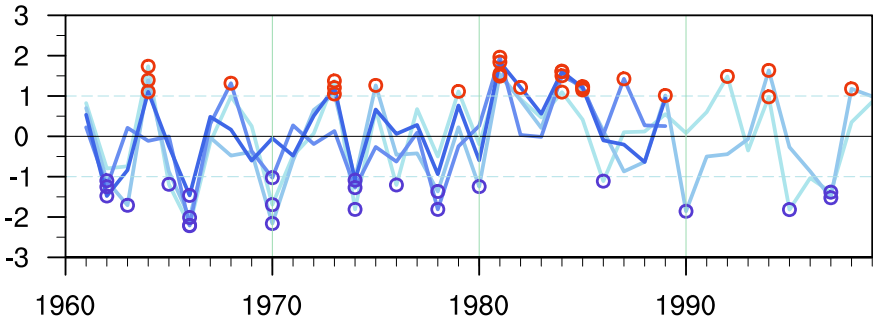

Figure 4.24: Principal component of the second EOF for the winter (DJF) mean sea level pressure of the ECHAM-forced experiments. The dashed lines indicate ± one standard deviation. The red circles mark all years exceeding one standard deviation and the blue circles mark all years underrunning minus one standard deviation.

4.1.2.2 Response in the atmosphere

Mean sea level pressure The response of the mean sea level pressure in DJF is mostly linear, showing a mainly similar pattern of the anomaly in the positive and negative EOF 2 years with opposite sign (Figure 4.25). However, in the positive EOF 2 years the positive signal is extending far into Siberia, while in the negative EOF 2 years this deviation is more restricted to the Arctic Ocean. In the positive years, there is a weaker than usual Icelandic low. The influence over Siberia leads to a stronger than usual Siberian high. This high pressure region extends into East Siberian Sea and leads to a shift in the pressure gradient southward, from across the Central Arctic Ocean, from Laptev Sea to the Canadian archipelago, more to Fram Strait. Furthermore, the Aleutian low pressure system is stronger than usual in the positive EOF 2 years. In the negative EOF 2 years, this Aleutian low is weaker, as well as the Siberian high pressure field. The positive bias over the Baltic leads to higher than usual pressure all over Europe. In the negative years, the Icelandic low is stronger than usual, increasing the pressure gradient over the North Atlantic. (See Figure C.6 in Appendix C.2 for absolute values.) In the next paragraphs, we analyze how these changes in the pressure field influence the heat and moisture transport.

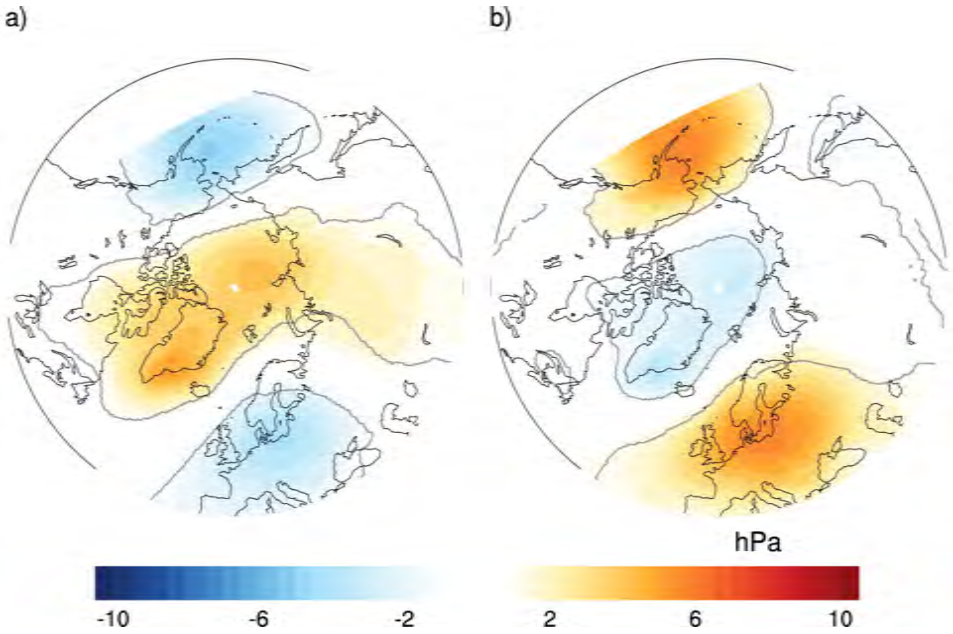

Figure 4.25: Difference between DJF mean sea level pressure in a) the positive EOF 2 years and b) the negative EOF 2 years and the overall mean of DJF mean sea level pressure. The grey contour line indicates the region where the composite years differ significantly from the mean value (as defined in equation A.6 in Appendix A.3).

2 m temperature In the positive EOF 2 years, the weaker than usual low pressure system south of Iceland weakens the heat transport into Northern Europe. The heat is deflected southward leading to a positive anomaly in south-eastern Europe and Central Eurasia (Figure 4.26). The stronger than usual Siberian high blocks the high temperatures, but the changes over Siberia are comparably small. The largest changes occur over the Canadian archipelago and along the North American coastline. A stronger than usual Aleutian low enhances poleward winds accompanied by high temperatures, leading to the positive anomaly over the North American continent.

The opposite is true for negative EOF 2 years. The weaker than usual Aleutian low is responsible for lower than usual temperatures over North America, while the stronger than usual Icelandic low leads to a cold anomaly over south-eastern Europe and Central Eurasia. The regression coefficient between PC 2 and 2 m temperature, shown in Figure 4.26, decreases with time. The values are largest for 2 m temperatures of December to February, showing a direct response on the mean sea level pressure changes. Figure C.7 in Appendix C.2, showing the anomalies of 2 m temperatures of positive and negative EOF 2 years, largely resembles the pattern of the regression coefficient in Figure 4.26.

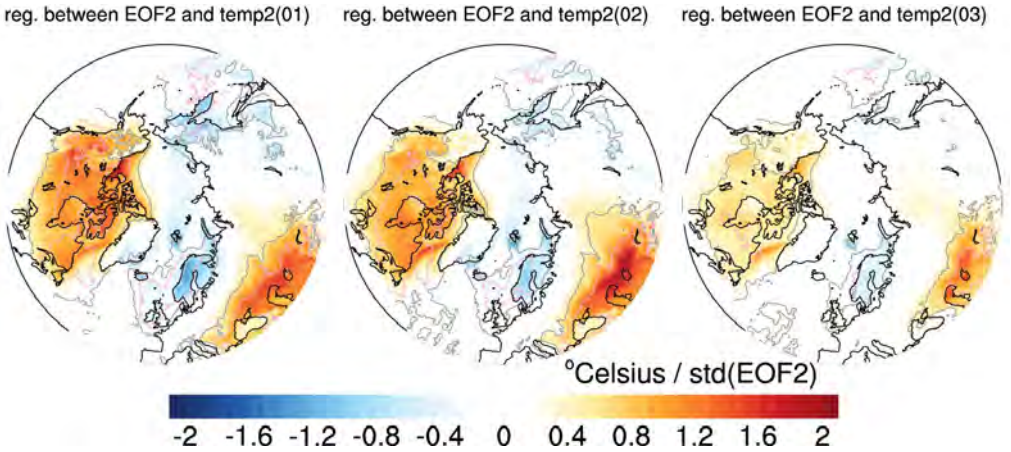

Figure 4.26: Regression coefficient between PC 2 and 3 months running mean 2 m temperature in °Celsius per standard deviation of PC 2. The term temp2(01) refers to a mean value of 2 m temperature for the period December - February, temp2(02) to the mean value for January - March, and so forth. The grey contour line indicates the level of highly significant ($\alpha = 0.01$) values for all model years and the pink line indicates the level of highly significant ($\alpha = 0.01$) values for 40 years.

Precipitation and river runoff As in the analysis of EOF 1, we also analyze precipitation for EOF 2. Yet, here we do not focus on precipiation only, because especially over the ice free ocean the heat loss in winter is immense and the influence of evaporation is partly larger than of precipitation itself. In Figure 4.27 the regression coefficient between precipitation minus evaporation and PC 2 is shown. The influence over the North American continent, where we see large changes in the winter 2 m temperature, is relatively small. The impact of the changes in the winter mean sea level pressure pattern in the EOF 2 years is largest over Europe, where the correlations between PC 2 and DJF precipitation exceed 0.8 in large areas. This influence on net precipitation is reflected in Figure 4.27, with the largest positive values over Europe and Central Eurasia. Furthermore, the weaker than usual Icelandic low in the positive EOF 2 years leads to a strong decrease in precipitation and an increase in evaporation in GIN Sea and Denmark Strait. This might be caused by enhanced advection of cold and dry polar air relative to warm moist subtropical air masses. In the Central Arctic and in Russia, the changes in net precipitation are rather small. Figure C.8 in Appendix C.2 shows the precipitation anomalies for positive and negative EOF 2 years. As before, the impact decreases with time, especially over Europe.

The impact of net precipitation changes on the river runoff is small. Nevertheless, in the positive EOF 2 years, the value of net precipitation over the Arctic Ocean plus runoff into the Arctic Ocean, given in Table 4.2, is about two standard deviations smaller than the overall mean value. This change is caused by less precipitation over the Arctic Ocean as well as by less runoff from the American continent. However, the signal in the runoff composites is negligible.

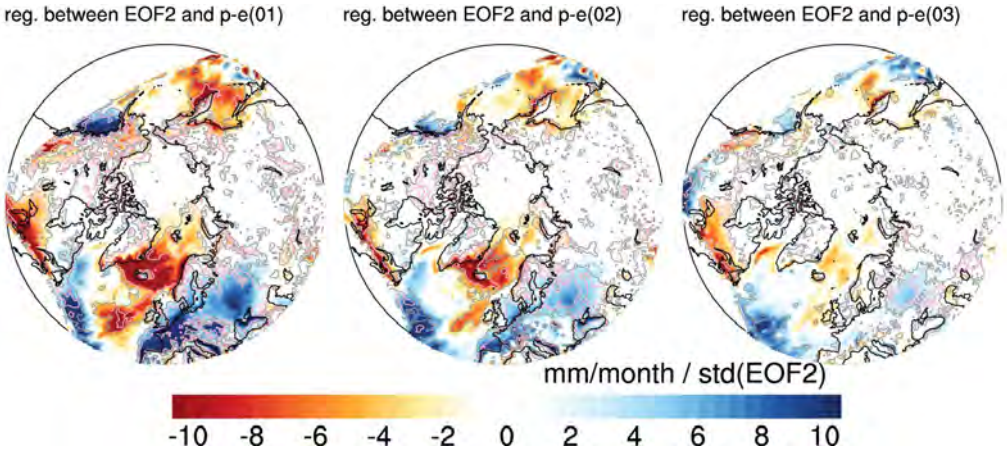

Figure 4.27: Regression coefficient between PC 2 and 3 months running mean precipitation minus evaporation in mm/month per standard deviation of PC 2. In the left plot p-e(01) refers to a mean value of precipitation minus evaporation for the period December - February, p-e(02) to the mean value for January - March, and so forth. The grey contour line indicates the level of highly significant ($\alpha = 0.01$) values for all model years and the pink line indicates the level of highly significant ($\alpha = 0.01$) values for 40 years.

4.1.2.3 Response in the ocean

Sea ice The sea ice thickness is affected by the changes in the wind circulation. While in the positive EOF 2 years, the anticyclonic circulation of the Beaufort Gyre is enhanced, comparable to the circulation in the negative EOF 1 years, the gyre is rather small in the negative EOF 2 years. Instead, there is a strong sea ice transport from the Eurasian coast to the Canadian archipelago and to the North American coast (Figure 4.28). This leads to an accumulation of sea ice at the North American coastline in the negative EOF 2 years. This positive bias in sea ice thickness persists for most of the year; Figure 4.29 shows the yearly mean sea ice thickness composites. The positive EOF 2 years are similar to the situation in the negative EOF 1 years, the sea ice is transported from the Central Arctic Ocean to the Siberian coast, leading to an accumulation of sea ice in that area.

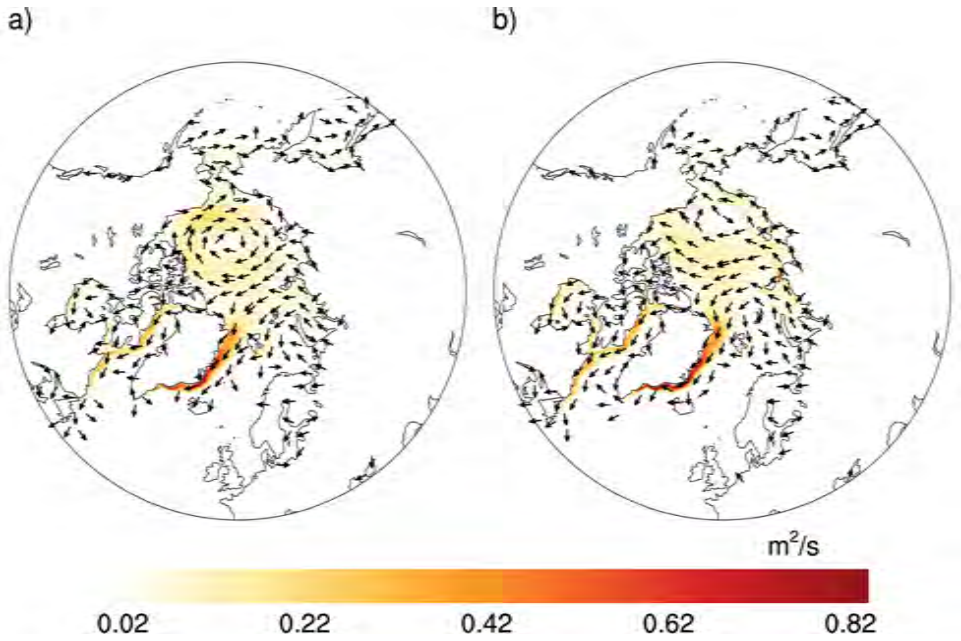

Figure 4.28: DJF sea ice transport in m^2/s from a) the positive EOF 2 years and b) the negative EOF 2 years. The strength of the velocity vector is given by the color coding.

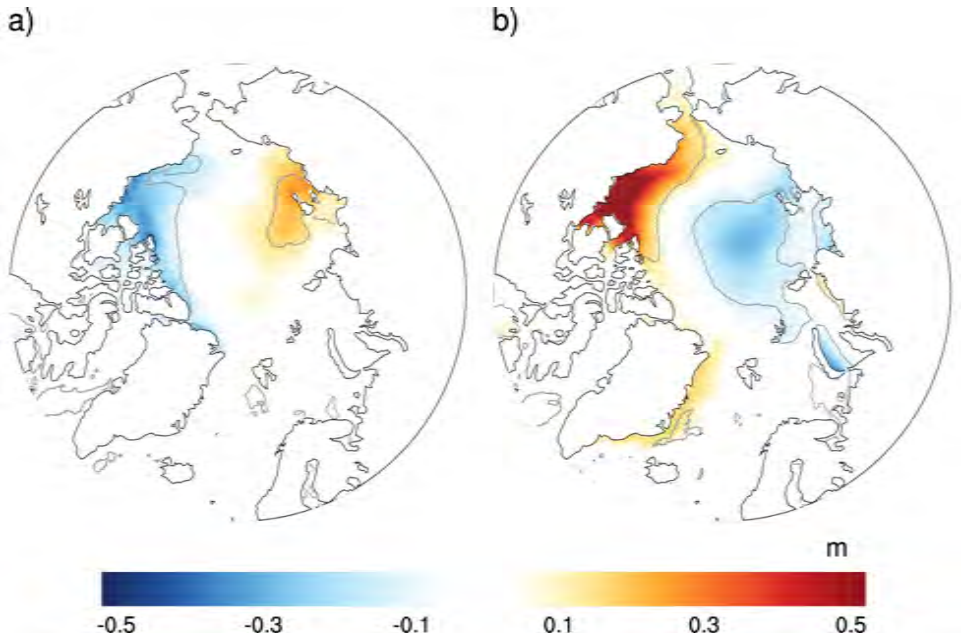

Figure 4.29: Difference between the yearly mean sea ice thickness in m in a) the positive EOF 2 years and b) the negative EOF 2 years and the overall yearly mean of sea ice thickness. The grey contour line indicates the region where the composite years differ significantly from the mean value (as defined in equation A.6 in Appendix A.3).

Sea surface height As in the negative EOF 1 years, the Beaufort Gyre is increased by more than 1 Sv in the positive EOF 2 years. This leads to an increase in sea surface height in the Central Arctic Ocean. The mechanism is again the convergence of surface waters within the gyre. In the negative EOF 2 years, the circulation is decreased all over the Arctic Ocean (Figure C.9 in Appendix C.2). This leads to a decrease in the sea surface height in the Central Arctic, but to a large increase along the coastlines and in Kara and Barents Sea. This response persists for most of the year, Figure 4.30 shows the yearly mean values of sea surface height. Other than in the EOF 1 composites, where we saw either a positive or negative anomaly throughout the Arctic Ocean, the EOF 2 composites show a redistribution with a maximum within the Arctic Ocean and a minimum along the coastlines or the other way around.

A particularly strong bias in the sea surface height is found in the negative years in the region of Bering Strait. The inflow from the Pacific into the Arctic Ocean is mainly density driven and thus by the difference in the sea surface height. This difference is reduced in the negative years and so is the import of FW into the Arctic Ocean through the strait. The inflow of 77.2 mSv is more than one standard deviation less than usual.

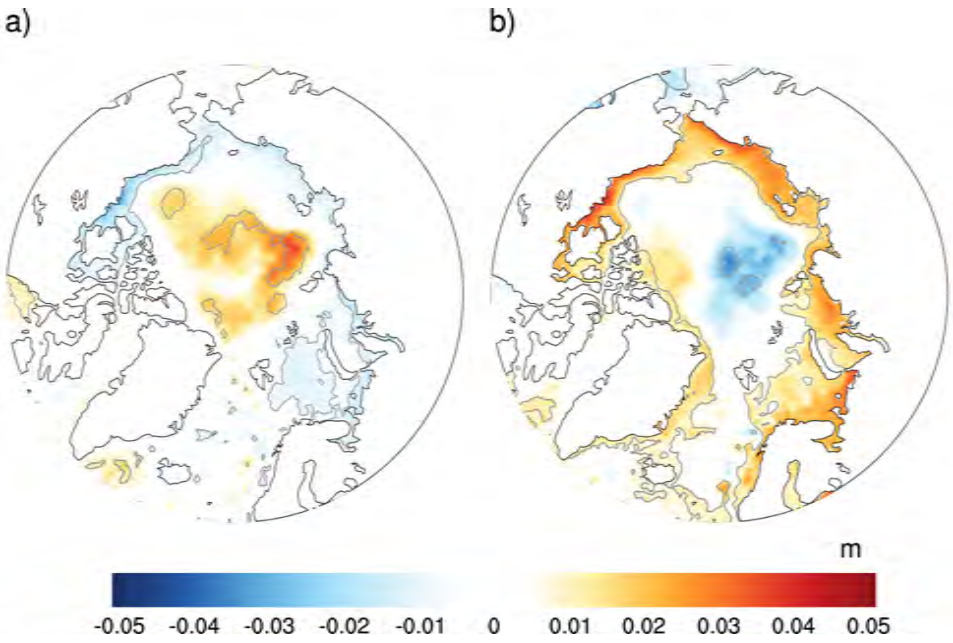

Figure 4.30: Difference between the yearly mean sea surface height in m in a) the positive EOF 2 years and b) the negative EOF 2 years and the overall yearly mean of sea surface height. The grey contour line indicates the region where the composite years differ significantly from the mean value (as defined in equation A.6 in Appendix A.3).

FW storage within the Arctic Ocean According to the pattern of the sea surface height, there is an increase of FW stored in the Central Arctic in the positive EOF 2 years and a decrease in the negative EOF 2 years. In the negative years, the FW is pushed to the North American coast and into the Canadian archipelago. Figure 4.31, displaying the change of

FW stored within the Arctic Ocean, mainly resembles the composites of sea surface height (Figure 4.30). One can clearly see the redistribution of FW, with an accumulation of FW in the Central Arctic and less FW stored along the coast in the positive EOF 2 years and a relocation from the Central Arctic Ocean to the coastal regions in the negative EOF 2 years.

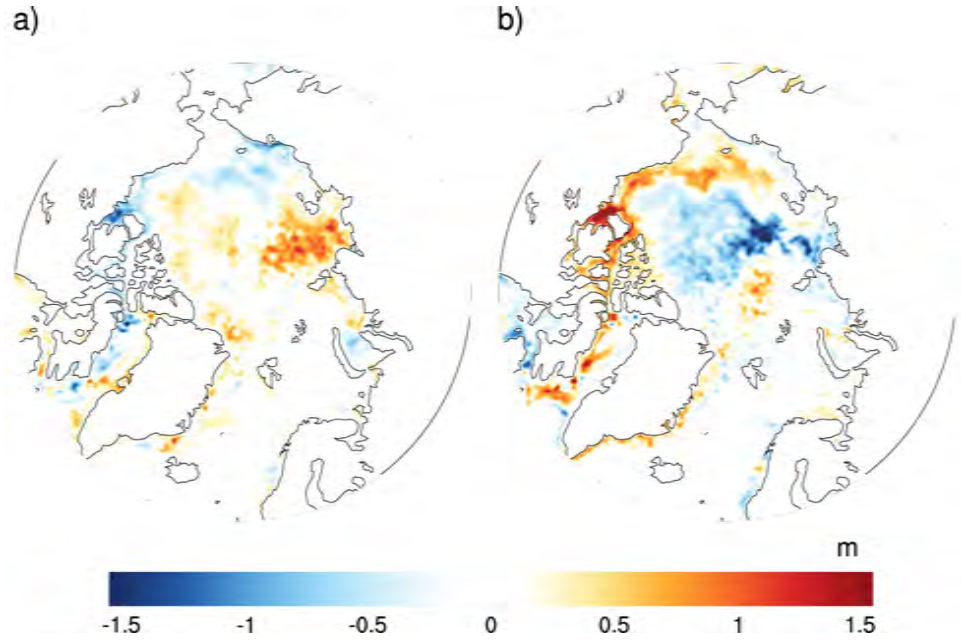

Figure 4.31: Difference of September FW content in m from a) the positive EOF 2 years and b) the negative EOF 2 years. The difference is calculated between September values of the year after and the year before the corresponding EOF 2 values that are defined for DJF.

Fram Strait ice and liquid FW export The liquid FW transport through Fram Strait is significantly increased in the negative EOF 2 years (Figure 4.32). With a yearly mean value of about 54 mSv it is increased by more than 17 % compared to the mean, while the change in the positive years is rather small. These changes in liquid FW transport in the negative EOF 2 years are dominated by changes in the FW export within the upper 100 m; the yearly value is with about 41 mSv approximately 6 mSv larger than in the mean. In contrast to the situation in the positive EOF 1 years, this goes along with an increase in the total liquid export not only in the upper 100 m but also in the deeper layers (which equals a decrease of liquid import). This enhanced total liquid export in the negative EOF 2 years is compensated by an increase of total liquid transport through Barents Sea into the Arctic Ocean. However, the water that enters the Arctic Ocean through Barents Sea is less saline than usual and the increase in liquid import does not increase the inflow of more saline water. This means that the Barents Sea saline inflow, serving as a FW sink, decreases even though the total inflow increases in the negative years. The yearly mean FW transport through Barents Sea (Table 4.2) is not only influenced by changes in the liquid circulation but also due to a change in ice export through Barents Sea into the

North Atlantic. In the negative EOF 2 years, the ice transport through Barents Sea is increased, leading to a smaller than usual FW sink.

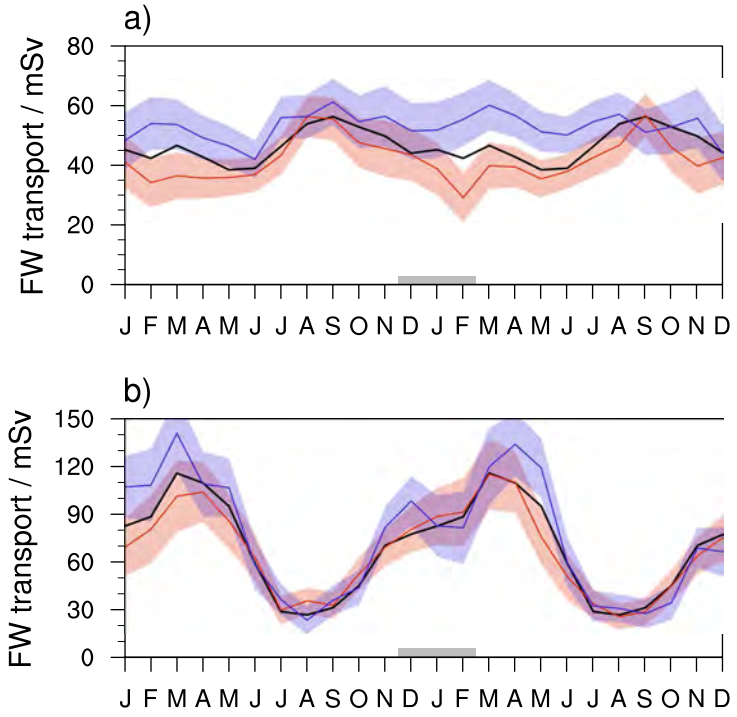

Figure 4.32: Annual cycle of FW transport in mSv through Fram Strait in a) liquid form, and b) in solid form. The black line shows the ensemble mean over the whole time period, the red and blue lines represent the positive and negative EOF 2 years, respectively. The shaded areas indicate ± two standard deviations of the given subsets for positive and negative EOF 2 years (see Appendix A.3). The months used for the composite definition are marked by the grey line at the bottom of the plots.

The change in the negative EOF 2 years in liquid FW transport through Fram Strait is largest from February to May. While in the mean liquid transport (Figure 4.33 a)) the anomalous mean flow (in green) changes the sign in winter and shows a clear annual cycle, it is positive also in the winter months for the negative EOF 2 years. As explained before, these changes are, as in EOF 1, dominated by changes in advection of the mean salinity by the volume flux anomaly (in blue) and thus by changes in the total liquid transport. However, in contrast to the EOF 1 composites, additional changes come from the salinity anomaly advected by the mean flow (in orange) (Figure4.33 c)). As mentioned above, these changes occur also in Barents Sea. Nevertheless, the standard deviation is large and the mean value does not differ more than two standard deviations from the mean of the negative EOF 2 years. To conclude, the changes in liquid FW export through Fram Strait are driven by changes in the total liquid export more than by changes in the salinity at the strait.

The changes in the amount of FW exported in solid form through Fram Strait are smaller than in liquid form. The reason for the comparably small changes is, that the difference

of the sea level pressure over the strait, as calculated already in the EOF 1 subsection, is rather small compared to the mean difference. It is smaller by about 2 hPa in the negative EOF 1 years (leading to a decrease in ice export), and larger by only 1 hPa in the positive EOF 2 years (leading to an increase in ice export). Although small, the increased export of liquid FW in the negative EOF 2 years is accompanied by increases ice export. Even though the maximum of the ice export in the negative EOF 2 years is more than 10 mSv larger than in the mean annual cycle, the standard deviation of ice export is large and the difference between the mean value of the negative EOF 2 years and the overall mean is smaller than two standard deviations (Table 4.2).

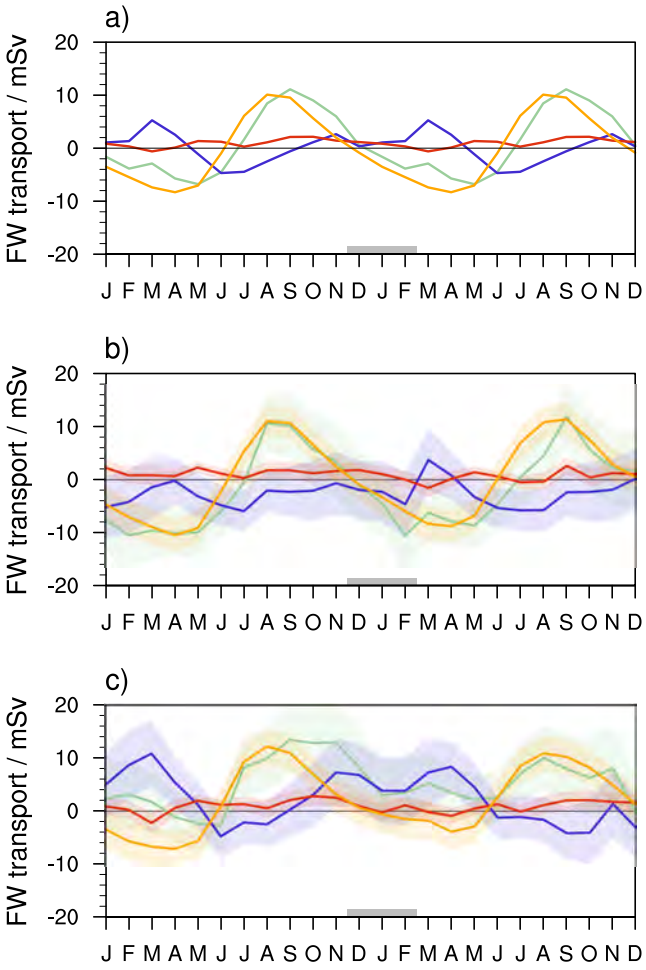

Figure 4.33: Annual cycle of liquid FW transport in mSv through Fram Strait for a) all years, b) the positive EOF 2 years and c) the negative EOF 2 years. The color coding is referred to equation 4.2 as follows: $F_{FW} - \int_A \overline{\mathbf{s}}\,\overline{\mathbf{v}_\perp}$, the difference between the total and the mean FW flux, in green, $\int_A \mathbf{v}'_\perp \overline{\mathbf{s}}$, the advection of the mean salinity by the volume flux anomaly, in blue, $\int_A \mathbf{s}'\overline{\mathbf{v}_\perp}$, the advection of the salinity anomaly by the mean flow, in orange, and $\int_A \mathbf{s}'\mathbf{v}'_\perp$, the advection of the salinity anomaly by the anomalous volume flow, in red. The shaded areas indicate ± two standard deviations from the respective terms. The months used for the composites definition are marked by the grey line at the bottom of the plots.

Canadian Arctic archipelago ice and liquid FW export As can be seen in Figure 4.34, the influence of the mean sea level pressure changes in the EOF 2 years on the FW transport through the Canadian archipelago is strongest in the winter months. In the positive EOF 2 years, where we see an increased anticyclonic Beaufort Gyre accompanied with an accumulation of sea ice at the Siberian coast, there is, consequently, a decrease of FW in liquid as well as in solid form through the archipelago. As explained already in the section of EOF 1, the liquid FW transport through the channels is mainly driven by the total liquid transport through the archipelago and thus dependent on the circulation and the sea surface height difference across the archipelago.

Ice transport is wind driven and as expected the largest changes in the transport occur during the winter months that are used for the decomposition of the EOF 2 years. However, the changes are rather small. The difference in the yearly mean value of the positive years is with 1 mSv larger than in the negative EOF 2 years, but still smaller than two standard deviations from the mean value.

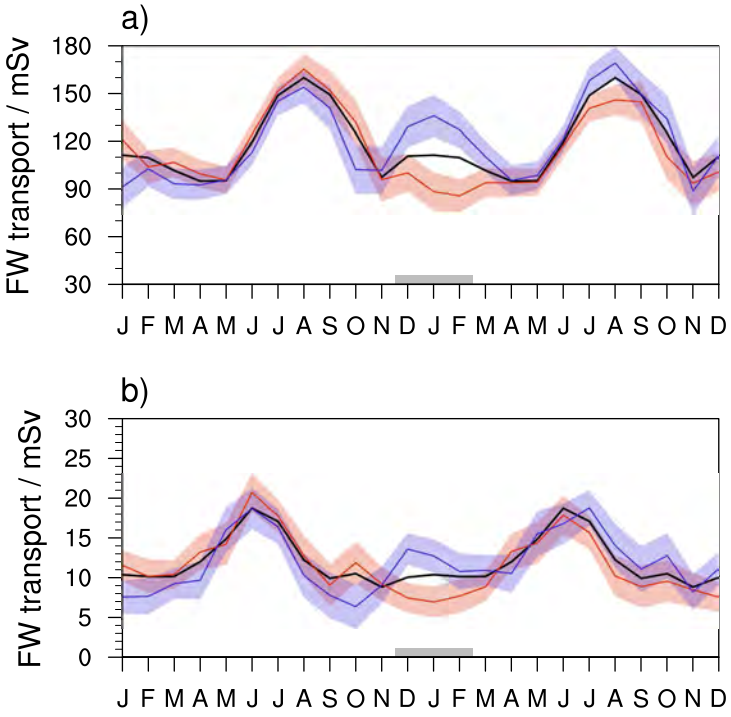

Figure 4.34: Annual cycle of FW transport in mSv through the Canadian Arctic archipelago in a) liquid form, and b) in solid form. The black line shows the ensemble mean over the whole time period, the red and blue lines represent the positive and negative EOF 2 years, respectively. The shaded areas indicate ± two standard deviations of the given subsets for positive and negative EOF 2 years (see Appendix A.3). The months used for the composite definition are marked by the grey line at the bottom of the plots.

Comparison of FW fluxes The changes in the EOF 2 mean sea level pressure pattern have largest influence on the liquid FW transports. In the positive EOF 2 years, where the atmospheric FW input into the Arctic Ocean is decreased, the FW export, in solid and

in liquid form, through Fram Strait and through the Canadian archipelago, is decreased as well. In the negative EOF 2 years, the liquid as well as solid FW transport through Fram Strait and the Canadian archipelago increases. This increase is largest, with 8 mSv, in Fram Strait liquid FW transport. The liquid FW transport through the archipelago is reduced in the positive EOF 2 years by about 6 % compared to the mean. Other than in the EOF 1 years, the influence on Fram Strait ice export in the EOF 2 years is comparably small, the difference in the FW transport through the strait and the overall mean is smaller than two standard deviations. The increased transport of FW in the negative EOF 2 years, which is supported by strong transpolar winds, leads to a decrease in FW storage, in liquid and in solid form, while the decrease in FW export through Fram Strait and through the Canadian archipelago in the positive EOF 2 years leads to an accumulation of liquid FW stored in the Arctic.

	all years	positive EOF 2 years	negative EOF 2 years
(P-E)+runoff	65.7 + 132.8 = 198.5	64.7 + 129.4 = *194.1* (±2.1)	66.7 + 132.5 = 199.2 (±2.23)
Bering Strait	81.2	82.2 (±2.86)	*77.2* (±3.02)
Barents Sea	−10.1	*-11.5* (±1.38)	*-7.7* (±1.46)
Fram Strait liquid	−46.2	*-42.0* (±2.53)	*-54.2* (±2.68)
Fram Strait ice	−69.4	−68.8 (±3.42)	*-76.2* (±3.62)
CAA liquid	−118.8	*-111.4* (±3.15)	*-125.2* (±3.33)
CAA ice	−12.2	*-11.2* (±0.60)	−12.6 (±0.63)
Oceanic storage liquid		17.2	−14.6
Oceanic storage ice		−3.68	−2.17
∑ transports	23	31.4	0.5

Table 4.2: Mean values in mSv of the FW budget of the Arctic for all modeled years, for the positive EOF 2 years and for the negative EOF 2 years. Mean values are calculated from the end of September one year before the EOF 2 event until the end of September from the next year. Displayed in brackets are ± one standard deviation of the subsets. Italic numbers in black differ more than one standard deviation from the mean value, italic numbers in red differ more than two standard deviations. The change in storage is calculated as the difference from the end of September until the end of September of the next year.

4.1.3 North Atlantic Oscillation

The North Atlantic Oscillation (NAO) is a large-scale mode of climate variability, which is strongest in winter. The NAO determines the weather and climate of the North Atlantic and of Europe. It refers to a redistribution of atmospheric mass over the North Atlantic and is a measure of the strength of the westerlies over the North Atlantic between about 40 °N and 60 °N. Thereby it affects the heat and moisture transport between the Atlantic and the neighboring continents (Hurrell et al. 2003; Greatbatch 2000). Numerous studies show that the surface temperatures over the North Atlantic, the Arctic, North America and

Eurasia are significantly correlated with the variability in the NAO (Hurrell 1996; Visbeck et al. 2001; Rind et al. 2005). The positive NAO phase is characterized by a strengthening of the Icelandic low and the Azores high resulting in increased westerlies over the North Atlantic. Consequently, in the positive phase warmer than usual temperatures can be seen over Europe, while in the negative NAO phase, the weaker than usual westerlies bring less than usual warm temperatures and allow more cold air to build up over the Eurasian continent.
In a model study, Condron et al. (2009) investigate the response of the Arctic freshwater budget on extreme NAO wind forcing. Using a coupled ocean sea ice model, they repeat atmospheric forcing from a negative and a positive NAO phase for several years and show that this leads to an increase in FW stored within the Arctic Ocean or an increase in export through CAA and through Fram Strait, respectively. Dickson et al. (2000) perform a composite analysis to explain to what extent the NAO controls the ice and FW export from the Arctic into the Atlantic. They conclude that the annual ice flux through Fram Strait is increased due to the shift to a positive NAO phase in the late 1980s and early 1990s. They define the NAO as the difference of winter (DJF) mean sea level pressure in the Icelandic low and the Azores high region. We use the same definition for the NAO. The domain in the vicinity of the Icelandic low and the Azores high used for the index definition is highlighted with white contours in Figure 4.35 a).

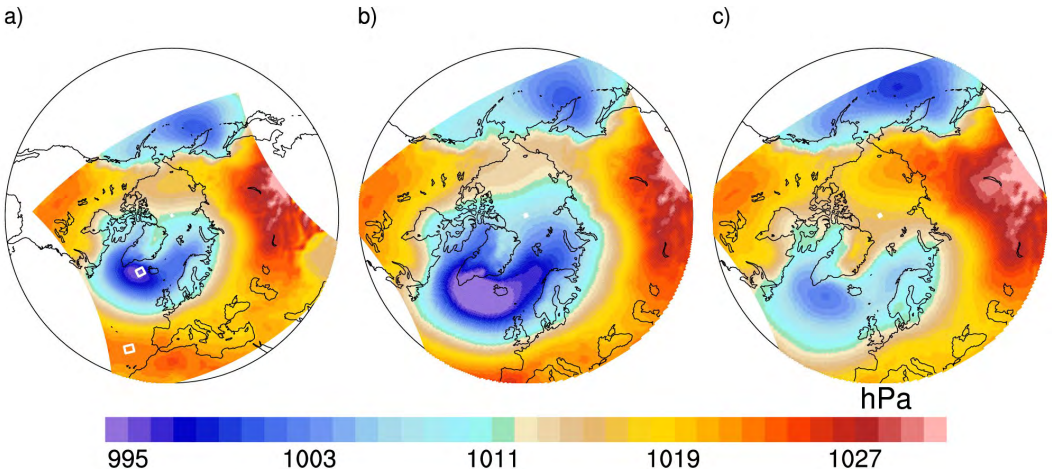

Figure 4.35: Winter (DJF) mean sea level pressure from a) all years, b) positive NAO years, and c) negative NAO years. In panel a), the domain for the NAO index definition is marked with white contour boxes. Note that the domain shown in the first plot is larger than in b) and c).

4.1.3.1 North Atlantic Oscillation index

There are several ways to define the NAO index. One is to use a sea level pressure difference between stations or (model) domains or the leading EOF from winter mean sea level pressure anomalies in the North Atlantic sector. The NAO indexes obtained as a result of these definitions usually show high correlations. More rarely, the definition of the NAO equals the AO definition as the principal component of the leading EOF for 20 °N.

In our case, the NAO is defined as the difference of the winter mean sea level pressure anomalies in the above mentioned domains, normalized by its standard deviation. The index calculated for our four model runs is presented in Figure 4.36.

The model shows a reasonable variability within the NAO. The correlation between the four experiments is very high and varies between 0.76 and 0.9 depending on the experiments. As can be seen in Figure 4.35 a), the domain of the Azores high region is close to the boundary of the domain of our atmosphere model. Especially in this domain, the influence of the forcing is very large because of the atmospheric large scale circulation. Thus, the forcing data plays a large role for the domain used for index definition, which leads to these high correlations.
Besides the high correlation between the ensemble members, the total NAO correlates with about 0.47 with the EOF 1. This is not surprising, since the correlation between the different definitions for NAO is high. The definition with the leading EOF over the North Atlantic region is very similar to our definition of EOF 1. Our EOF 1 does not describe the AO index, because we lack the influence of the North Pacific. This influence describes to large parts the difference between AO and NAO. Because our domain includes large parts of the North Atlantic, but only a small part from the North Pacific, the more regionally focused NAO variability is part of the EOF 1 variability.

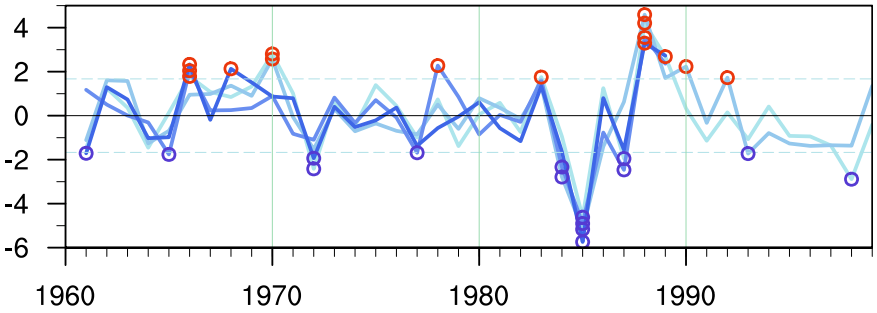

Figure 4.36: North Atlantic Oscillation index calculated from the winter (DJF) mean sea level pressure of the ECHAM-forced experiments. The dashed lines indicate ± one standard deviation. The red circles mark all years exceeding one standard deviation and the blue circles mark all years underrunning minus one standard deviation.

4.1.3.2 Response in the atmosphere

Mean sea level pressure Figure 4.35 shows the winter mean sea level pressure for a) all years, b) the positive NAO years and c) the negative NAO years. As stated already, the winter mean sea level pressure for the positive NAO years is characterized by a much stronger than usual Icelandic low and a stronger than usual Azores high. Consequently, the pressure gradient over the North Atlantic region is strongly enhanced. As can be seen in Figure 4.35 b), the Icelandic low is not only stronger but is also extending far into GIN and Barents Sea in the east and into Baffin Bay in the west. The sea level pressure in the Central Arctic is nearly everywhere lower than usual. In contrast to this, the sea level pressure south of about 60 °N is higher than usual. In the negative NAO years, the

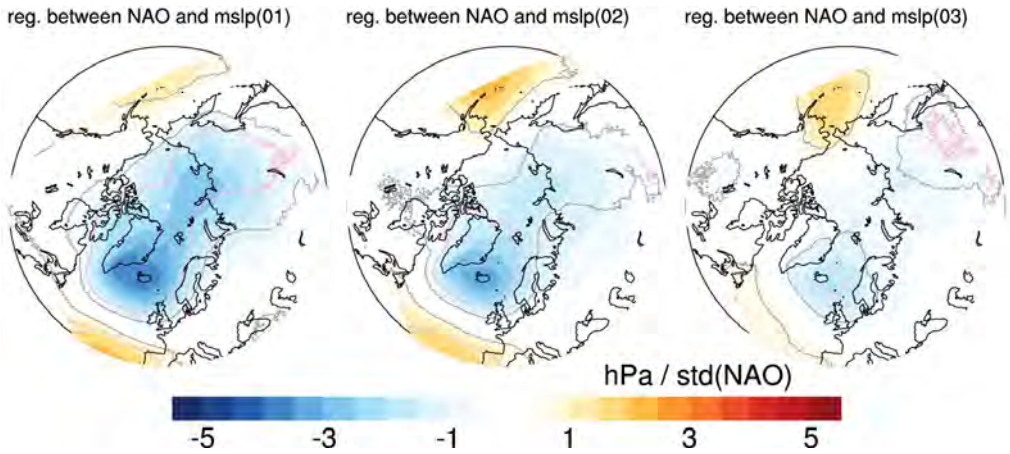

Figure 4.37: Regression coefficient between NAO and 3 months running mean sea level pressure in hPa per standard deviation of NAO. The term mslp(01) refers to the mean value of mean sea level pressure for the period December - February, mslp(02) to the mean value for January - March, and so forth. The grey contour line indicates the level of highly significant values for all model years. The pink line indicates the level of highly significant values for 40 years, which is the span of our model simulation 1960 - 1999 and the minimum of independent modeled years.

low over Iceland is much weaker than usual. Additionally, the weaker than usual Azores high leads to lower than usual mean sea level pressure over Europe. Because less winds bring warm and moist air into Eurasia, the Siberian high remains larger and stronger in the negative NAO years. A high pressure tongue reaches over Siberia into the Arctic Ocean. In large parts, the pressure over the Arctic Ocean does not differ anymore from the pressure over North America. Furthermore, the Aleutian low is somewhat stronger than usual in the negative NAO years. The pattern of the mean sea level pressure composites resembles largely the EOF 1 composites. However, Figure 4.37 shows that the regression coefficient between NAO and mean sea level pressure is not only smaller than between EOF 1 and mean sea level pressure (Figure 4.5), but also more restricted over ocean and does not extend as far into Eurasia as it does with EOF 1.

2 m temperature The influence of the mean sea level pressure changes on the 2 m temperature is shown in Figure 4.38. Again, the large scale response in the positive and negative NAO years is comparable to the changes in the EOF 1 years (Figure 4.6). In the positive NAO years, the enhanced westerlies bring warmer than usual temperatures to the Eurasian continent. In contrast to the EOF 1 response, the warming is more restricted to Europe and does not extend that far into Russia. Stronger than usual northerly winds over Greenland and the Canadian archipelago bring cold air southward and lead to a decrease in surface temperatures over northern Canada, Greenland and Baffin Bay. The North American continent is colder in the positive NAO years compared to the positive EOF 1 years, where the cooling is restricted to Greenland and Lincoln Sea. In the negative NAO years, the response of the mean sea level pressure changes on the 2 m temperature is much smaller compared to the negative EOF 1 years and the Eurasian impact is mainly

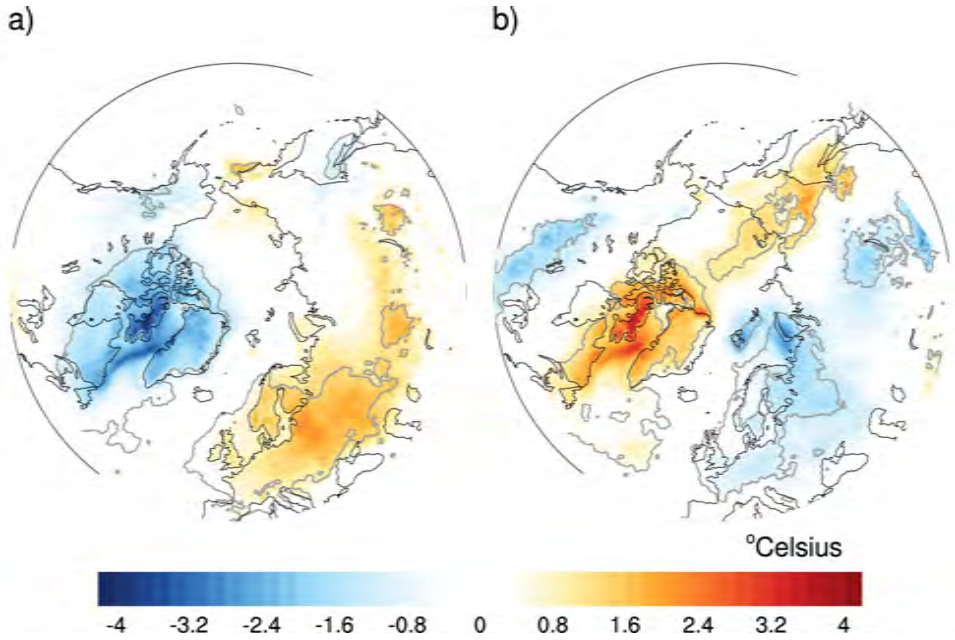

Figure 4.38: Difference between DJF 2 m temperature in a) the positive NAO years and b) the negative NAO years and the overall mean of DJF 2 m temperature. The grey contour line indicates the region where the composite years differ significantly from the mean value (as defined in A.3).

restricted to a cooling over northern Europe. The weaker than usual Icelandic low does not block the westerlies anymore, but allows for more moisture and heat transport to Greenland and Eastern Canada.

Again, the impact of NAO on the 2 m temperature is similar to the response on EOF 1, but its amplitude and extent, especially in Eurasia, are smaller.

Precipitation and river runoff In the positive NAO years, associated with a northeastward shift of the storm activities over the Atlantic, net precipitation is strongly increased over the Norwegian Sea. In the winter months of the positive NAO years, the mean value of net precipitation is increased by more than 15 mm/month in that region. Evaporation exceeds precipitation in Labrador Sea and south of Greenland, leading to dryer than usual conditions. Also most parts of southern Europe are dryer than usual, the overall influence of the NAO in its positive years is much stronger compared to the positive EOF 1 years. However, the negative anomaly over the Norwegian Sea does not extend that far into the northern Eurasian continent. Thus, the influence in the NAO composite is weaker over the Arctic adjacent land than it is in the EOF 1 composites. This is also true for the negative NAO years, where again the influence is largest over the Norwegian Sea and over the eastern North Atlantic. The changes in our model agree well with results from Dickson et al. (2000) having largest precipitation changes in the Norwegian-Greenland Seas and Scandinavia. Hurrell (1995) also found the largest precipitation changes in Scandinavia and Iceland, calculating a correlation of about 0.77 between the precipitation rates from coastal stations in Norway and the NAO index.

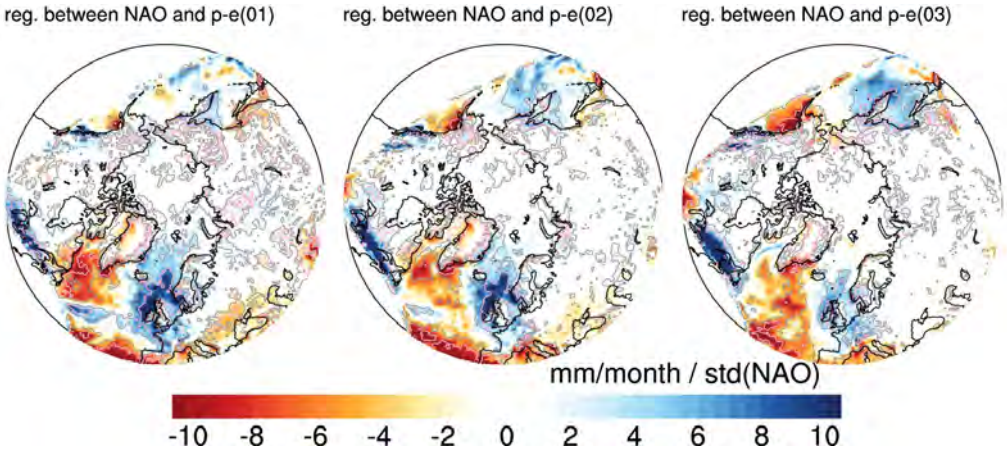

Figure 4.39: Regression coefficient between NAO and 3 months running mean net precipitation in mm / month per standard deviation of NAO. The term p-e(01) refers to the mean value of net precipitation for the period December - February, p-e(02) to the mean value for January - March, and so forth. The grey contour line indicates the level of highly significant values for all model years. The pink line indicates the level of highly significant values for 40 years, which is the span of our model simulation 1960 - 1999 and the minimum of independent modeled years.

To conclude, the influence of the NAO on net precipitation looks alike the changes in EOF 1, but while the changes in precipitation over Europe are large, the impact on the catchment areas of the rivers draining into the Arctic are relatively small (Figure 4.39).

Nevertheless, small differences in runoff can be seen. While the difference in the NAO composites in North American runoff is negligible, there is a slight increase in the Eurasian river runoff in the positive NAO years. The increase is present in Lena, Jenissey and Ob, but rather small in all river catchments. In the positive NAO years, the Eurasian runoff is with about 125 mSv approximately 2.8 % larger than in the mean. The response is even smaller in the negative NAO years, when the decrease in Eurasian runoff is smaller than 1.8 %.

4.1.3.3 Response in the ocean

Sea ice Comparable to the EOF 1 composite sea ice circulation, a strong transpolar drift from Laptev Sea to the Canadian Arctic coast (Figure 4.40 a)) leads to an accumulation of sea ice north of the Canadian archipelago and in Lincoln Sea in the positive NAO years (Figure 4.41). In the winter months, due to the cold bias in Labrador Sea, the sea ice boundary extends farther south as usual, while the ice drift leads to less ice than usual in Laptev Sea. As can be seen in Figure 4.41, this sea ice distribution persists for most of the year. While in the negative EOF 1 years, the enhanced Beaufort Gyre circulation leads to an accumulation of sea ice along the North American as well as along the Siberian coast, the effect is not present in the negative NAO years. Even though the extension of sea ice in the negative NAO years has been observed from ship, aircraft and satellite measurements (Dickson et al. 2000), the response of our model to the negative NAO forcing in the Central Arctic is too weak. Although the gyre is enhanced in large parts by more than 1 Sv, the sea

ice is not pushed strong enough to the coastal regions. The response in sea ice thickness along the Eurasian coast hence is rather small.

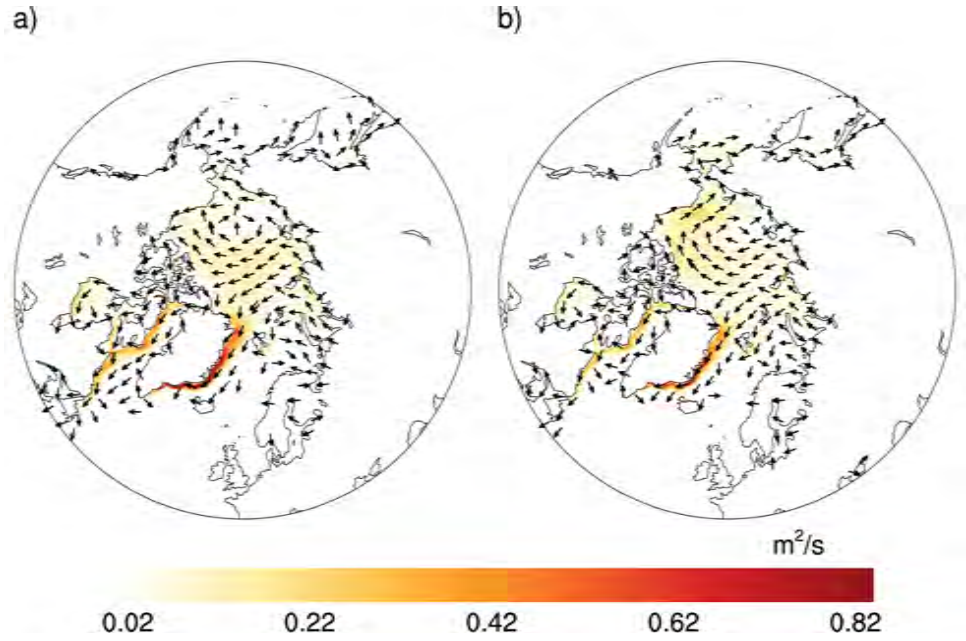

Figure 4.40: DJF sea ice transport in m^2/s in a) the positive NAO years and b) the negative NAO years. The strength of the velocity vector is given by the color coding.

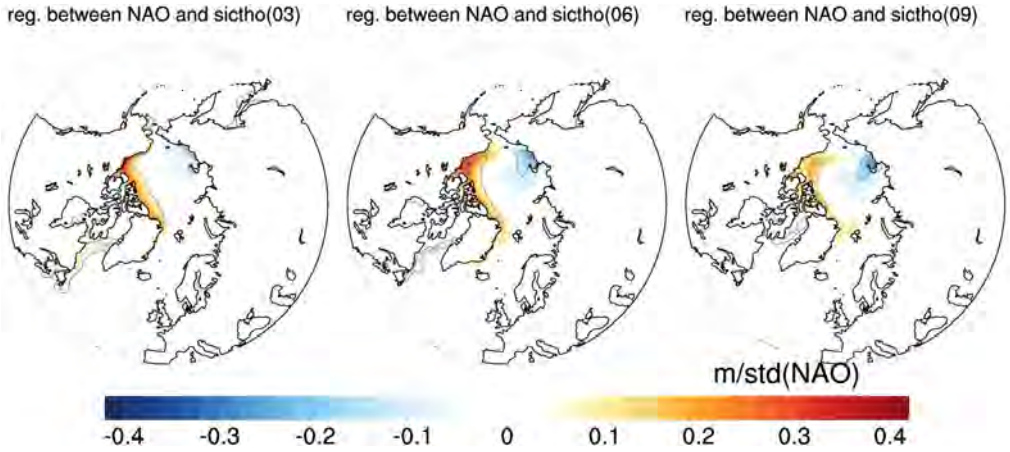

Figure 4.41: Regression coefficient between NAO and 3 months running mean sea ice thickness in m per standard deviation of NAO. The term sictho(03) refers to the mean value of sea ice thickness for the period February - April, sictho(06) to the mean value for May - July, and so forth. The grey contour line indicates the level of highly significant values for all model years. The pink line indicates the level of highly significant values for 40 years, which is the span of our model simulation 1960 - 1999 and the minimum of independent modeled years.

FW storage within the Arctic Ocean Condron et al. (2009) perform simulations with a regional setup of the MITgcm to analyze the response of the Arctic Ocean on changes in the NAO. After repeating 30 years of positive NAO atmospheric forcing, over a quarter of the FW, that is stored within the Arctic Ocean, is exported. With this increased FW export the model seems to approach a new equilibrium, the increased FW export through Fram Strait decreases at the end of these 30 years. However, the FW export through CAA remains higher than usual. In contrast, with a repeated negative NAO forcing, the FW content within the Arctic Ocean recovers completely after 10 years of integration. In our model simulation, the response is, of course, much smaller, since we do not use a repeated forcing. The FW change pattern from the NAO composites resemble the spatial pattern of the EOF 1 years (Figure 4.16). The signal in our model is consistent with the results from Condron et al. (2009); in the positive years, about 10 mSv more FW are exported from the Arctic Ocean, while in the negative years, the FW content increases by more than 20 mSv.

Fram Strait ice and liquid FW export Our model response to the NAO is relatively small, especially in the positive NAO years. In the positive NAO years, the liquid transport through Fram Strait is smaller than usual, but the mean does not differ significantly from

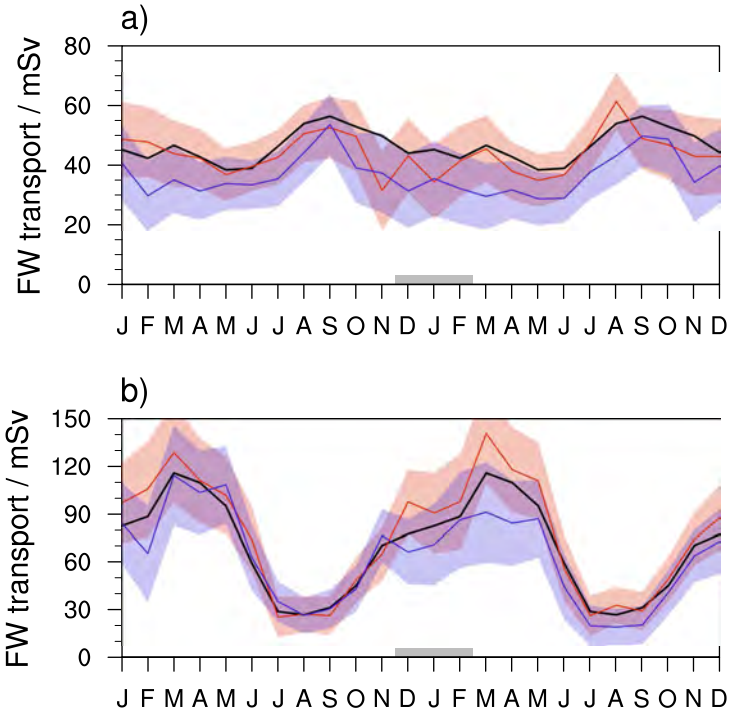

Figure 4.42: Annual cycle of FW transport in mSv through Fram Strait in a) liquid form, and b) in solid form. The black line shows the ensemble mean over the whole time period, the red and blue lines represent the positive and negative NAO years, respectively. The shaded areas indicate ± two standard deviations of the given subsets for positive and negative NAO years (as defined in A.3). The months used for the composite definition are marked by the grey line at the bottom of the plots.

the mean of the positive years (Figure 4.42 a)). In the negative NAO years, the decrease in FW transport through Fram Strait is more pronounced. With a yearly mean value of about 35.6 mSv, the FW transport through the strait is reduced by 23 %. Again, this change in liquid FW export is controlled by a change in the total liquid export within the upper 100 m. The total liquid export through the strait is reduced by about 0.1 Sv, which is mainly compensated by a decrease in the total import through Barents Sea of the same order of magnitude. Even though we see a decrease of liquid FW transport through Fram Strait in the positive as well as in the negative NAO years, the ice export increases slightly in the positive NAO years. The transpolar winds lead to a slightly increased ice export, but compared to the mean value, the difference is smaller than two standard deviations. In the negative NAO years, the ice transport is reduced from December until the end of the following year (Figure 4.42 b)). Even though the reduction is relatively small and the mean value is always within the two standard deviation range, this is not true for the yearly standard deviation. The sea ice export through Fram Strait is reduced by about 14 % in the negative NAO years because of a strengthening of the gyre circulation within the Arctic Ocean.

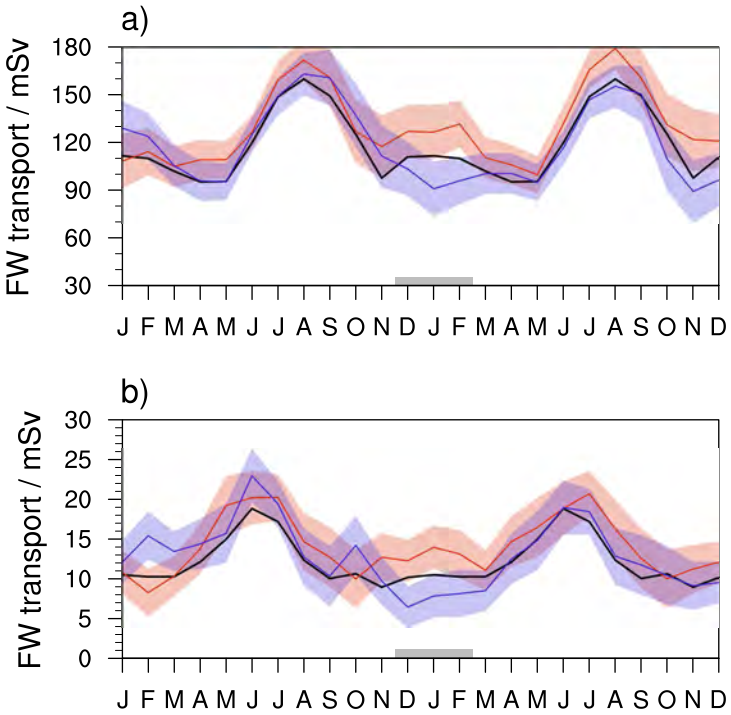

Figure 4.43: Annual cycle of FW transport in mSv through CAA in a) liquid form, and b) in solid form. The black line shows the ensemble mean over the whole time period, the red and blue lines represent the positive and negative NAO years, respectively. The shaded areas indicate ± two standard deviations of the given subsets for positive and negative NAO years (see A.3). The months used for the composite definition are marked by the grey line at the bottom of the plots.

Canadian Arctic archipelago ice and liquid FW export Consistent with the model results from Condron et al. (2009), our model shows an increase of ice and liquid FW transport through CAA in the positive NAO years, while in the negative NAO years solid and liquid FW transports are slightly reduced (Figure 4.43). The spatial wind pattern of the positive NAO years leads to a release of FW stored within the Arctic through the archipelago, while in the negative years, nearly all of the FW is retained within the gyre. Other than in the Fram Strait export, the influence is direct and only influencing the winter transport. Throughout the rest of the year, the NAO composites of ice and liquid transport through CAA do not differ strongly from the mean value.

Comparison of FW fluxes The FW budget of the Arctic shows a clear response on the NAO forcing (Table 4.3). In the positive NAO years, the FW transport accelerates through the Canadian archipelago as well as through Fram Strait. This leads to a release of FW stored within the Arctic Ocean. In contrast, in the negative NAO years, the FW stored within the Arctic Ocean is retained in the enhanced Beaufort Gyre, and FW export is strongly reduced, especially through Fram Strait.

	all years	positive NAO years	negative NAO years
(P-E)+runoff	65.7 + 132.8	67.5 + 134.65	63.2 + 129.83
	= 198.5	= *202.15* (±2.98)	= *193.03* (±2.98)
Bering Strait	81.2	*85.38* (±4.03)	81.90 (±4.03)
Barents Sea	−10.1	−10.34 (±1.94)	−11.72 (±1.94)
Fram Strait liquid	−46.2	−42.72 (±3.58)	*-35.55* (±3.58)
Fram Strait ice	−69.4	*-76.33* (±4.82)	*-59.39* (±4.82)
CAA liquid	−118.8	*-133.19* (±4.44)	−117.16 (±4.44)
CAA ice	−12.2	*-14.82* (±0.84)	−12.03 (±0.84)
Oceanic storage liquid		−7.61	12.06
Oceanic storage ice		−2.95	10.38
∑ transports		10.13	39.08

Table 4.3: Mean values in mSv of the FW budget of the Arctic for all modeled years, for the positive NAO years and for the negative NAO years. Mean values are calculated from the end of September one year before the NAO event until the end of September of the next year. Displayed in brackets are ± one standard deviation of the subsets. Italic numbers in black differ more than one standard deviation from the mean value, italic numbers in red differ more than two standard deviations. The change in storage is calculated as the difference from the end of September until the end of September of the next year.

4.1.4 Siberian high

The Siberian high, a climatic driver during winter in Eurasia, is centered in northeastern Siberia. The surface air layers over land cool while the anticyclonic pressure system forms

and leads to lowest temperatures in the northern hemisphere. The Siberian high "impacts on circulation and temperature patterns extend far outside the Siberian high source area extending from the Arctic to the tropical Pacific" (Panagiotopoulos et al. 2005). A decline in the Siberian high intensity has been observed since the late 1970s (D'Arrigo et al. 2005; Panagiotopoulos et al. 2005), which is commonly explained by a European warming. Jeong et al. (2011) discuss a recent recovery of the Siberian high intensity in the early 1990s; the general circulation models in the IPCC AR4, however, are not able to reproduce this recovery, but show a weakening for the entire 21st century caused by decreasing snow cover simulated over Eurasia.

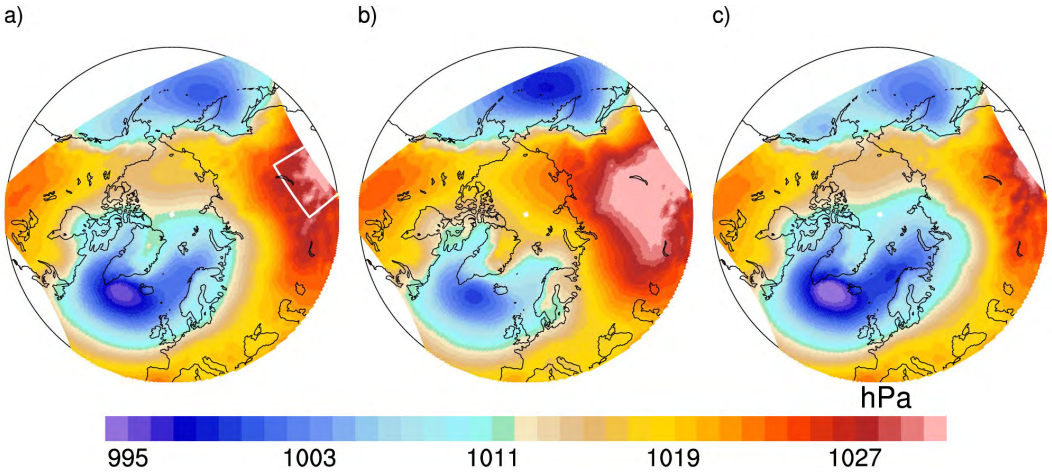

Figure 4.44: Winter (DJF) mean sea level pressure in hPa from a) all years, b) positive SH years, and c) negative SH years. In plot a) the domain for the SH index definition is marked with a white contour box.

In the following, we investigate whether our regional model setup reacts on changes in the Siberian high intensity and analyze, if and by how much the Arctic FW cycle is influenced.

4.1.4.1 Siberian high index

We define the Siberian high index, in the following denoted by SH, by calculating the normalized areal mean of winter mean sea level pressure in a region centered in the winter high pressure system over Siberia. The domain is marked in Figure 4.44 a).

The index time series from the ensemble members are presented in Figure 4.45. The members correlate between 0.33 and 0.6, depending on the experiments. Compared with the previously studied indexes, the correlation is highest with EOF 1 and exceeds -0.6.

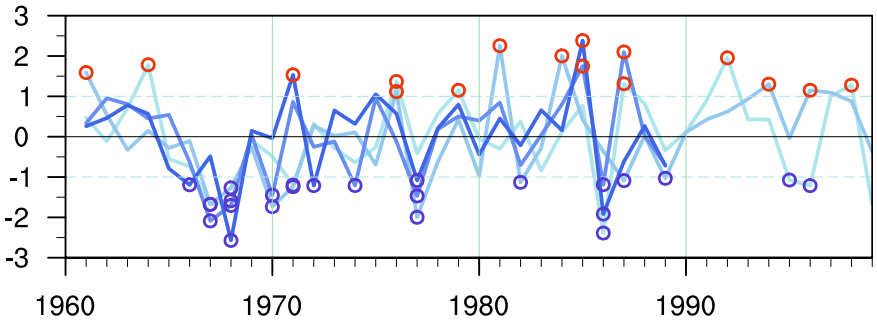

Figure 4.45: Siberian High index (SH) calculated from the winter (DJF) mean sea level pressure of the ECHAM-forced experiments. The dashed lines indicate ± one standard deviation. The red circles mark all years exceeding one standard deviation and the blue circles mark all years underrunning minus one standard deviation.

4.1.4.2 Response in the atmosphere

Mean sea level pressure The correlation between SH and winter mean sea level pressure exceeds 0.5 over Eurasia as well as over large parts of the Arctic Ocean; the changes in sea level pressure exceed in areal extend the Eurasian continent in the positive as well as in the negative SH years. As can be seen in the regression coefficient between mean sea level pressure and SH, large parts of our atmospheric model domain are strongly influenced. Most of the area differs significantly from the mean value and even fulfills the criterion for statistical significance of only 40 independent events (Figure 4.46). By definition, the Siberian high is strongly enhanced in the positive SH years (Figure 4.44 b)), describing an extension of the SH into the Arctic Mediterranean.

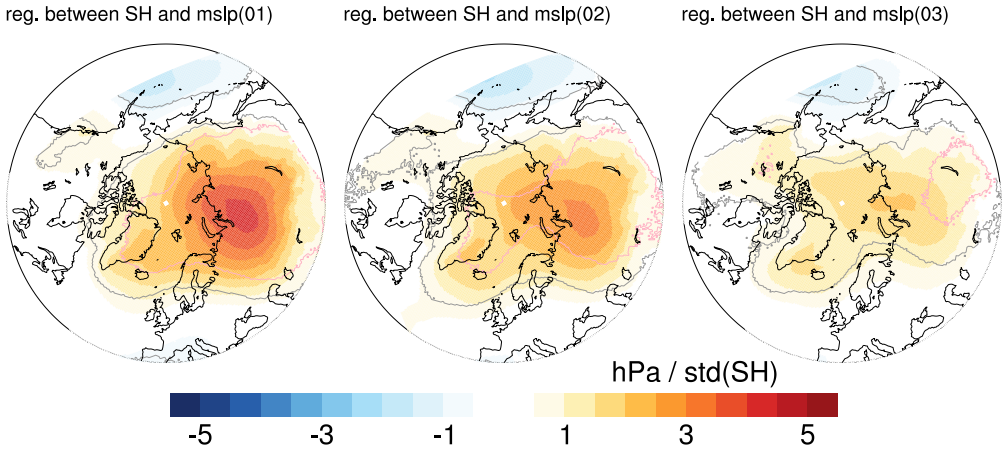

Figure 4.46: Regression coefficient between SH and 3 months running mean sea level pressure in hPa per standard deviation of SH. The term mslp(01) refers to the mean value of mean sea level pressure for the period December - February, mslp(02) to the mean value for January - March, and so forth. The grey contour line indicates the level of highly significant values for all model years. The pink line indicates the level of highly significant values for 40 years, which is the span of our model simulation 1960 - 1999 and the minimum of independent modeled years.

Over the ocean, the signal is strongest in Kara Sea and exceeds 10 hPa in a large region. The influence is somewhat smaller in the negative years, when the maximum change in winter mean sea level pressure is about -6 hPa. While in the positive SH years, the changes cover the complete Arctic Ocean, Greenland and Hudson Bay, in the negative SH years, the influence is mainly restricted to Laptev, Kara and Barents Sea. Similar to the change in EOF 1 in the North Pacific, but with different sign, the Aleutian low is stronger than usual in the positive SH years, while the Icelandic low is weakened. In the negative SH years, the situation is contrary. A weaker Aleutian low comes along with a weaker Siberian high, which allows the stronger than usual Icelandic low to expand far into Barents Sea.

2 m temperature In the spatial pattern of 2 m temperature in the positive SH years (Figure 4.47 a)), the similarity to the 2 m temperature in the negative EOF 1 years can clearly be seen (Figure 4.6 b)). The stronger than usual Siberian high blocks the anyway weaker (because of a weaker pressure gradient over the North Atlantic) incoming warm temperatures leading to a large scale cooling of the Eurasian continent. Temperatures decrease by more than 0.5 °Celsius corresponding to one standard deviation of SH in and around the area, where the high pressure cell is located. This amplitude is slightly smaller than in the results from Gong and Ho (2002), who use mean sea level pressure data from NCEP reanalysis and surface temperature from the Climate Research Unit (CRU) of the University of East Anglia for a similar regression analysis. Their focus is on the Asian continent only and does not include the changes over the Arctic Ocean. As in the negative EOF 1 years, the positive SH winter 2 m temperature show a warming over Greenland, Baffin Bay and Lincoln Sea. The reason for this warming might be the weaker than usual

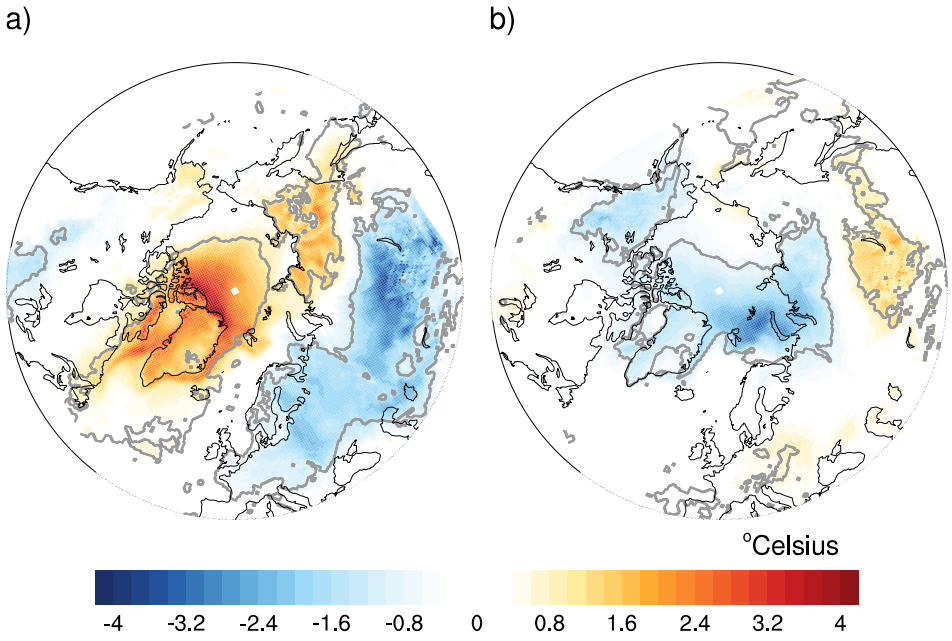

Figure 4.47: Difference between DJF 2 m temperature in a) the positive SH years and b) the negative SH years and the overall mean of DJF 2 m temperature. The grey contour line indicates the region where the composite years differ significantly from the mean value (as defined in A.3).

Icelandic low that allows for more heat and moisture transport from low latitudes and does not deviate the transport eastward. The 2 m temperature of the negative SH years, however, does not reflect the pattern of the positive EOF 1 years. As in the mean sea level pressure response on the negative SH years, the signal over Eurasia is rather small and primarily restricted to the SH domain. The weaker than usual Aleutian low does not bring as warm temperatures to the North American continent as usual, which leads to a cooling of about 1 °Celsius in Alaska. Even though the Icelandic low is stronger than usual in the negative SH years, the enhanced heat transport does not reach Barents Sea, but is deflected more south. Instead, a cooling can be seen being strongest at the winter sea ice edge. Increased sea ice extent leads to a decrease of the heat flux from the ocean to the atmosphere amplifying the cooling over Barents Sea.

Precipitation and river runoff The response of net precipitation on the positive SH years is very similar to the net precipitation changes in the negative EOF 1 years (Figure 4.8 b)). The strong and largely extended Siberian high leads to less precipitation than usual in the area of index definition. The moisture transport over the Atlantic is weakened and shifted southward, leading to negative biases larger than 15 mm/month over the North Atlantic. The signal is weaker in the negative SH years and again shows patchy responses that are below the significance level in large areas. Most probably, precipitation is too much influenced by local winds and other factors to show a large scale significant response on SH.
The influence on runoff is negligible in the negative SH years. In the positive years, the runoff of the river Ob in the following year is, with an annual mean of 16.72 mSv, significantly reduced by about 10 %. This leads to a reduction of the Eurasian river runoff, even though the changes in runoff of the other Arctic Eurasian rivers are rather small. The total reduction in net precipitation over the Central Arctic Ocean and Arctic runoff in the positive SH years adds up to more than 7 mSv.

4.1.4.3 Response in the ocean

Sea ice In the positive SH years, the sea ice distribution resembles the sea ice thickness in the negative EOF 1 years. The circulation in the Arctic Ocean is enhanced, ice is transported from the Canada Basin along the North American coast to the Siberian coast. In Lincoln Sea, the sea ice thickness is reduced by more than half a meter. In the negative SH years, the colder than usual temperatures in Barents Sea lead to a slightly thicker ice than usual in Barents and Kara Sea (Figure 4.48 b)). This model behavior supports the assumption of Wu et al. (2011) that the sea ice concentration of the Siberian coast in the previous autumn and winter and the corresponding sea surface temperature anomalies might trigger the SH strength. However, our model does not confirm a negative sea ice concentration anomaly in the previous autumns moving from East Siberian Sea along the coast reaching Barents Sea in the winter months. We use a regional model and partly prescribe the strength of the Siberian high via the boundary conditions. Thus, the influence of sea ice on the strength of the Siberian high remains arguable in our

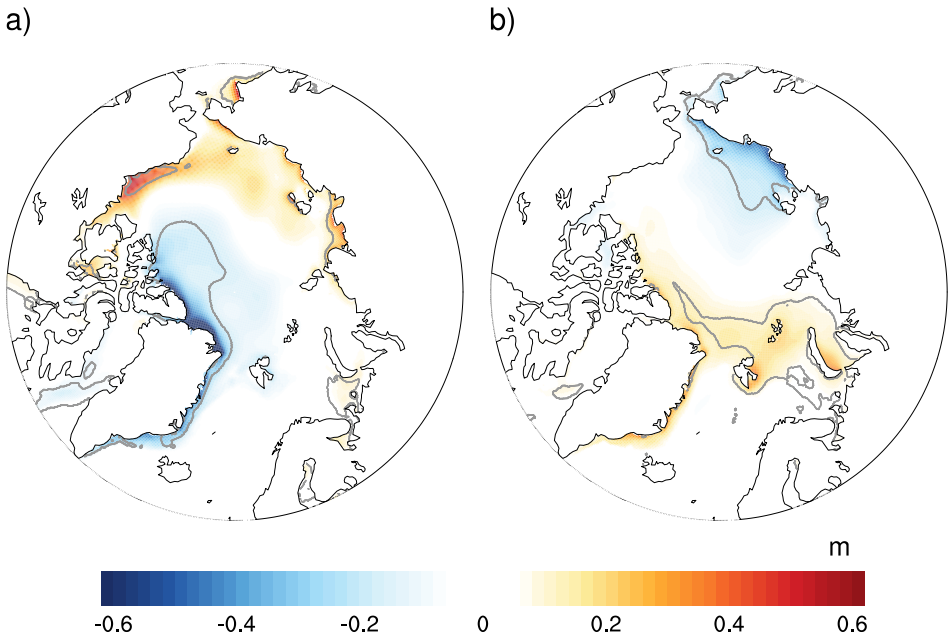

Figure 4.48: Difference between DJF sea ice thickness in m in a) the positive SH years and b) the negative SH years and the overall mean of DJF sea ice thickness. The grey contour line indicates the region where the composite years differ significantly from the mean value (as defined in A.3).

setup. Compared to the response of EOF 1, the changes in sea ice thickness are small, but persistent for the the whole year.

FW storage within the Arctic Ocean Also the change of FW stored within the Arctic in the positive SH years is similar to the changes in the negative EOF 1 years. FW is accumulated within the Beaufort Gyre. Large changes, with an increase of more than 1.5 m, can be seen in Laptev Sea. In the negative SH years, the changes are negative in large parts of the Arctic Ocean, but very small. In total, the liquid FW storage changes of about -13.6 mSv in the negative SH years.

Fram Strait ice and liquid FW export The change in FW stored within the Arctic Ocean is of obviously depends on the amount of FW transported into and out of the Arctic Ocean. Figure 4.49 a) shows that in the negative SH years the difference between the annual cycle of FW transport through Fram Strait and the mean annual cycle is very small. The mean value is within the range of two standard deviations in the negative SH years. In the positive SH years, there is a small reduction, but the yearly mean values from the composites do not differ significantly from the overall mean values.

In sea ice transport, however, the decrease in the positive SH years is larger compared to the response in liquid FW transport, and lasts for about three months (January to March). The decrease in transport is a result of sea ice drift, with the strengthened gyre circulation and a weaker than usual transpolar drift directed to Fram Strait. The yearly mean value of sea ice transport is reduced by about 15 mSv in the positive SH years. In

the negative SH years, there is a slight increase of FW transport through the strait, but the difference is within the variability.

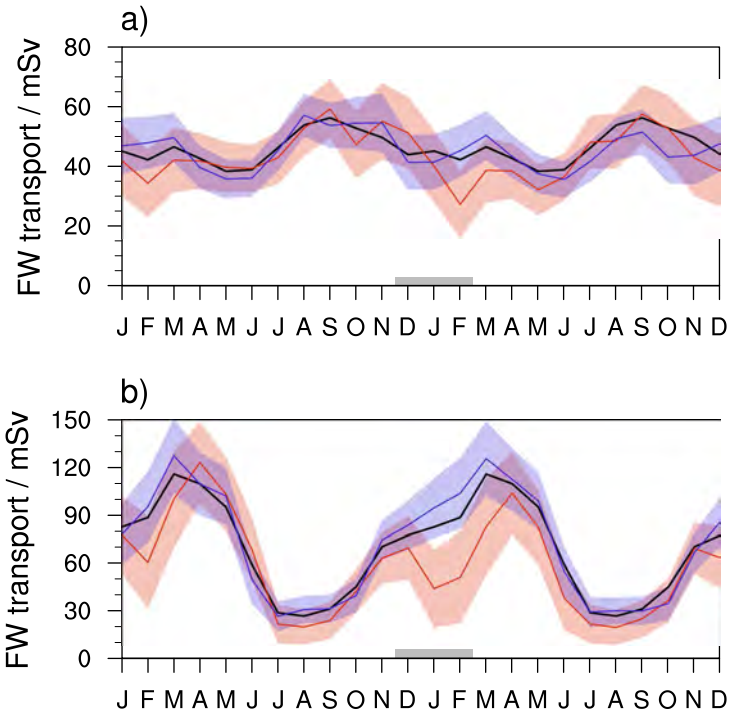

Figure 4.49: Annual cycle of FW transport in mSv through Fram Strait in a) liquid form, and b) in solid form. The black line shows the ensemble mean over the whole time period, the red and blue lines represent the positive and negative SH years, respectively. The shaded areas indicate ± two standard deviations of the given subsets for positive and negative SH years (see Appendix A.3). The months used for the composite definition are marked by the grey line at the bottom of the plots.

Canadian Arctic archipelago ice and liquid FW export The liquid transport of FW through the Canadian archipelago in the positive SH years is reduced in the long run, starting with an immediate response in the winter months and prevailing for the rest of the year (Figure 4.50 a)). The difference of the yearly value and the overall mean is larger than 10 mSv. In the negative SH years, the influence is again rather small and of short-term only. In February the liquid FW transport differs more than two standard deviations from the mean value. In the rest of the year, the annual cycle of the negative SH years does not differ significantly from the mean. The same is true for the sea ice transport through The Canadian archipelago (Figure 4.50 b)). In the negative SH years, the difference is negligible and also in the positive SH years, the difference to the mean value is smaller than two standard deviations.

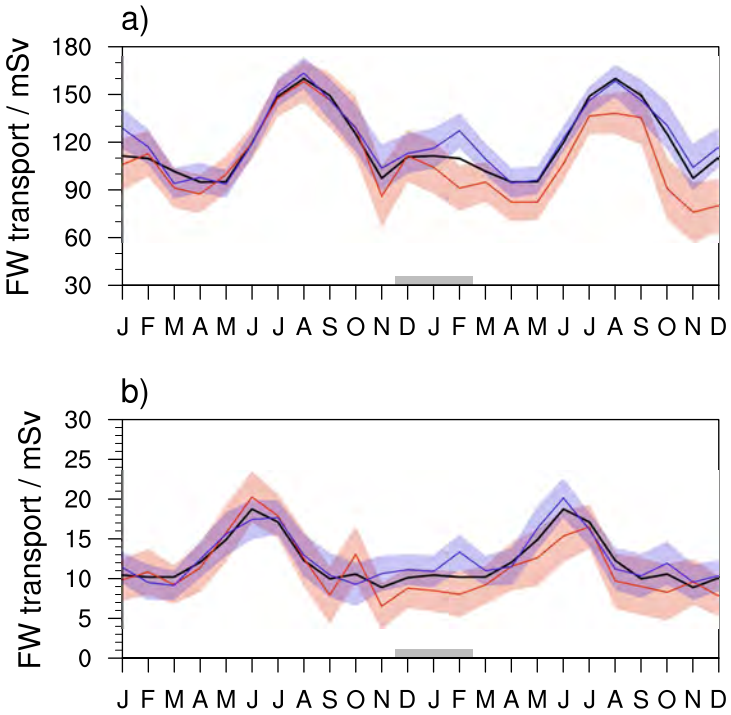

Figure 4.50: Annual cycle of FW transport in mSv through CAA in a) liquid form, and b) in solid form. The black line shows the ensemble mean over the whole time period, the red and blue lines represent the positive and negative SH years, respectively. The shaded areas indicate ± two standard deviations of the given subsets for positive and negative SH years (see Appendix A.3). The months used for the composite definition are marked by the grey line at the bottom of the plots.

Comparison of FW fluxes The influence of the SH on the FW fluxes is fairly small. This is reflected in the yearly values in Table 4.4 especially in the negative SH years, where none of the values exceeds two standard deviations from the mean value. The inflow through Bering Strait is slightly decreased caused by a weaker than usual Aleutian low. On the other hand, the stronger than usual Icelandic low provides an increase in Barents Sea inflow, serving as a FW sink.

In the positive SH years, the response to the mean sea level pressure change is stronger and similar to the response in the negative EOF 1 years, which are discussed in more detail in Section 4.1.1.3 and Section 4.1.1.4. Precipitation decreases over Eurasia, leading to a significant reduction in "P-E+runoff". An enhanced Beaufort Gyre weakens the drift through Fram Strait resulting in a significantly decreased ice export through the strait. The FW transport through CAA is also decreased in the positive years, more strongly in the liquid than in solid form.

To conclude, the changes caused by the SH are non-linear. While the response of atmospheric and oceanic FW components on the positive SH mean sea level pressure change is largely similar to the response in the negative EOF 1 years, the influence from the negative SH mean sea level pressure change is weaker and for all the FW composites less than the 95 % criterion of two standard deviations from the mean value.

	all years	positive SH years	negative SH years
(P-E)+runoff	65.7 + 132.8 = 198.5	62.2 + 129.04 = *191.24* (±2.98)	64.2 + 133.61 = 197.81 (±2.23)
Bering Strait	81.2	*87.30* (±4.03)	*77.02* (±3.02)
Barents Sea	−10.1	−8.85 (±1.94)	*-12.77* (±1.46)
Fram Strait liquid	−46.2	−43.57 (±3.58)	−45.74 (±2.68)
Fram Strait ice	−69.4	*-53.96* (±4.82)	*-73.79* (±3.62)
CAA liquid	−118.8	*-108.57* (±4.44)	*-122.44* (±3.33)
CAA ice	−12.2	*-10.82* (±0.84)	−12.76 (±0.63)
Oceanic storage liquid		25.88	13.56
Oceanic storage ice		12.83	0.62
∑ transports		52.77	7.33

Table 4.4: Mean values in mSv of the FW budget of the Arctic for all modeled years, for the positive SH years and for the negative SH years. Mean values are calculated from the end of September one year before the SH event until the end of September of the next year. Displayed in brackets are ± one standard deviation of the subsets. Italic numbers in black differ more than one standard deviation from the mean value, italic numbers in red differ more than two standard deviations. The change in storage is calculated as the difference from the end of September until the end of September of the next year.

4.2 Arctic runoff variability

The atmospheric changes described by the composite analysis of EOF 1, EOF 2, NAO and SH in the previous section show a large variability of the FW fluxes in the Arctic. Nevertheless, the influence on precipitation over the Arctic Ocean and on runoff is rather small. In this section, we analyze what drives the variability in Arctic runoff.

The total amount of FW originating from the atmosphere into the Arctic Ocean is dominated by precipitation over land and thus reflected in Arctic river runoff. The total amount in the model has a mean of about 196 mSv. The correlation between yearly mean net precipitation over the Arctic Ocean plus runoff and the yearly mean of Arctic river runoff is about 0.86. Because precipitation in high latitudes, over the Arctic Ocean, is rather small, in the following we investigate the variability of Arctic river runoff; about 189 mSv of the net FW input into the Arctic Ocean originate from river runoff. This includes the variability of precipitation in lower latitudes over the large catchment areas of the rivers draining into the Arctic Ocean. The yearly mean values from Eurasian runoff and from North American runoff correlate with about -0.3 in our model, indicating that different, and independent, mechanisms lead to the variability of Eurasian and North American runoff. The variability of the total runoff is dominated by the Eurasian runoff, which is not only larger in the total amount draining into the Arctic Ocean, but also has a larger standard deviation. The correlation between total Arctic runoff and the Eurasian fraction is 0.88, while the correlation between the total runoff and the North American fraction is negligible. The standard deviation of annual total runoff is with 6.8 mSv nearly as large as the standard deviation of annual net precipitation plus runoff (8.3 mSv).

To investigate the variability of Arctic runoff, we use yearly mean runoff values, as presented in Figure 4.51 and perform a regression analysis with atmospheric datasets from our model. Using a multi linear regression, Li et al. (2010) analyze the impact of observational data such as surface air temperature, precipitation or snow cover on the variability of four Arctic rivers, the rivers Yenisey, Ob, Lena and Mackenzie. They conclude that the response on the different climate factors, depending on the season and the river, is quite different. While for runoff in winter, the influence of surface air temperature is large for all four rivers, precipitation does not have an equally important role for all of the rivers. Snow cover, for instance, explains most of the variance for Yenisey, whereas it plays a minor role in the variability in all seasons of river Lena. Different to the approach by Li et al. (2010), we do not split the runoff in four seasons, but analyze the influence of different atmospheric variables with respect to time lags using three months running mean values. This allows for a lagged response of runoff.

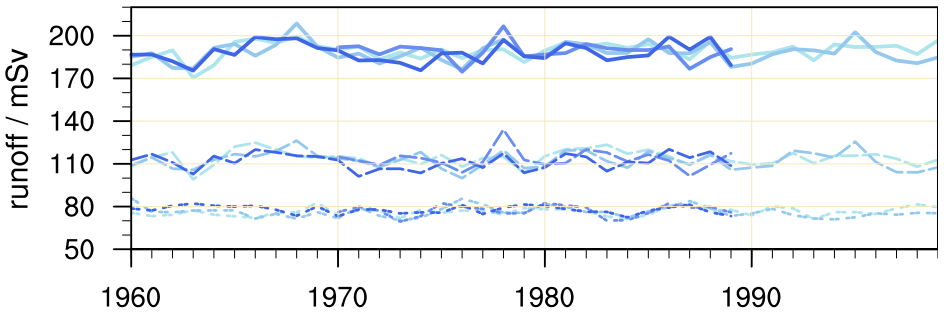

Figure 4.51: Yearly mean Arctic river runoff in mSv of the ECHAM-forced experiments. The solid lines stand for total Arctic runoff, the long dashed lines for the Eurasian fraction and the small dashed lines for the North American fraction. The data is the same as already presented in Figure 3.16.

4.2.1 Eurasian river runoff

Mean sea level pressure The regression coefficient between Eurasian river runoff and three months running mean sea level pressure (Figure 4.52) resembles the regression coefficient between EOF 1 and mean sea level pressure (Figure 4.5), but is weaker in amplitude. While in the indexes used before, the maximal impact can be seen in winter, this is not the case in the response on runoff. The correlation between mean sea level pressure and Eurasian runoff exceeds -0.3 over the Eurasian continent for November to January and reaches about -0.6 in February to April, just before the melting season. The correlation reduces again in April to June and is negligible afterwards.
In winter, before increased Eurasian river runoff, the Icelandic low is stronger than usual, extending far into Barents Sea and persisting longer than usual. This causes stronger than usual southwesterly winds to Barents Sea.

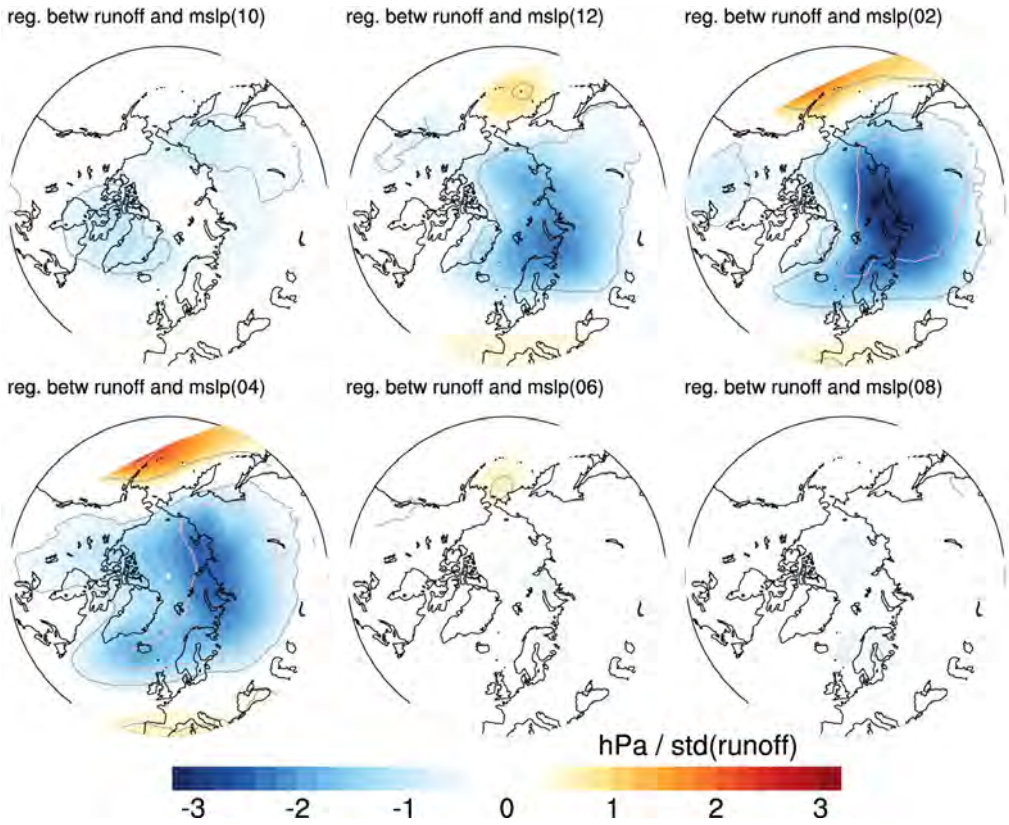

Figure 4.52: Regression coefficient between Eurasian runoff and 3 months running mean sea level pressure in hPa per standard deviation of Eurasian runoff. The term mslp(10) refers to the mean value of mean sea level pressure for the period September - November from the previous year, mslp(12) to the mean value for November - January, mslp(02) to the mean value for January - March, and so forth. The grey contour line indicates the level of highly significant values for all model years. The pink line indicates the level of highly significant values for 40 years, which is the span of our model simulation 1960 - 1999 and the minimum of independent modeled years.

2 m temperature The influence of 2 m temperature on enhanced river runoff is largest in early spring (January to March). Figure 4.53 shows that large parts of Eurasia warm by more than 1 °Celsius per standard deviation of Eurasian runoff. In contrast to that warming, there is a cooling, first in Laptev Sea and the adjacent coastal area, that is pushed aside in early spring to Greenland and Barents Sea by the stronger than usual warming. These cold temperatures might be transported from Canada over Labrador Sea northward earlier during winter (November to February), when anomalous transport of cold air can be seen in the model. The winds bringing warm temperatures over the Atlantic are weaker than usual, while the winds originating over the Canadian continent are stronger than usual and redirected northward. This change in temperature transport leads to the cold anomaly, in winter in Laptev Sea and the coastal area and later north of Greenland. Even though the circulation regime changes in January to March, bringing warmer temperatures from the south, the negative temperature anomaly only weakens slowly, vanishing in early summer.

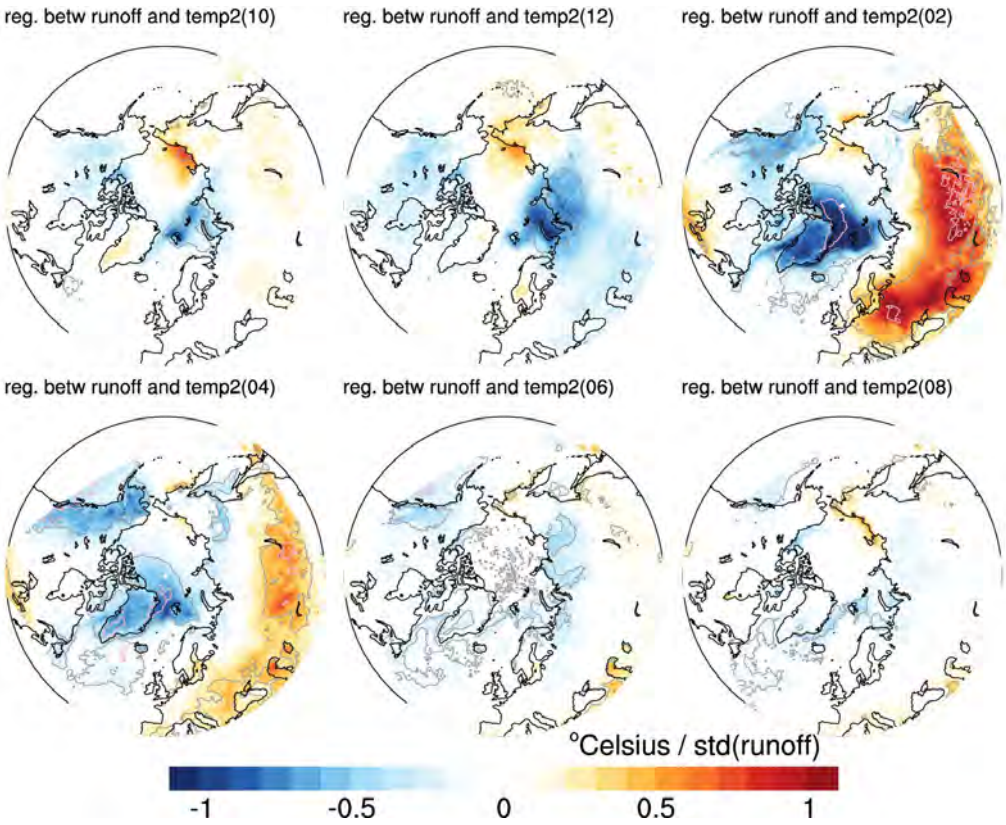

Figure 4.53: Regression coefficient between Eurasian runoff and 3 months running mean of 2 m temperature in °Celsius per standard deviation of Eurasian runoff. The term temp2(10) refers to the mean value of 2 m temperature for the period September - November from the previous year, temp2(12) to the mean value for November - January, and so forth. The grey contour line indicates the level of highly significant values for all model years. The pink line indicates the level of highly significant values for 40 years, which is the span of our model simulation 1960 - 1999 and the minimum of independent modeled years.

In eastern Siberia, the influence of temperature on Eurasian runoff is rather small. Thus, our model does not confirm the result of Li et al. (2010) that surface temperature is responsible for most of the explained variance from river Lena. They do not analyze the eastern rivers Indigirka and Kolyma, where we do not see any response in 2 m temperature. Thus, a comparison with our model results concerning these two rivers is not possible. In summer, when the changes in mean sea level pressure are small, the influence on 2 m temperature weakens.

Moisture transport and net precipitation A direct influence on Eurasian runoff is given by net precipitation in high latitudes. In winter, a stronger than usual Icelandic low leads to stronger than usual low pressure cells arriving from the Atlantic. They are directed more northward than usual, reaching Barents Sea and extending into the Russian continent (Figure 4.56), instead of taking the path over Europe (Figure 4.55). This leads to an increase during winter of a few mm/month in all Eurasian catchments, particularly in the

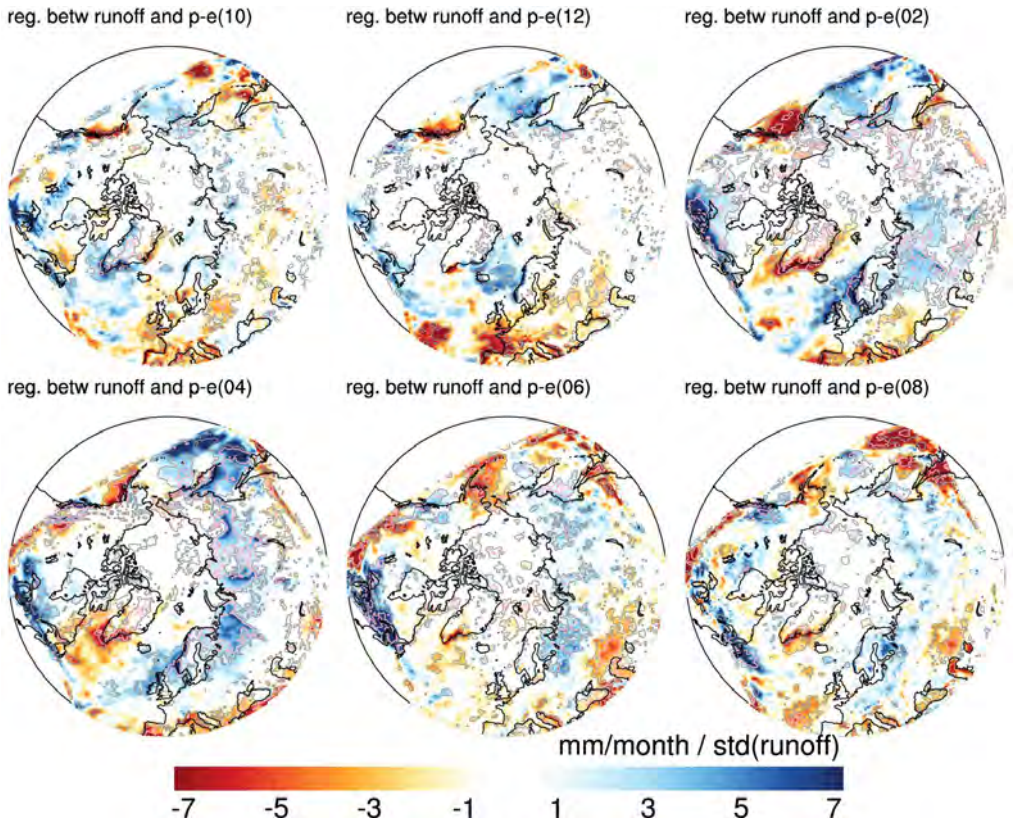

Figure 4.54: Regression coefficient between Eurasian runoff and 3 months running mean of net precipitation in mm / month per standard deviation of Eurasian runoff. The p-e(10) refers to the mean value of net precipitation for the period September - November, p-e(12) to the mean value for November - January, and so forth. The grey contour line indicates the level of highly significant values for all model years. The pink line indicates the level of highly significant values for 40 years, which is the span of our model simulation 1960 - 1999 and the minimum of independent modeled years.

Yenissey catchment. In late winter, the impact on the anyway small amount of precipitation seems to be restricted to West Eurasia (Figure 4.54, upper right panel). From March to May, precipitation gains influence also in Eastern Siberia (Figure 4.54), the weaker than usual Aleutian low allows for more moisture transport along the eastern Pacific coast into eastern Siberia. In early summer, the influence of precipitation is largest and explains between 20 - 30 % of the runoff variability. For all catchment areas in Eurasia, summer precipitation (April to August) increases significantly with up to 6 mm/month. Due to warmer than usual temperatures, evaporation also increases, but net precipitation remains increased. In summer, the changes in mean sea level pressure are negligible, but the summer cyclone activity over land is increased, probably caused by changes in the polar jet stream track, bringing more moisture than usual in high latitudes (Figure 4.56, lower middle and right panel).

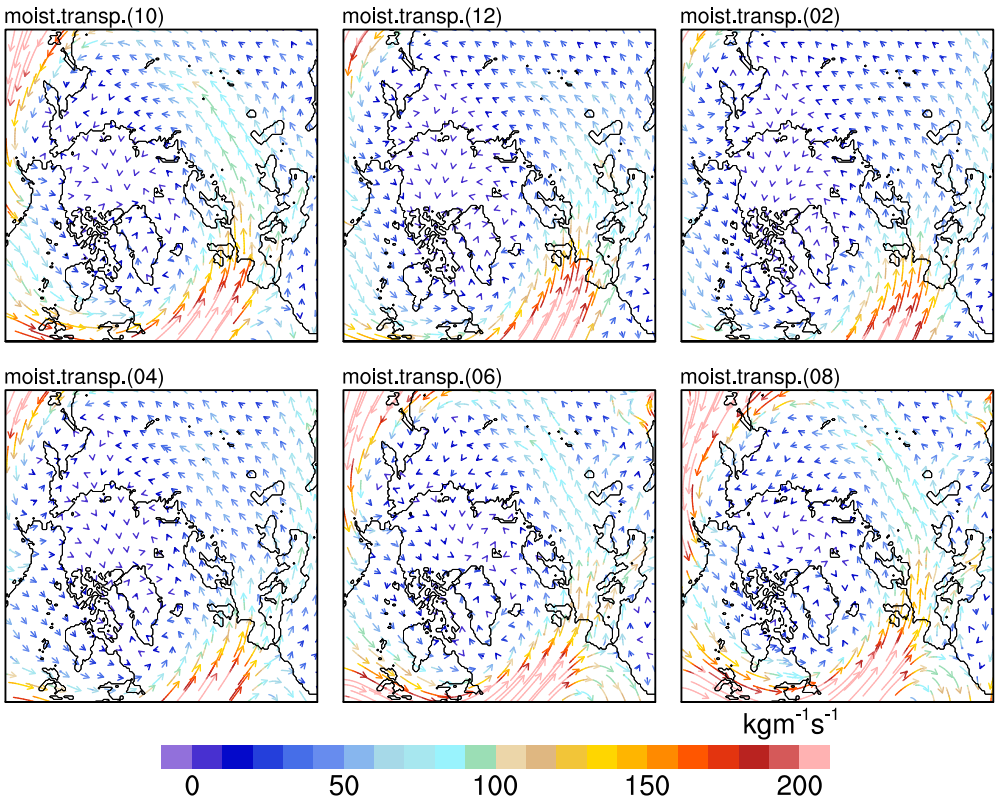

Figure 4.55: Vertically integrated mean moisture transport in kg/m/s. The term moist.transp.(10) refers to the mean value of vertically integrated moisture transport for the period September - November, moist.transp.(12) to the transport for November - January, and so forth.

The vertically integrated moisture transport calculated from 6 - hourly model output is presented in Figure 4.56, while the vertically integrated moisture transport calculated from monthly mean model data is presented in Figure 4.57. The stronger values, calculated by using the 6 - hourly data, indicate that there is enhanced activity on a synoptic scale that is not taken into account in the monthly mean values. In January to March as well as in March to May (upper right and lower left panel in Figure 4.56 and Figure 4.57), the difference, especially over land, implies an increase of cyclone tracks bringing more moisture into Eurasia.

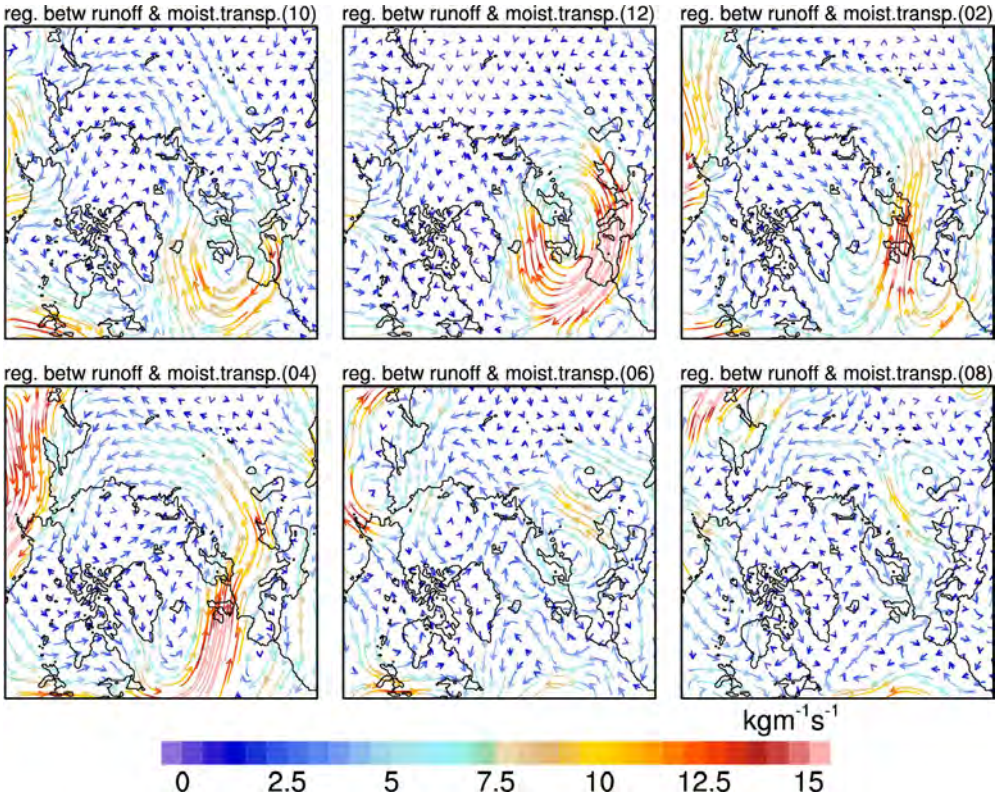

Figure 4.56: Regression coefficient between Eurasian runoff and 3 months running mean of vertically integrated moisture transport of 6 - hourly data in kg/m/s. The term moist.transp.(10) refers to the mean value of vertically integrated moisture transport for the period September - November, moist.transp.(12) to the transport for November - January, and so forth.

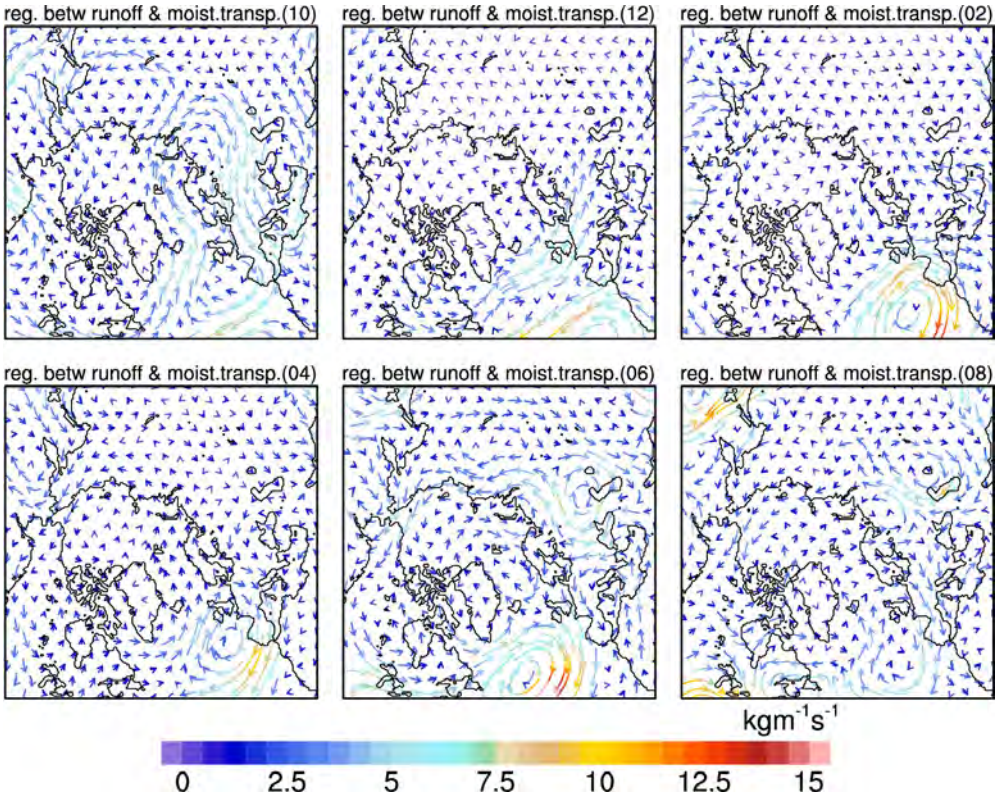

Figure 4.57: Regression coefficient between Eurasian runoff and 3 months running mean of vertically integrated moisture transport of monthly mean data in kg/m/s. The term moist.transp.(10) refers to the mean value of vertically integrated moisture transport for the period September - November, moist.transp.(12) to the transport for November - January, and so forth.

Snow cover In contrast to the influence of the 2 m temperature, the influence of snow cover on Eurasian runoff is restricted to high latitudes (Figure 4.58). In western Siberia, snow cover explains more than 20 % of the runoff's variability for spring and summer. An increase in snow cover in summer leads to increased FW input during the melting season and thus to an increased runoff. Snow cover in other seasons plays a minor role in the variability of Eurasian runoff. The annual cycles of precipitation and snow cover are phase delayed by about five to six months, precipitation is largest in all Eurasian catchment areas in summer, with a maximum in August. Surface temperature shows the same annual cycle as precipitation, leading to to summer temperatures of more than 10 °Celsius. Thus, only winter precipitation from October onwards accounts for the increasing snow depth, with a maximum in February. As mentioned before, the winter precipitation before an anomalous strong runoff year is enhanced slightly in all catchment areas. This leads to slightly increased snow depth of an areal mean over the catchments of up to 0.8 cm water equivalent.

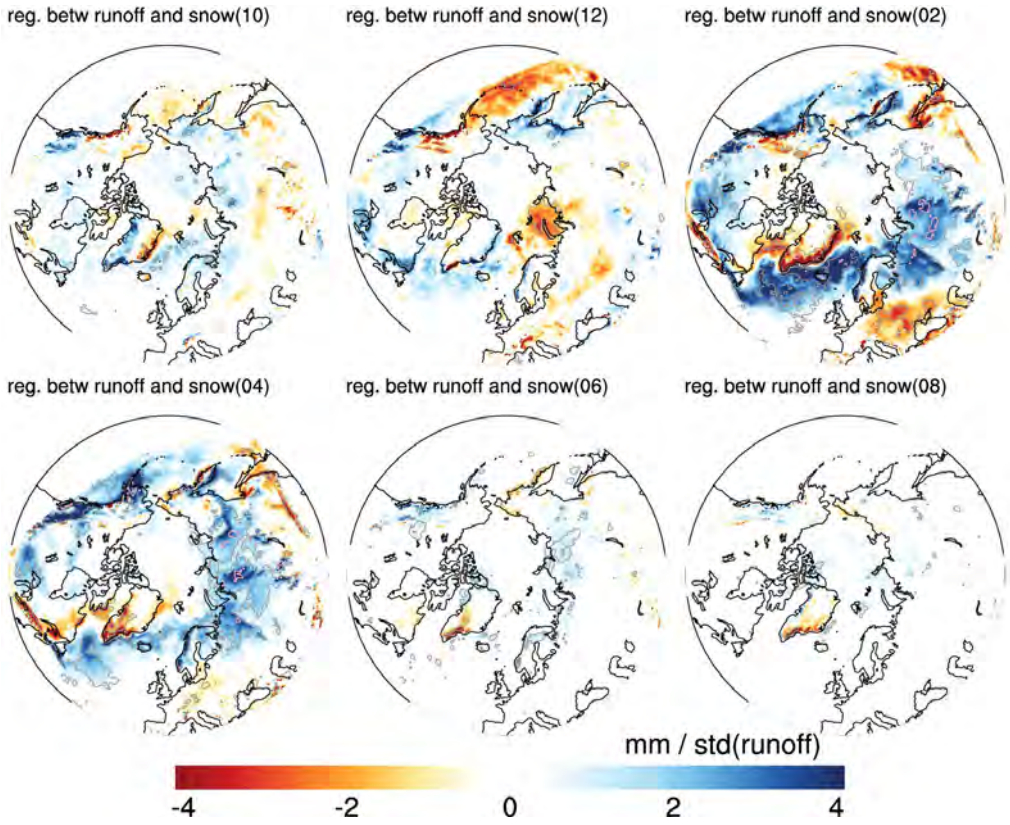

Figure 4.58: Regression coefficient between Eurasian runoff and 3 months running mean of snow depth in mm per standard deviation of Eurasian runoff. The term snow(10) refers to the mean value of snow depth for the period September - November, snow(12) to the mean value for November - January, and so forth. The grey contour line indicates the level of highly significant values for all model years. The pink line indicates the level of highly significant values for 40 years, which is the span of our model simulation 1960 - 1999 and the minimum of independent modeled years.

To conclude, in the winter season before a year with increased runoff, the anomalous strong Icelandic low deflects the moisture and heat transport northward taking a shortcut into Siberia. It is warmer and wetter than usual over the Eurasian continent. Increased precipitation during winter leads to more snow than usual. This increased snow depth plus increased precipitation in late spring and summer, lead to increased river runoff during the melting season. In summer, with enhanced Eurasian runoff, increased inflow of moist air originating from the Pacific reaches eastern Siberia , leading to enhanced runoff, especially of the rivers Kolyma and Indigirka. The enhanced summer cyclone activity over Northern Europe entering western Siberia supplies more moisture than usual, not only for the western Siberian rivers, but the moisture is also transported into eastern Siberia.

4.2.2 North American river runoff

The mean runoff of the North American continent accounts, with about 77 mSv, for approximately 40 % of the total Arctic runoff. The yearly standard deviation is about 5.7 mSv. The largest catchment, covering large parts of Alaska and north-eastern Canada, belongs to the Mackenzie river, with a mean runoff of 13.5 mSv. The mean annual cycle of that river is given in Figure 3.17 c).

Mean sea level pressure The changes of mean sea level pressure in the winter ahead of increased North American runoff is smaller than compared to the changes before years with increased Eurasian runoff. As can be seen in Figure 4.59, in the upper middle and right panel, the Aleutian low is shifted westward allowing for higher pressure than usual over the north eastern Pacific and the coastal areas. Over the Eurasian part of the Arctic Ocean and the adjacent coastal areas, the mean sea level pressure increases with largest changes in January to March of about 2 hPa in Kara Sea (upper right panel). From April during summer, the changes in mean sea level pressure are negligible (Figure 4.59, second row).

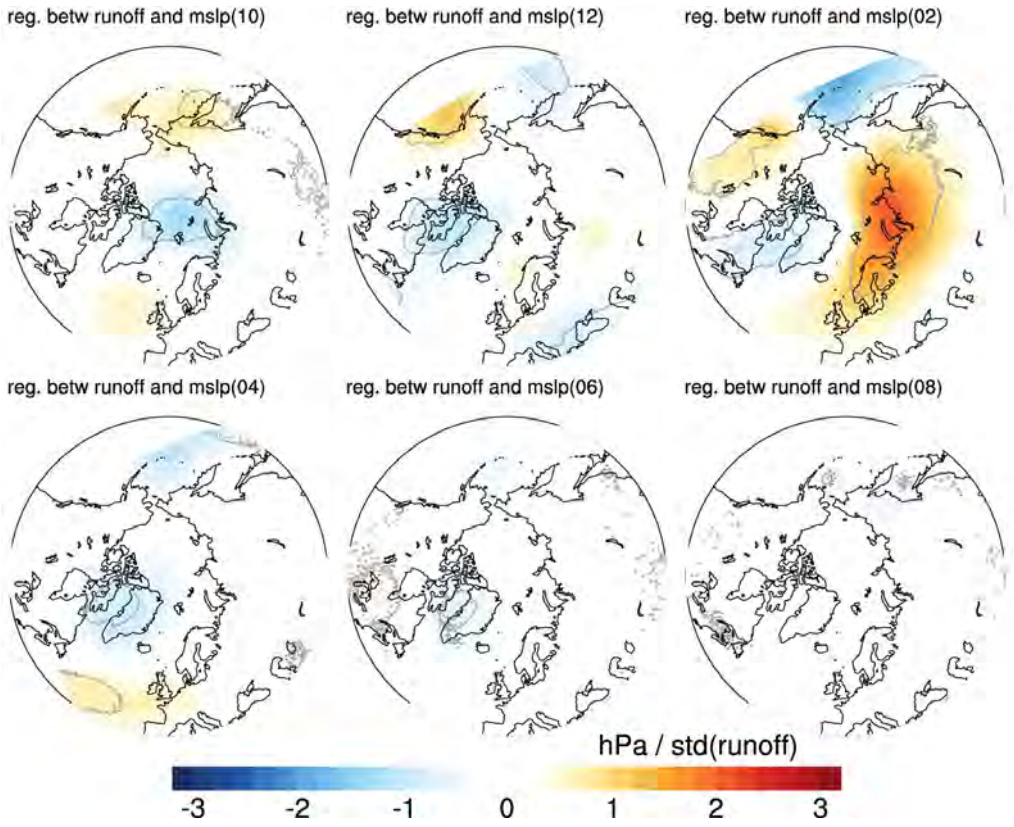

Figure 4.59: Regression coefficient between North American runoff and 3 months running mean sea level pressure in hPa per standard deviation of North American runoff. The term mslp(10) refers to the mean value of mean sea level pressure for the period September - November of the previous year, mslp(12) to the mean value for November - January, mslp(02) to the mean value for January - March, and so forth. The grey contour line indicates the level of highly significant values for all model years. The pink line indicates the level of highly significant values for 40 years, which is the span of our model simulation 1960 - 1999 and the minimum of independent modeled years.

2 m temperature In the years with increased North American runoff, the stronger than usual Aleutian low leads to more heat transport from low latitudes from the Pacific to North America. The warming is strongest in February to April exceeding 1 °Celsius (Figure 4.60). The warming is persistent for most of the summer, but the difference becomes rather small soon after summer. In January to March, the heat transport from the North Atlantic is deflected northward. This leads to lower than usual temperatures over Europe and higher than usual temperatures over Greenland and in Lincoln Sea. However, the changes in 2 m temperature over the Eurasian continent are small and do not even exceed the significance level for 40 years (indicated by the grey line).

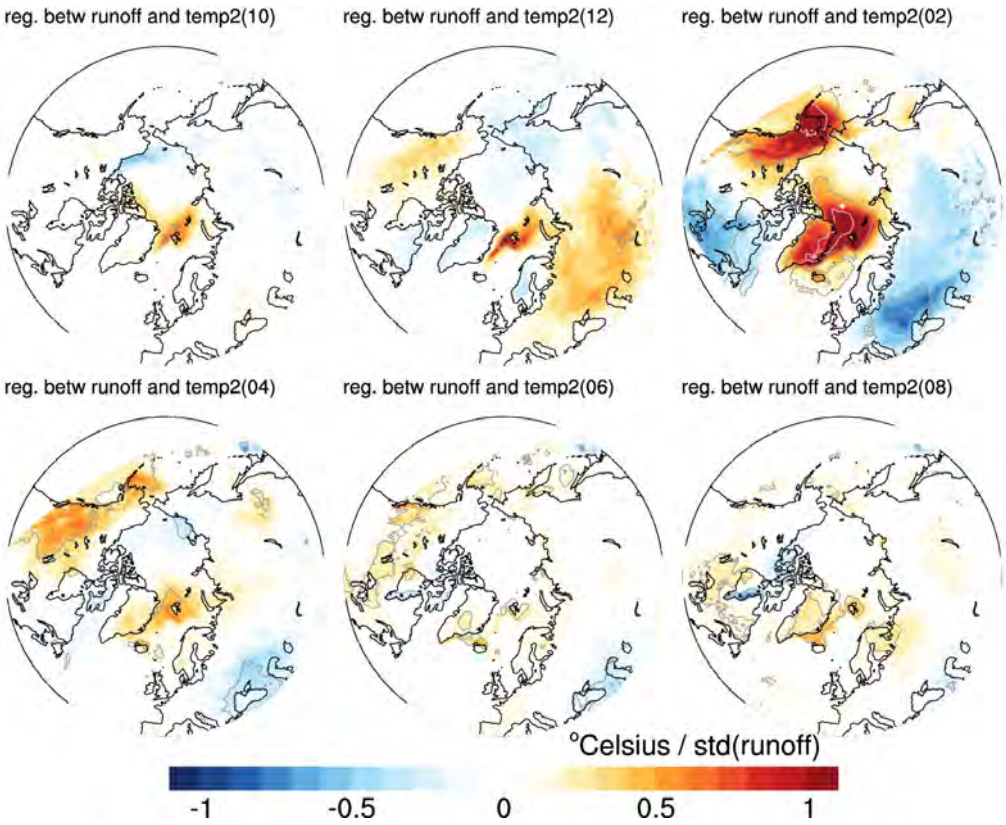

Figure 4.60: Regression coefficient between North American runoff and 3 months running mean of 2 m temperature in °Celsius per standard deviation of North American runoff. The term temp2(10) refers to the mean value of 2 m temperature for the period September - November of the previous year, temp2(12) to the mean value for November - January, and so forth. The grey contour line indicates the level of highly significant values for all model years. The pink line indicates the level of highly significant values for 40 years, which is the span of our model simulation 1960 - 1999 and the minimum of independent modeled years.

Moisture transport and net precipitation In autumn and early winter, increased net precipitation, blocked by the Rocky Mountains, can be seen along the Alaskan coastline over the Pacific (Figure 4.61, upper left and upper middle panel). In January to March, the stronger than usual Aleutian low does not only bring warmer temperatures, but also more cyclone activities from the western North Pacific to the American continent. The moisture transport from the Pacific along the Asian coast is strongest in March to May (Figure 4.62, lower left panel). The cyclone activity remains enhanced over North America during summer, while changes in the mean transport over North America are rather small. Figure 4.63 shows the regression coefficient between North American runoff and 3 months running mean vertically integrated moisture transport of monthly mean model data. Figure 4.62 also shows the regression coefficient, but calculated with 6 hourly model data. The enhanced activities on these synoptic scales indicate an increase in cyclone activity that is not taken into account when using monthly mean values. The mean vertically integrated moisture transport is shown in Figure 4.55. During summer, May to July, the mean mois-

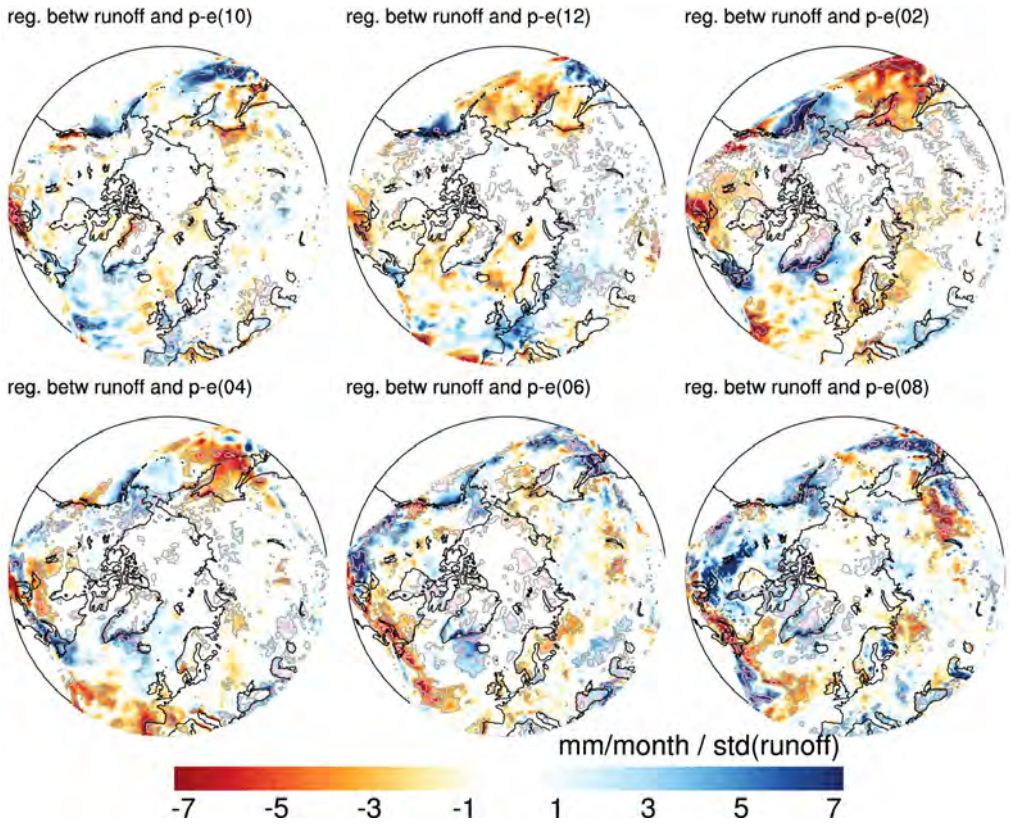

Figure 4.61: Regression coefficient between North American runoff and 3 months running mean of net precipitation in mm / month per standard deviation of North American runoff. The term plot p-e(10) refers to the mean value of net precipitation for the period September - November of the previous year, p-e(12) to the mean value for November - January, and so forth. The grey contour line indicates the level of highly significant values for all model years. The pink line indicates the level of highly significant values for 40 years, which is the span of our model simulation 1960 - 1999 and the minimum of independent modeled years.

ture transport is changed and moist air is transported over the Arctic Ocean, along the Siberian coast, reaching North America (Figure 4.63, lower middle panel). This leads to increased net precipitation also in summer over the catchment area of the Mackenzie river (Figure 4.61, lower right panel).

To conclude, the changes in mean sea level pressure before and within a year with enhanced North American river runoff are rather small. Nevertheless, the enhanced Aleutian low in January to March leads to enhanced heat and moisture transport to the North American continent. Even though the changes are small, Alaska remains warmer and wetter than usual for most of the year. Precipitation in summer is enhanced by increased cyclone activities over North America. Compared to Eurasian runoff, the changes are small and only give a small contribution to the Arctic river runoff.

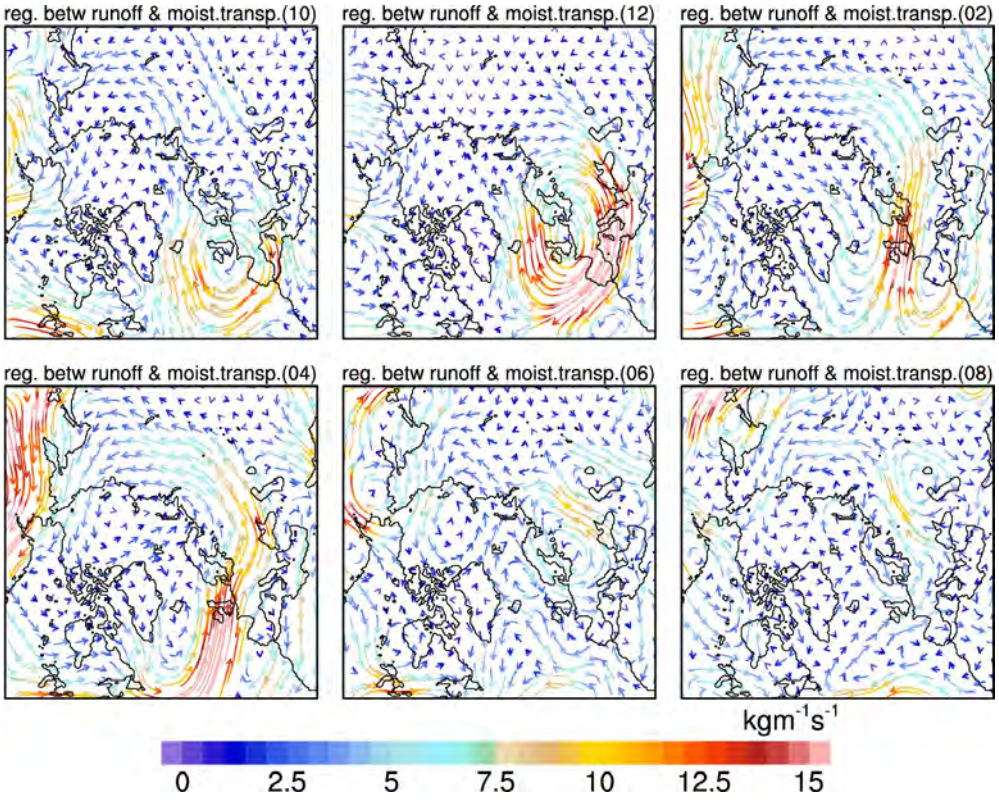

Figure 4.62: Regression coefficient between North American runoff and 3 months running mean of vertically integrated moisture transport of 6 - hourly data in kg/m/s. The term moist.transp.(10) refers to the mean value of vertically integrated moisture transport for the period September - November, moist.transp.(12) to the transport for November - January, and so forth.

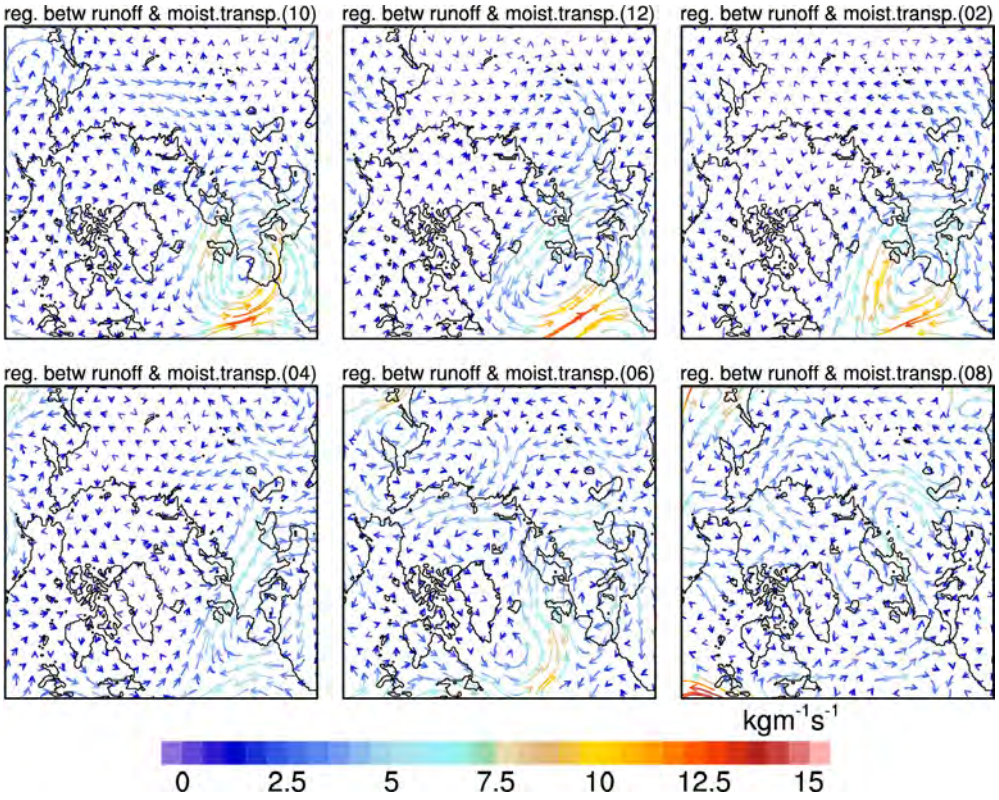

Figure 4.63: Regression coefficient between North American runoff and 3 months running mean of vertically integrated moisture transport of monthly mean data in kg/m/s. The term moist.transp.(10) refers to the mean value of vertically integrated moisture transport for the period September - November, moist.transp.(12) to the transport for November - January, and so forth.

4.3 Summary and conclusion

We have analyzed the variability of the Arctic FW components with respect to leading modes in the atmosphere. The domain of our regional coupled model is large enough to evolve its own shape of the leading modes of winter mean sea level pressure. While the spatial distribution of net precipitation and 2 m temperature as well as the Arctic Ocean sea ice circulation show large changes within these different modes, the variability of river runoff is not captured. That is why we have analyzed river runoff variability separately.

4.3.1 Main findings

Leading EOF of winter mean sea level pressure The leading EOF of winter mean sea level pressure is related to the well-known spatial distribution of the Arctic Oscillation. In its positive phase, stronger than usual westerly winds bring more moisture than usual over the North Atlantic into Eurasia leading to wetter and warmer conditions in Northern Europe and Russia. However, the signal in river runoff is within the interannual variability. While in the positive phase the ocean circulation is characterized by a strong transpolar drift enhancing especially the ice export through Fram Strait and through the Canadian archipelago, the negative phase of this leading mode is designated by a strong anticyclonic Beaufort Gyre circulation. This leads to a decrease in FW export particularly through Fram Strait and at the same time to an accumulation of FW within the Arctic Ocean.

Second EOF of winter mean sea level pressure Our second leading EOF is characterized by a tripole pattern with a strong Aleutian low and a second low over Northern Europe. In between, the Icelandic low is weaker than usual. This leads to warmer than usual winter temperatures over southern Europe as well as over North America. Changes in net precipitation are mostly restricted to Europe. In the Arctic Ocean, however, the response is comparably large; in the positive years a strong gyre retains sea ice and liquid FW within the Arctic, leading to an accumulation of liquid FW as well as to a reduction of FW export, especially in liquid form. In the negative years, the winds push the ice to the Canadian archipelago resulting in an enhanced FW export in liquid as well as in solid form through the archipelago and through Fram Strait.

North Atlantic Oscillation The variability caused by the NAO agrees well with previous studies. As also found by Dickson et al. (2000), we find largest precipitation changes in Norwegian-Greenland Seas and over Scandinavia. As in our EOF 1 composites, there is a strong transpolar drift from Siberia to the Canadian coast in the positive years leading to an increased export of FW through the archipelago, while in the negative years the FW is retained within a strong Beaufort Gyre. This is consistent with the results by Condron et al. (2009).

Siberian high The influence of the Siberian high on changes in winter mean sea level pressure covers large parts of our atmospheric model domain. Especially in the positive

years, the years with stronger than usual Siberian high, changes occur over large parts of the Eurasian continent as well as the Arctic Ocean. As in the negative EOF 1 years, the continent is colder and dryer than usual, leading to a reduction in the Eurasian river runoff. Again similar to the negative EOF 1 years, a strong Beaufort Gyre leads to reduced exports of FW through Fram Strait as well as through the Canadian archipelago. The impact of the negative Siberian high years, however, is rather small and changes in the FW fluxes are always below two standard deviations from the mean.

Variability in Arctic river runoff The variability of Arctic river runoff is dominated by the variability of runoff from the Eurasian continent into the Arctic Ocean rather than of North American runoff. In winters before increased Eurasian river runoff, the Icelandic low is anomalously strong, redirecting the moisture and heat over the North Atlantic northward into Siberia. Increased precipitation in late spring and summer, caused by enhanced cyclone activity, lead to increased Eurasian runoff during the melting season. Changes in the Aleutian low early in the year of enhanced North American runoff lead to enhanced moisture and heat transport from the North Pacific to North America. Precipitation is enhanced due to increased cyclone activities in summer, but changes in runoff are small compared to the variability in Eurasian runoff.

4.3.2 Concluding remarks

We have seen that the analyzed leading modes in winter mean sea level pressure have a large impact on the variability of the FW cycle within the Arctic. Comparing our results with previous studies we conclude that our model shows a realistic FW variability and responds sensitive to atmospheric changes.

With this study using our high-resolution coupled model setup, we provide a comprehensive analysis of different dominant modes of large-scale atmospheric variability driving large parts of the variability in the Arctic FW cycle in the 20th century. Thereby, we can detect the interactions of atmosphere, sea ice and ocean, because our model includes all of these components. Additionally, we are able to determine mechanisms driving the variability in river runoff, as the coupled model domain covers all catchment areas of rivers draining into the Arctic Ocean and the hydrological discharge model provides lateral terrestrial waterflows calculated internally in the model.

Chapter 5

Projection of the Arctic freshwater components in the 21st century

The changing Arctic FW budget is subject of ongoing research. The hydrologic cycle in the Arctic is expected to intensify in a warming climate which is confirmed by general circulation models (Meehl et al. 2007; Kattsov et al. 2007; Held and Soden 2006) as well as by observations (Rawlins et al. 2010; Lammers et al. 2001). A changing amount of FW export through the Canadian archipelago and through Fram Strait affects directly the sights where deep-water forms in Labrador Sea and GIN Sea. Since at low temperatures density is mostly a function of salinity even small changes in FW export might affect the global thermohaline circulation and thus the global climate. Nevertheless, the observational network is sparse, especially for the ocean fluxes and the natural variability in the FW terms is large as is the variability in and between different climate models.

In this chapter, we use results from our regional coupled model setup and analyze changes in the Arctic FW components in the 21st century. We perform model experiments forced with output from a global model run with ECHAM / MPIOM, where the A1B scenario is used. We analyze two scenario runs and compare them with a control run, where we repeat the forcing every 32 years. For more details on the performed experiments we refer to Section 2.4.

Initially, we planned to analyze experiments performed for the complete 21st century. Unfortunately, we could not finish in time, computing took longer than expected and we have not finished the experiments so far. The scenario runs are performed until the end of the years 2069 and 2043. The control run ends in 2049. We analyze time series of relevant variables and compare two time slices, 2020 - 2029 and 2060 - 2069, with the control run. For the first time slice we use an ensemble mean of the two scenario runs, for the second time slice we can only use the data from one experiment. Assuming, that the control run does not show a large model drift, we use the time span 2028 - 2037 to compare with, because the forcing for the years 2060 - 2069 would be the same as in these years.
Additionally, while analyzing the model results it turned out that the preprocessing of the forcing data had not worked correctly for a few years. The forcing data were not consistent with the corresponding data from the global model. In order to avoid potential artifacts, we exclude these years and the subsequent two years. This period was chosen to allow the system to buffer the perturbance caused by the inconsistent forcing fields. Therefore, in

the following, the time series contain gaps. Table D.1 in Appendix D lists all years, where problems appeared. We expect that our main findings would not change when repeating the model experiments.

In Section 5.1 we have a closer look at the changes in the atmospheric components, such as the mean sea level pressure, 2 m temperature and precipitation.

In Section 5.2 we focus on the changes taking place in the ocean and analyze how FW fluxes change within time.

We see in Section 5.3 that the changes in the FW transports have an influence on the deep-water formation in Labrador Sea and GIN Sea and thereby on the global thermohaline circulation.

We close the chapter with Section 5.4 by calculating budgets for the above mentioned time slices and compare them to the control run.

5.1 Changes in the atmosphere

As in the previous chapter, we decompose some of the variables in their empirical orthogonal functions and calculate the corresponding PC time series. Therefore, we use the two scenario experiments, starting in 1960 as well as the control run. The control experiment is split after 32 years, before year 1992, from one of the scenario experiments. These years are taken into account only once in the following EOF analysis, thus we use all years of the two scenario experiments, 1960 - 2069 and 1960 - 2043, and from the control experiment, 1992 - 2049. As anomaly time series, we calculate the difference of all of these years and the mean value of the control run (1960 - 2049), instead of substracting the mean value of the full time series. To separate the interannual and seasonal variability and potential climate signals with respect to the external forcing we use a temporal filter of 5 years running mean. All EOFs presented in the following are calculated with 5 years running mean data.

Mean sea level pressure Figure 5.1 a) shows the leading EOF of winter mean sea level pressure from the scenario experiments and the control run. Compared to the leading EOF of winter mean sea level pressure calculated for the second half of the 20$^{\text{th}}$ century (Figure 4.2 c)) the spatial distribution looks very similar. The center of the negative pole is shifted a bit into the Arctic Ocean, away from the Russian coastal area. Additionally, the gradient to lower latitudes is slightly enhanced, as well as the positive signal in the region of the Aleutian low. In Figures 5.1 b) and c) the two leading EOFs of yearly mean sea level pressure are shown. The leading EOF is, as the leading EOF from winter mean sea level pressure, characterized by a strong negative pole over the Arctic Ocean, and explains about 47 % of the total variance. In the second leading EOF, comparable to the second EOF of winter mean sea level pressure for the 20$^{\text{th}}$ century (Figure 4.23), a tripole pattern can be seen, with a strong negative pole north of the Aleutian low and a second, but weaker, one over Europe. Over the Arctic Ocean and over Greenland, with

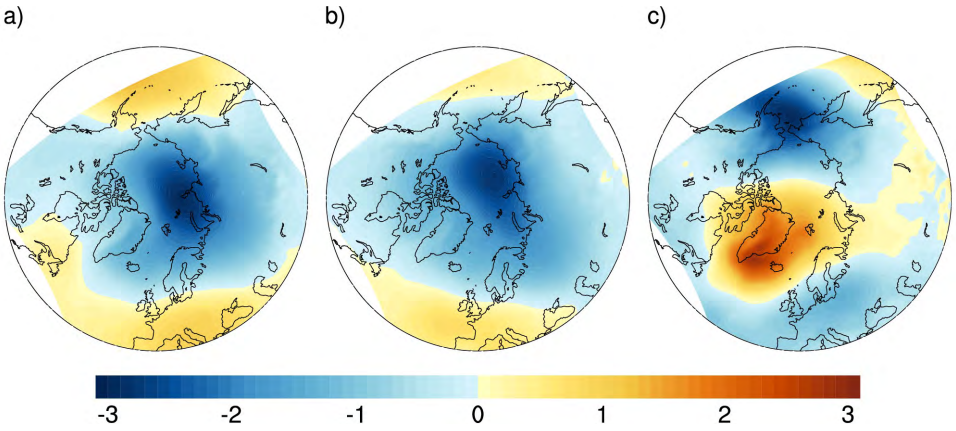

Figure 5.1: a) Leading EOF of DJF mean sea level pressure, b) leading EOF of yearly mean sea level pressure and c) second EOF of yearly mean sea level pressure of the control and the two scenario experiments. 5 years running mean values are used for calculation.

a maximum in Irminger Sea, is a positive pole. The second EOF explains about 9.6 % of the variance. The corresponding normalized principal component (PC) time series of the yearly mean sea level pressure EOFs are presented in Figure 5.2. The overall signal in the scenario experiments is rather small and noisy. Nevertheless, the leading PC of one of the scenario experiments is mostly positive in the 21st century, leading to a general decrease in mean sea level pressure over the Arctic Ocean. For the last 20 years of our experiment, the signal of the leading PC is clearly outside the range of natural variability, indicating a decreased mean sea level pressure over the Arctic.

Additionally, the second EOF with its corresponding PCs, that are also mostly positive in the 21st century, leads to a strengthening and northward shift of the Aleutian low. In large parts of the Arctic Ocean, the second EOF counteracts the leading EOF leading to a maximum of the signal in the Bering Strait region. Changes there are strongest in winter, reaching about -4 hPa for the years 2060 - 2069 compared to the control run.

Averaged over the Central Arctic Ocean, the decrease exceeds -2 hPa in the 2050 s in the yearly mean. The variability is large in all seasons without a clear trend in mean sea level pressure over the Central Arctic Ocean prior the year 2050. The strongest changes can be seen later than 2050, coherent with changes in the global run used as forcing. As our model domain does not cover large parts of the Pacific and largest changes occur around Bering Strait, the boundary forcing seems to be responsible for the decrease in the 2050s.

Chapman and Walsh (2007) analyze changes in surface temperature and sea level pressure from scenario experiments of several global climate models used in the Fourth Assessment Report of the IPCC and come to similar results. Even though the spread between the different models is large, all models show a decrease in sea level pressure over the Arctic Ocean as well as the negative change in winter over the Bering Strait region. They assume that the reduction in sea ice and with this a northward shift in the surface temperature gradient leads to the changes in sea level pressure.
Koenigk et al. (2010) use a regional coupled model for scenario experiments and conclude

that the reduction in sea ice and thus an increased cyclonic activity might be responsible for the increase of variability in mean sea level pressure over the Arctic. Increased moisture transport on a synoptic timescale can be seen in all seasons also in our model over the Bering Strait region. However, Overland and Wang (2010) analyze recent observations and conclude that the reduction in summer sea ice can indeed have an impact on the atmospheric circulation on the northern hemisphere but one should not expect a direct correspondence between sea ice and sea level pressure in every year.

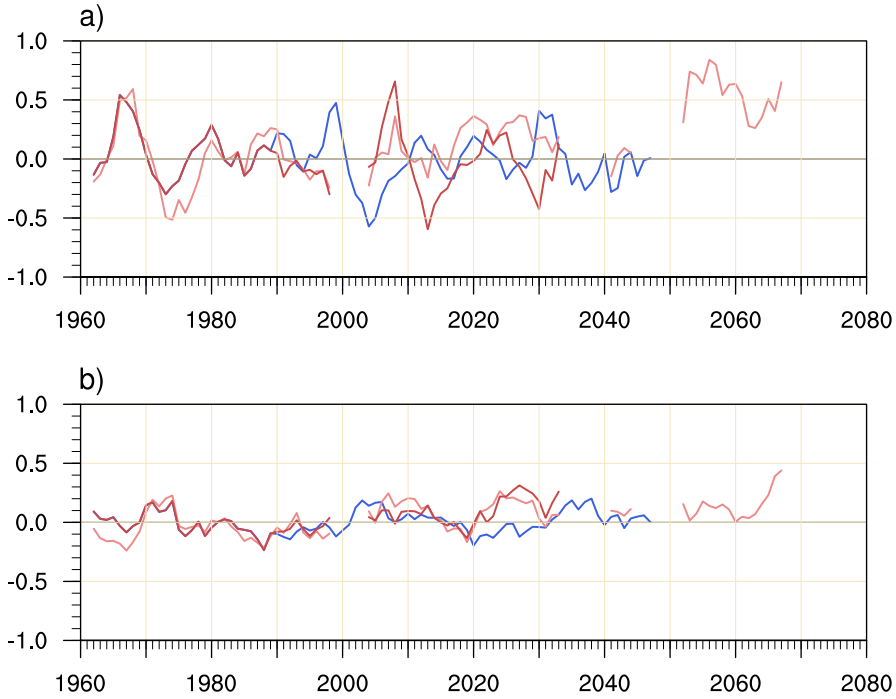

Figure 5.2: a) Principal component of the leading EOF and b) principal component of the second leading EOF for 5 years running mean sea level pressure. The control experiment is shown in blue, the scenario experiments in red.

2 m temperature Our model simulations show a mostly monotonically warming over the Arctic. This is strongest in winter but persistent for all seasons. The first and second EOF of 2 m temperature are presented in Figure 5.3 and the corresponding PC time series in Figure 5.4. The spatial distribution of the leading EOF, explaining 83.2 % of the total variance, is characterized by a positive anomaly in almost the entire model domain, strongest over the Central Arctic Ocean. Only in the North Atlantic region the values are very small and turn negative (Figure 5.3 a)). The second leading EOF shows a positive anomaly over the Arctic Ocean as well as over the North Atlantic, with strongest values along the present day ice edge east of Greenland and from Svalbard to Kara Sea. Over large parts of the adjacent continents the anomaly is negative, thus strengthening the contrast between the oceans and the mid-latitude land masses, the so-called Arctic amplification. The second leading EOF explains only 3.6 % of the total variance.

The positive trend in the PC of the leading EOF of 2 m temperature leads to an overall

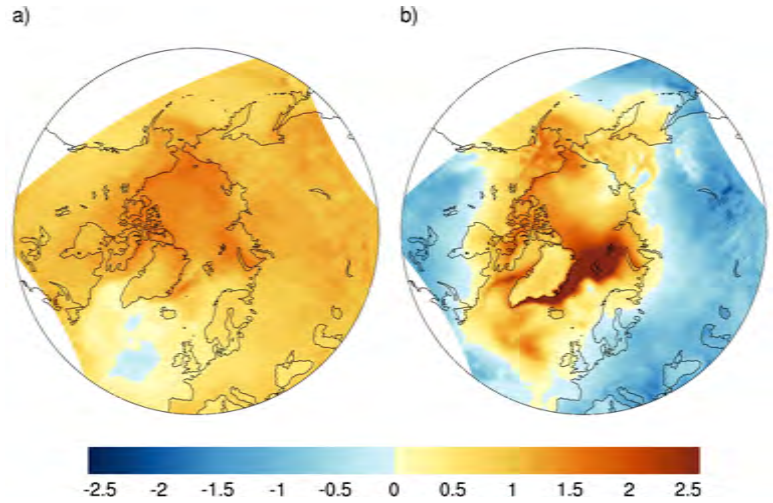

Figure 5.3: a) Leading EOF of 2 m temperature, b) second leading EOF 2 m temperature. 5 years running mean values are used for calculation.

warming amplified in the Arctic. It is strongest in winter, and exceeds over the Central Arctic Ocean, in both scenario experiments, 2 °Celsius already in 2000 (not shown). The increase in the yearly mean is smaller, ranging between 1 - 2 °Celsius in the years 2020 - 2029 (Figure 5.5 b)). The causes for the Arctic amplification are discussed to be beside a combination of atmospheric and oceanic circulation changes, changes in cloud cover and water vapour, the reduction in sea ice cover and the corresponding reduction in the albedo (Koenigk et al. 2010; Screen and Simmonds 2010; Koenigk et al. 2007). The temperature increase weakens from about 2040 as can be seen in the PC time series of the leading EOF. This is accompanied by a change in the PC of the second EOF. Before, the sign was mostly positive, thus strengthening the Arctic amplification, while the opposite is true in the second half of the 21st century. The change in the sign of this second PC leads to a weakening of the Arctic warming. For the winter season, the temperature change in this scenario experiment compared to the control run exceeds 6 °Celsius in 2040, but is less than 5 °Celsius again in the 2050 s. However, the system seems to change again in the 2060s. Figure 5.5 c), representing the temperature anomaly for the years 2060 - 2069, shows a large increase (3 - 5 °Celsius) over large parts of the Arctic Ocean as well as over the adjacent continents. Due to the changes in the PC of the second EOF, the contrast between the warming trend over the Arctic Ocean and the signal over the continents reduces. Whereas in 2020 - 2029 the warming is larger over the Arctic Ocean than the adjacent land masses (Figure 5.5 b)), the spatial distribution in the 2 m temperature anomaly in 2060 - 2069 does not show a clear land-ocean distribution anymore (Figure 5.5 c)) . The PC time series and the changes in the 2040s correspond well to the changes in the sea ice volume, reaching a minimum around 2040 with abrupt recovering afterward (see Section 5.2 for changes in sea ice). The *starting point* for this change can be found in GIN Sea. Due to a warming of the winter surface temperature, the convection in this area is strongly reduced around 2040 (see Section 5.3 for changes in deep-water formation). Thus the properties of the water

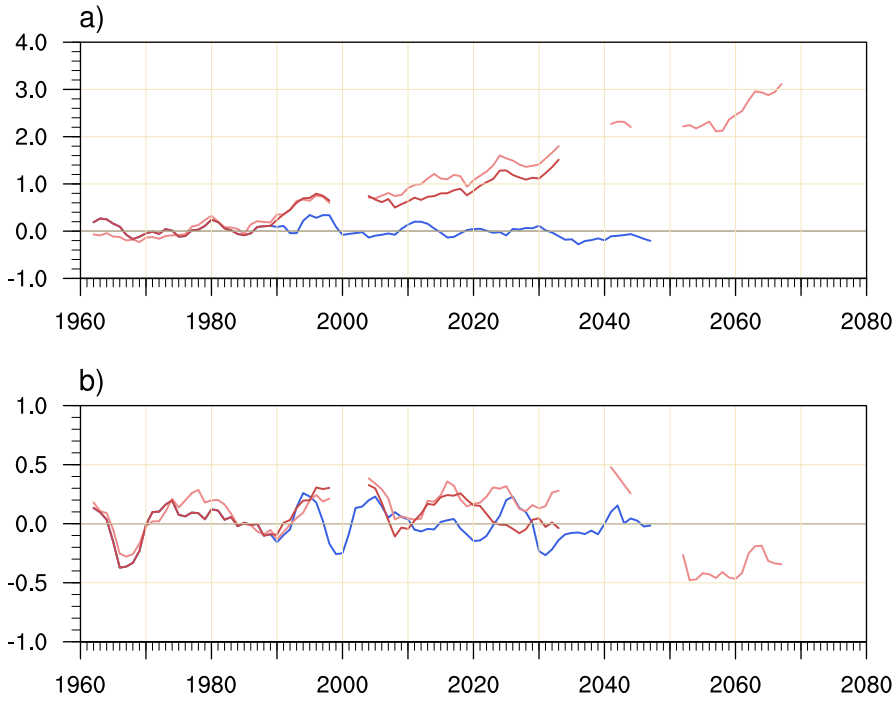

Figure 5.4: a) Principal component of the leading EOF and b) principal component of the second leading EOF for 5 years running mean 2 m temperature. The control experiment is shown in blue, the scenario experiments in red.

entering the Arctic Ocean via Barents Sea and the West Spitsbergen Current change; the water is fresher and colder than before. This leads to a partly recovery of sea ice; increased yearly mean sea ice cover north of Svalbard and in parts of Barents Sea can be seen, decreasing in winter the heat flux from the ocean to the atmosphere and thereby cooling the adjacent air mass.

The global coupled model does also show this weakening in the 2 m temperature increase in the 2040s, as a decade long stagnation in a linear trend. Around 2055, the increase restarts, reaching in 2080 approximately 10 °Celsius warmer yearly mean temperatures in the Arctic than compared to the beginning of the century.

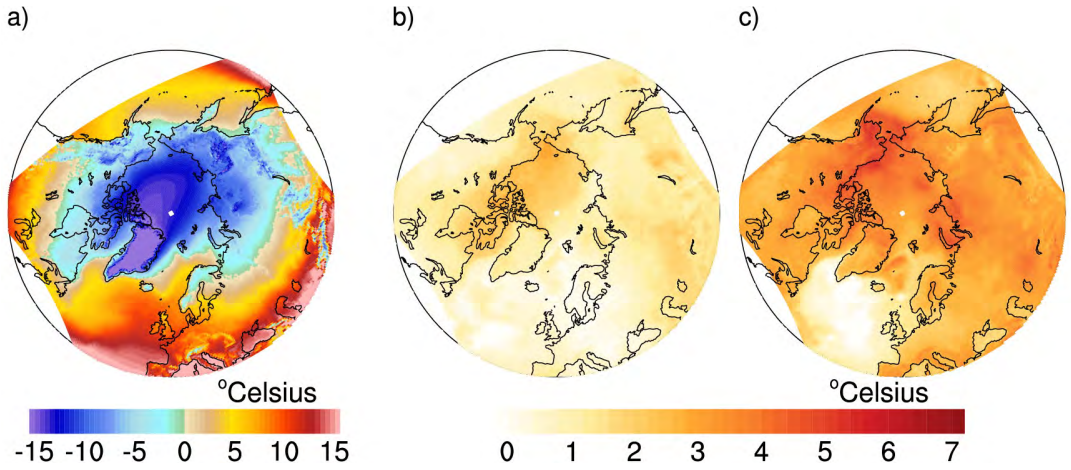

Figure 5.5: 2 m temperature from a) the mean of the control experiment, and the difference between the scenario experiments and the control run for b) the years 2020 - 2029, and c) the years 2060 - 2069.

Precipitation and runoff Our model projects increased net precipitation over the Arctic Ocean as well as over large parts of the catchment areas of the Arctic rivers (Figure 5.6). This feature is relatively robust among global models as well (Kattsov et al. 2007; Vavrus et al. 2011). Higher temperatures lead to an increase of atmospheric moisture transport from low to high latitudes, which results in this increase in precipitation in the Arctic region, where additionally evaporation is small (Kattsov et al. 2007).

The leading EOF of precipitation (Figure 5.7), explaining about 44 % of the total variance, shows the largest signals at the *inflow* boundaries of our model domain, in the Pacific and in the Atlantic / over the North American continent. This spatial distribution and the high correlation of the corresponding PCs (Figure 5.8) indicate that most of the variability is driven by the forcing at the lateral boundaries of our atmosphere model.

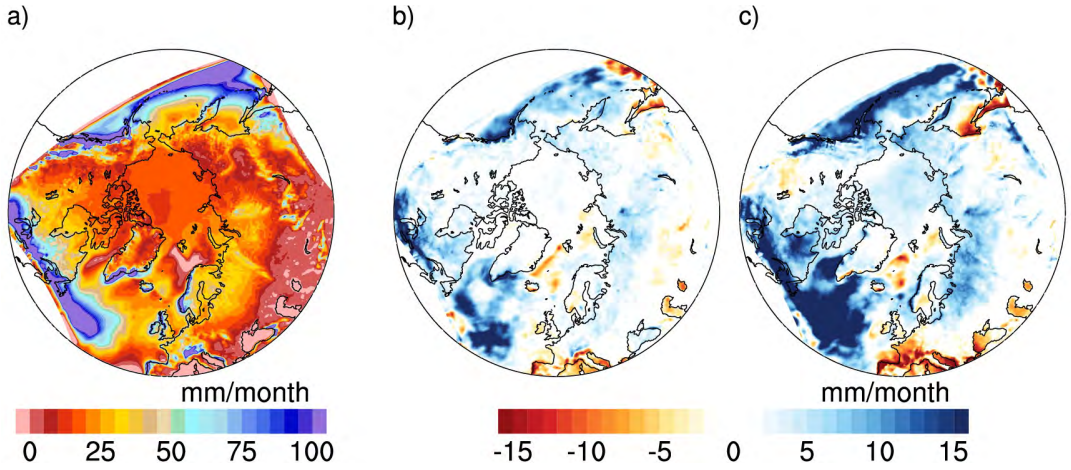

Figure 5.6: Net precipitation from a) the mean of the control experiment, and the difference between the scenario experiments and the control run for b) the years 2020 - 2029, and c) the years 2060 - 2069.

The leading PCs show a widely linear trend, but with large interannual variability (Figure 5.8). However, the large changes in net precipitation over the Atlantic (Figure 5.6 b) and c)) cannot be explained with this EOF. While precipitation is even slightly reduced in that region, evaporation is strongly reduced as well, resulting in a total increase of precipitation minus evaporation. The reason can be found again in the behavior of deep-water formation (see Section 5.3 for changes in deep-water formation). Convection is strongly reduced, especially after 2030, accompanied by a cooling of the ocean surface layer and thus decreasing the heat flux from the ocean into the atmosphere. All year round, temperature changes between the scenario experiments and the control run are very small in that region, and thus, the meridional surface pressure gradient in that area is reduced as well. The moisture transport is changed, taking a more southerly track and then passing the eastern Atlantic northward. Even though taking a more easterly track over the Atlantic, the overall moisture transport enhances in all seasons; especially in summer and autumn over Eurasia as well as over North America (Figure 5.9).

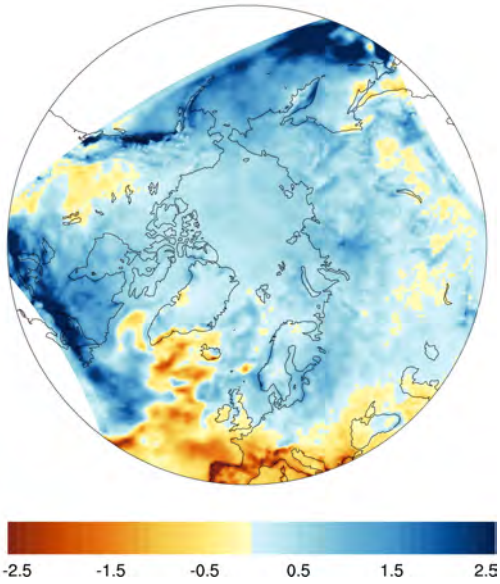

Figure 5.7: Leading EOF of yearly mean precipitation. 5 years running mean values are used for calculation.

As can be seen in Figure 5.6 b) and c), evaporation is enhanced in an area east of Greenland, in Barents and Kara Sea. These are exactly the regions of a substantial reduction of the sea ice cover with advection of cold air masses over open, relatively warm, ocean.

The total net FW input (net precipitation and runoff) into the Arctic Ocean shows an increase of more than 15 mSv for 2020 - 2029, reaching about 35 mSv in 2060 - 2969 (Figure 5.10 a)). The increase in net precipitation over the Arctic Ocean, however, is with about 3 mSv and approximately 12 mSv in the corresponding time slices, substantially smaller (Figure 5.10 b)).

In the global model net precipitation over the Arctic Ocean is overestimated, showing

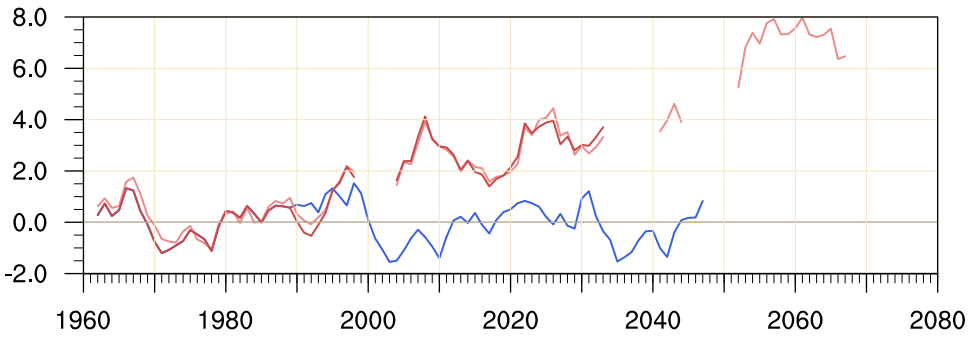

Figure 5.8: Principal component of the leading EOF for 5 years running mean precipitation. The control experiment is shown in blue, the scenario experiments in red.

values reaching 70 mSv already at the beginning of the century. The value in our control experiment is about 65 mSv. However, the trend in the 21st century in the global model is smaller than in our regional setup, reaching values of about 80 mSv in 2060 - 2069. Our model adds up to about 77 mSv in these years.

The variability in net FW input is driven by the variability in river runoff. Runoff variability is, as shown already for the variability in the 20th century in Chapter 4.2, dominated by the variability in Eurasian runoff (Figure 5.11 a)-c)). While the Eurasian runoff increases from the beginning of the 21st century, there is only a very small trend in the North American runoff in the first half of the 21st century. This might be due to the general northward shift of the Aleutian low and the corresponding shift of the low pressure cells into the Arctic Ocean rather than along the Aleutian islands. Thus the increase in precipitation over North America is rather small compared to the changes over Eurasia.

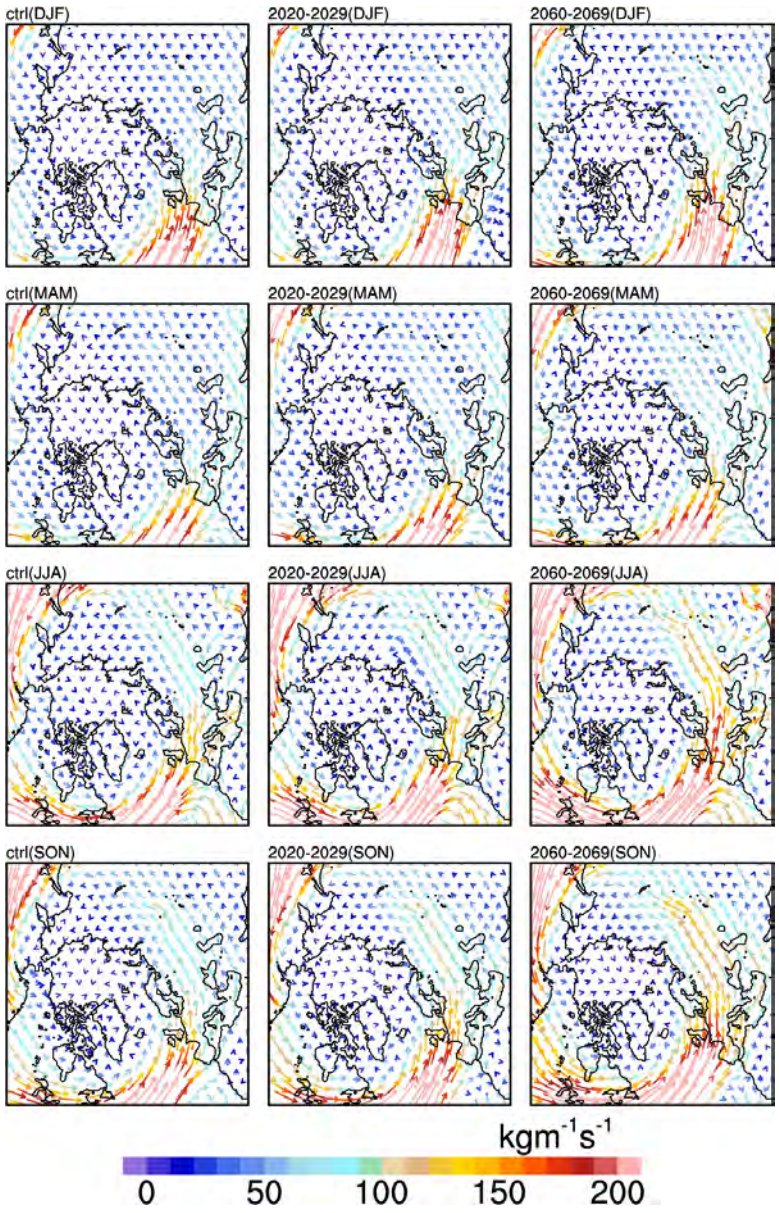

Figure 5.9: Seasonal mean of the moisture transport from the control experiment (left column), from the scenario experiments for the years 2020 - 2029 (middle column) and for the years 2060 - 2069 (right column). The moisture transport was calculated using 6 hourly model output.

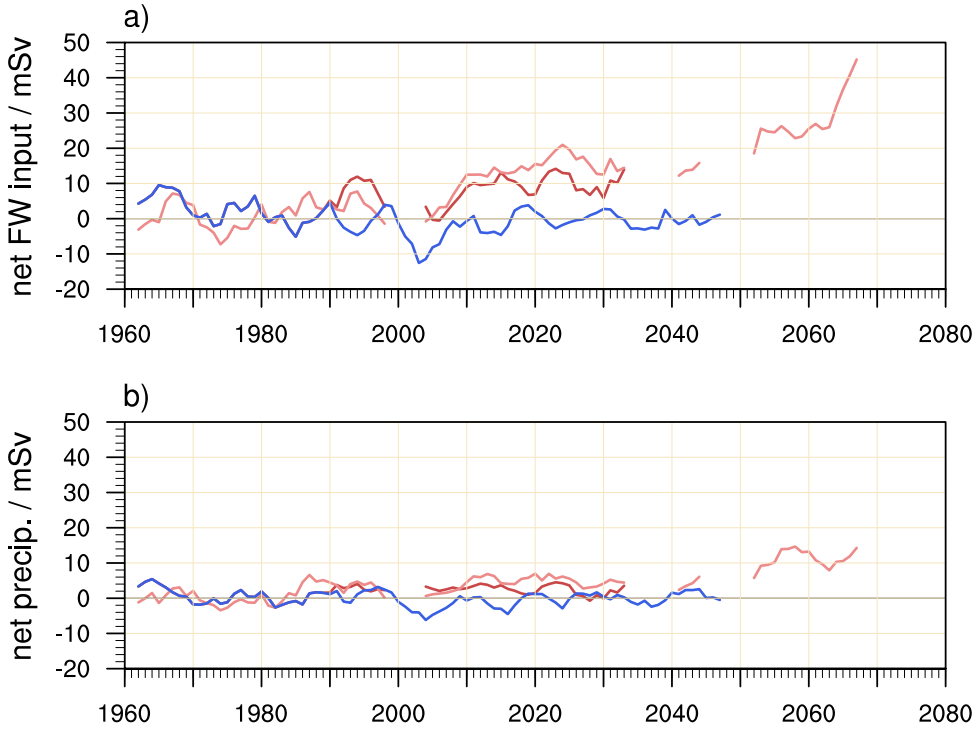

Figure 5.10: 5 years running mean values from the anomalies of a) net FW input (net precipitation and river runoff) into the Arctic Ocean and b) net precipitation over the Arctic Ocean. The anomalies are calculated as the difference between the scenario runs and the mean value of the control run, presented in red, and the difference between the control run and the mean, presented in blue.

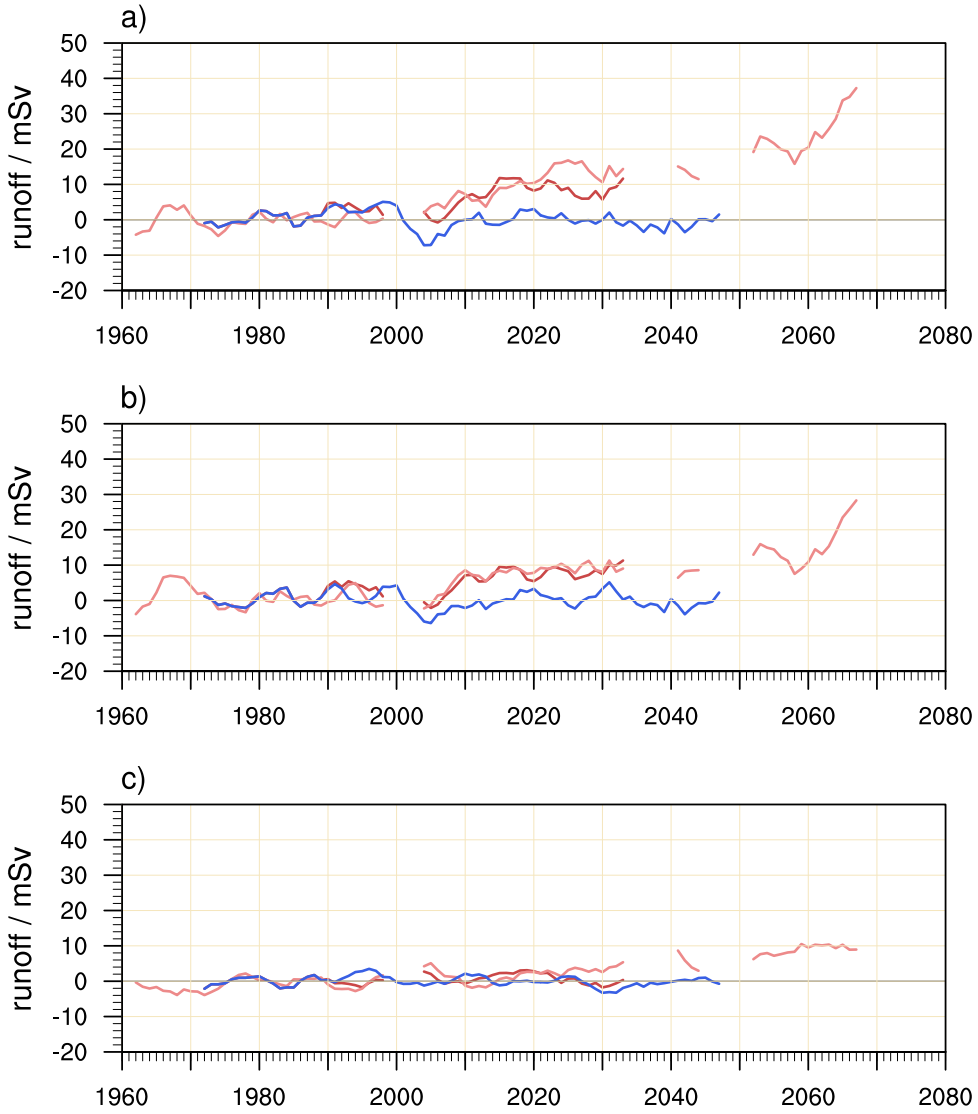

Figure 5.11: 5 years running mean values from river runoff anomalies for a) the total Arctic, b) Eurasia and c) North America. The anomalies are calculated as the difference between the scenario runs and the mean value of the control run, presented in red, and the difference between the control run and the mean, presented in blue.

5.2 Changes in the ocean

Sea ice As seen already in Chapter 3.1.1, our regional model simulates in the 20th century a rather small sea ice area, which is, especially in September, lower than observations. The scenario runs show in March as well as in September sea ice area a rather small but steady decline. The decline can be seen in all seasons, beeing largest in summer and autumn. However, the variability in September ice area increases strongly after 2040; beside strong reductions fast recoveries can be seen (Figure 5.12), reaching values in the range of todays observations and the control run. Figure 5.13 shows the annual number of months with a sea ice concentration exceeding 0.15 %, for the control run and the scenario runs for the years 2020 - 2029 and 2060 - 2069. The spatial distribution shows a decrease in all coastal regions of at least one month, while the overall distribution remains the same.

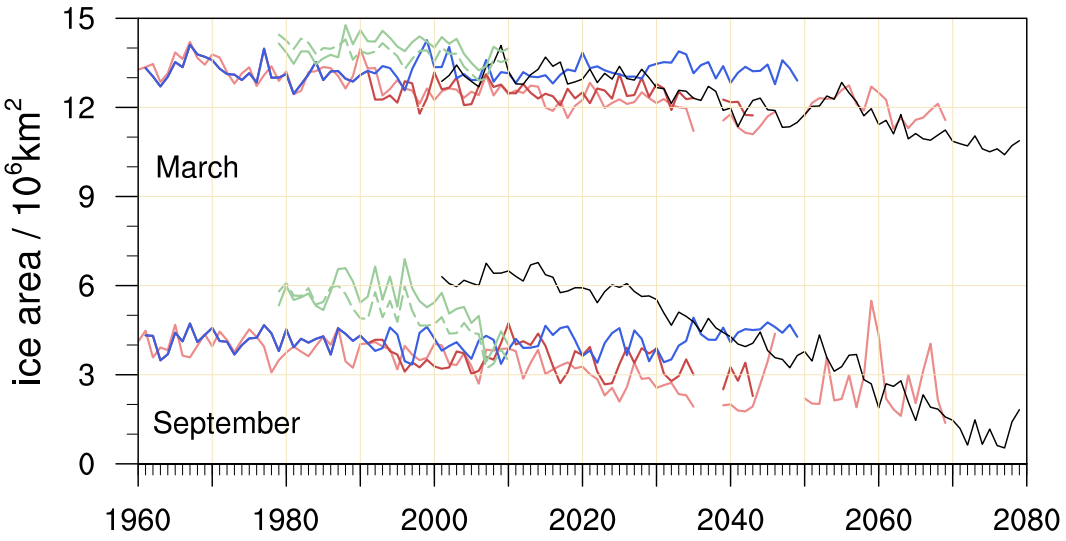

Figure 5.12: March and September sea ice area from the scenario experiments (in red), the control run (in blue), the global experiment (in black) and from NSIDC (in green). The green dashed line represents data calculated by using the NASA Team algorithm (Cavalieri et al. 1996), the green solid line represents data calculated by using the Bootstrap algorithm (Comiso 1999).

A similar behavior can be seen in sea ice volume, with a stronger decline in March sea ice volume compared to September sea ice volume (Figure 5.14). Again, from 2040 the variability increases strongly with local maxima in 2045 and 2059 and minima shortly before and after these years. The strongest decrease of sea ice thickness can be seen in the region of Beaufort and Chukchi Sea with mean values of 80 cm in 2020 - 2029 (Figure 5.15 b)). For 2060 - 2069 the decrease is strongest (larger than 1 m) in an area including East Siberian, Chukchi and Beaufort Sea; sea ice in Kara Sea disappears (Figure 5.15 c)). These regions correspond to the region with largest reduction of sea ice concentration, especially in autumn.

While global general circulation models show generally less variability, experiments with the regional Rossby Centre Atmosphere Ocean climate model show a similar behavior (Koenigk et al. 2010). The decline of sea ice area in several downscaling experiments is

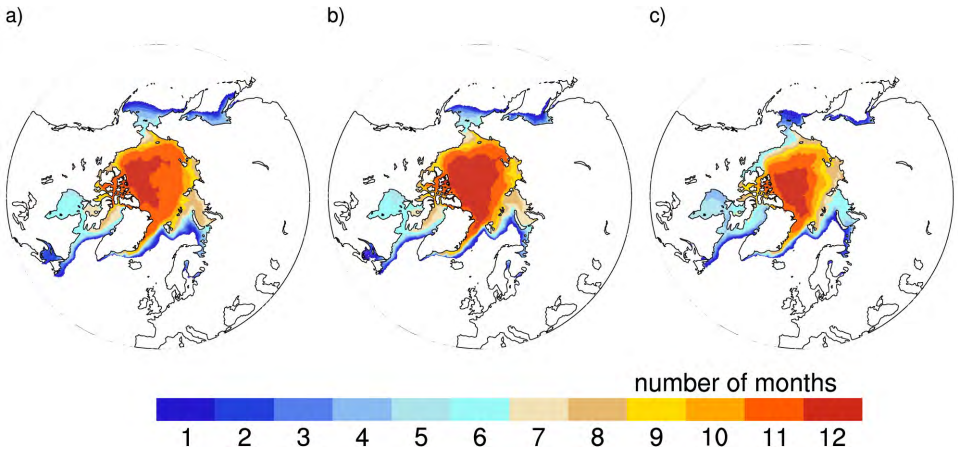

Figure 5.13: Number of months per year with sea ice concentration exceeding 0.15 for a) the control experiment, b) the ensemble mean of the scenario runs for 2020 - 2029 and b) one of the scenario runs for 2060 - 2069.

rather small for the period 2000 - 2040, with a strong decrease afterward combined with partial recovery.

In our experiments, the abrupt change in sea ice volume / area behavior coincides with the changes in 2 m temperature as well as changes in mean sea level pressure. One explanation might be, that the *unstable* mean sea level pressure field changes the frequency, intensity and pathways of low pressure cells arriving from the Pacific into high latitudes. This is probably caused by the changes in winter sea ice area and the corresponding heat release from the Arctic Ocean to the cold atmosphere, leading to a lower than usual sea level pressure and again to changes in sea ice (Chapman and Walsh 2007).

Some changes, however, especially in winter, occur in the region of Barents Sea and

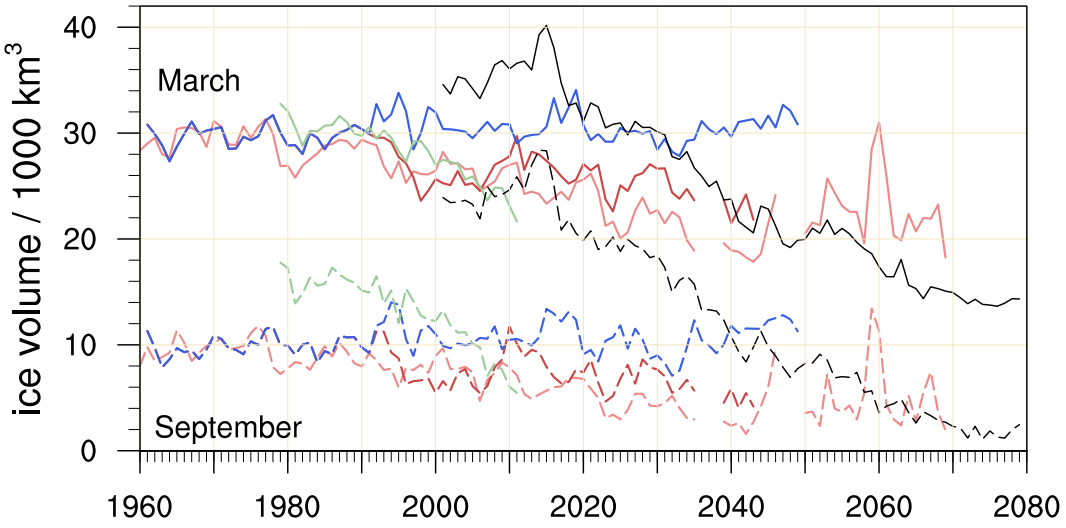

Figure 5.14: March and September sea ice volume from the scenario experiments (in red), the control run (in blue), from the global experiment (in black) and from PIOMAS data (in green). The solid lines represent March values and the dashed lines represent September values.

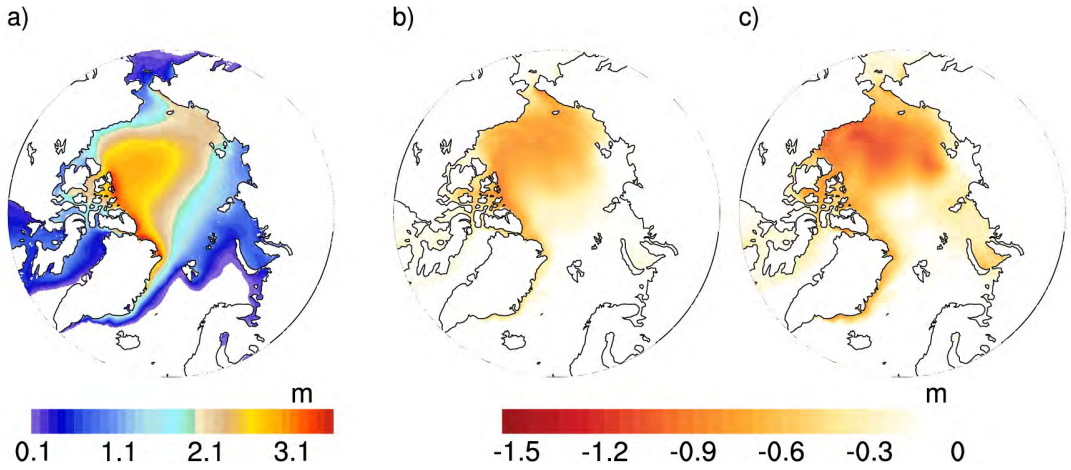

Figure 5.15: Sea ice thickness from a) the mean of the control experiment, and the difference between the scenario experiments and the control run for b) the years 2020 - 2029, and c) the years 2060 - 2069.

north of Svalbard. As discussed already shortly in Section 5.1, the reduced convection in GIN Sea leads to a recovery of sea ice in that region (see 5.3 for changes in deep-water formation). This can partly explain the decrease in the downward trend of sea ice volume / area.

FW storage within the Arctic Ocean The leading EOF from 5 years running mean FW content in the Arctic is characterized by a positive anomaly along the northeastern coast of Greenland, in Lincoln Sea and in large parts of the Canada Basin reaching Beaufort Sea, and a negative anomaly around the North Pole (Figure 5.16). This EOF explains about 37.2 % of the total variance of the FW content. The corresponding PC time series from the scenario experiments show a continuously positive trend starting before 2010, which leads to an accumulation of FW in Lincoln Sea, north of the Canadian archipelago and in Beaufort Sea (Figure 5.17). As can be seen in Figure 5.18, the FW is partly shifted from the Central Arctic Ocean to that region. Additionally, the FW content increases slowly but steadily in the 21st century, by about 17 % for 2020 - 2029 compared to the control run and by more than 45 % in 2060 - 2069. This increase is primarily caused by the increase in FW input from precipitation minus evaporation and by the increase in runoff (Figure 5.11 a)).

The only small changes in Beaufort Sea and along the Siberian coast might partly be explained by a compensation of the increased net FW input by increased export through Fram Strait. In contrast, the change in liquid FW transport through the Canadian archipelago remains small leading to the accumulation of the increased net FW input along the North American coast.

The spatial distribution of the accumulated FW within the Arctic Ocean is very similar in global experiments from ECHAM 5 / MPIOM (Koenigk et al. 2007) and comes along with changes in the general circulation within the Arctic Ocean. The Beaufort Gyre,

present in the control run, weakens steadily and is fully absent in 2060 - 2069 (Figure 5.19). While FW is trapped within a strong Beaufort Gyre, its reduction might lead to an increase in FW export instead of further accumulation of FW within the Arctic Ocean in the second half of the century.

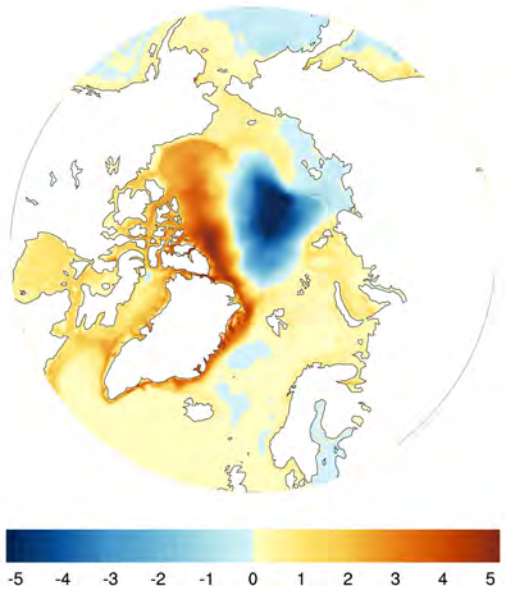

Figure 5.16: Leading EOF of yearly mean FW content. 5 years running mean values are used for calculation.

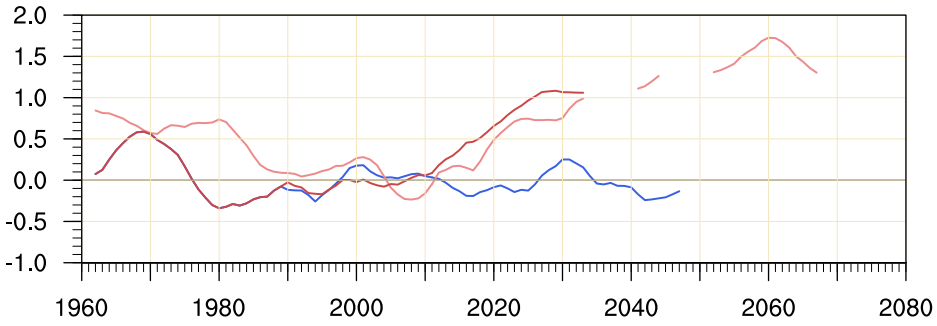

Figure 5.17: Principal component of the leading EOF for 5 years running mean FW content. The control experiment is shown in blue, the scenario experiments in red.

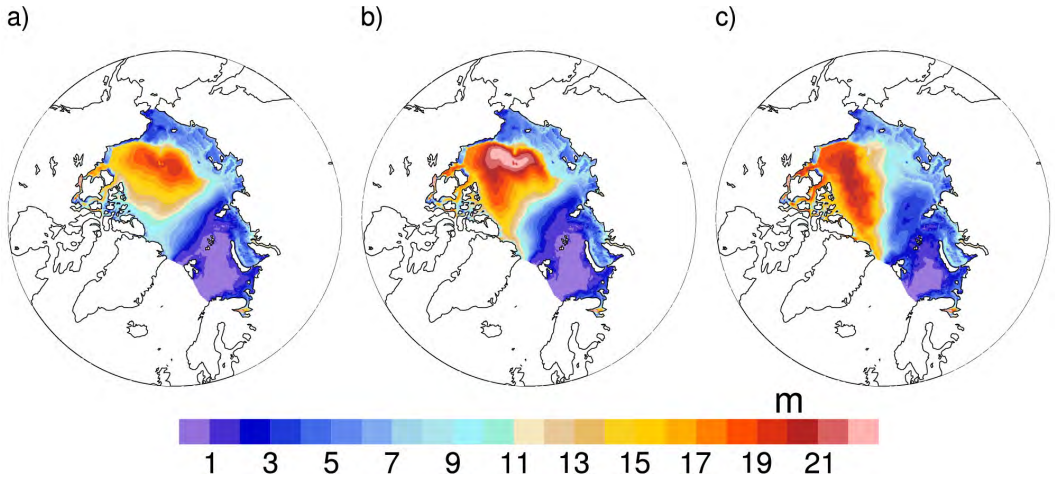

Figure 5.18: Liquid FW content in m from a) the control run, b) the ensemble mean for 2020 - 2029 and c) from one scenario experiment for 2060 - 2069.

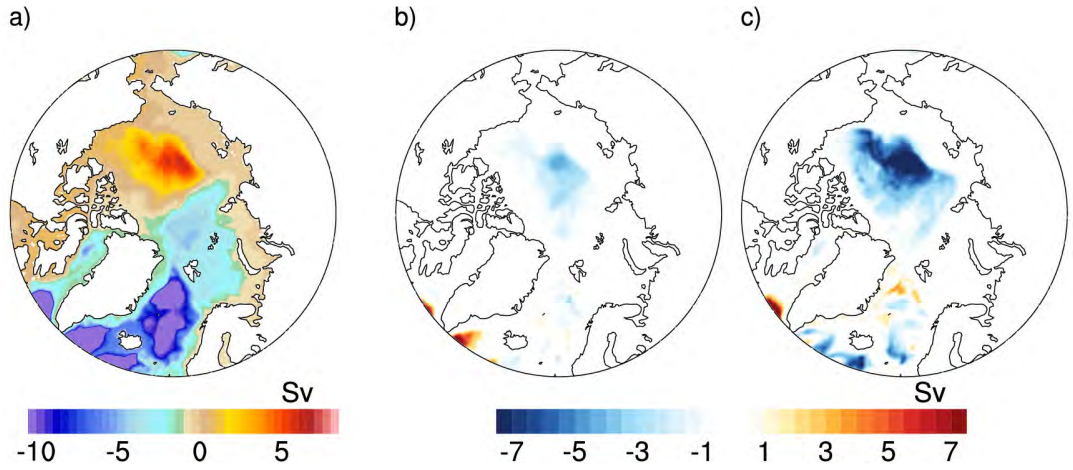

Figure 5.19: a) Mean barotropic stream function in Sv from the control run. Difference of the barotropic stream function of the scenario experiments and the control run for b) the years 2020 - 2029 and c) the years 2060 - 2069.

Salinity and temperature The change in the ocean circulation, the weakening of the Beaufort Gyre, might not only be caused by changes in the surface winds, but also by changes in the water mass properties. Figure 5.20 represents the vertical temperature and salinity profiles of areal mean values of the different Arctic basins (as defined in Figure 2.2). The mean of the control run is given in blue, the ensemble mean of the scenario experiments for the years 2020 - 2029 is given in dark red and the scenario experiment for the years 2060 - 2969 is given in light red. A warming in all basins can be seen. The warm Atlantic derived waters enter through GIN Sea and Barents Sea the Arctic Ocean, resulting in a stronger thermocline within the Arctic basin. The water reaches nearly 1 °Celsius in a depth of 400 - 500 m in 2060 - 2069, which is about 1.5 °Celsius warmer than in the control run. As seen already in Chapter 3, Figure 3.5, the modeled thermocline in the Arctic Ocean for the 20th century is too small compared to observations. The thermocline for 2060 - 2069 slightly exceeds today's observations. Further warming of this Atlantic layer might lead to increased ice melting from below the ice. Changes in the vertical salinity profile are rather small, especially in the Arctic basin. The strong halocline does not change in the yearly mean values between 2020 - 2029 and 2060 - 2069 and remains in a slightly steeper shape than the control run, indicating a freshening of the surface with the saline Atlantic water below. A fresher surface layer can be seen in all basins and is caused by the increased net FW input.

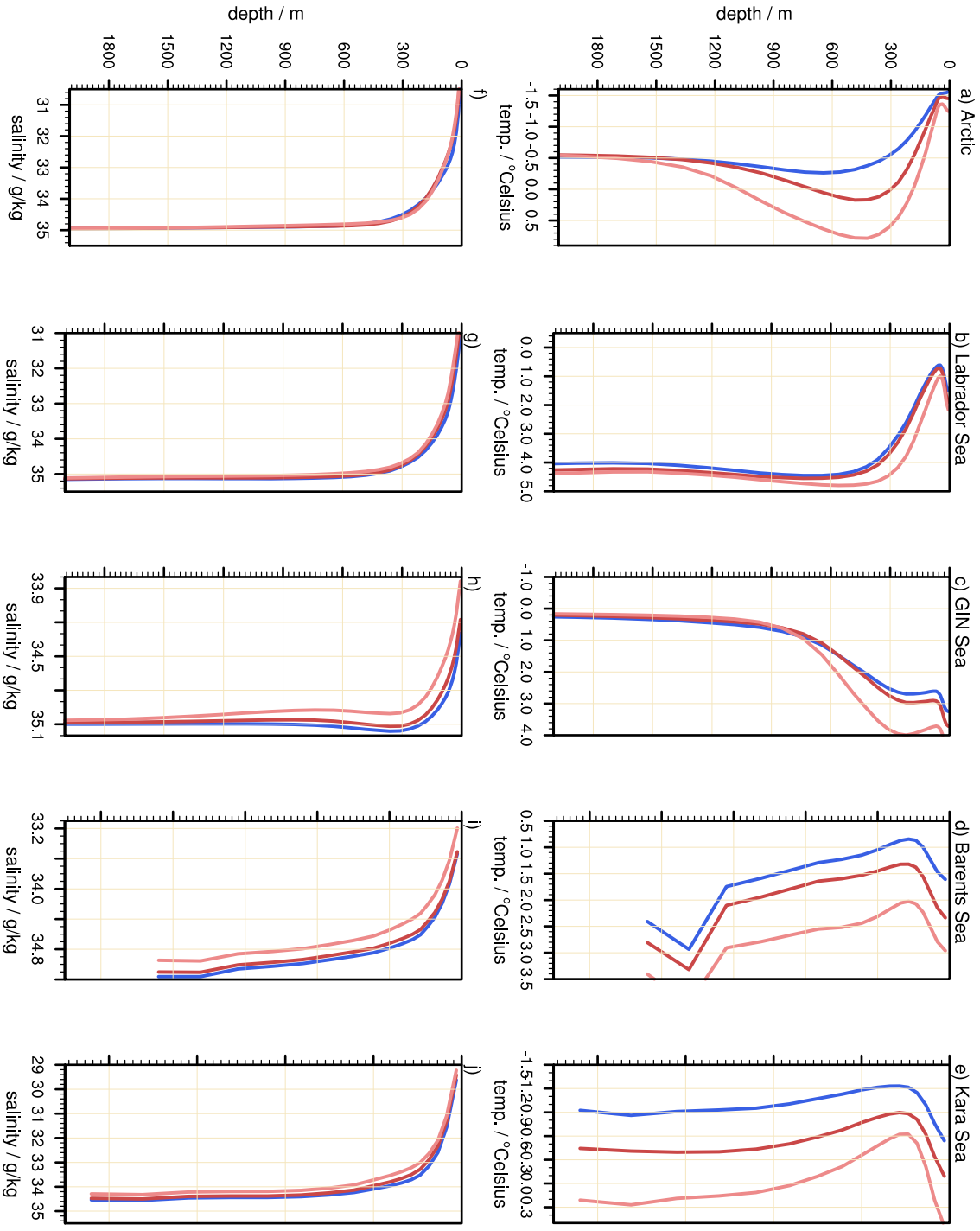

Figure 5.20: Temperature (a)-e)) and salinity (f)-j)) profiles from the control run (in blue), the scenario runs for the years 2020 - 2029 (in dark red) and for the years 2060 - 2069 (in light red). The domains used for these profiles are defined in Figure 2.2 b).

Fram Strait ice and liquid FW export In the 20th century, the amount of FW transported in solid form through Fram Strait exceeds the amount of FW exported in liquid form in all experiments (Figure 5.21). Compared to the control run the ice transport decreases by only 2 % in 2020 - 2029, while the liquid FW transport increases by more than 35 % in the same time period (Table 5.1). The liquid ratio dominates the total FW transport in one experiment from the end of the 20th century already, and in the second experiment from 2010. This experiment, however, does not show a clear trend, neither in the liquid nor in the solid FW transport through the strait.

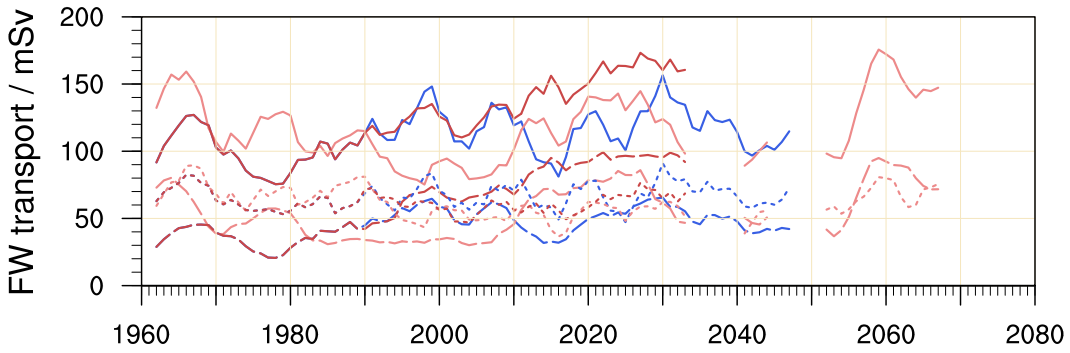

Figure 5.21: 5 years running mean from total FW transport (solid lines), liquid (long dashed lines) and solid (small dashed lines) FW transport through Fram Strait. The control run is given in blue and the scenario runs in red.

Regarding the total time span, Fram Strait total FW transport shows large variability, with a positive trend from 1980 - 2030 in one of the scenario experiments (Figure 5.21, dark red line), but without a clear trend in the second experiment. As seen in the sea ice behavior, the general climatic situation changes around 2040 and so does the export. With increasing ice north of Svalbard, the ice export through Fram Strait increases again. For instance the maximum in sea ice volume at the end of the 2050s (Figure 5.14) is followed by increased ice export through Fram Strait. This can even be seen in the 5 years running mean values of sea ice transport through the strait in Figure 5.21.

As can be seen in Figure 5.22 b), the overall increase in the FW transport through the strait at the beginning of the 21st century is governed by an increase in advection of the salinity anomaly by the mean flow (in orange). The freshening of the Arctic surface water leads to an increase of the term $\mathbf{s}' = \left(\frac{s_{ref}-s}{s_{ref}}\right)'$ and thus to an increase in the transport of the mean flow multiplied by this (increased) salinity anomaly. The abrupt change in the difference between the total and the mean FW flux (in green) before 2040, however, is not driven anymore by changes in this term, but by a decrease in the advection of the mean salinity by the volume flux anomaly (in blue) as well as by a decrease in the transport of the salinity anomaly by the anomalous volume flow (in red). This indicates a change in the circulation within the Arctic Ocean, with less export through the strait than before. The disappearance of the Beaufort Gyre (Figure 5.19 c)) supports the hypothesis of a general change from the transpolar drift through Fram Strait to a transport from the Siberian coast to the Canadian archipelago. Since the second scenario experiment (Figure 5.22 c))

does not show a similar behavior in these years it might be also an increasing variability caused by the freshening.

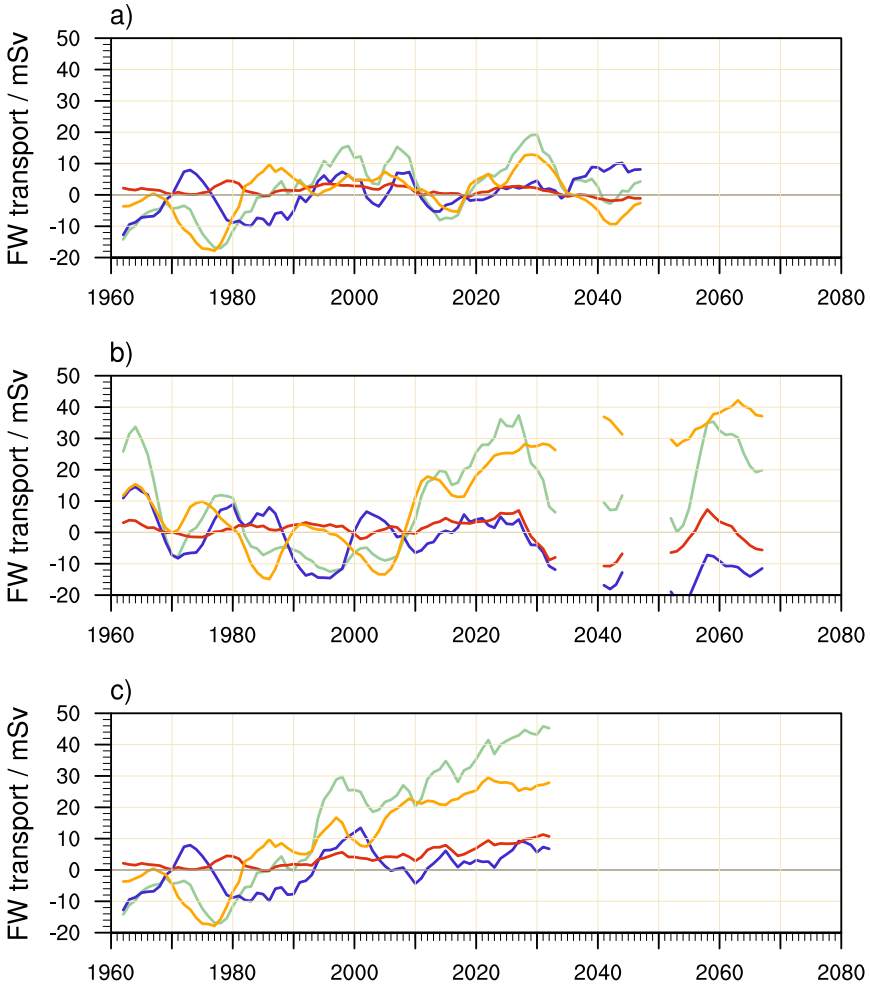

Figure 5.22: 5 years running mean values in mSv from liquid FW transport through Fram Strait for a) the control run, b) and c) scenario runs. The anomalies are calculated with respect to the control run. Color coding is the same as in Chapter 4; referred to equation 4.2 there is $F_{FW} - \int_A \bar{\mathbf{s}}\,\overline{\mathbf{v}_\perp}$, the difference between the total and the mean FW flux, in green, $\int_A \mathbf{v}'_\perp \bar{\mathbf{s}}$, the advection of the mean salinity by the volume flux anomaly, in blue, $\int_A \mathbf{s}'\overline{\mathbf{v}_\perp}$, the advection of the salinity anomaly by the mean flow, in orange, and $\int_A \mathbf{s}'\mathbf{v}'_\perp$, the adection of the salinity anomaly by the anomalous volume flow, in red.

Canadian Arctic archipelago ice and liquid FW export There is no clear trend in the total FW transport trough the Canadian archipelago (Figure 5.23). The anyway small amount of FW transported in solid form decreases with time to about 70 % compared to the control run in 2020 - 2029 and 60 % compared to the control run in 2060 - 2069 (Table 5.1 and Table 5.2). The FW transport through the Canadian archipelago is governed by the total volume transport, which does not change strongly in our scenario experiments. Even though the freshening of the Arctic leads as in Fram Strait to an increase of the advection

of the salinity anomaly by the mean flow, the changes in the liquid FW transport are negligible. The increase in liquid FW export, starting at the beginning of the 2060s, might be a first response on the changing climate, but the experiments were run too short to see a clear signal. Comparable simulations with the global model ECHAM 5/ MPIOM also show a clear trend only in the second half of the 21st century (see Figure 6 d) in the article from Koenigk et al. (2007)).

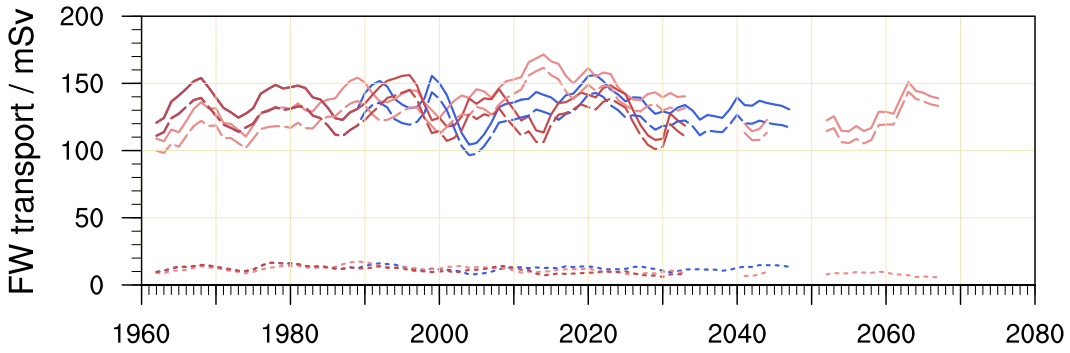

Figure 5.23: 5 years running mean from total FW transport (solid lines), liquid (long dashed lines) and solid (small dashed lines) FW transport through the Canadian Arctic archipelago. The control run is given in blue and the scenario runs in red.

5.3 Influence of Arctic freshening and global warming on the global ocean circulation

Changing FW exports from the Arctic have an influence on the deep-water formation in the North Atlantic, since convective mixing is very sensitive to changes in the FW balance. Häkkinen (1999) performed model simulations of an idealized *Great Salinity Anomaly* and showed, that short pulses of increased FW through Fram Strait can disrupt the deep water formation in Labrador Sea, resulting in a reduction of the overturning cell. Haak et al. (2003), using a global sea ice - ocean model, and Mikolajewicz et al. (2005), using a regional coupled model, came to a similar result. The export of FW through the Canadian archipelago seems to play a minor role in the influence of the deep-water formation in Labrador Sea. But not only fresher, also warmer water export from the Arctic has the potential to reduce the Denmark Strait overflow transport and thus affect the deep-water formation in Labrador Sea (Karcher et al. 2011). Dodd et al. (2009) conclude from their tracer study, that the phase of freshwater, rather than its origin, exiting through Fram Strait is important. While sea ice is mostly diverted into the Nordic Seas, the liquid FW is transported within the East Greenland current to Labrador Sea influencing the Labrador Sea deep-water formation. Thus a transition from the FW exported through Fram Strait from sea ice into liquid FW leads to a decrease in the mixed layer depth in Labrador Sea. Previous studies with coupled global models come to a similar result; convection in Labrador Sea is more sensitive than convection in Greenland Sea (Koenigk et al. 2007; Holland et al. 2006).

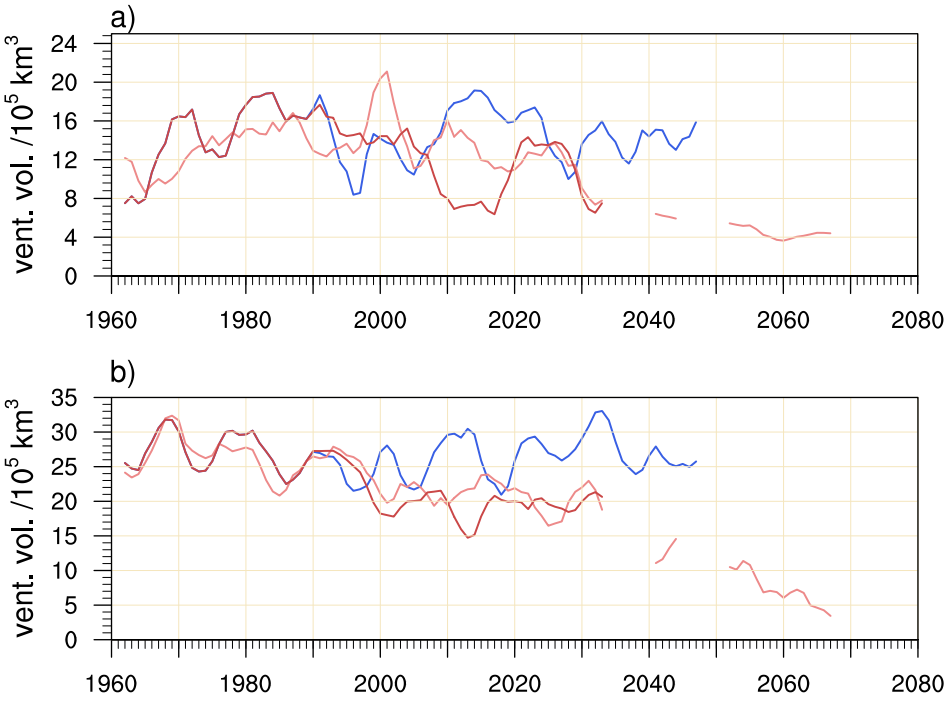

Figure 5.24: 5 years running mean mixed layer depth in February multiplied by the area in a) Labrador Sea and b) GIN Sea. The domain used for calculation is marked in Figure 2.2. The control experiment is shown in blue, the scenario experiments in red.

As the results from the global model ECHAM 5 / MPIOM, our regional setup shows a clear decrease in the volume of ventilated water in GIN Sea as well as in Labrador Sea (Figure 5.24). The fluctuations in the mixed layer depth in Labrador Sea, however, are large, in the control run as well as in the scenario experiments. The two scenario experiments show indeed a negative trend, but they remain in a range only a bit below that from the 20th century (and control run) variability for the first decades of the 21st century. Nevertheless, a clear downward trend can be seen from about 2030 onward. After 2060 the mixed layer depth is not changing anymore and remains on a strongly reduced level. Our model experiment is unfortunately too short to be able to distinguish between a possible stabilization at that level or natural variability and a continuation of the downward trend after a few years. The downward trend in one of the scenario experiments, presented in light red in Figure 5.24 a), as well as the first decline in the second experiment, presented in dark red, are rather due to a strong temperature increase of the ocean surface in that region than due to an increase in FW at the surface. But the reason for convection seems to change within time, starting in about 2020 the surface water becomes substantially fresher, reducing the density of the ocean surface and consequently the convection. As can be seen in Figure 5.6, net precipitation strongly increases within time, especially in that region. In these decades net precipitation is the main source for the fresh water at the surface, rather than increased FW export through the Canadian archipelago and Fram Strait, even if this is most probable to change at the end of the 21st century.

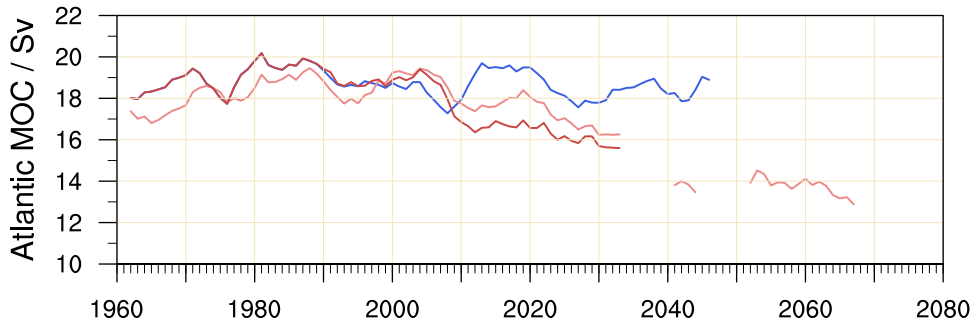

Figure 5.25: Atlantic meridional overturning circulation timeseries in Sv. The control experiment is shown in blue, the scenario experiments in red.

The behavior in GIN Sea looks similar as in Labrador Sea (Figure 5.24 b)); both scenario experiments show a reduced mixed layer depth from the beginning of the 21st century, remaining at the same level for about three decades. Starting after 2030 a clear downward trend can be seen, which is still ongoing at the end of our simulations. The reason for the reduction is different than in Labrador Sea; the 2 m temperature in February rose by more than 2 °Celsius around 2035 over GIN Sea, compared to the control run, leading to a reduction in the convection. These changes in GIN Sea, however, do not yet affect the strength of the Denmark Strait overflow. Our model does not show a trend in the overflow, calculated as the water masses transported below 300 m through Denmark Strait, with a mean value of about 2.6 Sv and an interannual standard deviation of 0.15 Sv. Further investigations would be needed to analyze potential changes in the water mass properties of the overflow waters and their influence on the Atlantic MOC. Latarius (2013) used hydrographic measurements from profiling floats to analyze the water mass transformations (from warm and saline into cold and relatively fresh waters) in the Nordic Seas in the first decade of the 21st century. She showed that within the Nordic Seas the contribution from the eastern basins is most important for the water mass transformation, while increased freshwater particularly influences the transformation in the western part. She concludes that an additional freshening due to climate change might lead to changes in temperature and salinity properties in the overflow waters, and thus to a decrease of the Atlantic MOC.

Our model results also show, that these changes in deep-water formation in GIN as well as in Labrador Sea, as being part of the global thermohaline circulation, affect the Atlantic meridional overturning circulation. Figure 5.26 shows the mean overturning circulation in the Atlantic for the control run. Values larger than 18 Sv can be seen; Figure 5.25 shows 5 years running mean values at the location marked in Figure 5.26. The difference between the scenario experiments and the control run for the years 2020 - 2029 and 2060 - 2069 is shown in Figure 5.27. As can be seen, the overturning cell reduces strongly, especially in the latter time slice. In our scenario experiments, the Atlantic MOC is reduced by about 1.2 Sv (7 %) in 2020 - 2029 and by nearly 5 Sv (26 %) in 2060 - 2069, compared to approximately 18.2 Sv of the control run (Figure 5.25). Schmittner et al. (2005) perform a multi-model ensemble analysis of global general circulation models using the A1B scenario

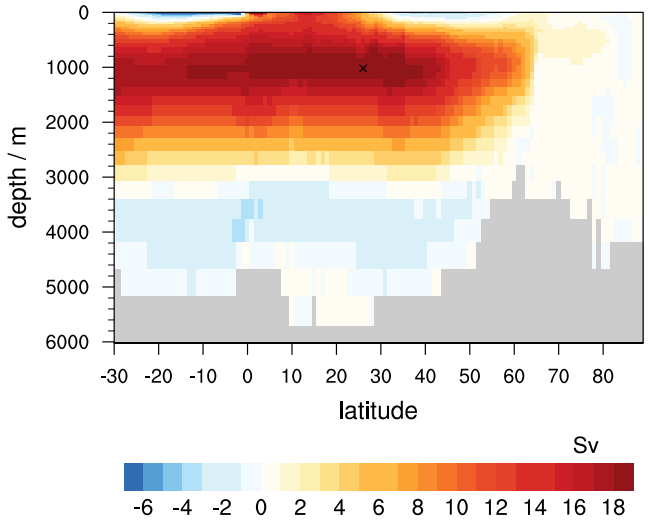

Figure 5.26: Mean Atlantic meridional overturning circulation in Sv from the control experiment.

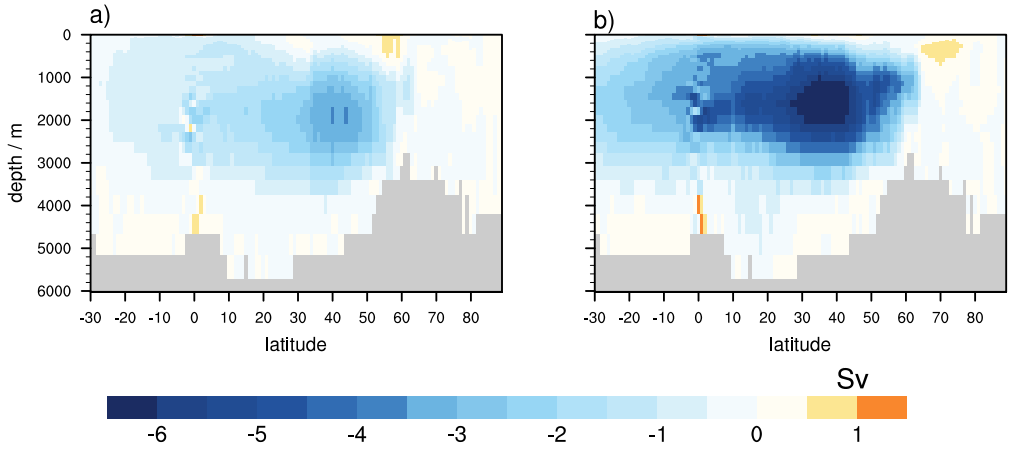

Figure 5.27: Difference between the Atlantic meridional overturning circulation in Sv from the scenario experiments and the control experiment in a) the years 2020 - 2029 and b) the years 2060 - 2069.

and predict a reduction of about 25 % at the end of the 21st century. This agrees well with our result, even though at the end of the century, the reduction in the Atlantic MOC in our model might be somewhat stronger. A complete shutdown until the end of the 21st century, however, of the Atlantic MOC is, as in most of the global models as well, very unlikely in our experiments.

5.4 Summary and conclusion

Changes in FW fluxes

We have discussed in the previous sections the changes in the FW fluxes of the Arctic Ocean. To summarize, we show in this section the changes in the distinct FW terms for

two time slices, 2020 - 2029 and 2060 - 2069. The hydrologic cycle intensifies in nearly all terms. Our model simulates an overall warming and an overall increase in net precipitation. Beside the mean moisture transport, also the cyclone summer activity over Europe strongly increases, resulting in increased river runoff into the Arctic Ocean. As shown in Table 5.1, the total FW input from the atmosphere and from land in 2020 - 2029 is, with approximately 212 mSv, enhanced by about 8 % compared to the control run. The increase of precipitation minus evaporation over the Arctic Ocean is with 4.5 % smaller than the increase of river runoff draining into the Arctic Ocean (increase of 10 %). The precipitation over land, especially over Europe, increases more strongly than over the Arctic Ocean itself. Additionally, the standard deviation of annual total FW input is nearly three times as large as in the control run. The total net FW input in 2060 - 2069 is even more than 18 % larger in the scenario experiment than in the control run and the standard deviation increases further. This indicates that wetter as well as dryer than usual years with only little runoff alternate more frequently.

The increased FW input leads to an overall surface freshening of the Arctic Ocean and the additional FW is mostly stored within the Arctic Ocean. The variability increases strongly in 2060 - 2069 compared to 2020 - 2029, in the FW content stored in solid as well as in liquid form. The amount of stored FW within the Arctic Ocean in liquid form in 2060 - 2069 is (with 56035 km^3) more than 45 % larger than the control run. Because the strength of the Beaufort Gyre strongly decreases within the 21st century, the FW is not trapped within the gyre anymore, but most of the FW is accumulated north of the Canadian archipelago. Nevertheless, we have seen in Section 5.2, that the changes in the FW export through the Canadian Arctic archipelago are rather small in the 21st century until the end of our experiments. The decrease in ice export can be seen in both time slices, while there is no signal in the transport of liquid FW through the strait. Changes can be expected in the second half of the century, as the FW in the Arctic Ocean accumulates north of the archipelago. Additionally, we know from the global experiments that the ocean model tends to accumulate the FW in the first half of the century, but shows a strong increase of liquid FW export through the archipelago in the second half (Koenigk et al. 2007).

The sea ice reduction is relatively small, compared to the underlying global model run. This might be caused by highly overestimated values from the global model at the beginning of the 21st century. The Arctic has not reached an ice - free state ($< 1000000\,km^2$) in September at the end of 2060s, neither in our nor in the global model. After 2040, the sea ice does even show reductions followed by fast recoveries reaching present day ice volume. This seems to be a property of high resolution models and can be seen in other regional models as well; the rapid ice loss is mostly driven by changes in the atmospheric circulation (Döscher and Koenigk 2013).

The new generation of the MPI global model, MPI-ESM, as well as most other models of the CMIP 5 initiative, however, show large improvements in reproducing observed trends in sea ice extent compared to the preceding models used for the CMIP 3 experiments (even though having comparably low resolution) (Stroeve et al. 2012). Notz et al. (2013) show that not only the sea ice distribution but also the trend and variability in sea ice coverage

2020 - 2029	ctrl	scenario	scenario - ctrl
(P-E)+runoff	65.85 + 129.08	68.81 + 143.13	
	= 194.93 (±3.44)	= 211.94 (±10.33)	17.01
Bering Strait	74.16 (±12.53)	80.85 (±16.69)	6.69
Barents Sea	−6.13 (±6.40)	−3.59 (±4.74)	2.54
Fram Strait liquid	−57.54 (±8.50)	−89.77 (±7.46)	−32.23
Fram Strait ice	−67.17 (±23.0)	−65.96 (±12.35)	1.21
CAA liquid	−132.79 (±13.62)	−131.39 (±16.46)	1.40
CAA ice	−12.79 (±1.83)	−8.87 (±2.00)	3.92
FW content liquid	41681 (±1769)	49510 (±1724)	7829
FW content ice	13082 (±1059)	10194 (±908)	−2888
$\sum$ transports	−7.33	−6.79	

Table 5.1: Mean values in mSv of the FW transports in the Arctic for the years 2020 - 2029. Displayed in brackets are ± one standard deviation of the yearly values. FW content is given in km^3.

2060 - 2069	ctrl	scenario	scenario - ctrl
(P-E)+runoff	64.54 + 131.14	77.21 + 153.77	
	= 195.68 (±5.20)	230.98 (±13.65)	35.30
Bering Strait	78.80 (±23.18)	90.53 (±18.08)	11.73
Barents Sea	−11.01 (±4.01)	−2.33 (±7.43)	8.68
Fram Strait liquid	−55.56 (±12.87)	−80.51 (±19.7)	−24.95
Fram Strait ice	−80.28 (±28.0)	−70.78 (±21.0)	9.50
CAA liquid	−114.87 (±16.29)	−132.49 (±17.48)	−17.62
CAA ice	−11.17 (±3.19)	−6.70 (±1.76)	4.47
FW content liquid	37941 (±1727)	56035 (±5064)	18094
FW content ice	12973 (±947)	9198 (±2061)	−3775
$\sum$ transports	1.59	28.7	

Table 5.2: Mean values in mSv of the FW transports in the Arctic for the years 2060 - 2069. Displayed in brackets are ± one standard deviation of the yearly values. FW content is given in km^3.

simulated by MPI-ESM improved compared to the preceding version ECHAM 5/ MPIOM, that is used in our experiments as forcing. Further investigations in comparing the variability in sea ice variables as simulated by MPI-ESM and by our model setup would be needed to explain the role of high resolution in simulating the variability in sea ice volume.

The large sea ice reductions and recoveries in our simulations result in large Fram Strait ice export events. Nevertheless, FW export in liquid form most often leads the FW transport through the strait in the 21st century and shows a clear positive trend. The total FW transport through the strait increases by nearly 25 % compared to the control run

in 2020 - 2029. The fast sea ice recovery events lead to an enhanced standard deviation of sea ice transport through the strait, that is of similar size as in the control run. The variability of the transport of FW in liquid form also increases strongly, being nearly twice as large as in the control run in 2060 - 2069.

A considerably change can be seen also in the import of saline water from the North Atlantic into Barents Sea. The water entering Barents Sea becomes fresher with time and thus the FW sink becomes smaller. The total volume transport from the North Atlantic does not show any trend and alternates around 2.5 Sv in all of the runs. Caused by decreased convection in GIN Sea, the FW input, more precisely the inflow of saline water into Barents Sea, becomes less and turns even to positive values in some years. This means, that the inflow is fresher than the reference salinity. Again, the standard deviation is large. These changes in deep-water formation in GIN Sea as well as the changes in Labrador Sea lead to a decrease of the Atlantic MOC by about 26 % in 2060 - 2069.

Concluding remark

To our knowledge, this is a first study about changes in the Arctic hydrologic cycle in the 21st century with a high-resolution model that calculates all of its components internally. Our results are promising, even if we could not finish the whole century. Compared to global model results, our model shows higher variability in the FW components, especially in the sea ice behavior. Better understanding between the interaction of atmosphere, sea ice and ocean is crucial to explain these ongoing changes and our model setup is a reliable tool for further investigations.

Chapter 6

Conclusions and outlook

To analyze the variability of the Arctic hydrologic cycle induced by dominant modes of large-scale atmospheric variability we performed simulations with a newly built regional coupled model setup, consisting of the global ocean model MPIOM, the regional atmosphere model REMO and the hydrological discharge model HD.

We have shown that our model setup is able to reproduce a reasonable mean climate of the Arctic for the second half of the 20^{th} century. Our model results from experiments with NCEP reanalysis forcing as well as with forcing from a global model experiment (ECHAM 5 / MPIOM) are in good agreement with observations. To our best knowledge, it is the first fully coupled model with high resolution that allows for the analysis of a closed Arctic hydrologic cycle. Our model is run without any salinity or freshwater (FW) flux restoring in the Central Arctic and includes all FW sinks and sources.

6.1 Answers to the research questions

We can now answer our research questions raised in Section 1.3:

- How do atmospheric leading modes influence the variability of the Arctic hydrologic cycle?

Atmospheric phenomena are a main driver of Arctic climate variability. The leading empirical orthogonal function (EOF) of winter mean sea level pressure, which is related to the Arctic Oscillation, leads in its positive phase to increased westerly winds transporting more moisture than usual over the North Atlantic into Eurasia. This leads to warmer and wetter conditions in Northern Europe and Russia. In the positive phase, the ocean circulation in the Arctic is characterized by a strong transpolar drift enhancing the export of FW through Fram Strait and through the Canadian archipelago. In contrast, an enhanced Beaufort Gyre in the negative phase leads to a decrease in FW export and to an accumulation of FW within the Arctic Ocean.

In our model, the second leading EOF of winter mean sea level pressure is characterized by a tripole pattern, with a strong Aleutian low and a second low over Northern Europe and a positive pole over the Central Arctic, indicating a weaker than usual Icelandic low in the positive phase. This leads to higher than usual winter temperatures over southern Europe as well as over North America. Changes in precipitation, however, are mostly restricted to Europe. In the Arctic Ocean the response on the second EOF is large. In

the positive phase a strong gyre, being similar as in the negative phase of the first leading EOF, retains sea ice as well as liquid FW within the Arctic. Consequently, the FW export is reduced, especially in liquid form. In the negative phase of the second leading EOF the winds push the sea ice to the Canadian archipelago and the export in liquid as well as in solid form is stronger than usual through the archipelago and through Fram Strait.

The variability caused by the North Atlantic Oscillation (NAO) agrees well with previous studies. We find largest precipitation changes in Norwegian-Greenland Seas and over Scandinavia. The response of NAO largely resembles the response of the leading EOF. A strong transpolar drift from Siberia to the Canadian coast can be seen in the positive phase leading to an increased export of FW through the archipelago. In the negative phase of the NAO the FW is retained again in the anticyclonic gyre circulation within the Arctic Ocean.

A stronger than usual Siberian high leads to changes over large parts of the Eurasian continent as well as over the Arctic Ocean. As in the negative phase of the leading EOF, the continent is colder and dryer than usual, reducing the Eurasian river runoff. A strong Beaufort Gyre leads again to reduced FW exports through Fram Strait and the Canadian archipelago. The impact of a weaker than usual Siberian high, however, is rather small.

- What drives the variability in Arctic river runoff?

The variability of Arctic river runoff is dominated by the variability of runoff from Eurasia into the Arctic Ocean. In winter before increased Eurasian runoff, the Icelandic low is anomalously strong, redirecting the moisture and heat arriving from the North Atlantic northward into Siberia. Increased precipitation in late spring and summer, caused by enhanced cyclone activity, lead to increased Eurasian runoff during the melting season. Changes in the Aleutian low at the beginning of the year with enhanced runoff from the North American continent lead to enhanced moisture and heat transport from the North Pacific to North America. Precipitation is enhanced due to increased cyclone activity in summer, but changes in North American runoff are small compared to the variability of Eurasian runoff.

- How do the components of the Arctic freshwater cycle change in the 21st century?

The Arctic hydrologic cycle intensifies in nearly all components in our model. An overall warming accompanied by an overall increase in net precipitation is projected. Not only the mean moisture transport but also the cyclone intensity enhances, resulting in increased Eurasian river runoff. This leads to an increase in the net FW input from the atmosphere and from land of about 18 % in 2060 - 2069 compared to the control experiment. Most of this additional FW remains within the Arctic Ocean and is stored north of the Canadian archipelago, leading to an overall increase of the amount of FW stored within the Arctic Ocean. The total FW transport through Fram Strait and through the Canadian archipelago increases (by more than 10 % in 2060 - 2069) and so does the variability. Fast reductions in sea ice after large recoveries lead to large ice export events through Fram Strait. Nevertheless, the overall FW export through Fram Strait is mostly led by liquid

FW export and increases already by about 25 % in 2020 - 2029 compared to the control run. Even though the Beaufort Gyre strongly weakens over time, the FW export through the archipelago does not show a clear trend. The inflowing water into Barents Sea becomes fresher, caused by decreased convection in GIN Sea. Thereby, the fresher inflow becomes a smaller sink for the Arctic FW budget than before.

- How do changes in the freshwater cycle affect the global ocean circulation?

Our model shows a large variability in the convection depth in GIN as well as in Labrador Sea. Nevertheless, a reduction in the volume of ventilated water can clearly be seen. In Labrador Sea, the mixed layer depth is only slightly reduced in the first three decades of the 21st century, but shows a clear decreasing trend afterward. While at the beginning of the century the reason for the reduction is a strong temperature increase of the ocean surface, after 2020 increased FW input by enhanced net precipitation seems to be the cause for the decrease in convection. In GIN Sea, the downward trend in deep-water formation looks similar as in Labrador Sea, showing a stronger reduction after 2030 than before. The surface temperature over GIN Sea increases by more than 2 °Celsius around 2035, leading to the reduction in convection. The changes in GIN Sea, however, do not yet affect the strength of the Denmark Strait overflow. Being part of the global thermohaline circulation, the reduced convection in GIN and in Labrador Sea lead to a reduction in the Atlantic meridional overturning circulation. Compared to the control run with about 18 Sv the Atlantic MOC is reduced by nearly 5 Sv at the end of our simulations.

6.2 Research perspectives

Our scenario experiments for the 21st were not run until the end of the century. After 2040, the variability of the FW fluxes strongly increases. It would be interesting to continue our experiments and further investigate the interplay between the rapidly changing atmospheric components and the ocean, where we detected large changes in sea ice volume. As we have seen a strong decrease in the Beaufort Gyre circulation in our experiments, but no strong positive trend in FW export, it remains unclear how the Arctic Ocean reacts on this freshening and how the Arctic Ocean circulation changes in the second half of the 21st century. Additionally, the changes in the formation of deep water in GIN Sea must sooner or later lead to changes in the exchange of waters between GIN Sea and the North Atlantic. Further investigations in the response of the Denmark Strait overflow on reduced convection in GIN Sea might explain further changes in the meridional overturning circulation in the Atlantic.

Sein and Sudarchikova (2013) investigate the importance of the domain of the coupled atmosphere - ocean model in regionally coupled models similar to ours. They compare several setups with the same ocean model configuration with high horizontal resolution in the Arctic coupled to different configurations of the regional atmosphere model. The atmosphere model always covers the Central Arctic region, but differs in the extent southward into different regions. Large differences can be seen, for instance, in the leading

EOF of winter mean sea level pressure depending on the location of the atmosphere model domain. In our model setup, the influence of the atmospheric large scale circulation over the Pacific is fully prescribed by the forcing fields. Thus the strength of the Aleutian low strongly depends on the underlying forcing. It would be interesting to perform experiments with a setup covering a larger region of the Pacific and compare these results with our experiments presented in this study. Differences in the prescribed versus modelled variability of the Aleutian low could give more insight in the internal model variability, especially of North American FW components. We have seen that changes in the moisture transport over the Pacific have large influence on North American runoff. When covering more of the Pacific region with the coupled model, one could study the development and evolution of these cyclones in more detail.

Since the experiments with new emission scenarios for the Fifth Assessment Report of the Intergovernmental Panel on Climate Change are finished by now, it would be interesting as well, to use this new global model output as forcing for our coupled model setup. As we have seen, our model domain is large enough to develop large variability internally. Assuming to have enough computing resources, it would be reasonable to come up with more ensemble members than we had so far to better quantify by how much the results depend on the internal variability of the model.

6.3 Concluding remark

This study provides the analysis of a closed freshwater cycle of the Arctic for the 20^{th} and for the 21^{st} century. Our model setup is to our knowledge the only high-resolution model that includes all FW sources. The atmosphere model covers the catchment areas of the Arctic rivers and the included hydrological discharge model provides the lateral terrestrial waterflows calculated within the model. Our method of using a freshwater climatology, set to zero in the Central Arctic, is a promising approach to model the FW budget with a regional model without any artificial term arising from salinity restoring.

Appendix A

Methods

We explain the methods used in this thesis for the analysis of the freshwater cycle. The following sections only give a short overview, but most of the methods are widely discussed in literature. For further reading we refer to von Storch and Zwiers (1999).

A.1 Correlation analysis

The correlation analysis is used to analyze the quality of linear relationship of two random parameters. The correlation coefficient measures the tendency of two random variables $\mathbf{X}$ and $\mathbf{Y}$ to co-vary. The corresponding correlation coefficient is given by

$$\rho_{\mathbf{XY}} = \frac{E\left(\left(\mathbf{X}-\mu_{\mathbf{X}}\right)\left(\mathbf{Y}-\mu_{\mathbf{Y}}\right)\right)}{\sigma_{\mathbf{X}}\sigma_{\mathbf{Y}}} \quad \in [-1,1]\,, \tag{A.1}$$

where $E(\mathbf{U}) = \mu_{\mathbf{U}}$ is the expectation operator of a variable $\mathbf{U}$ and $\sigma_{\mathbf{U}} = \sqrt{Var\left(\mathbf{U}\right)} = \sqrt{E\left(\left(\mathbf{U}-\mu_{\mathbf{U}}\right)^2\right)}$ the standard deviation of $\mathbf{U}$.

If $\mathbf{X}$ and $\mathbf{Y}$ are independent variables, it is $\rho_{\mathbf{XY}} = 0$. The other direction is not necessarily true, $\rho_{\mathbf{XY}} = 0$ does not imply that $\mathbf{X}$ and $\mathbf{Y}$ are independent. The significance of a correlation can be assessed by using a test statistics based on t-distribution if $\mathbf{X}$ and $\mathbf{Y}$ are normally distributed. In this study, we call a correlation coefficient highly significant if the hypothesis that $\mathbf{X}$ and $\mathbf{Y}$ are uncorrelated is rejected at a significance level (α error) of 0.01.

If $\left\{\left(\mathbf{X}_t, \mathbf{Y}_t\right)^T, t = 1, \cdots, n\right\}$ represents a paired sample of the random vector $\left(\mathbf{X}, \mathbf{Y}\right)^T$, an estimator of $\rho_{\mathbf{XY}}$, also called empirical correlation coefficient, is given by

$$\hat{\rho}_{\mathbf{XY}} = \frac{\sum_{t=1}^{n}\left(\mathbf{X}_t - \overline{\mathbf{X}}\right)\left(\mathbf{Y}_t - \overline{\mathbf{Y}}\right)}{\sqrt{\sum_{t=1}^{n}\left(\mathbf{X}_t - \overline{\mathbf{X}}\right)^2 \sum_{t=1}^{n}\left(\mathbf{Y}_t - \overline{\mathbf{Y}}\right)^2}}, \tag{A.2}$$

where $\overline{\mathbf{X}}$ and $\overline{\mathbf{Y}}$ are the mean values of $\mathbf{X}_t$ and $\mathbf{Y}_t$, respectively.

A.2 Linear regression

The linear regression is a simple tool to identify a functional relationship of the form $\mathbf{Y} = a + b\mathbf{X}$ between two variables $\mathbf{X}$ and $\mathbf{Y}$. The assumption for this method is, that for

a paired sample $\left\{(\mathbf{X}_t, \mathbf{Y}_t)^T, t = 1, \cdots, n\right\}$ of the random vector $(\mathbf{X}, \mathbf{Y})^T$ we have

$$\mathbf{Y}_t = a + b\mathbf{X}_t + \epsilon_t, \tag{A.3}$$

with ϵ_t being independent identically normally distributed around 0.

Minimizing the least squared error $\sum_{t=1}^{n} [\mathbf{Y}_t - (a + b\mathbf{X}_t)]^2$ leads to the following approximations for a und b:

$$\tilde{b} = \frac{\sum_{t=1}^{n} \left(\mathbf{X}_t - \overline{\mathbf{X}}\right)\left(\mathbf{Y}_t - \overline{\mathbf{Y}}\right)}{\sum_{t=1}^{n} \left(\mathbf{X}_t - \overline{\mathbf{X}}\right)^2}, \quad \tilde{a} = \overline{\mathbf{Y}} - \tilde{b}\overline{\mathbf{X}}. \tag{A.4}$$

The coefficients $\tilde{a}$ and $\tilde{b}$ are called regression coefficients. To detect the response of one variable on another variable after a certain time, one can calculate lag regressions (and correlations). This is done by shifting one variable $\mathbf{Y}_{t+dt}$ by any time interval dt and then calculating the linear relationship to $\mathbf{X}_t$.

A.3 Composite analysis

The general idea of a composite analysis is to form a set Θ of a specific index $\mathbf{z}_t$ and to estimate the expected value of a specific variable $\mathbf{V} = \mathbf{V}_t$ conditional on the index that is part of the chosen subset, on $\mathbf{z}_t \in \Theta$. The estimate of a composite of $\mathbf{V}$ is given by

$$\mathbf{V}_\Theta = \frac{1}{N} \sum_{j=1}^{N} \mathbf{V}_{t_j}, \tag{A.5}$$

where $t_j = t_1, t_2, \cdots, t_N$ for which $\mathbf{z}_{t_j} \in \Theta$. That means, that N is the sample size meeting the criterion that is used to form Θ.

The basic idea with composites is to calculate typical states of a variable $\mathbf{V}$ given a value of any external index $\mathbf{z}_t$. This is done by estimating the mean state on the value of this external index.

The criterion to choose the subset Θ is arbitrary and depends on the application. Typically, all values for t with $\mathbf{z}_t \geq \sigma_\mathbf{z}$ or $\mathbf{z}_t \leq -\sigma_\mathbf{z}$, with $\sigma_\mathbf{z}$ being the standard deviation of $\mathbf{z}_t$, are used to define Θ. This criterion is also used in this work.

In contrast to a regression analysis the composite analysis has the advantage that it does not make specific assumptions about the link between $\mathbf{z}_t$ and $\mathbf{V}_t$ and thus their relationship can be linear as well as nonlinear. Examples for a composite analysis are, for instance, given in von Storch and Zwiers (1999). To determine whether the signal captured by $\mathbf{z}_t \in \Theta$ is expressed by the mean state of $\mathbf{V}_\Theta$ one can apply the idea of a confidence interval to the pattern $\mathbf{V}_\Theta$. In this study, we therefore calculate the variance $\sigma^2_\mathbf{V}$ of the statistical population $\mathbf{V}$ and formulate, employing the finite population correction, the following criterion:

$$|\mathbf{V}_\Theta - \overline{\mathbf{V}}| > 2\frac{\sigma_\mathbf{V}}{\sqrt{N}}\sqrt{\frac{n-N}{n-1}}, \tag{A.6}$$

beeing n the number of all members of $\mathbf{V}$, N the sample size of $\mathbf{V}_\Theta$, $\overline{\mathbf{V}}$ the mean value of $\mathbf{V}$ and $\sigma_\mathbf{V}$ the standard deviation of $\mathbf{V}$. If the criterion A.6 is fullfilled we call the deviation

of $\mathbf{V}_\Theta$ to $\overline{\mathbf{V}}$ significant; this can be confirmed by assuming the normal distribution for the statistical population and therefore one expect this to be true for less than 5 %.

A.4 EOF analysis

The aim of the analysis of empirical orthogonal functions (EOFs) is to achieve a decomposition of a space - time field $\mathbf{X} = \mathbf{X}(t, s)$, where t and s denote the time and spatial dimension, respectively. The goal is to achieve a new set of variables that capture most of the variance of $\mathbf{X}$. This is done through linear combinations of the original variables:

$$\mathbf{X}(t, s) = \sum_{k=1}^{M} c_k(t)\, u_k(s), \tag{A.7}$$

where M is the number of modes contained in a field, using a set of basis functions of space $u_k(s)$ and expansion functions of time $c_k(t)$. The basis functions, called empirical orthogonal functions, are sorted, so that $u_1(s)$ explains the largest amount of variance and so forth. The coresponding coefficients $c_k(t)$ are called principal component (PC) time series. The EOFs can be obtained by diagonalizing the cross-covariance matrix $\overline{\mathbf{X}}^T\overline{\mathbf{X}}$, with the matrix $\overline{\mathbf{X}}$ containing temporal anomalies of $\mathbf{X}$ in its columns.

The EOF analysis is often used to extract individual modes of variability, such as the Arctic Oscillation, that might be of physical relevance. Most of the variance of $\mathbf{X}$ can often be represented by the first few EOFs. This can lead to a significant reduction of the amount of data while retaining most of its variance. EOFs has been extensively studied in literature, for further details we refer again to von Storch and Zwiers (1999) and Hannachi et al. (2007).

Appendix B

Supplementary material for Chapter 3

B.1 Seasonal cycle from climatologies

In Chapter 3 we show time mean data from some variables und its differences to observations. We add here the seasonal mean values of some of the variables mean sea level pressure (Figure B.1), 2 m temperature (Figure B.2) as well as precipitation (Figure B.3).

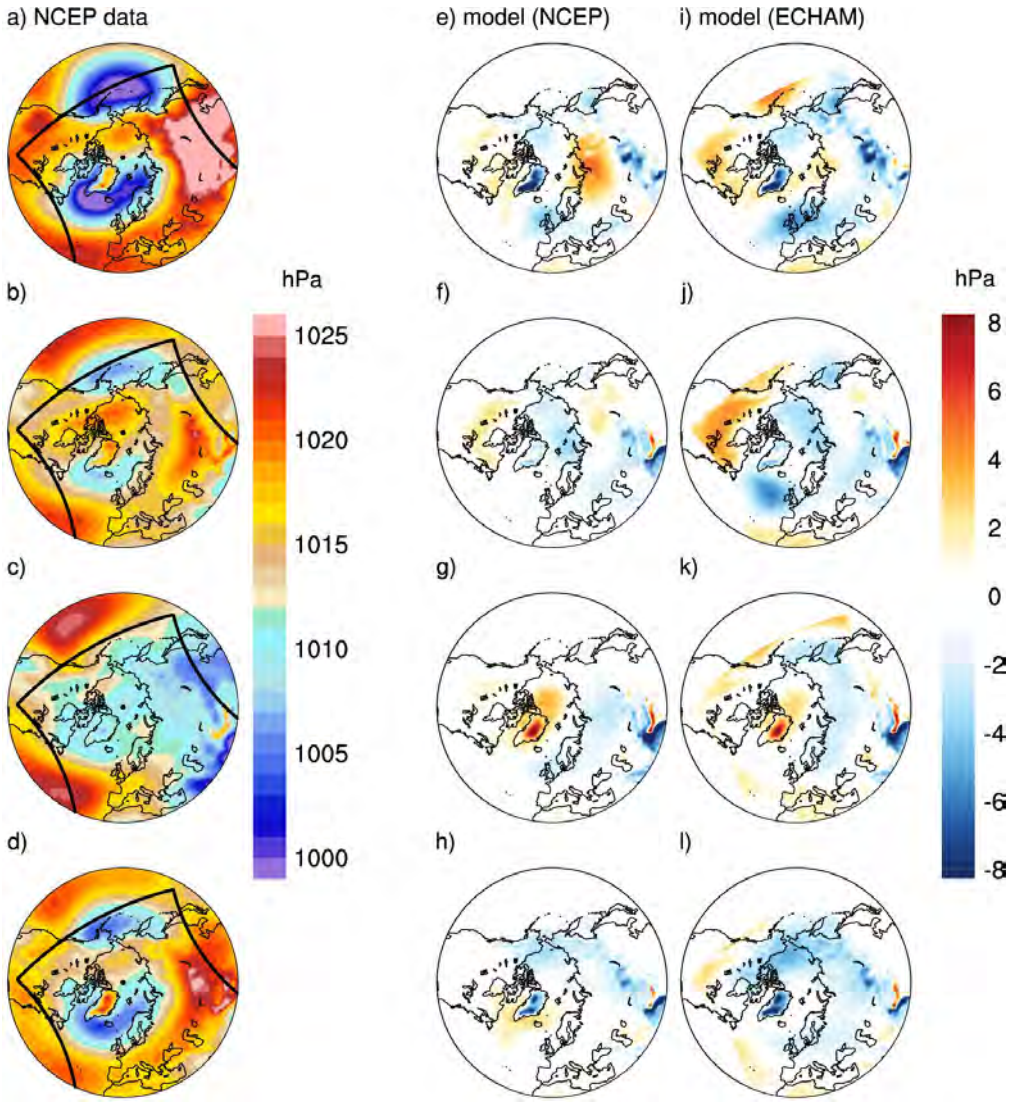

Figure B.1: a) - d) Seasonal means, starting with DJF, of mean sea level pressure from NCEP reanalysis data for the years 1980 - 1999. e) - h) Difference of the seasonal means of mean sea level pressure from the NCEP forced experiments with NCEP reanalysis data, for the years 1980 - 1999. i) - l) Difference of the seasonal means of mean sea level pressure from the ECHAM forced experiments with NCEP reanalysis data, either for the years 1980 - 1989 or 1980 - 1999.

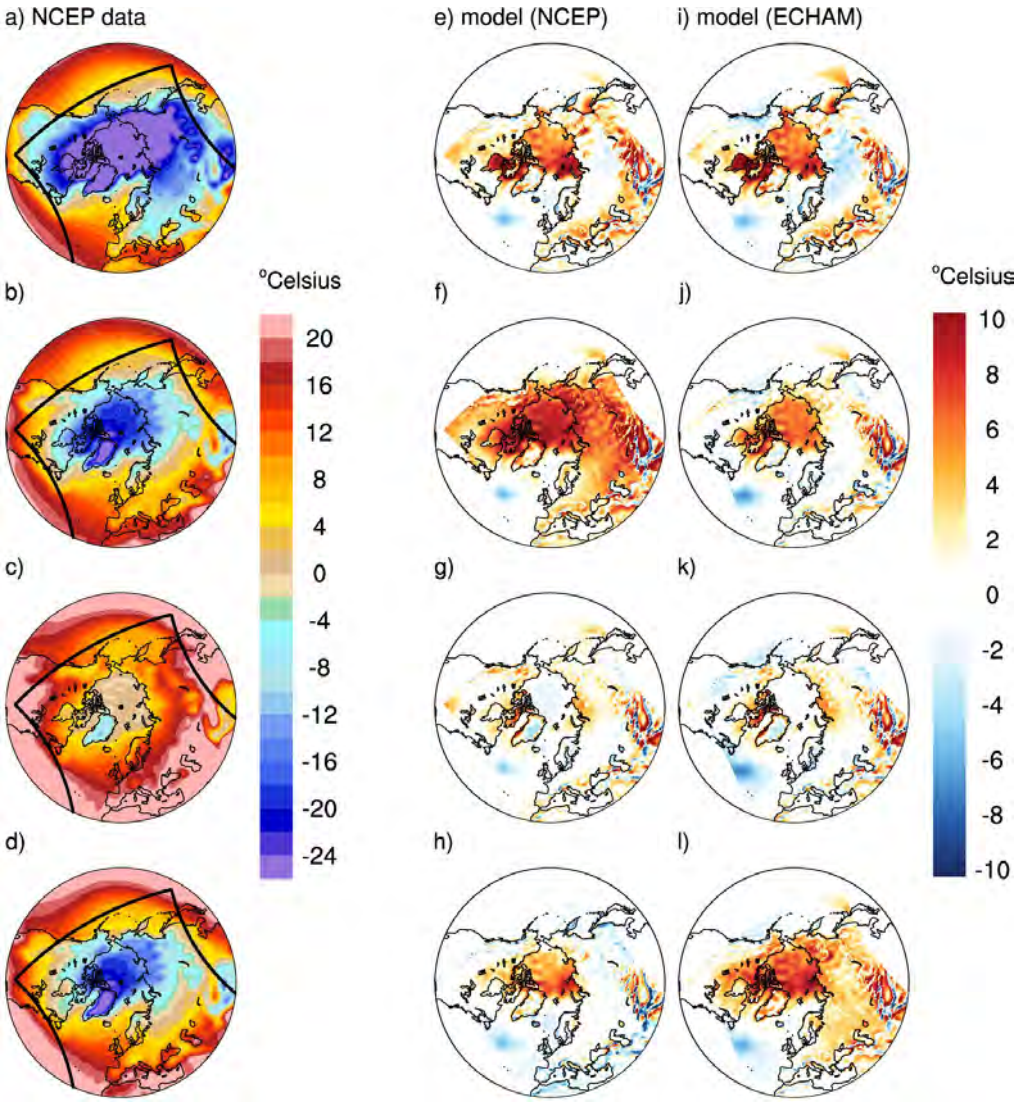

Figure B.2: a) - d) Seasonal means, starting with DJF, of 2 m temperature from NCEP reanalysis data for the years 1980 - 1999. e) - h) Difference of the seasonal means of 2 m temperature from the NCEP forced experiments with NCEP reanalysis data, for the years 1980 - 1999. i) - l) Difference of the seasonal means of 2 m temperature from the ECHAM forced experiments with NCEP reanalysis data, either for the years 1980 - 1989 or 1980 - 1999.

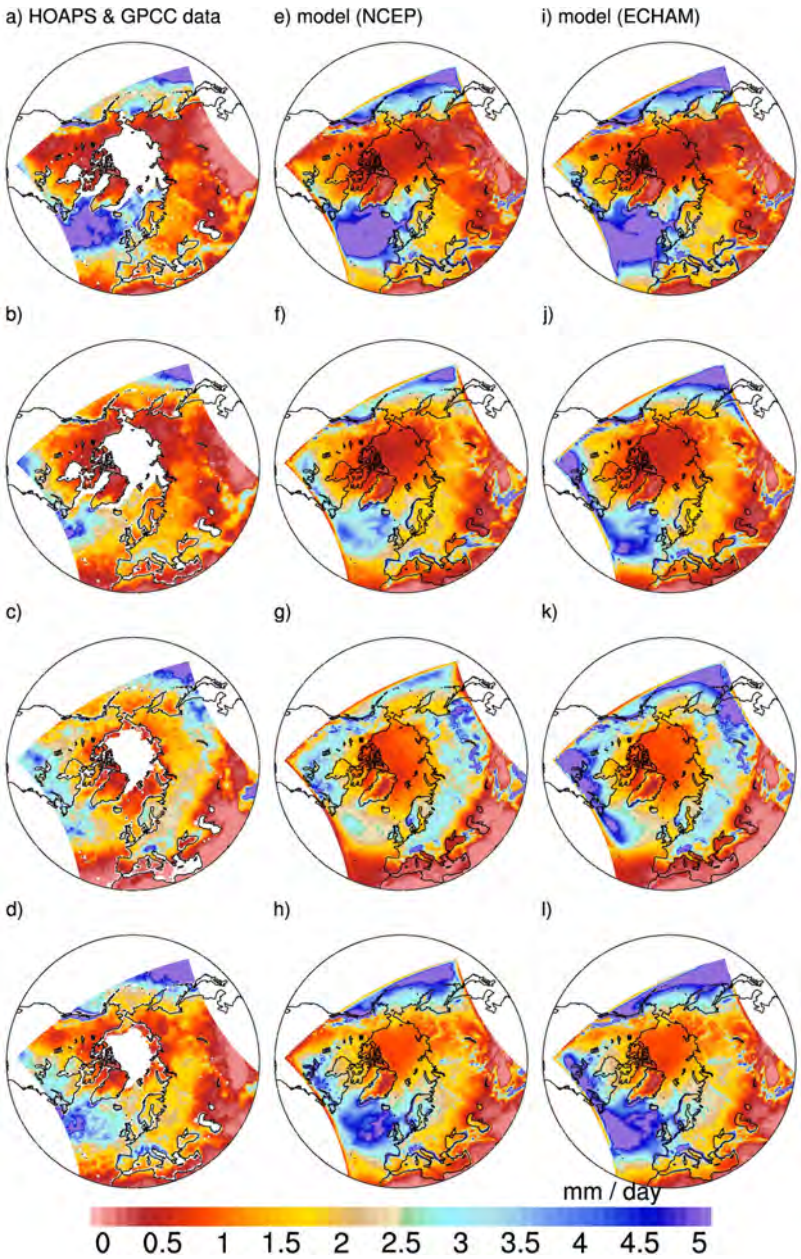

Figure B.3: a) - d) Seasonal means, starting with DJF, of precipitation from GPCC and HOAPS data for the years 1990 - 1999. e) - h) Seasonal means of precipitation from the NCEP forced experiments, for the years 1980 - 1999. i) - l) Seasonal means of precipitation from the ECHAM forced experiments, either for the years 1980 - 1989 or 1980 - 1999.

B.2 Stream function of the Atlantic ocean meridional overturning

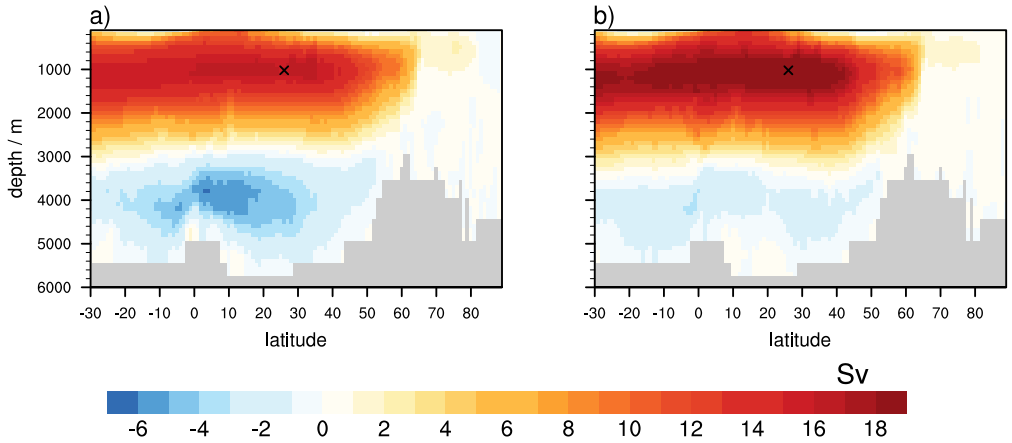

Figure B.4: Meridional overturning circulation in Sv from a) one NCEP forced experiment for the years 1980 - 1999 and b) one ECHAM forced experiment for the years 1980 - 1989. The black cross indicates the location of the timeseries shown in Figure 3.23. Positive values indicate clockwise and negative values counterclockwise circulation.

Appendix C

Supplementary material for Chapter 4

C.1 Leading empirical orthogonal function

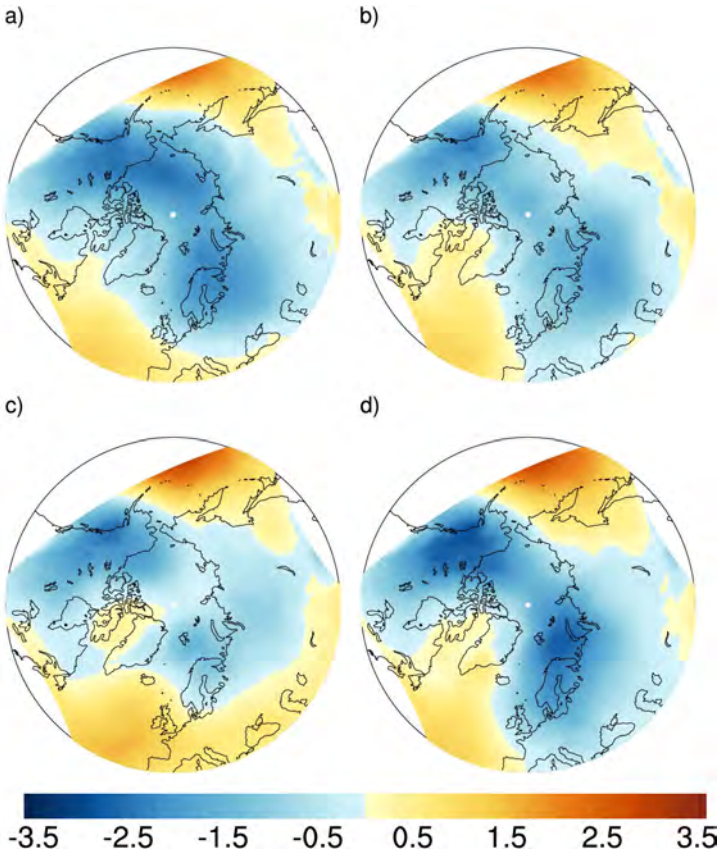

Figure C.1: Regression coefficient between DJF mean sea level pressure from our four model ensemble members (a)-d) and the AO index from the global ECHAM data in hPa per standard deviation of the AO index.

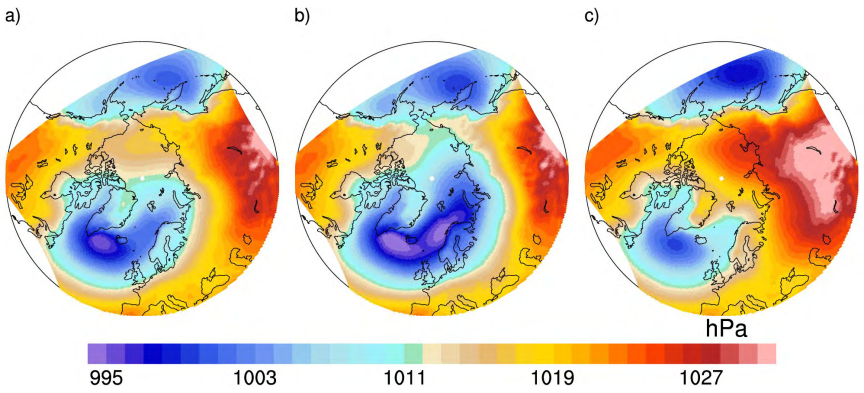

Figure C.2: DJF mean sea level pressure for a) the ensemble mean of four ECHAM forced experiments, b) the posivite EOF 1 years and c) the negative EOF 1 years of these experiments.

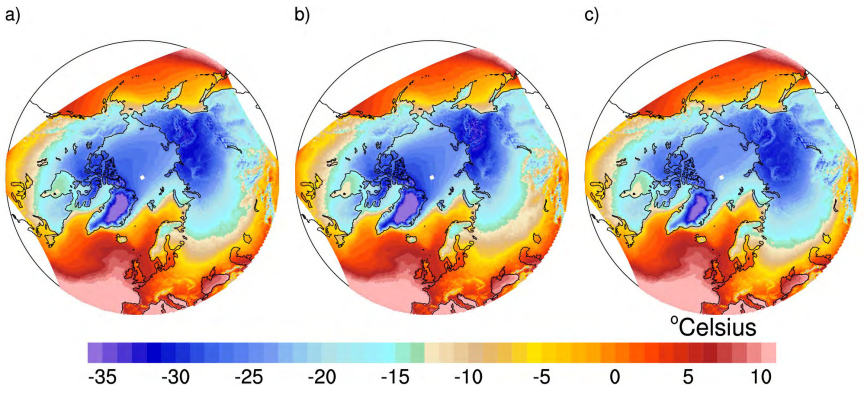

Figure C.3: DJF 2 m air temperature for a) the ensemble mean of four ECHAM forced experiments, b) the posivite EOF 1 years and c) the negative EOF 1 years of these experiments.

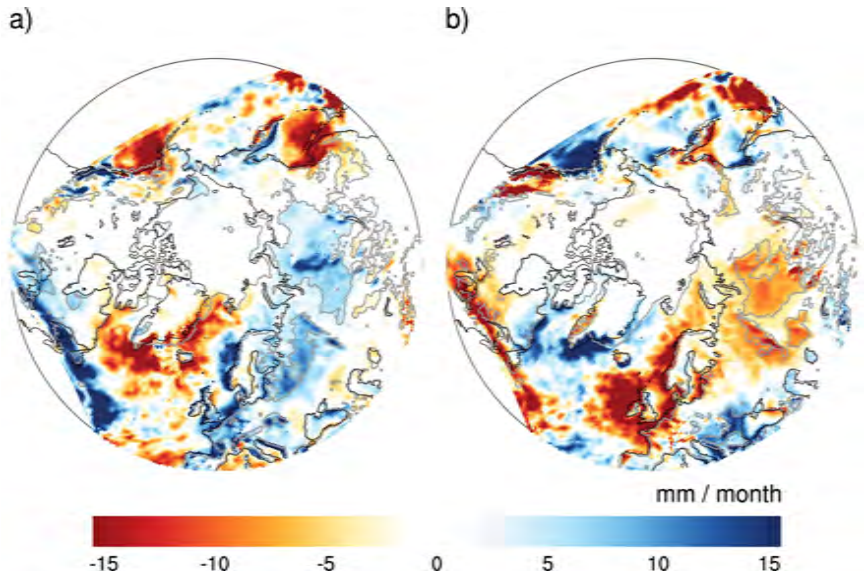

Figure C.4: Difference between DJF net precipitation (= precipitation minus evaporation) from a) the positive EOF 1 years and b) the negative EOF 1 years and the overall mean of DJF precipitation. The grey contour line indicates the region where the composite years differ significantly from the mean value (as defined in A.3).

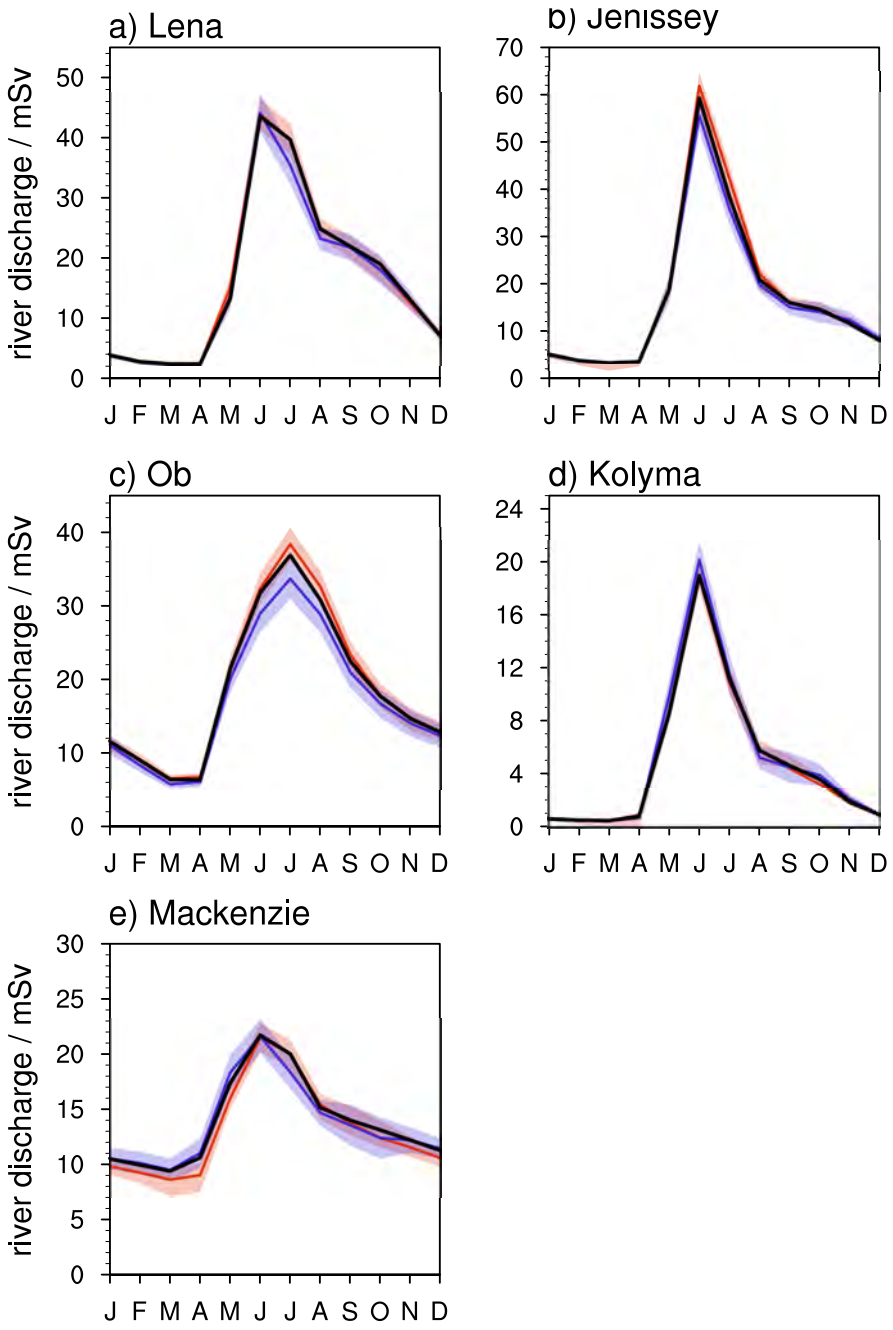

Figure C.5: Annual cycle of river discharge of large Arctic rivers. The green line shows the ensemble mean over the whole time period, the red and blue lines represent the positive and negativ EOF 1 years, respectively. The shaded areas indicate ± two standard deviations of the given subsets for positive and negative EOF 1 years (see A.3).

C.2 Second leading empirical orthogonal function

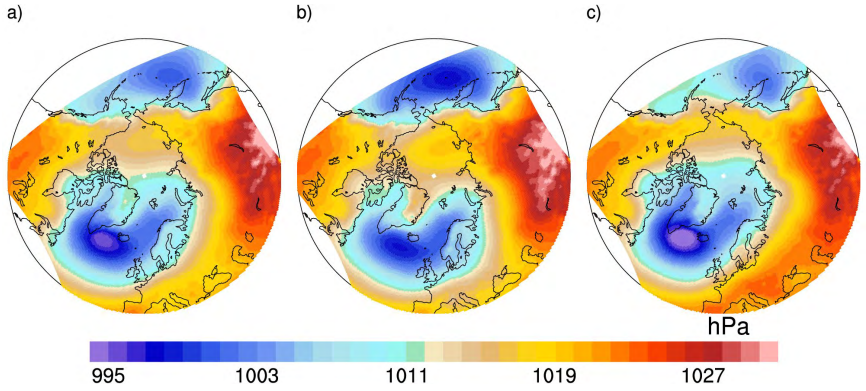

Figure C.6: DJF mean sea level pressure for a) the ensemble mean of four ECHAM forced experiments, b) the posivite EOF 2 years and c) the negative EOF 2 years of these experiments.

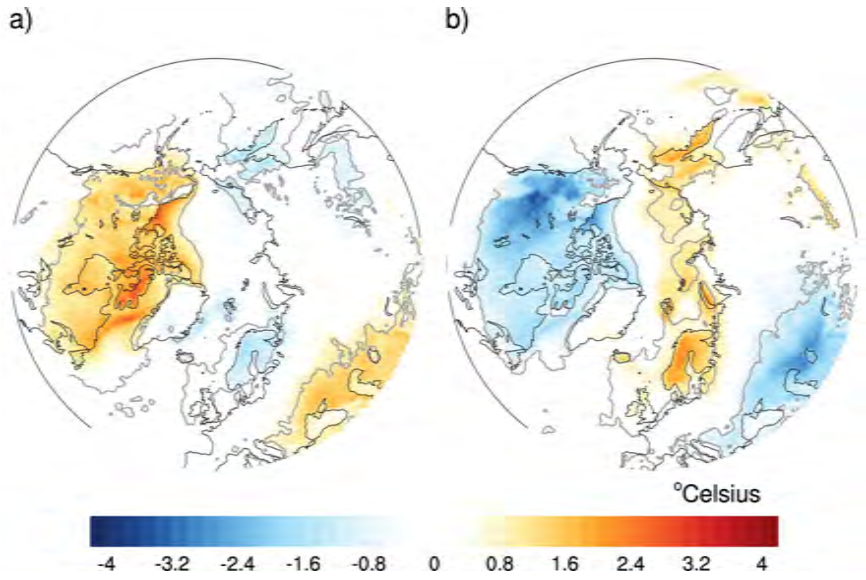

Figure C.7: Difference between DJF 2 m temperature from a) the positive EOF 2 years and b) the negative EOF 2 years and the overall mean of DJF 2 m temperature. The grey contour line indicates the region where the composite years differ significantly from the mean value (as defined in A.3).

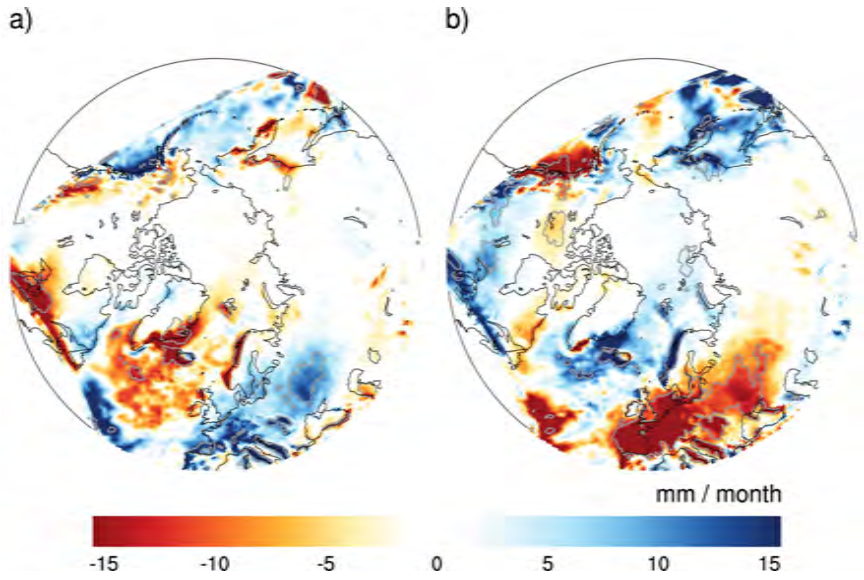

Figure C.8: Difference between DJF precipitation in mm / month from a) the positive EOF 2 years and b) the negative EOF 2 years and the overall mean of DJF precipitation. The grey contour line indicates the region where the composite years differ significantly from the mean value (as defined in A.3).

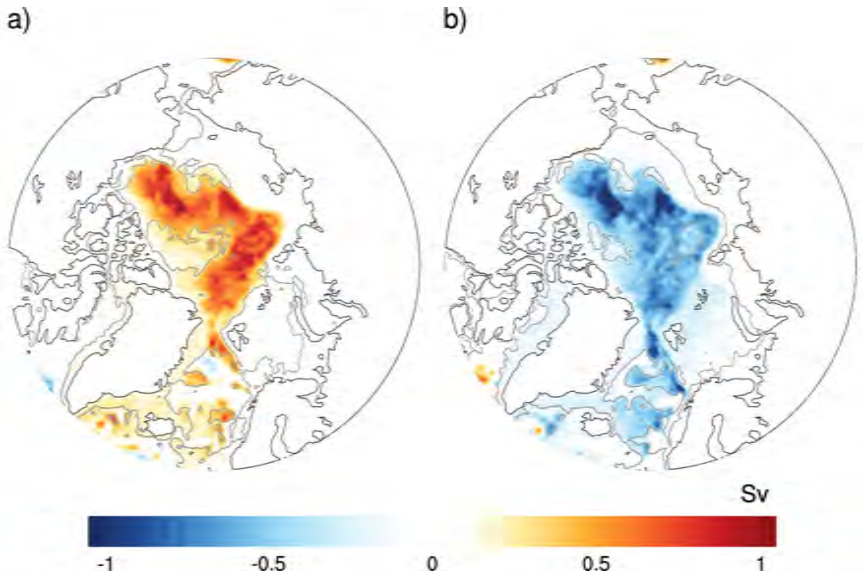

Figure C.9: Difference between the yearly mean barotropic stream function in Sv from a) the positive EOF 2 years and b) the negative EOF 2 years and the overall yearly mean of the barotropic stream function. The grey contour line indicates the region where the composite years differ significantly from the mean value (as defined in A.3).

Appendix D

Additional remarks on the forcing

While the forcing fields for the 20^{th} century experiments seem to be correct, we faced problems with the forcing fields for the 21^{st} century. When we were analyzing our model results, it turned out that some forcing fields in some months do not correspond to the underlying global model that was used to produce the forcing. The underlying experiment (A1B_3) was performed with the global coupled model ECHAM 5/ MPIOM within the framework of the Fourth Assessment Report of the Intergovernmental Panel of Climate Change and was using the emission scenario A1B. Table D.1 documents the years where problems appeared. We detected the inconsistencies either in the forcing fields or in the model output.

Year	Problem	Procedure
2001	interpolation of topography wrong in Asia in atmosphere fields; influence only regional in atmosphere	exclude 2001 in analysis of atmospheric variables
2032	ocean forcing does not match with global model	do not exclude year, because no systematic warm or cold bias could be seen
2036	large anomalies in heat flux over ocean	exclude years 2036 - 2038
2042	error in atmospheric sea level pressure forcing; only in December	do not exclude year, no systematic bias
2043	error in atmospheric sea level pressure forcing; only in December	do not exclude year, no systematic bias
2047	large positive anomaly in atmospheric temperature forcing	exclude 2047 - 2049

Table D.1: List of years where problems were detected.

Bibliography

Aagaard, K. and E. C. Carmack, 1989: The Role of Sea Ice and Other Fresh Water in the Arctic Circulation. *Journal of Geophysical Research*, **94**.

Aldrian, E., D. Sein, D. Jacob, L. Dümenil Gates, and R. Podzun, 2005: Modelling of Indonesian Rainfall with a Coupled Regional Model. *Climate Dynamics*, **25**, 1–17, doi: 10.1007/s00382-004-0483-0.

Andersson, A., K. Fennig, C. Klepp, S. Bakan, H. Grassl, and J. Schulz, 2010: The Hamburg Ocean Atmosphere Parameters and Fluxes from Satellite Data- HOAPS-3. *Earth System Science Data*, **2**, 215–234, doi:10.5194/essd-2-215-2010.

Anisimov, O., D. Vaughan, T. Callaghan, C. Furgal, H. Marchant, T. Prowse, H. Vilhjálmsson, and J. Walsh, 2007: *Climate Change 2007: The Physical Science Basis. Contribution of Working Group II to the Fourth Assessment Report of the Intergovernmental Panel on Climate Change*, chap. Polar regions (Arctic and Antarctic), 653–685. Cambridge University Press.

Antonov, J., S. Levitus, T. Boyer, M. Conkright, T. O'Brien, and C. Stephens, 1998: World Ocean Atlas 1998 Vol. 2: Temperature of the Atlantic Ocean. *NOAA Atlas NESDIS*, **27**.

Arctic Climatology Project, 1997: *Environmental Working Group joint U.S.-Russian Atlas of the Arctic Ocean - winter period*. Environmental Research Institute of Michigan in association with the National Snow and Ice Data Center, CD-ROM.

———, 1998: *Environmental Working Group joint U.S.-Russian Atlas of the Arctic Ocean - summer period*. Environmental Research Institute of Michigan in association with the National Snow and Ice Data Center, CD-ROM.

Bacon, S., W. J. Gould, and Y. Jia, 2003: Open-ocean convection in the Irminger Sea. *Geophysical Research Letters*, **30**, doi:10.1029/2002GL016271.

Baldwin, M. P. and T. J. Dunkerton, 1999: Propagation of the Arctic Oscillation from the stratosphere to the troposphere. *Journal of Geophysical Research*, **104 (D24)**.

Boyer, T., S. Levitus, J. Antonov, M. Conkright, T. O'Brien, and C. Stephens, 1998: World Ocean Atlas 1998 Vol. 4: Salinity of the Atlantic Ocean. *NOAA Atlas NESDIS*, **30**.

Cavalieri, D., C. Parkinson, P. Gloersen, and H. Zwally, 1996: Sea Ice Concentrations from Nimbus-7 SMMR and DMSP SSM/I-SSMIS Passive Microwave Data, 1979-2010, updated yearly. *Boulder, Colorado USA: National Snow and Ice Data Center. Digital media.*

Chapman, W. L. and J. E. Walsh, 2007: Simulations of Arctic Temperature and Pressure by Global Coupled Models. *Journal of Climate*, **20**, doi:10.1175/JCLI4026.1.

Comiso, J., 1999: Bootstrap Sea Ice Concentrations from Nimbus-7 SMMR and DMSP SSM/I, 1970-2010, updated 2012. *Boulder, Colorado USA: National Snow and Ice Data Center. Digital media.*

Comiso, J. C., C. L. Parkinson, R. Gersten, and L. Stock, 2008: Accelerated decline in the Arctic sea ice cover. *Geophysical Research Letters*, **35**, doi:10.1029/2007GL031972.

Committee on Designing an Arctic Observing Network, N. R. C., 2006: *Toward an Integrated Arctic Observing Network*. The National Academies Press, URL `http://www.nap.edu/openbook.php?record_id=11607`.

Condron, A., P. Winsor, C. Hill, and D. Menemenlis, 2009: Simulated Response of the Arctic Freshwater Budget to Extreme NAO Wind Forcing. *Journal of Climate*, **22**, doi:10.1175/2008JCLI2626.1.

Cullather, R. I., D. H. Bromwich, and M. C. Serreze, 2000: The Athmospheric Hydrologic Cycle over the Arctic Basin from Reanalysis. Part I: Comparison with Observations and Previous Studies. *Journal of Climate*, **13**.

Dai, A. and K. E. Trenberth, 2002: Estimates of Freshwater Discharge from Continents: Latitudinal and Seasonal Variations. *Journal of Hydrometeorology*, **3**, URL `www.cgd.ucar.edu/cas/catalog/surface/dai-runoff/index.html`.

D'Arrigo, R., G. Jacoby, R. Wilson, and F. Panagiotopoulos, 2005: A reconstructed Siberian High index since A.D. 1599 from Eurasian and North American tree rings. *Geophysical Research Letters*, **32**, doi:10.1029/2004GL022271.

Dickson, R., T. Osborn, J. Hurrell, J. Meincke, J. Blindheim, B. Adlandsvik, T. Vinje, G. Alekseev, and W. Maslowski, 2000: The Arctic Ocean Response to the North Atlantic Oscillation. *Journal of Climate*, **13**.

Dickson, R., B. Rudels, S. Dye, M. Karcher, J. Meincke, and I. Yashayaev, 2007: Current estimates of freshwater flux through Arctic and subarctic seas. *Progress in Oceanography*, **73**, 210–230, doi:10.1016/j.pocean.2006.12.003.

Dickson, R. R., J. Meincke, S.-A. Malmberg, and A. J. Lee, 1988: The "great salinity anomaly" in the Northern North Atlantic 1968-1982. *Progress in Oceanography*, **20**, 102–151.

Dodd, P. A., K. J. Heywood, M. P. Meredith, A. C. Naveira-Garabato, A. D. Marca, and K. K. Falkner, 2009: Sources and fate of freshwater exported in the East Greenland Current. *Geophysical Research Letters*, **36**, doi:10.1029/2009GL039663.

Dorn, W., K. Dethloff, and A. Rinke, 2012: Limitations of a coupled regional climate model in the reproduction of the observed Arctic sea-ice retreat. *The Cryosphere*, **6**, 985–998, doi:10.5194/tc-6-985-2012.

Döscher, R. and T. Koenigk, 2013: Arctic rapid sea ice loss events in regional coupled climate scenario experiments. *Ocean Science*, doi:10.5194/os-9-217-2013.

Dümenil Gates, L., S. Hagemann, and C. Golz, 2000: Observed historical discharge data from major rivers for climate model validation. Tech. Rep. 307, Max-Planck-Institut für Meteorologie.

ECMWF, 2002: ECMWF 40 Year Re-analysis (ERA-40) Data Archive. URL `http://www.ecmwf.int/products/data/archive/descriptions/e4/index.html`.

Elizalde, A. and D. Jacob, 2012: Water vapor transport and precipitation over the Mediterranean region as simulated by a regional atmosphere-ocean coupled model, submitted. *Climate Dynamics*.

Elizalde, A., D. Sein, U. Mikolajewicz, and D. Jacob, 2011: Atmosphere-ocean-hydrology coupled regional climate model. Tech. rep., Max-Planck-Institut für Meteorologie.

Fyfe, J., G. Boer, and G. Flato, 1999: The Arctic and Antarctic Oscillations and their Projected Changes Under Global Warming. *Geophysical Research Letters*, **26**, 1601–1604.

Giles, K. A., S. W. Laxon, and A. L. Ridout, 2008: Circumpolar thinning of Arctic sea ice following the 2007 record ice extent minimum. *Geophysical Research Letters*, **35**, doi:10.1029/2008GL035710.

Giles, K. A., S. W. Laxon, A. L. Ridout, D. J. Wingham, and S. Bacon, 2012: Western Arctic ocean freshwater storage increased by wind-driven spin-up of the Beaufort Gyre. *Nature Geoscience*, doi:10.1038/NGEO1379.

Gong, D.-Y. and C.-H. Ho, 2002: The siberian high and climate change over middle to high latitude Asia. *Theoretical and Applied Climatology*, **72**, 1–9.

Greatbatch, R. J., 2000: *The North Atlantic Oscillation*. Stochastic Environmental Research and Risk Assessment; Entretiens Jacques-Cartier, Montreal.

Haak, H., J. Jungclaus, U. Mikolajewicz, and M. Latif, 2003: Formation and propagation of great salinity anomalies. *Geophysical Research Letters*, **30**, doi:10.1029/2003GL017065.

Hagemann, S. and L. Dümenil, 1998: Documentation for the Hydrological Discharge Model. Tech. Rep. 17, Max-Planck-Institut für Meteorologie.

Häkkinen, S., 1999: A Simulation of Thermohaline Effects of a Great Salinity Anomaly. *Journal of Climate*, **12**.

Hannachi, A., I. Jollcliffe, and D. Stephenson, 2007: Empirical orthogonal functions and related techniques in atmospheric science: A review. *International Journal of Climatology*, **27**, Copernicus Publications, doi:10.5194/tc-6-985-2012.

Held, I. M. and B. J. Soden, 2006: Robust Responses of the Hydrological Cycle to Global Warming. *Journal of Climate*, **19**, doi:10.1175/2010JCLI4045.1.

Hibler, W., 1979: A Dynamic Thermodynamic Sea Ice Model. *Journal of Physical Oceanography*, **9**.

Holland, M. M., J. Finnis, and M. C. Serreze, 2006: Simulated Arctic Ocean Freshwater Budgets in the Twentieth and Twenty-First Centuries. *Journal of Climate*, **19**, doi: 10.1175/JCLI3967.1.

Hurrell, J. W., 1995: Decadal Trends in the North Atlantic Oscillation: Regional Temperatures and Precipitation. *Science*, **269**, 676–679.

———, 1996: Influence of variations in extratropical wintertime teleconnections on Northern Hemisphere temperature. *Geophysical Research Letters*, **6**, 665–668.

Hurrell, J. W., Y. Kushnir, G. Ottersen, and M. Visbeck, 2003: *The North Atlantic Oscillation: Climatic Significance and Environmental Impact*, chap. An Overview of the North Atlantic Oscillation. American Geophysical Untion, doi:10.1029/134GM01.

International Arctic Science Committee, 2010: Freshwater discharge in the Arctic. *The Encyclopedia of Earth*, URL `http://www.eoearth.org/article/Freshwater_discharge_in_the_Arctic`.

Jacob, D., 2001: A note to the simulation of the annual and inter-annual variability of the water budget over the Baltic Sea drainage basin. *Meteorology and Atmospheric Physics*, **77**, 61–73.

Jahn, A., B. Tremblay, L. a. Mysak, and R. Newton, 2010: Effect of the large-scale atmospheric circulation on the variability of the Arctic Ocean freshwater export. *Climate Dynamics*, **34**, 201–222, doi:10.1007/s00382-009-0558-z.

Jahn, A., y. Aksenov, B. de Cuevas, L. de Steur, S. Häkkinen, E. Hansen, C. Herbaut, M.-N.Houssais, M. Karcher, F. Kauker, C. Lique, A. Nguyen, P. Pemperton, D. Worthen, and J. Zhang, 2012: Arctic Ocean freshwater: How robust are model simulations? *Journal of Geophysical Research*, **117**, doi:10.1029/2012JC007907.

Jeong, J.-H., T. Ou, H. W. Linderholm, B.-M. Kim, S.-J. Kim, J.-S. Kug, and D. Chen, 2011: Recent Recovery of the Siberian High Intensity. *Journal of Geophysical Research*, in press, doi:10.1029/2011JD015904.

Kaleschke, L., N. Maaß, C. Haas, S. Hendricks, G. Heygster, and R. Tonboe, 2010: A sea-ice thickness retrieval model for 1.4 GHz radiometry and application to airborne measurements over low salinity sea-ice. *The Cryosphere*, **4**, 583–592, doi: 10.5194/tc-4-583-2010.

Kalnay, E., M. Kanamitsu, R. Kistler, W. Collins, D. Deaven, L. Gandlin, M. Iredell, S. Saha, G. White, J. Woollen, Y. Zhu, M. Chelliah, W. Ebisuzaki, W. Higgins, J. Janowiak, K. Mo, C. Ropelewski, J. Wang, A. Leetmaa, R. Reynolds, R. Jenne, and D. Joseph, 1996: The NCEP/NCAR 40-Year Reanalysis Project. *Bulletin of the American Meteorological Society*, **77**, 437–470.

Kanzow, T., S. Cunningham, W. Johns, J.-M. Hirschi, J. Marotzke, M. Baringer, C. Meinen, M. Chidichimo, C. Atkinson, L. Beal, H. Bryden, and J. Collins, 2010: Seasonal variability of the atlantic meridional overturning circulation at 26.5 °N. *Journal of Climate*, **23**, 5678–5698, doi:10.1175/2010JCLI3389.1.

Karcher, M., A. Beszczynska-Möller, F. Kauker, R. Gerdes, S. Heyen, B. Rudels, and U. Schauer, 2011: Arctic Ochean warming and its consequences for the Denmark Strait overflow. *Journal of Geophysical Research*, **116**, doi:10.1029/2010JC006265.

Kattsov, V. M., J. E. Walsh, W. L. Chapman, V. A. Govorkova, T. V. Pavlova, and X. Zhang, 2007: Simulations and Projection of Arctic Freshwater Budget Components by IPCC AR4 Global Climate Models. *Journal of Hydrometeorology*, **8**, doi:10.1175/JHM575.1.

Kodera, K. and Y. Kuroda, 2000: Tropospheric and Stratospheric Aspects of the Arctic Oscillation. *Geophysical Research Letters*, **27 (20)**.

Koenigk, T., R. Döscher, and G. Nikulin, 2010: Arctic future scenario experiments with a coupled regional climate model. *Tellus*, doi:10.1111/j.1600-0870.2010.00474.x.

Koenigk, T., U. Mikolajewicz, H. Haak, and J. Jungclaus, 2006: Variability of Fram Strait sea ice export: causes, impacts and feedbacks in a coupled climate model. *Climate Dynamics*, **26**, doi:10.1007/s00382-005-0060-1.

———, 2007: Arctic freshwater export in the 20th and 21st centuries. *Journal of Geophysical Research*, **112**, doi:10.1029/2006JG000274.

Koldunov, N. V., D. Stammer, and J. Marotzke, 2010: Present-Day Arctic Sea Ice Variability in the Coupled ECHAM5/MPI-OM Model. *Journal of Climate*, **23**, doi: 10.1175/2009JCLI3065.1.

Kwok, R., 2011: Observational assessment of Arctic Ocean sea ice motion, export, and thickness in CMIP3 climate simulations. *Journal of Geophysical Research*, **116**, doi: 10.1029/2011JC007004.

Kwok, R., G. Cunningham, and S. Pang, 2004: Fram Strait sea ice outflow. *Journal of Geophysical Research*, **109**, doi:10.1029/2003JC001785.

Lammers, R. B., A. I. Shiklomanov, C. J. Vörösmarty, B. M. Fekete, and B. J. Peterson, 2001: Assessment of contemporary Arctic river runoff based on observational discharge records. *Journal of Geophysical Research*, **106 (D4)**, 3321–3334.

Latarius, K., 2013: Über die Wassermassentransformation im Europäischen Nordmeer; Prozess-Studien und Budgets. *PhD thesis, University of Hamburg*.

Lavender, K. L., R. E. Davis, and W. B. Owens, 2002: Observations of Open-Ocean Deep Convection in the Labrador Sea from Subsurface Floats. *Journal of physical oceanography*, **32**.

Li, P., Y. Zhang, and J. Liu, 2010: Dominant climate factors influencing the Arctic runoff and association between the Arctic runoff and sea ice. *Acta Oceanologica Sinica*, **29**, 10–20.

Lichota, G. B. and S. Wilson, 2010: SAON Data Management Workshop Report; Developing a Strategic Approach. Tech. rep., URL `http://www.arcticobserving.org/reports`.

Limpasuvan, V. and D. L. Hartmann, 2000: Wave-Maintained Annular Modes of Climate Variability. *Journal of Climate*, **13**.

Majewski, D., 1991: The EUROPA-model of the Deutscher Wetterdienst. *Conference proceedings; ECMWF Seminar on numerical methods in atmospheric models*, **2**, 147–193.

Marsland, S., H. Haak, J. Jungclaus, M. Latif, and F. Röske, 2003: The Max-Planck-Institute global ocean/sea ice model with orthogonal curvilinear coordinates. *Ocean Modelling*, **5**, 91–127.

Maslanik, J., 1999: Near-Real-Time DMSP SSM/I-SSMIS Daily Polar Gridded Sea Ice Concentrations, updated daily. *Boulder, Colorado USA: National Snow and Ice Data Center*.

Massonnet, F., T. Fichefet, H. Goosse, C. Bitz, G. Philippon-Berthier, M. Holland, and P. Barriat, 2012: Constraining projections of summer Arctic sea ice. *The Cryosphere*, **6**, doi:10.5194/tc-6-1383-2012.

McCarthy, G., E.Frajka-Williams, W. Johns, M.O.Baringer, C. Meinen, H. Bryden, D. Rayner, A. Duchez, C. Roberts, and S. Cunningham, 2012a: Mean Atlantic meridional overturning circulation across 26.5 °N from eddy-resolving simulations compared to observations. *Journal of Geophysical Research*, **117**, doi:10.1029/2011JC007586.

McCarthy, G., E. Frajka-Williams, W. Johns, M. Baringer, C. Meinen, H. Bryden, D. Rayner, A. Duchez, C. Roberts, and S. Cunningham, 2012b: Observed interannual variability of the Atlantic meridional overturning circulation at 26.5 °N. *Geophysical Research Letters*, **39**, doi:10.1029/2012GL052933.

Meehl, G., T. Stocker, W. Collins, P. Friedlingstein, A. Gaye, J. Gregory, A. Kitoh, R. Knutti, J. Murphy, A. Noda, S. Raper, I. Watterson, A. Weaver, and Z.-C. Zhao, 2007: *Climate Change 2007: The Physical Science Basis. Contribution of Working Group I to the Fourth Assessment Report of the Intergovernmental Panel on Climate Change*, chap. Global Climate Projections. Cambridge University Press.

Mikolajewicz, U., D. Sein, D. Jacob, T. Königk, R. Podzun, and T. Semmler, 2005: Simulating Arctic sea ice variability with a coupled regional atmosphere-ocean-sea ice model. *Meteorologische Zeitschrift*, **14**, 793–800.

Morawitz, W., P. Sutton, P. Worcester, and B. Cornuelle, 1996: Three-Dimensional Observations of a Deep Convective Chimney in the Greenland Sea during Winter 1988/89. *Journal of Physical Oceanography*, **29**.

Notz, D., F. A. Haumann, H. Haak, and J. H. Jungclaus, 2013: Arctic sea-ice evolution as modeled by Max Planck Institute for Meteorology's Earth system model. *Journal of Advances in Modeling Earth Systems*, **5**, doi:10.1002/jame.20016.

Overland, J. E., M. C. Spillane, D. B. Percival, M. Wang, and H. O. Mofjeld, 2004: Seasonal and Regional Variation of Pan-Arctic Surface Air Temperature over the Instrumental Record. *Journal of Climate*, **17**, doi:http://dx.doi.org/10.1175/1520-0442(2004)017⟨3263:SARVOP⟩2.0.CO;2.

Overland, J. E. and M. Wang, 2010: Large-scale atmospheric circulation changes are associated with the recent loss of Arctic sea ice. *Tellus A*, **62**, 1–9, doi:10.1111/j.1600-0870.2009.00421.x.

Panagiotopoulos, F., M. Shahgedanova, A. Hannachi, and M. Shahgedanova, 2005: Observed Trends and Teleconnections of the Siberian High: A Recently Declining Center of Action. *Journal of Climate*, **18**.

Parkinson, C. L., D. J. Cavalieri, P. Gloersen, H. J. Zwally, and J. C. Comiso, 1999: Arctic sea ice extents, areas, and trends, 1978 - 1996. *Journal of Geophysical Research*, **104**, 837–856.

Peterson, B. J., R. M. H. abd James W. McClelland, C. J. Vörösmarty, R. B. Lammers, A. I. Shiklomanov, I. A. Shiklomanov, and S. Rahmsdort, 2002: Increasing River Discharge to the Arctic Ocean. *Science*, **298 (5601)**, 2171–2173, doi:10.1126/science.1077445.

Polyakov, I., G. Alekseev, L. Timokhov, U. Bhatt, R. Colony, H. Simmons, D. Walsh, J. Walsh, and V. Zakharov, 2004: Variability of the Intermediate Atlantic Water of the Arctic Ocean over the Last 100 Years. *Journal of Climate*, **17**.

Prinsenberg, S. and J. Hamilton, 2005: Monitoring the Volume, Freshwater and Heat Fluxes Passing through Lancaster Sound in the Canadian Arctic Archipelago. *Atmosphere Ocean*, **43**, 1–22.

Proshutinsky, A., R. H. Bourke, and F. A. McLaughlin, 2002: The role of the Beaufort Gyre in the Arctic climate variability: Seasonal to decadal climate scales. *Geophysical Research Letters*, **29 (23)**, doi:10.1029/2002GL015847.

Proshutinsky, A., R. Krishfield, M.-L. Timmermans, J. Toole, E. Carmack, F. McLaughlin, W. J. Williams, S. Zimmermann, M. Itoh, and K. Shimada, 2009: Beaufort Gyre freshwater reservoir: State and variability from observations. *Journal of Geophysical Research*, **114**, doi:10.1029/2008JC005104.

Rawlins, M. A., M. Steele, M. M. Holland, J. C. Adam, J. E. Cherry, J. A. Francis, P. A. Groisman, L. D. Hinzman, T. G. Huntington, D. L. Kane, J. S. Kimball, R. Kwok, R. B. Lammers, C. M. Lee, D. P. Lettenmaier, K. C. McDonald, E. Podest, J. W. Pundsack, B. Rudels, M. C. Serreze, A. Shiklomanov, O. Skagseth, T. J. Troy, C. J. Vörösmarty, M. Wensnahan, E. F. Wood, R. Woodgate, D. Yang, K. Zhang, and T. Zhang, 2010: Analysis of the Arctic System for Freshwater Cycle Intensification: Observations and Expectations. *Journal of Climate*, doi:10.1175/2010JCLI3421.1.

Rind, D., J. Perlwitz, and P. Lonergan, 2005: AO / NAO response to climate change: 1. Respective influences of stratospheric and tropospheric climate changes. *Journal of Geophysical Research*, **110**, doi:10.1029/2004JD005103.

Roeckner, E., K. Arpe, L. Bengtsson, M. Christoph, M. Claussen, L. Dümenil, M. Esch, M-Giorgetta, U. Schlese, and U. Schulzweida, 1996: The atmospheric general circulation model ECHAM-4: Model description and simulation of present-day climate. Tech. Rep. 218, Max-Planck-Institut für Meteorologie.

Rothrock, D., Y. Yu, and G. Maykut, 1999: Thinning of the Arctic sea-ice cover. *Geophysical Research Letters*, **26**, 3469–3472, doi:10.1029/1999GL010863.

Rudels, B., D. Quadfasel, H. Friedrich, and M.-N. Houssais, 1989: Greenland Sea convection in the winter of 1987 - 1988. *Journal of Geophysical Research*, **94**, 3223–3227.

Rudolf, B., A. Becker, U. Schneider, A. Meyer-Christoffer, and M. Ziese, 2010: GPCC Status Report. Tech. rep., Global Precipitation Climatology Centre.

Rudolf, B. and U. Schneider, 2005: *2nd workshop of the International Precipitation Working Group*, chap. Calculation of gridded precipitation data for the global land-surface using in-situ gauge observations.

Schmittner, A., M. Latif, and B. Schneider, 2005: Model projections of the North Atlantic thermohaline circulation for the 21st century assessed by observations. *Geophysical Research Letters*, **32**, doi:10.1029/2005GL024368.

Schweiger, A., R. Lindsay, J. Zhang, M. Steele, H. Stern, and R. Kwok, 2011: Uncertainty in Modeled Arctic Sea Ice Volume. *Journal of Geophysical Research*, **116**, doi:10.1029/2011JC007084.

Screen, J. A. and I. Simmonds, 2010: The central role of diminishing sea ice in recent Arctic temperature amplification. *Nature Letters*, **464**, doi:10.1038/nature09051.

Sein, D. and N. Sudarchikova, 2013: Coupled ocean - atmosphere feedbacks in Arctic. *Poster presentation at DKRZ user workshop, Hamburg, Germany*, URL `http://www.dkrz.de/Klimaforschung-en/projects/poster-zum-nutzerworkshop-2013`.

Serreze, M. C., A. P. Barrett, A. G. Slater, R. A. Woodgate, K. Aagaard, R. B. Lammers, M. Steele, R. Moritz, M. Meredith, and C. M. Lee, 2006: The large-scale freshwater cycle of the Arctic. *Journal of Geophysical Research*, **111**, doi:10.1029/2005JC003424.

Serreze, M. C. and R. G. Barry, 2005: *The Arctic Climate System*. Cambridge University Press.

Shiklomanov, I. A., R. Lammers, B. Peterson, and C. Vorosmarty, 2000: *The Freshwater Budget of the Arctic Ocean*, chap. The Dynamics of River Water Inflow to the Arctic Ocean. Kluwer Academic Publishers, Netherlands.

Shiklomanov, I. A. and A. I. Shiklomanov, 2003: Climatic Change and the River Runoff into the Arctic Ocean. *Water Resources*, **30**, doi:0097-8078/03/3006-0593.

Spreen, G., S. Kern, D. Stammer, and E. Hansen, 2009: Fram Strait sea ice volume export estimated between 2003 and 2008 from satellite data. *Geophysical Research Letters*, **32**, doi:10.1029/2009GL039591.

Steele, M., R. Morley, and W. Ermold, 2001: PHC: A Global Ocean Hydrography with a High-Quality Arctic Ocean. *Journal of Climate*, **14**.

Stroeve, J. C., V. Kattsov, A. Barrett, M. Serreze, and T. Pavlova, 2012: Trends in Arctic sea ice extent from CMIP5, CMIP3 and observations. *Geophysical Research Letters*, **39**, doi:10.1029/2012GL052676.

Thompson, D. W. and J. M. Wallace, 1998: The Arctic Oscillation signature in the wintertime geopotential height and temperature fields. *Geophysical Research Letters*, **25**, 1297–1300.

Tsukernik, M., C. Deser, M. Alexander, and R. Tomas, 2009: Atmospheric forcing of Fram Strait sea ice export: a closer look. *Climate Dynamics*, doi:10.1007/s00382-009-0647-z.

Valcke, S., 2006: OASIS 3 User Guide. Tech. Rep. 3, CERFACS.

Vavrus, S. J., M. M. Holland, A. Jahn, D. A. Bailey, and B. A. Blazey, 2011: Twenty-First-Century Arctic Climate Change in CCSM4. *Journal of Climate*, **25**, doi:10.1175/JCLI-D-11-00220.1.

Vinje, T., 2001: Fram Strait Ice Fluxes and Atmospheric Circulation: 1950-2000. *Journal of Climate*, **14**, 3508–3517.

Visbeck, M. H., J. W. Hurrell, L. Polvani, and H. M. Cullen, 2001: The North Atlantic Oscillation: Past, present, and future. *PNAS*, **23**.

von Storch, H. and F. W. Zwiers, 1999: *Statistical Analysis in Climate Research*. Cambridge University Press.

Vörösmarty, C. J., B. Peterson, R. Lammers, I. Shiklomanov, and A. Shiklomanov, 1998: R-ArcticNET dataset. URL `http://www.R-arcticnet.sr.unh.edu/`.

Wadhams, P., J. Holfort, E. Hansen, and J. Wilkinson, 2002: A deep convective chimney in the winter Greenland Sea. *Geophysical Research Letters*, **26**, doi:10.1029/2001GL014306.

Weeks, W., 2010: *On Sea Ice*. University of Alaska Press.

Woodgate, R. A. and K. Aagaard, 2005: Revising the Bering Strait freshwater flux into the Arctic Ocean. *Geophysical Research Letters*, **32**, doi:10.1029/2004GL021747.

Woodgate, R. A., K. Aagaard, and T. Weingartner, 2005: Monthly temperature, salinity, and transport variability of the Bering Strait throughflow. *Geophysical Research Letters*, **32**, doi:10.1029/2004GL021880.

Wu, B. Y., J. Su, and R. Zhang, 2011: Effects of autumn-winter Arctic sea ice on winter Siberian High. *Chinese Science Bulletin*, **56**, 3220–3228, doi:10.1007/s11434-011-4696-4.

Zhang, X., J. He, J. Zhang, I. Polyakov, R. Gerdes, J. Inoue, and P. Wu, 2012: Enhanced poleward moisture transport and amplified northern high-latitude wetting trend. *Nature Climate Change*, doi:10.1038/NCLIMATE1631.

Acknowledgements

First of all, I would like to thank my advisor Uwe Mikolajewicz for his guidance, for his support, for sharing his tremendous knowledge, for always having his office door open for discussions, and for his patience in answering my questions. I also would like to thank Lars Kaleschke for advising me, his constructive comments, for inviting me to be a member of the Sea Ice Remote Sensing group and for his encouragement, whenever I needed help. Special thanks go to Detlef Quadfasel for being the chair of my Advisory Panel and his guidance throughout. I would like to thank all, former and current, members of the Ocean Physics group for the great working environment with helpful discussions and coffee breaks. Special thanks go to the REMO-Beratung, Christine and Thomas, as well as to Alberto, for their all-day availability in answering all questions related to REMO and atmospheric dynamics.

This work was supported through the Cluster of Excellence CliSAP, University of Hamburg, funded through the German Science Foundation (DFG). Additionally, I would like to acknowledge CliSAP for the membership in the School of Integrated Climate System Science (SICSS). The model integrations were performed at the German Climate Computing Center (DKRZ). Many thanks also go to the Central IT Service for giving technical support.

Thanks go to *tanh* and to *28 psu* for allowing me to start with my simulations all over again and again. In this context, I would like to thank especially Rosi, Florian, Freja, Juliane, Julia, Florian, Werner, Melanie, Andrea and Nina for their encouraging words, support, their patience and motivation. Your help made me finish this thesis!
Special thanks also go to my office mates Antonija, Eleftheria, Nina and Alex for the perfect mix of working atmosphere and chats all sorts of, especially for their NCL support.

I would like to thank also Sebastian, Florian, Freja, Alberto and Werner for proofreading and their constructive comments, and Philipp for his English phrasing service.

I thank the Aggro-Kicker-team, Florian, Alex, Christine, Alberto, Werner, Thomas and Kevin, for the daily half hour break and the MPI tennis team for all the nice matches and evenings on the tennis court.

I would like to thank my parents, Jutta and Klaus, and my sisters, Lisa and Maren with Bernd, Timmi and Mats, for everything.
Thank you, Sebastian, for always supporting me, believing in me and for always being there!
The last years were exhausting and working on my thesis often felt themed:

"Hast Du Scheiße am Schuh, dann hast Du Scheiße am Schuh." (Andreas Brehme)

It is time to buy new shoes now.

Eidesstattliche Erklärung

Hiermit versichere ich, dass ich diese Arbeit selbständig verfasst habe und keine anderen als die angegebenen Quellen und Hilfsmittel benutzt habe.

Laura Niederdrenk



ISSN 1614-1199